GENERATION OF TERAHERTZ-MODULATED

OPTICAL SIGNALS

USING AlGaAs/GaAs LASER DIODES

by

Dan Andreyevitch Yanson

A thesis submitted for the degree of

Doctor of Philosophy

to the Department of Electronics and Electrical Engineering,

Faculty of Engineering,

University of Glasgow

UNIVERSITY
of
GLASGOW

December 2003

ACKNOWLEDGEMENTS

ABSTRACT

The Thesis reports on the research activities carried out under the Semiconductor-Laser Terahertz-Frequency Converters Project at the Department of Electronics and Electrical Engineering, University of Glasgow.

The Thesis presents the work leading to the demonstration of reproducible harmonic modelocked operation from a novel design of monolithic semiconductor laser, comprising a compound cavity formed by a 1-D photonic-bandgap (PBG) mirror. Modelocking was achieved at a harmonic of the fundamental round-trip frequency with pulse repetition rates from 131 GHz up to a record-high frequency of 2.1 THz. The devices were fabricated from GaAs/AlGaAs material emitting at a wavelength of 860 nm and incorporated two gain sections with an etched PBG reflector between them, and a saturable absorber section.

Autocorrelation studies are reported, which allow the device behaviour for different modelocking frequencies, compound cavity ratios, and type and number of intra-cavity reflectors to be analyzed. The highly reflective PBG microstructures are shown to be essential for subharmonic-free modelocking operation of the high-frequency devices. It was also demonstrated that the multi-slot PBG reflector can be replaced with two separate slots with smaller reflectivity.

Some work was also done on the realisation of a dual-wavelength source using a broad-area laser diode in an external grating-loaded cavity. However, the source failed to deliver the spectrally-narrow lines required for optical heterodyning applications. Photomixer devices incorporating a terahertz antenna for optical-to-microwave down-conversion were fabricated, however, no down-conversion experiments were attempted. Finally, novel device designs are proposed that exploit the remarkable spectral and modelocking properties of compound-cavity lasers.

The ultrafast laser diodes demonstrated in this Project can be developed for applications in terahertz imaging, medicine, ultrafast optical links and atmospheric sensing.

CONTENTS

LIST OF PUBLICATIONS

CONFERENCE AND JOURNAL PUBLICATIONS
ARISING FROM THIS WORK

1. D. A. Yanson, M. W. Street, S. D. McDougall, L. G. Thayne, J. H. Marsh, and E. A. Avrutin, "Terahertz-Frequency Mode-Locking of Monolithic Compound-Cavity Laser Diodes," *Proc. 15th Annual LEOS Meeting,* Glasgow, UK, vol.2, p.710, 10-14 Nov. 2002 *(Invited Paper).*

2. [*]D. A. Yanson, M. W. Street, S. D. McDougall, L. G. Thayne, J. H. Marsh, and E. A. Avrutin, "Ultrafast harmonic mode-locking of monolithic compound-cavity laser diodes incorporating photonic-bandgap reflectors," *IEEE Journal of Quantum Electronics. vol. 38(1),* pp. 1-11, 2002.

3. D. A. Yanson, M. W. Street, S. D. McDougall, L. G. Thayne, J. H. Marsh, and E. A. Avrutin, "Ultrafast harmonic mode-locking of monolithic compound-cavity laser diodes incorporating photonic-bandgap reflectors," *Photonics Technology in the 21st Century, SPIE International Symposium on Photonics & Applications, Singapore, 26-30 Nov. 2001. (Invited Paper).*

4. D. A. Yanson, M. W. Street, E. A. Avrutin, S. D. McDougall, I. G. Thayne, and J. H. Marsh, "THz-frequency mode-locking of monolithic compound-cavity laser diodes incorporating photonic-bandgap reflectors," presented at *Quantum Electronics & Photonics (QEP-15)*, Glasgow, UK, 3-6 September 2001.

5. D. A. Yanson, M. W. Street, S. D. McDougall, I. G. Thayne, and J. H. Marsh, "Terahertz frequency mode-locking of monolithic compound-cavity laser diodes incorporating photonic-bandgap reflectors," *International Topical Meeting on Microwave Photonics. Technical Digest. MWP'01,* pp. 25-28, 2001.

6. D. A. Yanson, M. W. Street, E. A. Avrutin, S. D. McDougall, I. G. Thayne, and J. H. Marsh, "Terahertz Modelocking Frequencies From Monolithic Compound-

---

[*] Full paper is included in the Appendix

Cavity Laser Diodes," presented at *Mini-Symposium on Terabit Optical Networks (Rank Prize Funds),* Grasmere, Cumbria, UK, 2-5 April 2001.

7. D. A. Yanson, M. W. Street, S. D. McDougall, I. G. Thayne, J. H. Marsh, and E. A. Avrutin, "Terahertz repetition frequencies from harmonic mode-locked monolithic compound-cavity laser diodes," *Applied Physics Letters. Vol. 78(23),* pp. 3571-3, 2001.

8. D. A. Yanson, M. W. Street, E. A. Avrutin, S. D. McDougall, I. G. Thayne, and J. H. Marsh, "Near-terahertz passive harmonic modelocking in monolithic compound-cavity laser diodes," *LEOS '00. 13th IEEE Annual Meeting, Puerto Rico, vol. 2,* pp. *438-9*, 15 Nov. 2000.

9. D. A. Yanson, M. W. Street, E. A. Avrutin, S. D. McDougall, I. G. Thayne, and J. H. Marsh, "Monolithic Compound-Cavity Laser Diodes modelocked at THz Frequencies," *8th IEEE International Symposium on High Performance Electron Devices for Microwave and Optoelectronic Applications,* Glasgow, UK, pp.46-50, 13-14 Nov.2000

10. D. A. Yanson, M. W. Street, E. A. Avrutin, S. D. McDougall, I. G. Thayne, and J. H. Marsh, "Ultrafast Passive Harmonic Modelocking in Monolithic Compound-Cavity Laser Diodes," *Scottish LEOS Regional Chapter Meeting,* St Andrews, UK, 11 Oct 2000.

11. D. A. Yanson, M. W. Street, E. A. Avrutin, S. D. McDougall, I. G. Thayne, and J. H. Marsh, "Passive harmonic modelocking in monolithic compound-cavity laser diodes," *Electronics Letters, Vol. 36(23),* pp.1930-1, 2000.

12. D. A. Yanson, M. W. Street, E. A. Avrutin, S. D. McDougall, I. G. Thayne, and J. H. Marsh, "THz Modelocking Rates From Harmonic Modelocked Monolithic Compound-Cavity Laser Diodes," *CLEO-Europe '00,* Nice, France, Postdeadline Session 1, paper CPD1.10, p.6, 14 Sept. 2000.

13. D. A. Yanson, M. W. Street, E. A. Avrutin, S. D. McDougall, I. G. Thayne, and J. H. Marsh, "Sub-THz passive harmonic mode-locking effects in monolithic and external-reflector compound cavity laser diodes," *MTT/ED/AP/LEO Societies*

Joint Chapter United Kingdom and Republic of Ireland Section. High Frequency Postgraduate Student Colloquium, pp. 152-7, 1999.

14. E. A. Avrutin, F. Camacho, A. C. Bryce, C. J. Hamilton, D. Yanson, J. M. Arnold, and J. H. Marsh, "Analysis of monolithic parallel-compound-cavity semiconductor lasers for high brightness, single-frequency, and short pulse operation," *CLEO '99, Technical Digest. Summaries of papers presented at the Conference on Lasers and Electro Optics. Postconference Edition,* p. 147, 1999.

15. M. W. Street, D. A. Yanson, E. A. Avrutin, S. D. McDougall, I. G. Thayne, J. H. Marsh, and J. S. Roberts, "Sub-THz passive harmonic modelocking effects in external-reflector compound cavity laser diodes," *LEOS 1999. 12th Annual Meeting. IEEE Lasers and Electro Optics Society, vol. 2,* pp. 703-4, 1999.

16. M. W. Street, D. A. Yanson, E. A. Avrutin, S. D. McDougall, I. G. Thayne, and J. H. Marsh, "Sub-THz Passive Harmonic Modelocking Effects in Monolithic and External-Reflector Compound Cavity Laser Diodes," presented at *Quantum Electronics & Photonics (QEP-14),* Manchester, UK, 6-9 September 1999.

RELATED PUBLICATIONS AND PATENTS

1. [*]K. Zetie, "Compound-Cavity Diodes Promise T-Rays," *Technology World, Photonics Spectra,* p. 55, Sept. 2001.

2. C. J. M. Smith, D. A. Yanson, and J. H. Marsh, "Multi-section laser with photonic crystal mirrors." *UK Patent No. 0218548.6,* 2002.

---

[*] This article is included in the Appendix

LIST OF ABBREVIATIONS

Abbreviations are normally defined upon their first use in the text. For ease of reference, their definitions are summarised in the alphabetical list below:

AR   Anti-Reflection

BPM   Beam Propagation Method

C^3 Cleaved-Coupled Cavity

CC   Compound Cavity

CCM   Compound Cavity Mode-Locking/Mode-Locked

CPM   Colliding-Pulse Mode-Locking/Mode-Locked

CRT   Cavity Round-trip Time

CW   Continuous Wave

DBR   Distributed Bragg Reflector

DC   Direct Current

DFB   Distributed FeedBack

DTD   Distributed Time Domain

DQW   Double Quantum Well

EBL   E-Beam Lithography

FEL   Free-Electron Laser

FROG   Frequency-Resolved Optical Gating

GPIB   General Purpose Interface Bus

GSG   Ground-Signal-Ground

HF   High-Frequency; Hydrofluoric acid

HML   Harmonic Mode-Locking/Mode-Locked

HR   High-Reflection

ICR	Intra-Cavity Reflector
IF	Intermediate Frequency
IR	Infra-red
L-I	Optical power versus pump current (characteristic)
LTG	Low-Temperature-Grown
MBE	Molecular Beam Epitaxy
ML	Mode-Locking/Mode-Locked
MOCVD	Metal Organic Chemical Vapour Deposition
MULINREC	MULti INstrument RECorder
MW	Microwave
PBG	Photonic Band-Gap
OTDM	Optical Time-Domain Multiplexing
PC	Personal Computer
QW	Quantum Well
RF	Radio Frequency
RIE	Reactive Ion Etching
SA	Saturable Absorber
SCH	Separate Confinement Heterostructure
SESAM	SEmiconductor Saturable-Absorber Mirror
SHG	Second-Harmonic Generation
SPM	Self-Phase Modulation
TBP	Time-Bandwidth Product
TPA	Two-Photon Absorption
T-ray	Terahertz ray
UTC-PD	Uni-Travelling-Carrier Photodiode
WDM	Wavelength Division Multiplexing

THESIS OUTLINE

The Thesis comprises 11 chapters with appendices and is organised in the following manner.

Chapters 1 and 2 give a general introduction into the field of terahertz-frequency signals and provide a justification for the need for, and choice of, the ultrafast laser source described in the following chapters. Chapter 1 focuses on the applications, generation and detection of free-space terahertz radiation, while Chapter 2 does the same for optical signals that are modulated at terahertz frequencies and illustrates how such modulation can be converted into terahertz waves for use in many of the applications listed in Chapter 1.

Chapter 3 gives a general description of semiconductor lasers and explains how they can be used to generate the type of microwave-modulated optical signals described in Chapter 2. A particular emphasis is placed on the high-frequency operation of semiconductor lasers, with modelocking highlighted as the most promising method for extending the frequency range into the terahertz domain.

Chapter 4 is concerned with the theoretical description of the ultrafast modelocking method, called harmonic modelocking. As the chosen realisation of this method requires a perturbation of the laser cavity, the Chapter begins by giving an overview of compound-cavity lasers. This is followed by a description of the theoretical model used to predict the modelocked behaviour of such devices and the modelling results obtained.

Chapter 5 reports on the design activities for the compound-cavity harmonic-modelocked lasers, the fabrication of which is the subject of Chapter 7. In both chapters, the design and technology of the sub-micron intra-cavity perturbations are discussed in great detail, as these features have proved to be essential for the modelocking of the fabricated lasers. In Chapter 6, the description and modelling of the semiconductor material used for the laser fabrication are given and the characterisation results presented.

In Chapter 8, an overview of utrafast measurement techniques is given, with a focus on autocorrelation studies, which are used to characterise the modelocked behaviour of the fabricated devices. The autocorrelator set-up is fully described and the performance of several types of non-linear detectors is assessed.

Chapter 9 presents the measurement results from all types of the fabricated compound-cavity lasers, demonstrating both their continuous-wave and high-frequency operation. The terahertz-frequency modelocking of these devices is confirmed by both spectral and autocorrelation studies.

In Chapter 10, parallel activities on the fabrication of photomixers for optical-to-microwave frequency down-conversion are presented. Also, the implementation of a dual-wavelength external-cavity laser set-up is described and the results shown.

Finally, Chapter 11 draws conclusions from the whole body of research conducted in this Project and lists its highlights. A number of recommendations and suggestions for future work are given.

*"The Universe is very quiet in the terahertz region
for many of the same reasons that it is difficult to
generate terahertz radiation artificially".*

F.G.De Lucia and T.M.Goyette, *SPIE* vol.2145

To my wife and my mother

CHAPTER 1.

APPLICATIONS, GENERATION AND DETECTION OF

FREE-SPACE TERAHERTZ RADIATION

The aim of this Chapter is to give a general overview of the applications of terahertz radiation and concisely describe the various techniques for the generation and detection of terahertz-frequency waves. While this Chapter deals with free-space terahertz radiation, terahertz-modulated optical signals and optical down-conversion techniques will be discussed in Chapter 2.

1.1. Introduction

The term "terahertz" (THz) is traditionally applied to electromagnetic frequencies in the 10^{12} Hz region, specifically, between about 300 GHz and 5 THz, which, in spectral terms, corresponds to wavelengths from 1 mm to 60 μm. The Oxford English Dictionary dates the term "terahertz" back to at least 1970, when it was used to describe the frequency range of a HeNe laser. In 1947, the International Telecommunications Union designated the highest official radio frequency bands [extremely high frequency (EHF)] as bands 12–14, 300 kMc–300 MMc (1 MMc = 1 THz). Depending on one's background, one can also associate this frequency range with other physical quantities: 1 THz ~ 1 ps ~ 300 µm ~ 33 cm^{-1} ~ 4.1 meV ~ 47.6 K. In spectroscopy, the names "sub-millimetre" and "far-infrared" (FIR) have gained more currency and are used interchangeably with "terahertz". Recently, a new term, "T-rays", was coined for beams of terahertz power, especially in imaging applications. In general (and less careful) use, the THz band is often included within broad definitions of radio-frequency (RF), high-frequency (HF) and microwave (MW) ranges.

On the spectrum scale, the THz band falls in the gap between radio waves and light waves. It occupies a large portion of the electromagnetic spectrum between the infrared and microwave bands, as shown in Figure 1.1. However, compared to

the relatively well-developed imaging techniques at microwave and optical frequencies, basic research, new initiatives and advanced technology developments in the THz band are still very limited.
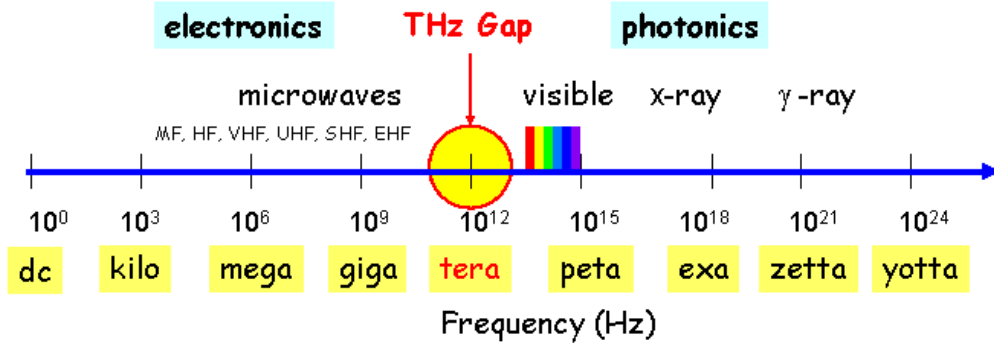
Figure 1.1. The electromagnetic spectrum and the "terahertz gap".

The THz range is a scientifically rich but technologically limited frequency band, due to the less developed wave emitters and receivers, compared with its neighbouring bands (microwave and optical bands). Indeed, for electron-circuit based transmitters, terahertz is an ultra-high frequency region, while for laser light sources, this region lies too far in the infrared. On the one hand, transistors and other quantum devices based on electron transport [1] are limited in frequency to about 500 GHz (200 GHz being the rough practical limit; devices much above that are extremely inefficient). On the other hand, the wavelength of semiconductor lasers can be extended to only 10 µm (about 30 THz) [2], or several tens of microns for quantum-cascade lasers. Between the two technologies lies the so-called terahertz gap, where no semiconductor technology can efficiently convert electrical power into electromagnetic radiation. Optoelectronic methods of generating THz signals look very promising, however, the deliverable power levels are still very modest. The chart of Figure 1.2 presents a comparison of various THz generation techniques against their achievable powers.

Because of its in-between nature, the THz band has not been investigated thoroughly in the past. It was only recently that significant improvements in sources and detectors opened up new areas of THz research, with the effort being very much focused on applications and systems rather than pure investigation. It is hoped that the research presented in this Thesis will further the knowledge of terahertz

generation and can be used to develop a novel optoelectronic THz source suitable for a wide range of applications.
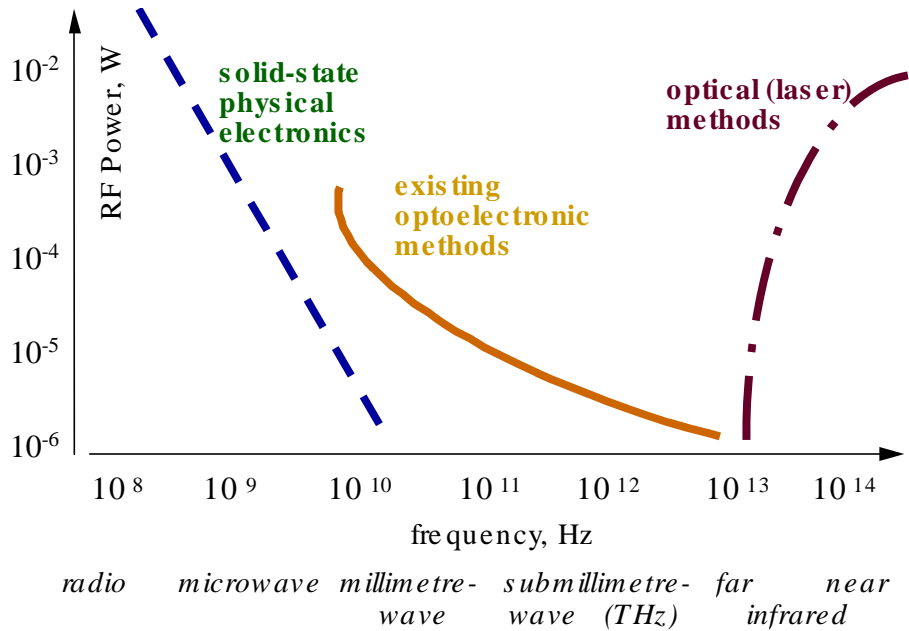
Figure 1.2. Power levels currently attainable in different frequency bands

1.2.   **Applications of THz signals**

Because of its low energy quanta, terahertz radiation is mostly employed in observation and communications applications. During the past decade, THz waves have been used to characterize the electronic, vibrational and compositional properties of solid, liquid and gas phase materials. It is a common belief that the future 'killer application' of THz waves will be in biomedicine, since THz imaging can potentially supersede X-rays as a safe diagnostic tool. One can anticipate that commercialisation of THz technology will fuel further research and development in the field, unlocking the full potential of this largely disused frequency band.

Listed below are the key application areas of THz-frequency radiation, followed by a more detailed description of some of them:

- Atmospheric sensing
- Radio-astronomy
- Spectroscopy
- Electromagnetic & radio Earth exploration

3

- Imaging & tomography

- Ranging & radars

- T-ray microscopy

- Biology

- Wireless telecommunications

There exists a further uncountable number of applications, and even a brief description of these would be ambitious. Here, only the most important ones will be described, while the reader is referred to Ref.[3] for a more complete review

1.2.1. Atmospheric research

The ozone layer is the ultimate sunshield protecting life on this planet from the harmful exposure to ultraviolet radiation. This layer, however, is susceptible to erosion by various chemical processes, with man-made emissions and pollutants serving as catalysts. Particularly damaging are chlorine-based compounds, e.g., chlorofluorocarbons (CFC's), which are broken down by strong ultraviolet light in the stratosphere and release chlorine atoms that then deplete the ozone layer. It is also believed that there is a link between the ozone concentration in the lower stratosphere and global climate change. The sensing and monitoring of the atmospheric distributions of many species of atoms and molecules are, therefore, essential for the understanding and prediction of climatic behaviour.

Satellite-based sub-millimetre heterodyne spectroscopy is the preferred method of monitoring the infrared radiation emitted by the outer strata of Earth's atmosphere [4]. These strata have a low temperature (~200 K), which determines both its spectral range and its low radiation emission intensity. The rarefied stratospheric gases consist of weakly interacting molecules and ions, which radiate quanta of specific energies. These emissions, registered as monochromatic spectral lines, form "signatures" of individual species. An analysis of the spectral and intensity properties of these signals can provide information on the composition of atmospheric gases, including any pollutants, as well as their temperature, pressure, wind speed and even magnetic fields.

Satellites performing atmospheric sensing are equipped with scanning terahertz aerials and super-heterodyne detectors. Compact, space-borne, high-

sensitivity, coherent infrared detectors are therefore required to sense and process these low-level electromagnetic signals.

1.2.2. Heterodyne spectro-radiometry in Radioastronomy

The spectral analysis of the sub-millimetre-wave spectra of cosmic radiation is a powerful tool for gathering information in astrophysics [5]. It allows one to study the spectral and spatial distribution of background radiation, obtain data on remote galaxies and learn about the formation of stars in our own galaxy. It is often the only alternative to optical telescopes, e.g., for the observation of young galaxies, which are often concealed by dense clouds of dust.

Of particular interest is the investigation of the composition and properties of the interstellar medium, in whose dense molecular dust clouds stars are formed. Having completed its lifecycle, a star loses its outer shell, which is returned to the pool of interstellar matter. The molecular, atomic and isotopic composition of the latter contains important information about the activity of star formation and death at a location of interest. The temperature of interstellar gas varies from ~10 K in cold regions up to ~200 K in warmer and denser ones. The quantum energy at this temperature is similar to thermal energy kT and lies within the terahertz frequency band. A typical emission spectrum contains a multitude of highly monochromatic lines, most of which can be associated with the vibrational and rotational resonances of various molecules. One can then infer the composition of the interstellar matter from these measurements [6].

Radiotelescopes are usually positioned on mountain tops at high altitude, where the signals of interest are least attenuated by atmospheric absorption. For example, the 10.5 m telescope at Hawaii uses a super-heterodyne receiver with a superconductor mixer. There are also radiotelescopes mounted on aircraft and satellites, which overcome some of the shortcomings of the terrestrial systems at the expense of a higher operational cost. Nonetheless, cosmic radiation is extremely weak and requires high-sensitivity, broadband receivers capable of registering monochromatic spectral lines over a wide spectral range [7, 8].

1.2.3. Terahertz time-domain spectroscopy

Terahertz spectroscopy is based on observing changes in the terahertz spectrum after transmission through, or reflection from, a material, the most common system being terahertz time-domain spectroscopy [9]. It provides an excellent signal-to-noise ratio and is insensitive to blackbody radiation (thermal background). Coherent T-ray signals can be detected in the time domain by mapping the transient of the electric field in amplitude and phase. In its most simplistic form, the Fourier spectrum of a free-space terahertz pulse is first characterised, then compared to the spectrum of a pulse that already has passed through the sample. The difference between the two spectra reveals the sample's molecular absorption lines.

Unlike common optical spectroscopes, which only measure the intensity of light at specific frequencies, the THz time-domain spectroscopic technique can directly record the THz wave's temporal electric field. Fourier transformation of the time-domain data gives the amplitude and phase of the THz wave pulse, thus providing the real and imaginary parts of the dielectric constant without the use of the Kramers-Krönig relations. This allows precise measurements of the refractive index and absorption coefficient of samples that interact with the THz waves. Many rotational and vibrational spectra of various liquid and gas molecules lie within the THz frequency band, with their unique resonance lines enabling identification of the corresponding molecular structures. Raman spectroscopy uses the frequency domain directly to fingerprint lattice vibrations. Similarly, THz wave spectroscopy describes molecular rotational and vibrational spectra from 10 GHz to 10 THz using the real and imaginary parts of the dielectric function, obtained by measuring the THz wave in the time-domain. This is not possible with any current optical or microwave technique.

Another attractive feature of THz spectroscopy is that, in the far infrared, it allows one to study chemical reactions, which is very important for understanding how chemical and biological systems operate and interact [10].

1.2.4. Terahertz imaging

Imaging is regarded, by far, perhaps as the most promising application for THz waves [11, 12]. Imaging in the visible and near-infrared regions of the spectrum

has been studied extensively for over two decades using a variety of laser-based techniques such as fluorescence imaging and optical coherence tomography. However, the Rayleigh scattering of light – from biological tissue and many inorganic materials – has traditionally hindered the development of optical-based techniques. This scattering attenuates the light and blurs the image. As the probability of Rayleigh scattering is proportional to λ^{-4}, λ being the wavelength of the probe light, one should expect the quality of an image to improve with increased wavelength. However, the microwaves emitted by conventional radiation sources have wavelengths between several millimetres and tens of centimetres. Such relatively long wavelengths limit the spatial resolution of the objects that can be discerned to around 5 mm, thereby precluding the use of microwaves in many applications.

On the contrary, the THz (sub-millimetre) band is ideally suited to overcome both the scattering and resolution limitations. The interaction of THz light with a given material is different from that of visible light. Non-polar solids such as plastics and ceramics are at least partially transparent in the 0.2–5 THz range. Non-polar liquids are transparent as well, whereas polar liquids, such as water, are highly absorptive. Metals completely block or reflect T-rays, while gases exhibit distinctive spectroscopic fingerprints.
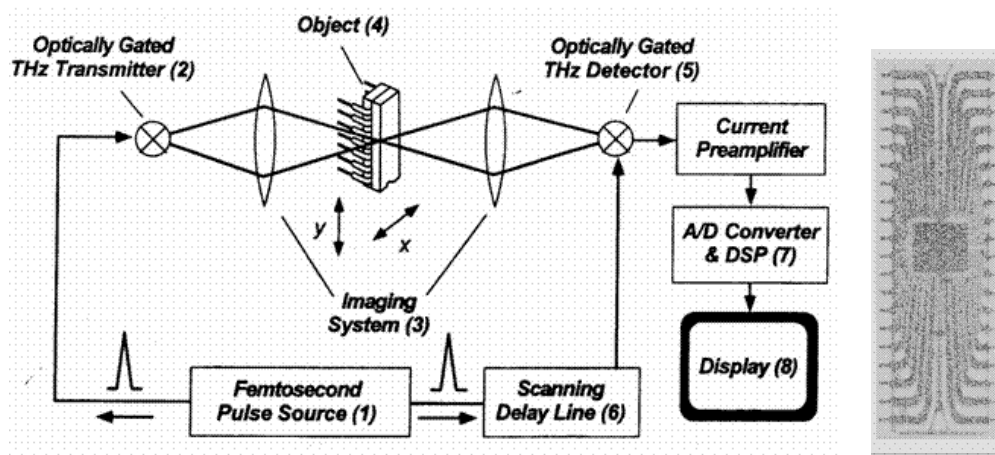
Figure 1.3. Schematic of a single-scan THz imaging system (left) and THz photograph of a Motorola chip (right) [13].

Current THz imaging systems fall into two broad categories: single pixel scan [13] and parallel processing systems [14]. The former involves forming an image pixel-by-pixel while the sample is translated through the focal point of the THz probe

beam. A schematic of such a system along with a THz image of an integrated circuit is given in Figure 1.3. Here, a Ti:sapphire laser is used as a source of femtosecond pulses, which are converted into bursts of THz power focused on the object. Despite the fact that this technique suffers from long acquisition times (several minutes), the first turn-key imaging systems have recently become commercially available [15].

Parallel image processing relies on a CCD camera to take a snapshot of the complete object with the use of a free-space electro-optic sampling technique, as shown in Figure 1.4. By illuminating a ZnTe crystal with an optical sampling beam and detecting the beam with a digital CCD camera, time-resolved images of pulsed far-infrared radiation reflected from the object (e.g. a butterfly) are recorded. The measurement can be performed in real time, albeit with a limited dynamic range.
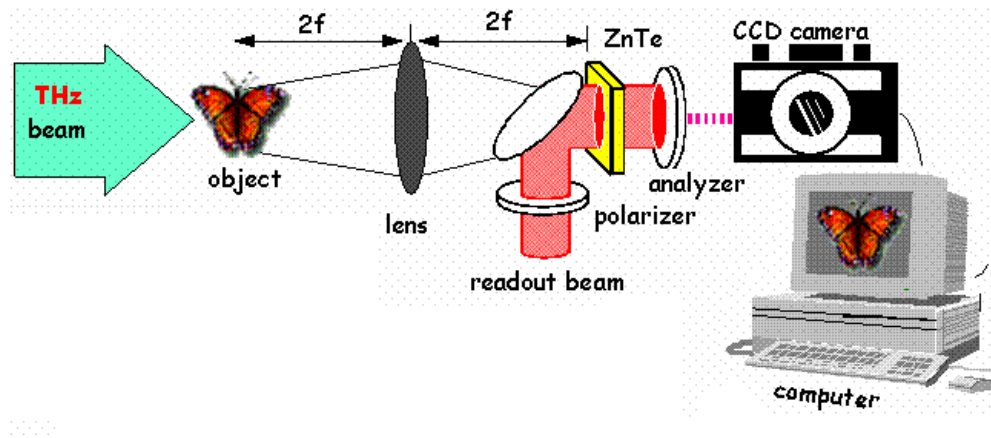
Figure 1.4. Parallel processing THz imaging system [14]

1.2.5. Biology and Biomedicine

T-rays have low photon energies (~ 4 meV at 1 THz), which do not cause harmful photo-ionisation in biological tissues. At THz frequencies, numerous organic molecules exhibit strong absorption and dispersion due to dipole-allowed rotational and vibrational transitions. These transitions are specific to the molecule and enable T-ray fingerprinting. Moreover, the average power levels used for THz imaging are low, typically in the nanowatt to microwatt range, thanks to the short (< 200 fs) probe pulses being used. Due to the diffraction limit, the standard imaging resolution at 1 THz cannot be much smaller than 300 μm. This is adequate for the spatial sensing and imaging of biological objects at the cell level.

These properties make THz-based techniques ideally suited for the diagnostics and investigation of living tissue. There are reports of various biomedical applications, e.g., density mapping of wood, THz spectroscopy of DNA [16, 17], mammography, and dental imaging. The latter looks particularly promising, as it will allow dentists to identify early stages of tooth decay without the hazards associated with X-ray radiography. An image of a human tooth taken in T-rays is shown in Figure 1.5. T-rays are also sensitive to different types of tissue, such as nerves, blood vessels, fat and sinews, which allows, for example, early diagnostics of skin cancer.
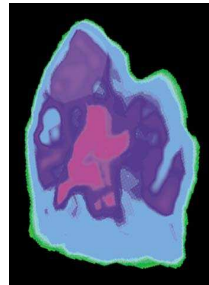
Figure 1.5. Image of a human tooth formed from THz radiation. The red area in the centre shows a cavity [11].

Another exciting application is in tomography, a scanning technique that enables one to reconstruct the dielectric layers buried within a solid structure. It can be used for imaging surfaces both in organic and inorganic materials [18].

1.2.6. Wireless telecommunications

As spare bandwidth is now at a premium at conventional telecommunications frequencies, it is very tempting to extend the frequency band available into the THz region. Nevertheless, two main points need to be kept in mind. First, the atmosphere becomes very opaque above 1 THz, by strongly absorbing radiation at these frequencies. Second, no efficient or fast terahertz detectors are yet available. The challenge is, therefore, to move to even lower frequencies — although meeting this challenge would mean moving into a competitive arena with the existing transistor technology. Sub-terahertz wireless systems may well find applications in urban and in-building mobile networks.

1.3. Generation and detection of free-space THz radiation

The terahertz region has been devoid of robust, coherent, solid-state sources and detectors. Recent developments, however, have begun to close this gap. An overview of existing THz sources and detectors will be given below.

1.3.1. THz sources

Certainly the most difficult component to realize in the sub-millimeter-wave bands has been the terahertz source. There are several fundamental explanations for this [3]. Traditional electronic solid-state sources based on semiconductors, i.e., oscillators and amplifiers, are limited by reactive parasitics and transit times that cause high-frequency roll-off, or they have simple resistive losses that tend to dominate the device impedance at these wavelengths. Gunn and Schottky diodes and Bloch oscillators [3, 19] have a fundamental frequency of operation as high as ~200 GHz that can be multiplied up to ~800 GHz. Multiplication is rather inefficient, however, and the maximum powers, which can be generated, are typically no greater than 10 mW. In addition, the problem of manipulating the resulting signal remains. Other solid-state sources include direct semiconductor oscillation with resonant tunnelling diodes (RTD) [20] and Josephson junction oscillations [21]. Tube sources suffer from simple physical scaling problems, metallic losses, and the need for extremely high fields (both magnetic and electric), as well as high current densities.
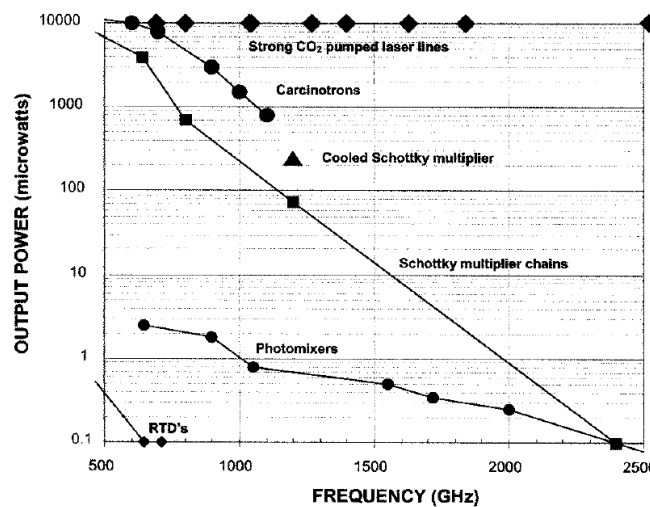
Figure 1.6. Performance of some CW sources in the sub-millimeter-wave range [3].

For frequencies above 800 GHz, far-infra-red gas lasers are often the preferred source, but these are extremely bulky, have large power requirements and critical alignment problems, which limit their use as, e.g., field or satellite-based instruments for radiometric applications. At the same time, gas-laser systems still offer the highest THz powers available today, which can be seen from the comparison chart of Figure 1.6, where the performance of most common (sub)-THz sources is summarised.

Research is underway into other methods of generating power in the sub-millimetre band. The free-electron laser (FEL) is another promising source of THz radiation. Conventional lasers rely on the inversion of population in an atomic or molecular transition, thus the wavelength at which they operate is determined by the active medium they use. The FEL is different in that it does not rely on specific transitions. Potentially, FEL's offer three main characteristics that are often hard to achieve with conventional lasers, namely, wide tuneability, high power and efficiency. These are achieved by using a relativistic beam of free electrons that interact with a periodic structure, typically in the form of a static magnetic field. This structure exerts a Lorentz force on the moving electrons, causing them to oscillate. The basic idea is to have all the electrons share approximately the same phase, thereby producing constructive interference (stimulated emission). A key feature of this laser is that the emitted radiation is a function of the electron energy, hence the wavelength of the FEL can be adjusted simply by accelerating the electrons to different speeds. The FEL is therefore a widely tuneable system and can be tuned to emit terahertz radiation.

Recently, there has been a report of a new semiconductor laser that produces intense radiation of 2 mW at 4.4 THz (at a wavelength of 67 µm), by injecting electrons into a quantum-cascade structure [22]. It is based on inter-miniband transitions in the conduction band of a semiconductor (GaAs/AlGaAs) heterostructure. In conventional semiconductor lasers, light is generated by the radiative recombination of conduction band electrons with valence band holes across the bandgap of the active material; in contrast, electrons in a quantum-cascade laser propagate through a potential staircase of coupled quantum wells, where the conduction band is split by quantum confinement into a number of distinct sub-bands. By an appropriate choice of the layer thicknesses and applied electric field,

the lifetime and tunnelling probabilities of each level are engineered in order to obtain population inversion between two sub-bands in a series of identical repeat units. Injector/collector structures connect these active regions, allowing electrical transport through injection of carriers into the upper laser level, and extraction of carriers from the lower laser level. The radiation frequency is determined by the energy spacing of the lasing sub-bands, allowing, in principle, operation at arbitrarily long wavelengths.

Another promising THz source is the optical parametric oscillator (OPO) [23]. It uses a non-linear optical crystal to split the pump photon into two photons of lesser energy (signal and idler). Rotating the crystal changes the ratio between the signal and idler photon energies, and thus tunes the frequency of the output. The use of new non-linear crystals has enabled the extension of the OPO tuning range to 3 – 19 μm.

Historically, it was the seminal work by Auston [24] that set off the wave of research into the generation of THz pulses by the illumination a photoconductive emitter with sub-picosecond pulses of visible or near-infrared light. When a femtosecond pulse strikes a photoconductive emitter, such as a GaAs dipole antenna, electron-hole pairs are generated in the semiconducting layer within the device. These charge carriers are then accelerated by a bias voltage. The resulting transient photocurrent is proportional to this acceleration and radiates at THz frequencies.
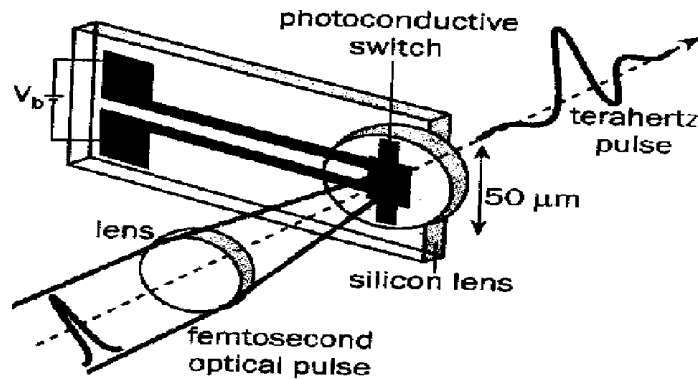
Figure 1.7. Generation of THz pulses with photoconducting antennas [25].

In the arrangement shown in Figure 1.7, the optical pulse is focused on the photoconductive switch antenna, which radiates THz power through the silicon lens attached to the back side of the substrate. These antennas have a spectral response from 100 GHz to 2 THz when illuminated by a modelocked dye laser. Further

research into the pulsed generation of THz power has demonstrated that photoconductive antennas can be used as detectors as well as emitters [26].

Another way of converting pico and femtosecond optical pulses into THz radiation is based on emission by optical rectification [27]. Optical rectification is a process first observed in the 1960's that describes how a pulse at optical frequencies can be downshifted by degenerate difference frequency generation inside a non-linear crystal. This effect arises from the second order susceptibility χ of a crystal. The susceptibility, $\chi = P / \varepsilon_0 E$, measures the degree of polarisation, P, caused when an electric field, E, is applied to a dielectric material (ε_0 is the permittivity of a vacuum) [28]. Higher order terms, such as $\chi^{(2)}$, denote the non-linear response of the materials and are important for the high electric fields found in laser pulses. By using an ultrafast visible pulse to excite a crystal that has a large second-order susceptibility, such as zinc telluride, a time-varying polarisation of the electron cloud inside the crystal is produced. The time variation can be at the difference frequency between a set of any two optical frequency components making up the laser pulse. The resulting electromagnetic wave $E_{THz}(t)$ emitted by the current $I(t)$ of the electron cloud contains a broad range of frequency components, from zero up to the bandwidth of the visible radiation, including the THz band:

$$E_{THz}(t) \propto \frac{\partial^2 P(t)}{\partial^2 t} \propto \chi^{(2)} \frac{\partial^2 I(t)}{\partial^2 t} .$$

A schematic of this process is shown in Figure 1.8. In contrast to photoconductive emitters, the power of the terahertz pulse is derived entirely from the incident laser pulse, so generation by optical rectification delivers less power than the aforementioned technique.
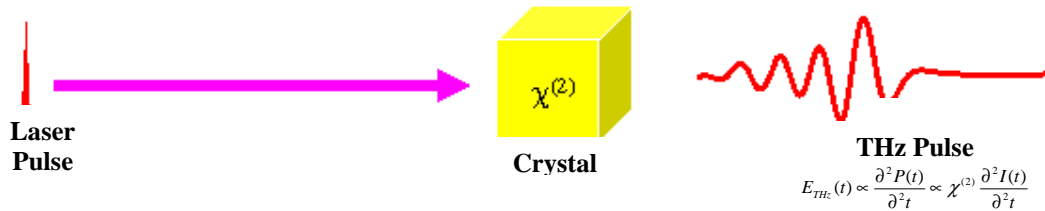
Figure 1.8. Generation of THz power by optical rectification

More successful techniques for generating terahertz power have come from frequency conversion, either up from millimetre wavelengths, or down from the

optical or infrared. The use of optical down-conversion techniques to produce THz power will be discussed in Chapter 2.

1.3.2. Detection of THz power

Detecting terahertz signals is difficult, because blackbody radiation at room temperature is strong at these frequencies. This can be overcome by using a helium-cooled bolometer, which is desensitised to ambient temperature and responds only to the heating effect of the terahertz radiation. The bolometer is an incoherent detector, registering only the incident amplitude but not the phase.

Using a pump-probe configuration, on the other hand, allows for a far greater sensitivity and full coherent signal acquisition of THz pulses. Pump-probe techniques are essentially the inverse of the respective generation mechanisms: photoconductive antennas can be used as detectors, and optical rectification as electro-optic sampling.
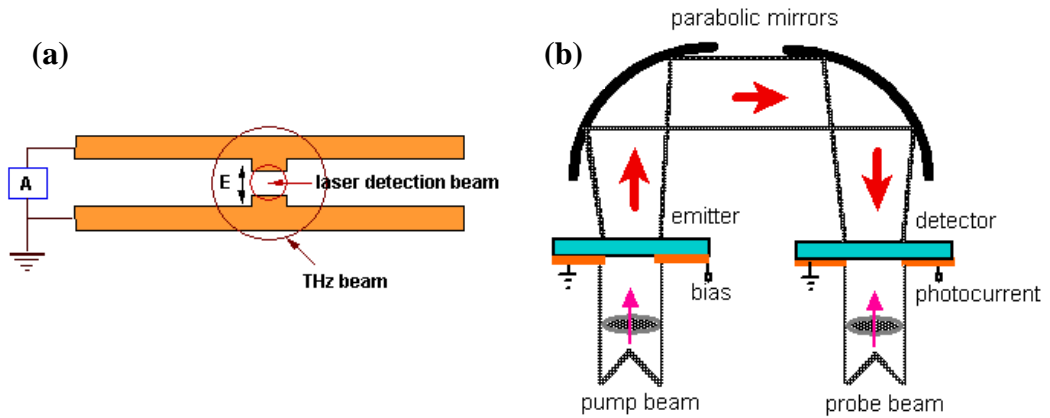
Figure 1.9. (a) Dipole antenna and **(b)** pump-probe configuration for coherent THz detection [26, 29]

The former, e.g., Grischkowsky antennas [see Figure 1.9 (a)], produce photocurrent when a THz pulse incident on the antenna is gated with a replica of the optical pulse used for exciting that THz pulse in the emitter [29] using a pump-probe arrangement such as the one shown in Figure 1.9 (b). Electron–hole pairs are generated when an optical gate pulse illuminates the photoconductor in the gap of the dipole antenna. These carriers are driven by the THz electric field, producing a current, whose magnitude is proportional to the THz field and the carrier concentration and whose direction is determined by the polarity of the THz field. An ammeter, connected across the dipole, will only register a photocurrent when a laser pulse arrives at the switch gap at the same time as the coherent THz wave. Since the

laser pulse is narrow in comparison to the time duration of the THz pulse, the laser acts as a gated sampling signal. The impedance of the antenna and of the transmission line in which it is embedded should be matched to the frequency of the incident THz radiation. Since the basic operation principle of a photoconducting antenna is the same as that of an electronic boxcar, a rapid recovery of the electron–hole population is essential in order to obtain good time resolution. Usually, radiation-damaged silicon-on-sapphire and low-temperature-grown GaAs are used as the photoconductor material. The main problem with antenna detection is the bandwidth limitation, with a frequency limit determined by the speed of the photocurrent response.

The second detection mechanism relies on an electro-optic effect known as the AC Pockel's effect. A THz pulse incident on an electro-optic medium – such as zinc telluride – alters its refractive index perpendicular to the optical axis of the crystal. If, at the same time, the medium is sampled by an optical pulse, the latter becomes elliptically polarised after it has traversed the medium. The degree of elliptical polarisation of the pulse is readily measured using inexpensive and commercially available optical components and photodetectors, as in the setup of Figure 1.10 [30]. Owing to the instantaneous response of the electro-optic material, electro-optic sampling has a very high bandwidth (up to 37 THz) and allows a direct measurement of the amplitude, phase and spatial distribution of the THz field.
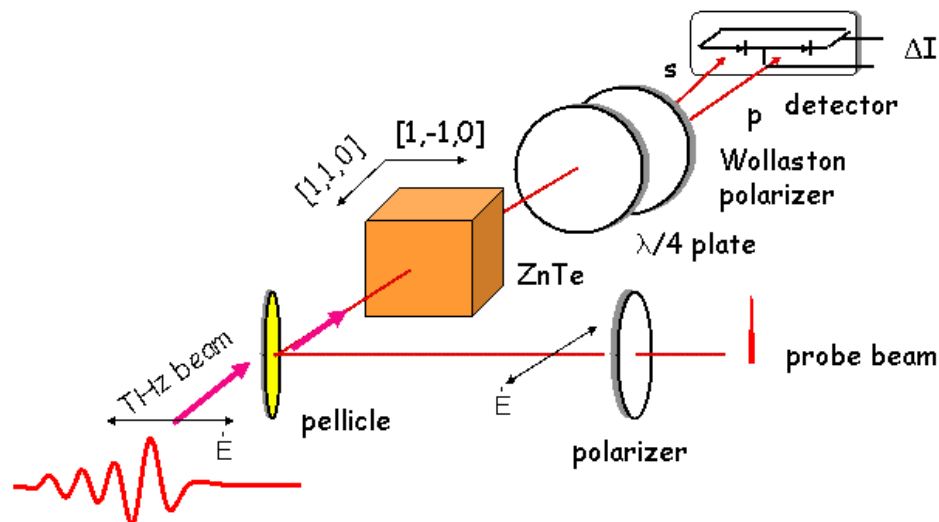
Figure 1.10. THz detection by electro-optic sampling [30]

1.4. References

[1]   M.J.W. Rodwell et al, "Submicron scaling of HBTs," *IEEE Trans. Electron Devices*, vol. 48 (11), pp. 2606-2624, 2001.

[2]   M. Beck and et al., "Continuous wave operation of a mid-infrared semiconductor laser at room temperature," *Science*, vol. 295, pp. 301-305, 2002.

[3]   P.H. Siegel, "Terahertz technology," *IEEE Trans. Microw. Th. and Techn.*, vol. 50, pp. 910-928, 2002.

[4]   J.W. Waters, "Submillimeter-Wavelength Heterodyne Spectroscopy and Remote Sensing of the Upper Atmosphere," *Proceedings of the IEEE*, vol. 30, pp. 1679, 1992.

[5]   T.G. Phillips and J. Keene, "Submillimeter Astronomy," *Proceedings of the IEEE*, vol. 80, pp. 1662, 1992.

[6]   F.C. De Gacia and T.M. Goyette, "Terahertz source requirements for molecular spectroscopy," *Proceedings of SPIE*, vol. 2145, pp. 239-247, 1994.

[7]   T.G. Phillips, "THz source requirements for astrophysics receivers," *Proceedings of SPIE*, vol. 2145, pp. 230-238, 1994.

[8]   M.A. Frerking, "Submillimetre source needs for NASA applications," *Proceedings of SPIE*, vol. 2145, pp. 222-229, 1994.

[9]   D. Grischkowsky, S. Keiding, M. van Exter, and Ch. Fattinger, "Far-infrared time-domain spectroscopy with terahertz beams of dielectrics and semiconductors," *J. of Opt. Society of America*, vol. 7 (10), pp. 2006, 1990.

[10]   B.N Flanders, D.C. Arnett, and N.F. Scherer, "Optical pump-terahertz probe spectroscopy utilizing a cavity-duped oscillator-driven terahertz spectrometer," *IEEE J. of Sel. Topics in Q. Electronics*, vol. 4 (2), pp. 353-359, 1998.

[11]   D. Arnone, C. Ciesla, and M. Pepper, "Terahertz imaging comes into view," *Physics World*, vol. 13, pp. 35-40, 2000.

[12]   D. M. Mittleman, R.H. Jacobsen, and M.C. Nuss, "T-ray imaging," *IEEE J. Sel. Top. Quant. Electron*, vol. 2, pp. 679-692, 1996.

[13]   B.B. Hu and M.C. Nuss, "Imaging with terahertz waves," *Optics Letters*, vol. 20, pp. 1716, 1995.

[14]   Q. Wu Lu, T. D. Hewitt, and X.-C. Zhang, "Two-dimensional electro-optic imaging of THz beams," *Appl. Phys. Lett.*, vol. 69, pp. 1026, 1996.

[15]   D. Zimdars, "Commercial T-ray systems accelerate imaging research," *Laser Focus World*, pp. 91-96, July 2001.

[16]   A.G. Markelz, A. Roitberg, and E.J. Heilweil, "Pulsed terahertz spectroscopy of DNA, bovine serum albumin and collagen between 0.1 and 2.0 THz," *Chem. Phys. Lett.*, vol. 320, pp. 42, 2000.

[17]   M. Nagel et al., "Integrated THz technology for label-free genetic diagnostics," *Appl. Phys. Lett.*, vol. 80, pp. 154 - 156, 2002.

[18]   D.M. Mittlemean, S. Hunsche, L. Boivin, and M.C. Nuss, "T-ray tomography," *Optics Letters*, vol. 22, 1997.

[19]   B.D. Guenther, "Terahertz Sources," *Proceedings of SPIE*, vol. 2145, pp. 120-129, 1994.

[20]   C. L. G. Sollner, W. D. Goodhue, P. E. Tannenwald, C. D. Parker, and D. Peck, "Resonant tunneling through quantum wells at frequencies to 2.5 THz," *Appl. Phys. Lett.*, vol. 43, pp. 588–590, 1993.

[21]   I. Song, K.-Y. Kang, and G. Park, "Frequency-locked submillimeter wave generation from Josephson junction arrays," *Jpn. J. Appl. Phys.*, vol. 38, pp. 44–47, 1999.

[22]   R. Kohler et al, "Terahertz semiconductor-heterostructure laser," *Nature*, vol. 417 (6885), pp. 156-9, 2002.

[23]   K. Vodopyanov, "OPOs target the longwave infrared," *Laser Focus World*, vol. May 2001, pp. 225-232, 2001.

[24]   D. Auston, "Impulse response of photoconductors in transmission lines," *IEEE J. of Q. Electronics*, vol. QE-19 (4), pp. 639-648, 1983.

[25]   P. U. Jepsen, R.H. Jacobsen, and S.R. Keiding, "Generation and detection of terahertz pulses from biased semiconductor antennas," *J. of Opt. Society of America*, vol. 13 (11), pp. 2424-2436, 1996.

[26]   P.R. Smith, D.H. Auston, and M.C. Nuss, "Subpicosecond photoconducting dipole antennas," *IEEE Journal of Quantum Electronics*, vol. 24, pp. 255-261, 1988.

[27]   A. Bonvalet, M. Joffre, J.L. Martin, and A. Migus, "Generation of ultra-broadband femtosecond pulses in the mid-infrared by optical rectification of 15 fs light pulses at a 100 MHz repetition rate," *Appl. Phys. Lett.*, vol. 67, pp. 2907, 1995.

[28]   K.H. Yang, P.L. Richards, and Y.R. Shen, "Generation of far-infrared radiation by picosecond light pulses in LiNnO3," *Appl. Phys. Lett.*, vol. 19 (9), pp. 320, 1971.

[29]   M. van Exter and D. Grischkowsky, "Characterisation of an optoelectronic terahertz beam system," *IEEE Trans. Microwave Theory and Techniques*, vol. 38 (11), pp. 1684-1691, 1990.

[30]   Q. Wu and X.C. Zhang, "Free-space electro-optic sampling of terahertz beams," *Appl. Phys. Lett.*, vol. 67 (24), pp. 3523-3526, 1995.

CHAPTER 2.

GENERATION, APPLICATIONS AND DOWN-CONVERSION OF

MICROWAVE-MODULATED OPTICAL SIGNALS

In this Chapter, the existing body of research into the generation and applications of terahertz signals on an optical carrier is presented and the various techniques for the down-conversion of these signals into free-space terahertz radiation are described.

2.1. Generation of microwave-modulated optical signals

It has already been mentioned in Chapter 1 that the terahertz region lies beyond the capability of solid-state electronic devices, with fundamental physical limitations precluding their use at these ultrahigh frequencies. At the optical end, however, there are virtually no lasers that emit photons at so long a wavelength, i.e. so low a frequency. Yet there is a way of accessing this frequency range, by creating a terahertz signal on an optical carrier and then down-converting the optical output into the THz domain. The basic principle is that an optical carrier frequency, determined by the type of material used as the laser gain medium, can be modulated at a much lower signal frequency, which is governed by the device structure rather than the device material.

Microwave (MW) intensity modulation can be encoded on an optical carrier in a number of ways, as illustrated in Figure 2.1. The most straightforward approach is to up-convert an electrical MW signal into the optical domain by applying intensity modulation to a continuous-wave (CW) monochromatic source (laser). In semiconductor lasers, this can be achieved either by modulating the driving voltage of the laser or using an external modulator to impart a MW envelope to the CW beam. As predicted by Fourier analysis, the sidebands and harmonics generated by optical intensity modulation will stand on both sides of the carrier frequency. The resulting optical spectrum is shown in Figure 2.1(I-a) along with the corresponding

time-domain signal in Figure 2.1(I-b). This modulation method, which we will call a Type I signal, is inherently limited by the electrical bandwidth of the driving circuit and therefore holds no promise for generating terahertz frequencies.

Another approach consists of extracting the difference frequency between two or more monochromatic optical signals, which lie relatively close to each other in the frequency domain. For a semiconductor laser operating at a wavelength of 860 nm (or, in frequency terms, at 350 THz), two spectral lines offset by 2.4 nm would give a difference frequency of 1 THz. For a 1550 nm laser, a 1 THz offset would be equivalent to a spectral difference of 8 nm. Both of these wavelength offset values correspond to approximately 15–30 longitudinal mode spacings in a conventional laser diode and can be covered by its gain spectrum. Thus it should be possible to generate terahertz-offset optical lines using either a single multi-colour laser or a set of several (at least two) single-frequency lines, however, the practical realisation of such sources presents a challenge. Generation of two coherent, phase-locked spectral lines, as in Figure 2.1(II-a), will produce a time-varying electromagnetic field, which is amplitude-modulated at the difference frequency between the two lines. The resulting envelope will be purely sinusoidal, as shown in Figure 2.1(II-b). However, such a high degree of coherence is achievable in practice only if the two lines are generated within one laser cavity, ideally with some degree of locking between them. In what follows, we will refer to this type of signal as Type II modulation.

An alternative approach relies on the use of two monochromatic sources, which are detuned by the required MW frequency. Unless special techniques are employed to phase-lock the output of each source, the linewidths are likely to be somewhat broader than in the previous case because of phase noise, as schematically shown in Figure 2.1(II-c). Stabilisation control and phase lock loops are required to reduce the phase noise. The time-domain envelope of Figure 2.1(II-d) was obtained by partial randomisation of phases of the two constituent optical frequencies and is typical of the beating signal between two separate sources, e.g., single-mode lasers.
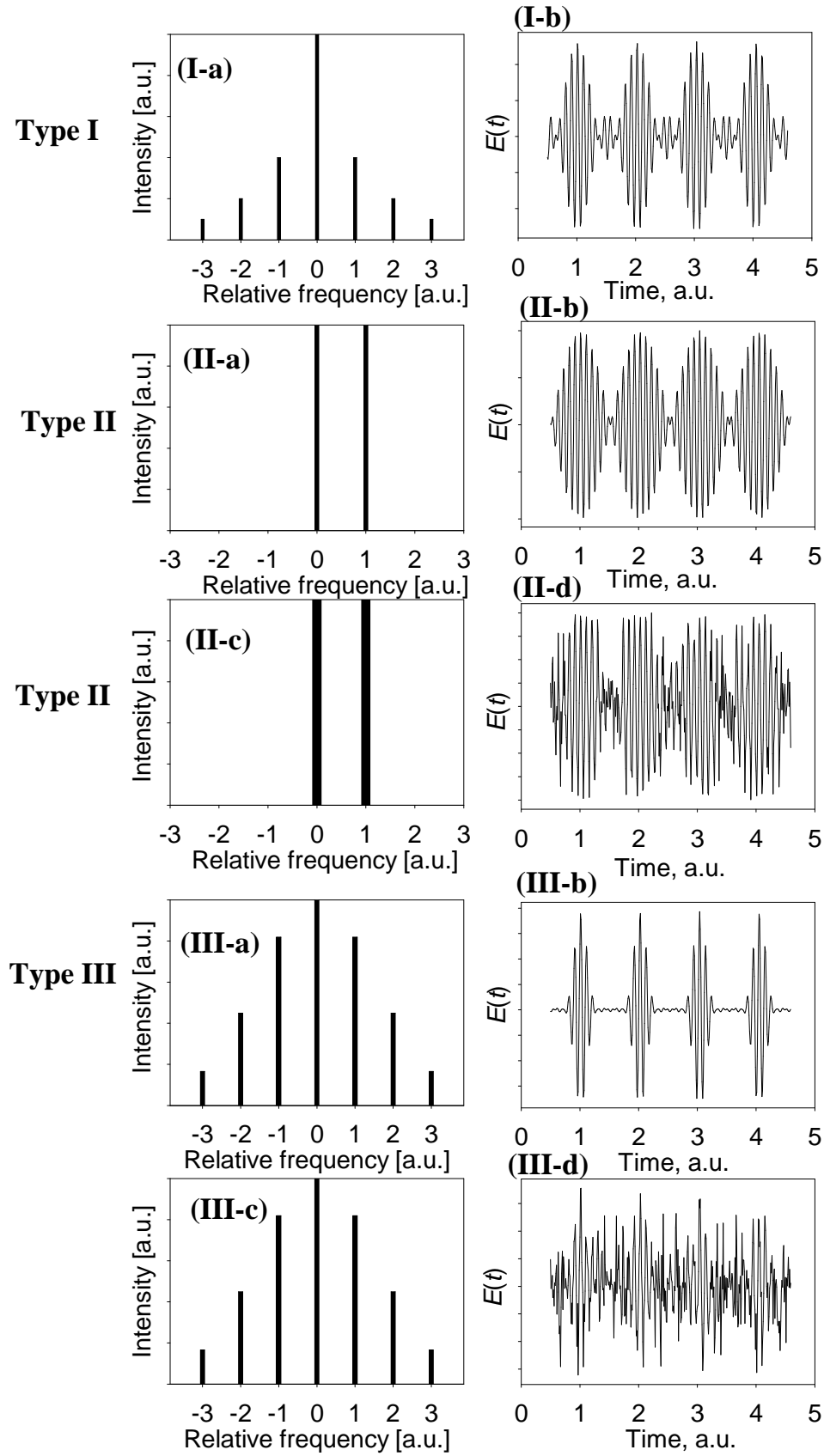
Figure 2.1. Optical frequency spectra (left) and corresponding time-domain electromagnetic field modulation (right) illustrating several techniques of placing a microwave signal on an optical carrier.

Finally, a set of equidistant longitudinal modes emitted by a laser, as shown in the spectrum of Figure 2.1(III-a), can deliver a MW envelope at the frequency defined by the spectral mode spacing of the laser cavity. This can only take place if these modes are phase-locked with respect to each other. Such a regime of laser operation is called mode-locking. The gain curve of a semiconductor laser defines the wavelength dependence of light amplification and usually takes a Gaussian shape centred around a peak wavelength. This shape is superimposed on a set of oscillating Fabry-Perot cavity modes, with the lasing spectrum also taking a Gaussian envelope. As can be verified by applying the Fourier transform, a Gaussian-shaped spectrum of phase-locked, equidistant narrow lines results in a train of pulses in the time domain, with a repetition frequency matching the optical frequency spacing between adjacent modes. For example, the superposition of seven such modes in the spectrum of Figure 2.1(III-a) produces short optical pulses with the electromagnetic field of Figure 2.1(III-b). However, if the mode phases are randomised, an identical spectrum of Figure 2.1(III-c) gives only random intensity fluctuations, as in Figure 2.1(III-d). This suggests that a fixed-phase relationship between the modes is essential for the generation of a MW envelope on an optical carrier, as is a spectrum of equidistant oscillating modes[1]. Both of these requirements are fulfilled in a modelocked laser. We will call the spectrum and signal of Figure 2.1(III-a, b) Type III modulation.

For the purposes of this discussion, we will distinguish this type of modulation from the generation of ultrashort pulses using modelocked lasers such as Ti:Sapphire and dye lasers. These lasers emit very broad spectra spanning hundreds of closely-spaced modes. The resulting pulses are extremely short (several femtoseconds) and are routinely used to excite broad-bandwidth terahertz pulses in semiconductors and as probe pulses in optical rectification, as described in Chapter 1. In such applications, advantage is taken of the ultrashort duration and very high peak power of the pulses, whilst their repetition frequency is usually less important and is relatively low (up to ~100 MHz). By contrast, the Type III signal discussed here is relevant to semiconductor lasers, where the pulse repetition frequency is much higher, with a pulse width that must be adequately short (e.g., half a period of THz radiation or less). Therefore, the microwave operation of such

---

[1] Other fixed-phase relationships may exist, e.g., such as in a frequency-modulated modelocked laser. However, this modelocking method is rather uncommon, particularly with diode lasers, and is not considered here.

sources is very narrowband and is determined by the pulse repetition frequency rather than the pulse width.

In conclusion, we also note that a Type II(a) signal can be regarded as a special case of Type III with only two locked modes, however, the term "modelocking" characteristic of Type III is conventionally applied to a spectrum containing at least three modes [31]. The theory and methods of modelocking will be discussed in more detail in Chapter 3.

2.2.   Applications of MW-modulated optical signals

The use of optoelectronics in microwave systems has now become a commercial reality in fibre-radio access networks, and there are emerging applications in phased-array antennas, electronic warfare, ultrafast non-invasive measurements, and radio astronomy.

Microwave-modulated optical signals are increasingly being used in preference to electrical signals. While challenges remain, optically-enabled MW generation is looking very attractive, particularly at very high, (sub)-terahertz frequencies. Optically encoded THz signals are much simpler to process and guide than THz electromagnetic waves, with optical fibre being an ideal medium for their distribution, switching and even amplification. These advantages justify implementation of as much of the signal processing as possible in the optical domain, leaving down-conversion as a final stage in system design.

All three types of optical carrier modulation discussed above can be utilised, with some more suitable for specific applications. Generally speaking, Type I modulation is the most technologically simple solution, provided that the MW frequencies being addressed are modest (up to ~100 GHz). Applications in analogue MW optoelectronics, where an optical signal is used to generate MW (sub)carriers and reference frequencies, favour a Type II modulation signal, as the beating of two optical lines yields a sinusoidal signal. Conversely, a modelocked Type III signal producing short optical pulses is important in digital telecommunications and OTDM applications.

Optical down-conversion for the generation of free-space THz power can be considered as a separate class of applications and will be reviewed in Section 2.3.

2.2.1. Local oscillator sources

A key element of the heterodyne receivers found in satellites and radiotelescopes for atmospheric sensing and spectroscopy applications is the local oscillator [4]. Such a source provides a stable reference signal, against which the incoming signal of interest is measured. A simplified diagram of a heterodyne receiver is shown in Figure 2.2. The incoming THz signal is fed from the receive antenna to the THz mixer (typically, a Schottky diode or a superconducting tunnel diode), where heterodyning with the local oscillator signal results in an intermediate-frequency (IF) signal at the output. The IF signal has the spectral content of the received THz signal but at a much lower frequency, which can be readily measured using conventional electronics.
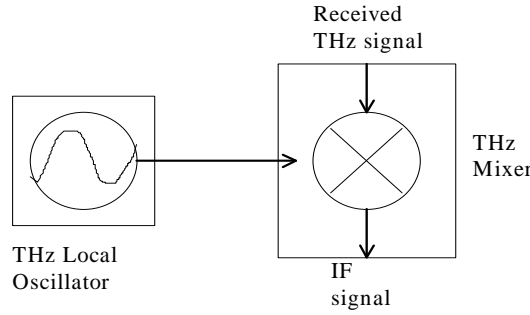
Figure 2.2. Schematic of a heterodyne THz receiver

The above configuration assumes that both the reference and detected signals lie in the THz domain. If an optical source producing an envelope of Type I, III, or preferably II, is used as a local oscillator, its output must first be down-converted before it can be mixed with the detected THz signal.

A more elegant approach would be to perform both the down-conversion and mixing in the mixer element itself. This technique is called super-heterodyne conversion and is illustrated in Figure 2.3. Here, the output of the local oscillator producing the optical carrier at a frequency f_{opt} with microwave modulation at f_{LO} is fed directly into the optoelectronic mixer/downconverter, where the MW envelope is simultaneously extracted and mixed with the received MW signal, with an intermediate frequency $f_{IF} = |f_{LO} - f_{MW}|$. A GaAs Schottky diode would be an ideal

candidate for such a mixer element, as it is sensitive to photons at both near-infrared ($\lambda \sim 1\ \mu m$) and far-infrared ($\lambda \sim 300\ \mu m$) wavelengths.
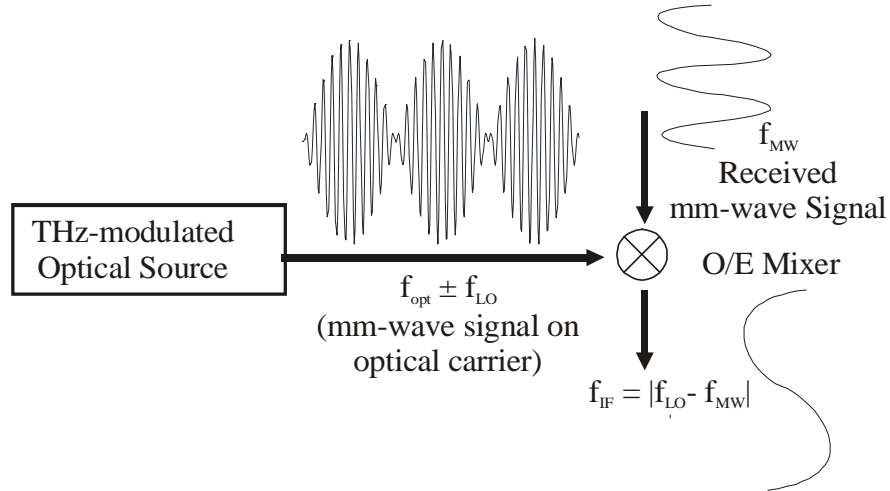
Figure 2.3. Super-heterodyne detection.

The tuning possibilities of such receivers are usually very limited because of the limited tuning range of the lasers used as optical local oscillator sources.

2.2.2. Fibre radio

It was already mentioned in Chapter 1 that terahertz radiation does not hold much promise as a signal carrier for telecommunications. While microwaves at the low-frequency end (up to several GHz) have been extensively harnessed for radio and television broadcasting, satellite links, and particularly mobile communications, exploitation of the largely disused THz-frequency band would also seem very attractive. However, at terahertz frequencies, coaxial cables are extremely lossy (> 100 dB/km), while free-space mm-waves are strongly attenuated in the atmosphere, with the exception of a few narrowband windows.

A compromise solution can be found if the MW signal is first generated in the optical domain, then transmitted via optical fibre (at a low loss of < 0.5 dB/km) to the antenna unit nearest to the subscriber and irradiated. The free-space signal can then be received by a mobile receiver unit within the local range (~ 1 km for a 40 GHz MW carrier, or ~ 200 m for a 60 GHz carrier). Such networks have been nicknamed "fibre radio" and may be used to provide, e.g., high-capacity in-building systems and local-area networks (LANs). Thanks to a higher carrier frequency, they can offer much higher bandwidths than mobile telephony, albeit at the expense of a

reduced range. In its simplest form, a fibre radio system is illustrated in Figure 2.4. A microwave-modulated laser transmits a Type I optical signal with two sub-bands offset by the microwave frequency f_{MW}. An information signal is then encoded onto the microwave sub-carrier, usually by means of a Mach-Zehnder modulator, giving rise to two further signal sidebands on either side of $\pm f_{MW}$. At the antenna station, the signal is down-converted, and the microwave component carrying the data signal is emitted into free space. In a multi-subscriber network, the MW signal usually contains a further radio-frequency (RF) carrier, at a frequency of several megahertz, on which data is encoded. Thus multiple channels can be supported, each having its own RF sub-carrier. Channels are then selectable either at the subscriber end or by localised emission from a specified antenna unit ("picocell").
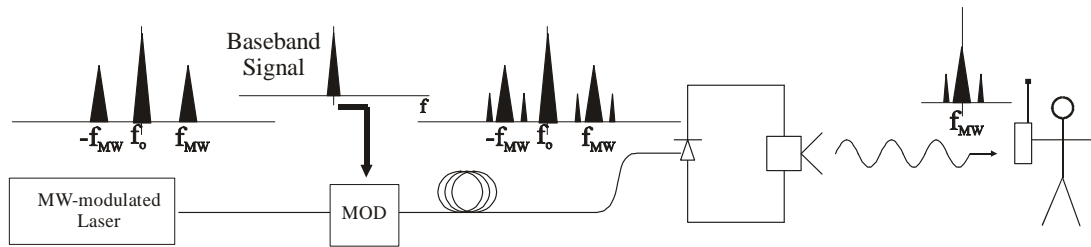
Figure 2.4. Schematic of a fibre radio system.

A major challenge with fibre radio systems is to alleviate fibre dispersion, which causes signal distortion at high MW frequencies. A number of techniques have been proposed to overcome this limitation, e.g. single-sideband modulation, at the cost of extra complexity in system and modulator design [32, 33]. Type II optical signals can also be used in preference to Type III ones, since the former require less bandwidth and are less susceptible to fibre dispersion. There are reports of filtering a Type III signal to produce a Type II carrier for fibre-radio applications [34] and MW generation [35].

2.2.3. Clock generation and recovery in optical telecommunications

Optical communications systems are, perhaps, the most important application for microwave-modulated optical signals. The operating wavelengths of lasers used for communications are dictated by optical fibre, which is the preferred transmission medium. The loss curve of optical fibre in relation to photon wavelength has minima at wavelengths of 1300 and 1550 nm, which are the standard values used for modern

optical communications. In semiconductor lasers, the emission wavelength can be controlled by engineering the band gap of the laser. The lowest transmission loss can be achieved in the 1550 nm region, with the typical alloys used to form the laser medium being GaAsInP/InP and AlGaInAs/InP. Alloys of GaAs/AlGaAs with an emission wavelength of 860 nm are also commonly used, particularly in short-range data communications, even though light at this wavelength suffers from higher attenuation in fibre. Such lasers are also popular in other applications, e.g., as optical pumps.

Digital optical fibre systems now carry the bulk of terrestrial long-distance communications traffic, and fibre is increasingly being brought into local access networks. With the evolution of the Ethernet standard to encompass a transmission rate of 10 Gb/s, most future optical communication systems will utilise microwave photonic techniques. It is believed that current transmission rates of 2.5 – 10 Gb/s per channel will be superseded by 40 Gb/s systems in the next few years. To increase fibre capacity, data multiplexing is used, which allows multiple channels to be transmitted simultaneously, with a total link capacity of several Tb/s [36, 37]. The multiplexing can be performed either in the time domain (optical time-domain multiplexing, OTDM) or in the frequency, or wavelength, domain (wavelength division multiplexing, WDM).

In OTDM, the optical data stream is constructed by time-multiplexing a number of lower bit-rate optical streams. The multiplexing operation of a bit-interleaved OTDM scheme is illustrated in Figure 2.5(a). The periodic pulse train (framing pulses) generated by a modelocked laser is split, and copies are created and incrementally delayed for each data channel to be multiplexed. This delay can be achieved by passing the pulse train through an appropriate length of optical fibre, so that the pulses no longer overlap in time. The undelayed pulse stream is used for the framing pulses. Each data stream is used to modulate the appropriately delayed periodic pulse stream. The outputs from the modulators and the framing pulse stream are combined to give the bit-interleaved optical TDM stream. The power level of the framing pulses is chosen to be distinctly higher than that of the data pulses.

The corresponding demultiplexing operation is illustrated in Figure 2.5(b). The multiplexed input is split into two streams using a coupler. A thresholding

operation, called clock recovery, is performed to extract the framing pulses. In order for the signal in a particular channel to be recovered, the demultiplexer, which is a logical "AND" gate, also called a comparator, needs to have a pulse train at the frequency of the incoming data, so that the comparisons are done at the correct time. In most working systems today, however, the raw optical signal is converted into an electrical signal before any decoding operations take place. This means that a bottleneck is created as a high-speed optical link meets standard electronics with its corresponding speed restrictions.
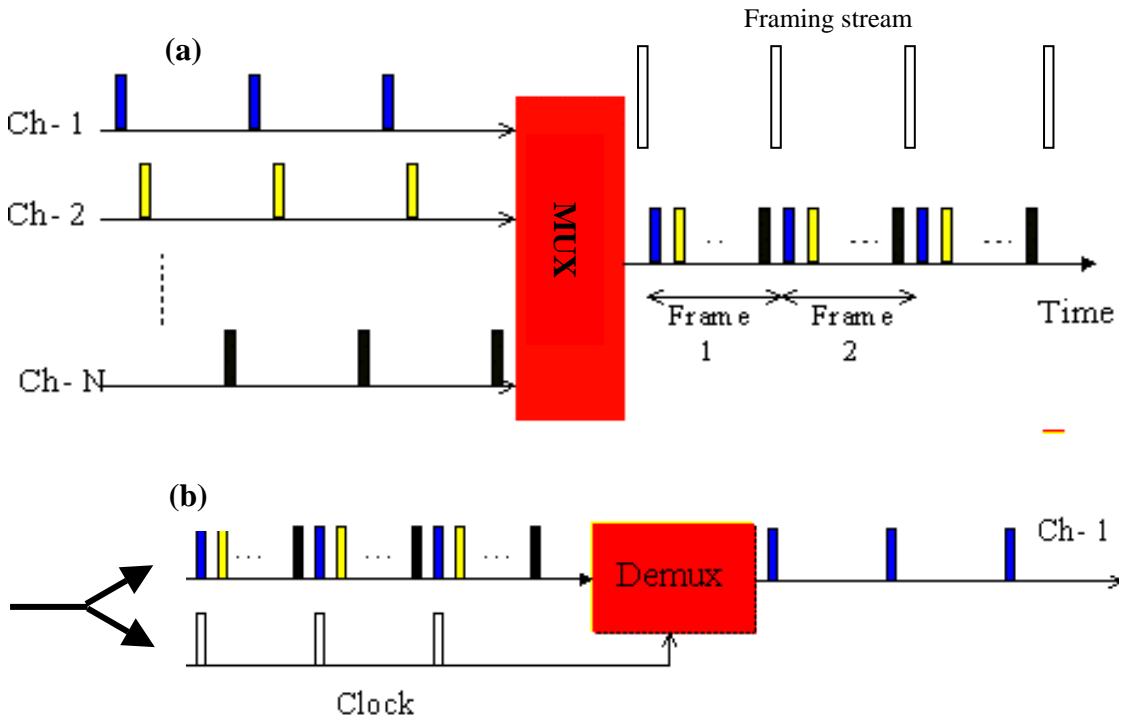
Figure 2.5. Diagram of OTDM coding (a) and decoding (b) schemes [38].

To eliminate the low-speed electronic circuitry, data decoding must be carried out in the optical domain, part of which is all-optical clock recovery [39]. This is usually achieved using a laser modelocked at an approximate clock frequency, which is further optically locked to the required bit rate by the incoming data stream itself. The requirements for a laser construction suitable for this function are high stability, short pulse duration and a wide locking range. In [40], error-free clock recovery was achieved using an external-cavity semiconductor optical amplifier, which showed a locking bandwidth of 830 kHz and remained locked for almost 8000 bits without an incoming data signal.

2.2.4. Modelocked lasers as frequency etalons

Other applications of modelocked lasers take advantage of their Type III spectrum, which provides a comb of equidistant narrow spectral lines. In spectroscopy, a "frequency ruler" defined by mode spacings in ultra-stable Type-III spectra emitted by modelocked dye lasers has been applied to the precision measurement of atomic transitions of cesium lines and to improving the accuracy of the Rydberg constant [41]. The technique has the promise of superseding the bulky and complicated set-ups based on frequency chains stabilised to a cesium clock. Other uses include optical filtering to produce a Type II spectrum for fibre radio applications [34].
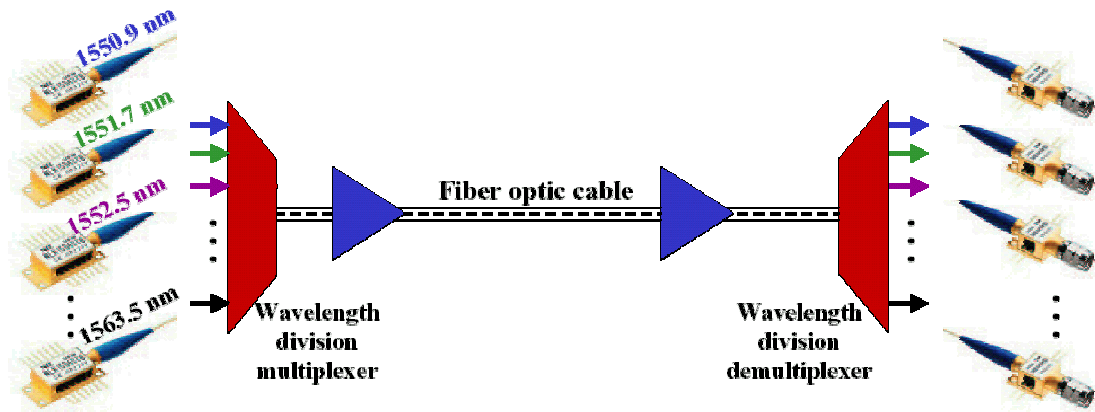
Figure 2.6. A typical WDM link, composed of multiple laser transmitters/modulators (each at a unique wavelength), a wavelength multiplexer and demultiplexer, wideband optical amplifiers, and photoreceivers for each channel [42].

Of particular importance is the deployment of Type III sources as comb generators in wavelength-division multiplexing (WDM). WDM, like OTDM as discussed above, also relies on multiplexing, but in the frequency domain, with individual channels carried on different wavelengths, as shown in Figure 2.6. Presently, individual wavelengths are generated by individual single-mode distributed feedback (DFB) lasers, which are expensive and require accurate controls. A modelocked laser is a promising candidate capable of delivering a Type-III comb of equidistant optical lines (modes), which may be individually extracted with optical filters to provide wavelength channels in WDM networks. Channel separations of 100, 50 and 25 GHz are easily achievable with a laser modelocked at these frequencies. Owing to their short cavity lengths, modelocked diode lasers are particularly suitable for dense WDM (DWDM) systems with up to

40 or 80 channels and a spacing < 25 GHz. The main requirement in this application is that the absolute wavelength position of each of the lines corresponds to the values assigned to the WDM grid. In practice, this means a very accurate control of the spacing between the lines, i.e. of modelocking frequency, and of the absolute wavelength of one of the modes. In [43], these controls were implemented by active modelocking in combination with temperature adjustment. Injection locking to a wavelength standard source has also been demonstrated. An optical frequency comb generator, as reported in [44], offers precise control of channel spacing and the central frequency using external optical and microwave reference signals. The generation of over 100 comb lines, spaced by 1-25 GHz centred at 1532 nm, has been demonstrated, the maximum spacing being limited by the bandwidth of the $LiNbO_3$ phase modulator employed.

2.2.5. Frequency stabilisation of microwave optical sources

High-speed modelocked lasers producing a Type III signal are ideally suited for both optical clock generation and recovery, although, to be truly practical, their timing jitter (random fluctuations in the time period between pulses) often needs to be reduced through external stabilisation [45]. The stabilisation can be achieved by a number of techniques, one of which relies on synchronisation to an electrical or optical pulse train or one of its harmonics. The latter approach is particularly appropriate at (sub)-THz frequencies, where even sub-harmonic electrical locking may prove prohibitively difficult.

An interesting all-optical stabilisation scheme involves optical feedback and was first proposed in [46]. A modelocked laser of optical cavity length L is placed in an external (free-space or fibre) cavity so that only a small fraction of the light is returned to the cavity. A collapse of the microwave linewidth of the laser was observed when the optical length of the external cavity was adjusted to accommodate an integer multiple of the laser cavity L.

A promising synchronisation scheme is illustrated in Figure 2.7(a) and consists of using an electrical MW signal to lock a "low-frequency" laser at a subharmonic of its modelocking rate, which, in turn, is used as a master laser to optically lock a "high-frequency" slave laser, with the master laser pulses also at a subharmonic of the slave's modelocking frequency [47]. Such a cascaded

synchronisation scheme allows (sub)-terahertz pulse repetition rate lasers to be locked and linewidth-narrowed using a low-frequency electrical clock. Recently, sub-harmonic synchronous modelocking of a colliding-pulse laser at 480 GHz has been achieved by the same team [48].
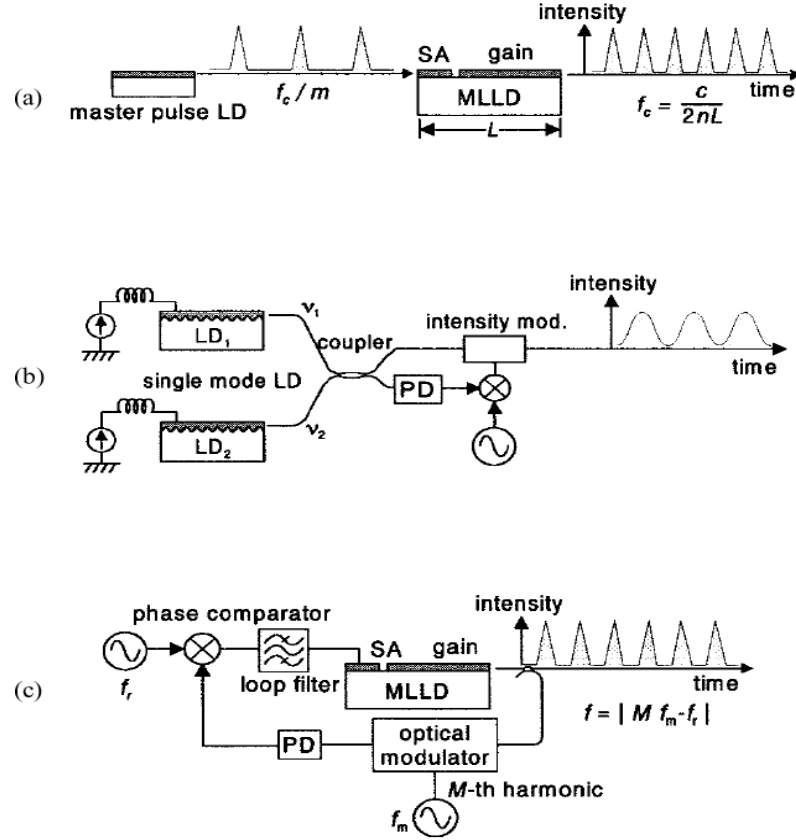
Figure 2.7. Frequency synchronisation schemes: (a) Subharmonic optical pulse injection. (b) Feedforward noise compensation. (c) Phase-locked loop. [49]

Another technique for frequency stabilisation that is suitable for both Type II and III signals is called the phase-locked loop (PLL). Most generally, it consists in down-converting the output of the laser under control, comparing the resulting signal with a stable reference clock, and, finally, using any phase difference between the two to adjust the operating conditions of the laser being stabilised. In a Type-II generation scheme, for example, as in Figure 2.7(b), where each of the two spectral lines is produced by a separate single-mode laser, a feed-forward phase-locked loop can be employed to lock one of the lasers to the other. In this technique, the combined two-mode light beam is modulated by an intensity modulator. The drive signal applied to the modulator is a beat note down-converted by a reference oscillator. The detection of intensity modulated light yields a low phase-noise beat. The phase noise is then cancelled out by the intensity modulation driven by the same

phase noise. As in all feed-forward techniques, because the RF beat signal should be detected and applied to the modulator, the upper frequency of this technique is limited by an electrical circuit.

PLL's have been shown to reduce the microwave linewidths of Type II [50] and Type III [49] signals considerably. In the latter scheme, shown in Figure 2.7(c), the generated optical pulses are modulated by an optical intensity modulator before being detected. The RF frequencies of the beat notes newly generated between the modulation sidebands and neighbouring original modes are lower than the repetition rate of pulses by a multiple of the modulation frequency. The modelocked laser source is then stabilised by applying the filtered beat signal to the saturable absorber section.

PLL's avoid the necessity to feed a high-frequency signal directly to the laser, but they often require a stable high-frequency electrical reference signal and a complex control circuitry. A reference signal at a sub-harmonic of the MW frequency can also be used to stabilise a high-speed laser modelocked at that frequency, with modelocking rates of up to 200 GHz [51]. Overall, however, it is believed that PLL's are less suitable for near-THz frequency stabilisation than the optical injection methods described above.

2.3. Optical downconversion

In applications where the microwave component of a MW-modulated optical signal is required in electrical form, it needs to be extracted, or down-converted, by means of an appropriate detector. It can then be radiated into free space from an antenna or transmitted along a waveguide, if further processing is required. The basic principle is illustrated in the schematic of Figure 2.8.
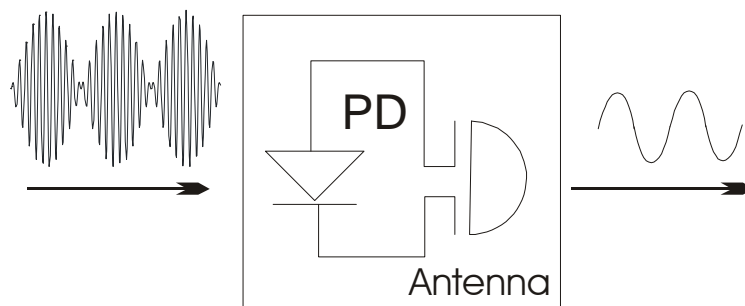
Figure 2.8. Optical to THz down-converter

Very broadly, there are two key methods for down-converting optical signals: direct detection and photomixing, albeit the distinction between the two is somewhat blurred. While the choice of material and detector design may differ, the underlying principle is the same for both methods: an incident optical signal having a time-varying intensity modulation at a MW frequency generates charge carriers, which contribute to a photocurrent also modulated at that MW frequency.

2.3.1. Direct detection

Direct detection is most commonly implemented with the so-called PIN photodetectors. These incorporate a PIN *(p-i-n)* junction, which consists of *p*-doped and *n*-doped semiconductor layers with a fully depleted intrinsic semiconductor layer in between. The depletion ensures that the carriers (electrons and holes) move through the intrinsic layer at their saturated drift velocity, which results in a short transit time. Depletion is obtained by applying an electric field across the intrinsic layer through an external bias. If the intrinsic layer is very thin, then the semiconductor potential barriers will provide depletion without any bias on the diode.
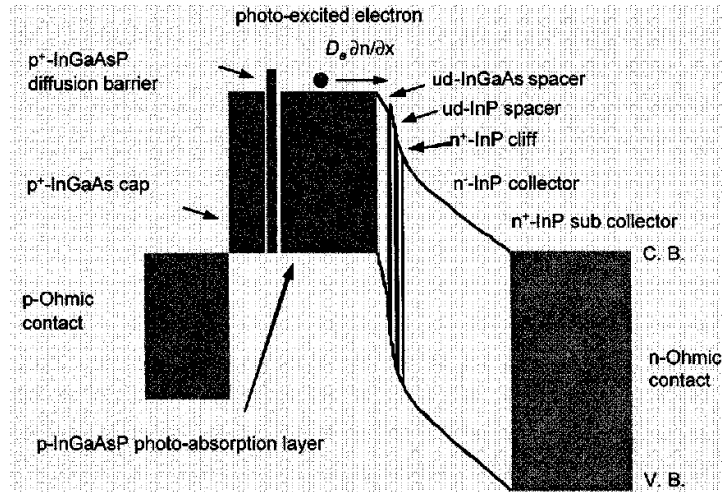
Figure 2.9. Energy band diagram of a uni-travelling-carrier photodiode (after [52]).

PIN photodetectors are intrinsically low-pass devices with a speed limited, at best, by the intrinsic layer transit time. Usually, other factors, e.g., junction capacitance and velocity mismatch, reduce the maximum available bandwidth. For high-speed operation, waveguide photodiodes with light incidence parallel to the junction plane have been extensively studied [53], with multimode designs offering a

110-GHz bandwidth with 50% quantum efficiency [54]. By locating an evanescent coupling passive waveguide underneath the absorption layer, high-power operation of waveguide PIN detectors has been demonstrated.

The depletion capacitance limit can be circumvented by applying travelling-wave design techniques [55]. It is also possible to increase the detection efficiency by making use of carrier velocity overshoot effects, as in the uni-travelling-carrier photodiode (UTC-PD) [52, 56]. Figure 2.9 shows the energy band diagram of a UTC-PD structure. The absorption and drift regions are separate and the absorption region is doped so that the holes are majority carriers. The electrons are injected at high energy into the thin drift region, where they travel at overshoot velocity, typically five times static saturated drift velocity, thus giving rise to much reduced space charge for a given terminal current. UTC-PDs have been reported with bandwidths exceeding 300 GHz and output powers over 8 dBm [52].

Metal–semiconductor–metal (MSM) photodetectors have been used in a number of microwave photonic applications, where surface illumination is the preferred detection method [56]. The main attraction has been their compatibility for integration with field-effect-transistor devices in optically controlled monolithic microwave integrated circuits (MMICs). Bandwidths as high as 78 GHz have been reported [57] with an external quantum efficiency of 7.5% due to electrode blockage effects. Higher efficiencies are generally obtainable with depletion photodetectors.

The upper limit to depletion photodiode frequency response is set both by transit time effects and by the depletion capacitance of the photodiode. Optimisation involves conflicting requirements, since reducing the depletion width to increase the transit-time limited frequency increases the depletion capacitance and may lead to incomplete absorption of light in geometries where light is incident normal to the junction plane.

2.3.2. Photoconductive detectors and photomixing

A photoconductive photodetector simply consists of a uniform piece of semiconductor (as opposed to a *p-i-n* junction) with two interdigitated electrodes on top. An electrical field is induced across the semiconductor gaps by applying an external bias to the electrodes. The incident light changes the conductivity of the

semiconductor by generating electron-hole pairs. This change is measured through the electrodes, with the speed of operation ultimately limited by the carrier lifetime of the semiconductor material and the device capacitance.

When two beams with different wavelengths but common polarisation are combined and direct-detected, a MW signal is generated in the detector with the centre frequency equal to the optical frequency difference between these two beams. This process is called photomixing, or optical heterodyning, and is normally used with two wavelengths (i.e., a Type-II signal), although it should also be suitable for a Type-III signal. This method can be thought of as heterodyne detection of one beam using the other beam as a local oscillator. The advantage of this method is the possibility to generate very high-frequency signals by making the frequency difference between the two lightwaves correspondingly large.

Photomixing was proposed over three decades ago as a means of generating coherent radiation in the microwave region. However, useful levels of output power have not been obtained because of the lack of robust photomixers and high-quality tuneable lasers. With recent advances in high-speed III-V optoelectronic devices and solid-state lasers, interest in photomixing has been revived and new methods pursued. A few remarkable achievements have been made in recent years using diode lasers and GaAs photomixers [58-61]. Down-conversion experiments were performed by Brown et al. on a low-temperature grown (LTG) GaAs photomixer pumped with two 100 mW DBR lasers. Continuous free-space electromagnetic waves at up to 3.8 THz have been generated [58].

As this method of down-conversion has demonstrated the highest photomixing bandwidth reported to date, it is worth considering the physics behind it in more detail. Photomixing is an essentially non-linear effect and can only occur in a non-linear medium such as a semiconductor. When light containing two frequency components is absorbed in a semiconductor, the concentration of photo-generated carriers will oscillate at the difference frequency and modulate the resistance of the structure if an external bias is applied. The equivalent circuit of a photomixer is given in Figure 2.10.
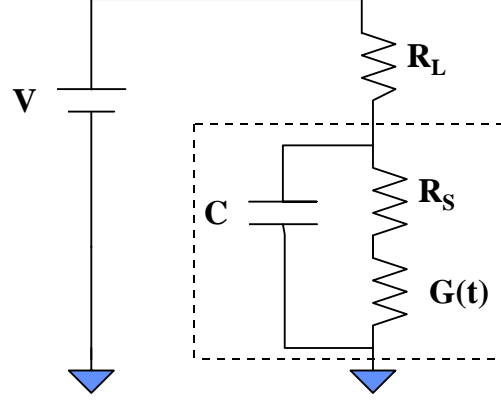
Figure 2.10. Equivalent photomixer circuit.

When two CW laser beams of powers $P_{i1}(t) = P_1 \cos(\omega_1 t)$ and $P_{i2}(t) = P_2 \cos(\omega_2 t)$ are mixed in the semiconductor, they give rise to the mixing products $P_i(t) = P_1 + P_2 + 2\sqrt{m P_1 P_2}[\cos(\omega_2 - \omega_1)t + \cos(\omega_2 + \omega_1)t]$

In what follows, we shall denote $P_0 = P_1 + P_2$ and $\omega \equiv \omega_2 - \omega_1$. Under external bias *V*, the resulting current is the sum of a DC offset and a harmonic component:

$$I(t) = G(t)V = G_0 \left[1 + \frac{\beta}{\sqrt{1 + (\omega\tau)^2}} \sin(\omega t + \phi) \right] V \,,$$

where the DC photoconductance $G_0 \sim \frac{\eta_i \mu \tau}{A^2} P_0$; here, η_i is the internal quantum efficiency, μ is the carrier mobility, τ is the carrier lifetime and *A* is the illuminated area. In the small-signal limit, $G_0 R_L \leq 1$, the power delivered to R_L at frequency ω is

$$P_\omega = \frac{1}{2} \frac{(G_0 V)^2 R_L}{\left[1 + (\omega R_L C)^2\right]\left[1 + (\omega\tau)^2\right]}$$

At the lower frequency end, a longer carrier lifetime increases the absolute power:

$$\omega \to 0: \quad P_\omega \approx (G_0 V)^2 R_L \sim \tau^2$$

In the high-frequency limit, the THz output rolls off as ω^{-4} regardless of carrier lifetime τ. However, roll-off begins when $\omega\tau > 1$, therefore short lifetimes are required for large bandwidths. This behaviour is illustrated in Figure 2.11 for several lifetimes τ.

$$\omega \to \infty : P_\omega \approx \frac{(G_0 V)^2}{R_L C^2 \tau^2 \omega^4} \sim \omega^{-4}$$
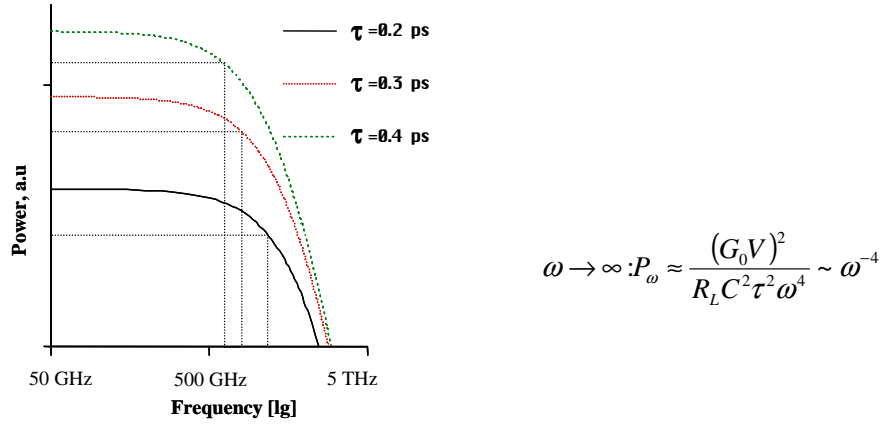
Figure 2.11. Photomixing power roll-off curves for different lifetimes (other parameters taken from [58]).

A typical photomixer consists of two sets of interdigitated metal electrodes on top of a semiconductor (GaAs, InGaAsP, InP) epitaxial layer grown on a semi-insulating substrate. The carrier lifetime in the epitaxial layer often needs to be shortened, e.g., by ion implantation. The electrodes are connected to a planar distributed circuit (antenna or waveguide), which is represented by a load resistance, as shown in Figure 2.12.
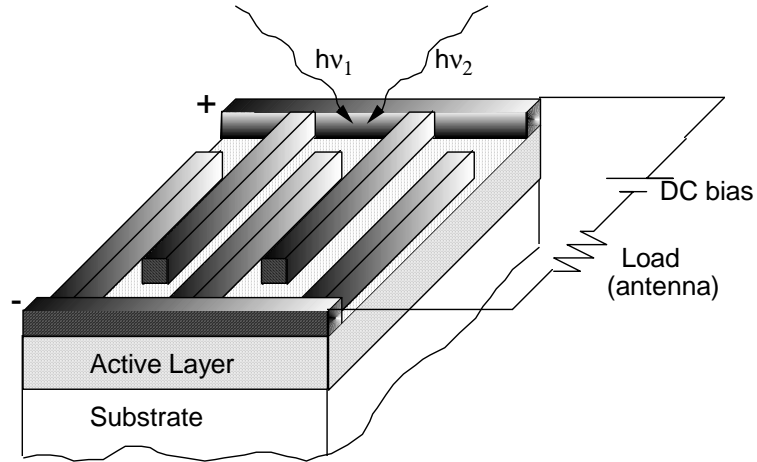
Figure 2.12. Schematic of photomixer design and operation.

The photomixer is pumped with either two lasers (one of which is fixed and the other is tuneable) or two modes of one laser. The generated photocarriers modulate the structure's resistance and give rise to the difference-frequency photocurrent, which drives the integrated antenna, emitting microwave radiation. A spiral antenna can have several loops of varying diameter (circumference) to accommodate several wavelengths. For example, an antenna for the band of 500 GHz - 5 THz must have loops with a circumference from 60 µm to 600 µm.

Longer wavelengths are emitted by outer loops, and shorter by inner ones. Photographs of fabricated photomixer antenna structures are shown in Figure 2.13. The fabrication of these devices will be discussed in Chapter 10.

Finally, it is worth noting that the photomixing scheme may be potentially both simplified and improved by replacing two laser beams with a single optical source generating a comb of narrow-linewidth, equidistant modes offset by the required THz frequency – such as an ultrafast modelocked laser emitting a Type III spectrum. Ultimately, it has been suggested that such mixing can be performed within the saturable absorption section of the laser itself [62]. It is believed that photomixing is the preferred down-conversion method for the semiconductor laser-based optical THz sources presented in this Thesis.
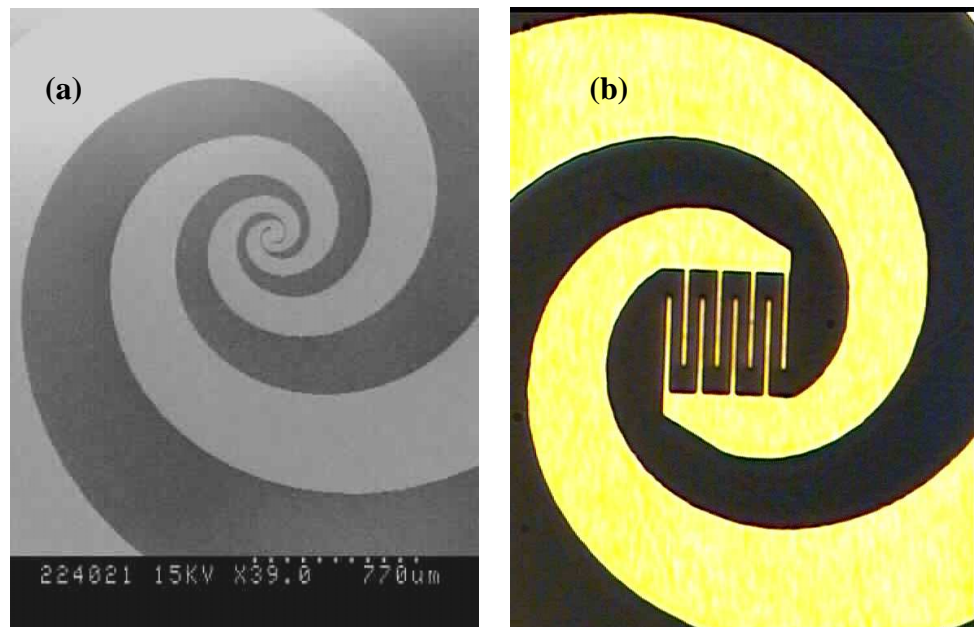
Figure 2.13. SEM image **(a)** and optical photograph **(b)** of the interdigitated structure of the fabricated photomixer devices.

2.4.   References

[1]   H. Weber and R. Dandliker, "Intensity interferometry by two-photon excitation of fluorescence," *IEEE J. Quant. Electronics*, vol. 4, pp. 1009 - 1013, 1968.

[2]   J.W. Waters, "Submillimeter-Wavelength Heterodyne Spectroscopy and Remote Sensing of the Upper Atmosphere," *Proceedings of the IEEE*, vol. 30, pp. 1679, 1992.

[3]   P. Lane, "Fibre-supported mm-wave systems," presented at OMW '99 (Interactions Between Microwaves & Optics), Autrans, France, 1999.

[4]   D. Wake, "Microwave and millimeter photonics for telecommunications," presented at OMW '99 (Interactions Between Microwaves & Optics), Autrans, France, 1999.

[5]   D. Novak, Z. Ahmed, R.B. Waterhouse, and R.S. Tucker, "Signal generation using pulsed semiconductor lasers for application in millimeter-wave wireless links," *IEEE Trans. Microwave Th. and Techn.*, vol. 43, No.9, 1995.

[6]   S. Fukushima, C. F. C. Silva, Y. Muramoto, and A. J. Seeds, "Optoelectronic Synthesis of Milliwatt-Level Multi-Octave Millimeter-Wave Signals Using an Optical Frequency Comb Generator and a Unitraveling-Carrier Photodiode," *IEEE Phot.Techn. Lett.*, vol. 13, No.7, pp. 720-722, 2001.

[7]   S. Kawanishi, "High Bit Rate Transmission over 1 Tbit/s," *IEICE Trans. Electron.*, vol. E84-C, No.5, pp. 509-515, 2001.

[8]   S. Kawanishi, "Ultrahigh-Speed Optical Time-Division-Multiplexed Transmission Technology Based on Optical Signal Processing," *IEEE J. Quant. Electronics*, vol. 34, No.11, pp. 2064-2079, 1998.

[9]   Z. Ghassemlooy, C.Y. Cheung, G. Swift, R. Gao, J. Wang, and A. Decker, "All Optical Time Division Multiplexing - an overview," *http://www.shu.ac.uk/ocr/downloads/otdm/*.

[10]   R. Ludwig, A. Ehrhard, W. Pieper, E. Jahn, N. Agrawal, H.J. Ehrke, L. Kuller, and H.G. Weber, "40 Gbit/s demultiplexing experiment with 10GHz all-optical clock recovery using a modelocked semiconductor laser," *Electron. Lett.*, vol. 32, pp. 327-329, 1996.

[11]   B. K. Mathason and P. J. Delfyett, "Pulsed Injection Locking Dynamics of Passively Mode-Locked External-Cavity Semiconductor Laser Systems for All-Optical Clock Recovery," *J. Lightwave Techn.*, vol. 18, pp. 1111-9, 2000.

[12]   U. Brinkmann, "Frequency comb spans the spectrum," *Laser Focus World*, vol. 7, pp. 38-42, July 2001.

[13]   Ian M. White, "A new architecture and technologies for high-capacity next-generation metropolitan networks." Thesis: Stanford University, 2002.

[14]   H. Sanjoh, H. Yasaka, Y. Sakai, K. Sato, and H. Ishii, "Multiwavelength light source with precise frequency spacing using a mode-locked semiconductor laser and an arrayed waveguide grating filter," *IEEE Phot.Techn. Lett.*, vol. 9, pp. 818-820, 1997.

[15]   S. Bennett, B. Cai, E. Burr, O. Gough, and A. J. Seeds, "1.8-THz Bandwidth, Zero-Frequency Error, Tunable Optical Comb Generator for DWDM Applications," *IEEE Phot.Techn. Lett.*, vol. 11, No.5, pp. 551-553, 1999.

[16]   M. Attygalle, H. F. Liu, and A. Nirmalathas, "Robust All-Optical Harmonic Clock Signal Generation Through Optical Injection into Passively Mode-Locked Semiconductor Lasers," *IEEE Phot.Techn. Lett.*, vol. 13, No.9, pp. 1017-1019, 2001.

[17]   O. Solgaard and K.Y. Lau, "Optical feedback stabilisation of the intensity oscillations in ultrahigh-frequency passively modelocked monolithic quantum-well lasers," *IEEE Phot.Techn. Lett.*, vol. 5, pp. 1264-1266, 1993.

[18]   S. Arahira, S. Kutsuzawa, and Y. Ogawa, "Extreme Timing Jitter Reduction of a Passively Mode-Locked Laser Diode by Optical Pulse Injection," *IEEE J. Quant. Electronics*, vol. 35, No. 12, pp. 1805-1811, 1999.

[19]   S. Arahira and Y. Ogawa, "480-GHz subharmonic synchronous mode locking in a short-cavity colliding-pulse mode-locked laser diode," *IEEE Phot.Techn. Lett.*, vol. 14, pp. 537-539, 2002.

[20]   E. Hashimoto, A. Takada, and Y. Katagiri, "High-Frequency Synchronized Signal Generation Using Semiconductor Lasers," *IEEE Trans. Microwave Th. and Techn.*, vol. 47, No.7, pp. 1206-1218, 1999.

[21]   U. Gliese, "THz Signal Generation by Laser Mixing," LO Technology Assessment Report, European Space Agency Contract No. 11653/95/NL/PB, Technical University of Denmark 1996.

[22]   E. Hashimoto, A. Takada, and Y. Katagiri, "Synchronization of subterahertz optical pulse train from PLL-controlled colliding pulse modelocked semiconductor laser," *Electron. Lett.*, vol. 34, pp. 580-582, 1998.

[23]   H. Fukano, Y. Muramoto, K. Takahata, and Y. Matsuoka, "High efficiency edge illuminated uni-travelling-carrier structure refracting facet photodiode," *Electron. Lett.*, vol. 35, pp. 1664–1665, 1999.

[24]   J. E. Bowers and C. A. Burrus, "High-speed zero-bias waveguide photodetectors," *Electron. Lett.*, vol. 22, pp. 905-906, 1986.

[25]   K. Kato, A. Kozen, Y. Muramoto, Y. Itaya, T. Nagatsuma, and M. Yaita, "110 GHz 50% efficiency mushroom mesa waveguide p-i-n photodiode for a 1.55 μm wavelength," *IEEE Phot.Techn. Lett.*, vol. 6, pp. 719-721, 1994.

[26]   K.S. Giboney, R.L. Ngarajan, T.E. Reynolds, S.T. Allen, R.P. Mirin, M.J.W. Rodwell, and J.E. Bowers, "Travelling-wave photodetectors with a 172-GHz bandwidth and 76-GHz bandwidrh-efficiency product," *IEEE Phot.Techn. Lett.*, vol. 7, 1995.

[27]   A. J. Seeds, "Microwave Photonics," *IEEE Trans. Microwave Th. and Techn.*, vol. 50, No.3, pp. 877-977, 2002.

[28]   E. Droge, E. H. Bottcher, S. Kollakowski, A. Strittmatter, O. Reimann, R. Steingruber, A. Umbach, and D. Bimberg, "Distributed MSM photodetectors for the long wavelength range," presented at Eur. Opt. Commun. Conf.,, Oslo, 1998.

[29]   E. R. Brown, K. A. McIntosh, K. B. Nichols, and C. L. Dennis, "Photomixing up to 3.8 Thz in Low-temperature-grown GaAs," *Appl. Phys. Lett.*, vol. 66, pp. 285-287, 1995.

[30]   S. Matsuura, M. Tani, and K.Sakai, "Generation of Coherent Terahertz Radiation by Photomixing in Dipole Photoconductive Antennas," *Appl. Phys. Lett.*, vol. 70, pp. 559-561, 1997.

[31]   O. Acef, F. Nez, and G.D. Rovera, "Optical Heterodyning with a Frequency Difference of 1 THz in the 850nm Range," *Opt. Lett.*, vol. 19, pp. 1275-1277, 1994.

[32]   K. A. McIntosh, E. R. Brown, K. B. Nichols, O. B. McMahon, W. F. DiNatale, and T. M. Lyszczarz, "Terahertz Photomixing with Diode Lasers in Low-temperature-grown GaAs," *Appl. Phys. Lett.*, vol. 67, pp. 3844, 1995.

[33]   E.L. Portnoi, B.B. Gorfinkel, E.A. Avrutin, I.G. Thayne, D.A. Barrow, J.H. Marsh, and Y.Li, "Optoelectronic microwave-range frequency mixing in semiconductor lasers," *IEEE J. Sel. Top. Quantum Electron.*, vol. 1 (2), pp. 451-6, 1995.

CHAPTER 3.

HIGH-FREQUENCY OPERATION OF QUANTUM-WELL

SEMICONDUCTOR LASERS

3.1.   Aims of the Thesis

In the previous two chapters, a review of state-of-the-art applications and technologies employing microwave/terahertz signals, both as free-space radiation and as an envelope on an optical carrier, was presented. It was demonstrated that microwave photonics, i.e., the generation, transmission and processing of high-frequency signals in the optical domain, is much better suited for addressing the (sub)terahertz region than any electronic means. There also exist several down-conversion techniques for the extraction of microwave components from optical carriers, if electronic processing or radiation into free space is required.

Despite the variety of THz generation techniques, there are still very few sources capable of delivering a stable, narrow-linewidth THz signal, either in the optical or electrical domain. The research presented in this Thesis aims at developing a terahertz source based on an ultrafast modelocked semiconductor laser with a frequency ceiling of up to 2 THz. The laser can be frequency-stabilised using the optical injection techniques described in Section 2.2.5 of Chapter 2, and its output down-converted, if required, to produce a free-space THz beam using a photomixer converter (see Section 2.3.2). Such a source would then be a promising candidate for the many applications outlined in Chapter 1, from radio-astronomy to THz imaging. Without down-conversion, the source may be suitable for the uses described in Section 2.2, primarily as a local oscillator source and an optical clock and frequency comb generator in optical telecommunications systems.

Within the timescales of the project covered by this Thesis, the author was able to fabricate ultrafast laser diodes and successfully demonstrate their terahertz operation. Some work was also done on realising the photomixer, and a two-

wavelength mixing experiment was attempted. Parallel to this work, the author's colleagues at the University of Glasgow were also investigating electrical locking techniques for multi-gigahertz modelocked lasers [1-3], which can be used to optically stabilise the high-frequency laser developed by the author. Despite being a proof-of-principle university project, it is hoped that this research will pave the way for the realisation of a novel semiconductor laser-based terahertz source with viable commercial applications.

The rest of the Thesis will be concerned with the concept, development and measurement of the terahertz-modelocked semiconductor laser source described above. In this Chapter, some pertinent theory of diode lasers and their high-frequency operation will be presented, followed by a more detailed discussion of ultrafast modelocked lasers and a review of their state-of-the-art.

3.2. Basics of quantum-well semiconductor lasers

This section is intended to give a brief introduction into the field of semiconductor lasers and is based on the concise tutorial by Weisbuch [4]. A knowledge of the basics of solid-state and semiconductor physics is assumed, while the reader wishing to find a more comprehensive treatment of the subject is referred to the excellent textbooks [5-8].

3.2.1. Semiconductor materials

Semiconductor lasers are capable of covering a vast range of the spectrum extending from the near ultraviolet to the far infrared (0.3 μm – 10 μm). This has become possible by the careful engineering of the bandgap energy of compound semiconductor materials. These are typically alloys of elements of various groups of the Periodic Table grown as crystals, with closely matched lattice constants between adjacent layers of different compositions. The graph of Figure 3.1 shows material compositions against their bandgap energy, with vertical lines connecting the materials with matching lattice constants. Of these, three material systems are particularly versatile: GaAs/AlGaAs covering the spectrum between 0.8 μm and 1 μm, and InGaAsP/InGaAs/InP or InGaAs/InAlGaAs/InP with wavelengths from 0.9 μm – 1.67 μm (1.1 μm being the shortest practical wavelength for a laser). The

latter two are of particular importance in telecommunications applications, as mentioned in Chapter 2.
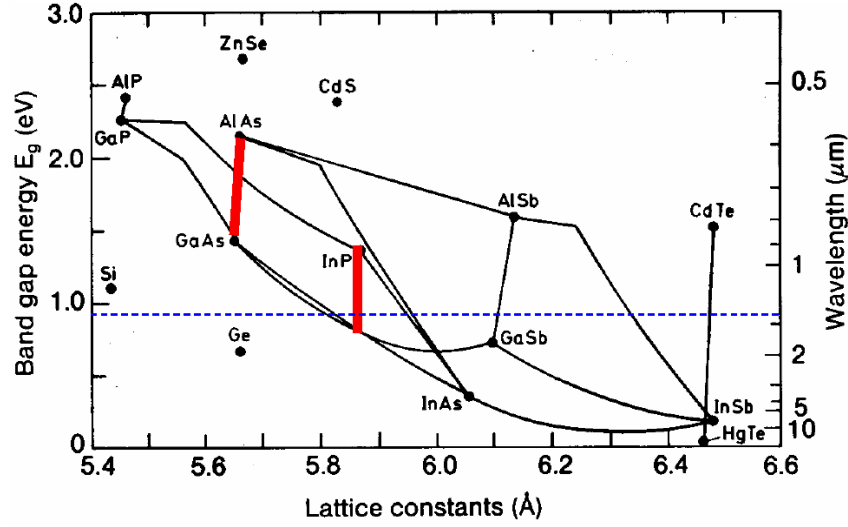
Figure 3.1. Compositional dependence of lattice constants and bandgap energy.

In this project, lasers were fabricated from GaAs/AlGaAs material due to it being one of the most mature and well-researched semiconductor systems. The lattice constants of GaAs and AlGaAs are almost identical, enabling growth of heterostructures with a low concentration of defects and low stress at the interfaces. The bandgap of $Al_xGa_{1-x}As$ material increases with increasing aluminium fraction x. At a heterostructure interface between GaAs and AlGaAs, potential barriers are formed, whose magnitudes have been determined experimentally as $\Delta E_c = 0.67\ \Delta E_g$ and $\Delta E_v = 0.33\ \Delta E_g$ for the conduction and valence bands, respectively, where ΔE_g is bandgap energy. When GaAs is used as the active region with an AlGaAs cladding, carriers injected into the GaAs are confined, causing a high population density and, hence, a lower required threshold current density to achieve the transparency condition. For maximum usable gain it is essential to confine the generated light to the region of population inversion. This is achieved with heterostructures, as, in most cases, the increase in bandgap corresponds to a decrease in refractive index.

Growth of such structures relies on the development of sophisticated epitaxial techniques. The ones most commonly used are liquid phase epitaxy (LPE), molecular beam epitaxy (MBE), vapour phase epitaxy (VPE), and it variants metal organic vapour phase epitaxy (MOVPE) and metal organic chemical vapour deposition (MOCVD). In LPE, a semiconductor substrate is placed in a saturated solution of the epitaxial layer constituents, which then crystallise on the substrate when cooled. In

MBE, the epitaxial layer is grown by reacting atomic or molecular beams of the constituent elements with a high-temperature substrate in a high vacuum. In VPE, the layers are formed by reaction of gaseous elements or compounds at the heated surface of the substrate, with the composition being controlled by varying the relative flow rates. Here, the reactants are in the form of metal chlorides and hydrides.

A variant of this technique called MOVPE, more commonly known as MOCVD, uses metal alkyls as sources. Reactant velocities are higher in MOVPE than in hydride VPE, allowing quicker changes of composition and smoother heterojunction profiles. The process employs chemical reactions, which transform gaseous molecules, called precursors, into solid material, in the form of thin film, on the surface of a substrate. The material used in the Project was grown using the MOCVD technique.

3.2.2. Threshold and gain of a semiconductor laser

A schematic of a most basic Fabry-Pérot semiconductor laser with a cavity length L is given in Figure 3.2(a) [4]. Emission of light takes place between two mirrors formed by cleaved semiconductor-air interfaces. For an optical wave that is an eigenmode of the Fabry-Pérot cavity (i.e., satisfies the phase condition $2kL = 2\pi n$), the threshold condition is obtained by stating that the intensity is unchanged after a round trip of the cavity, as illustrated in Figure 3.2(b).

$$R_1 R_2 e^{(g-\alpha)2L} = 1 \tag{3.1}$$

where R_1 and R_2 are the reflection coefficients of the mirrors (typically 0.3 for cleaved facets), and g and α are the gain and loss coefficients, respectively, per unit length. The gain at threshold can then be expressed as

$$g = \alpha + \frac{1}{2L} \ln \frac{1}{R_1 R_2} \tag{3.2}$$

With typical numbers $R_1 = R_2 = 0.3$ for an uncoated laser, $L = 250$ μm, $\alpha = 10$ cm^{-1}, the threshold gain g is found to be ~ 50 cm^{-1}.
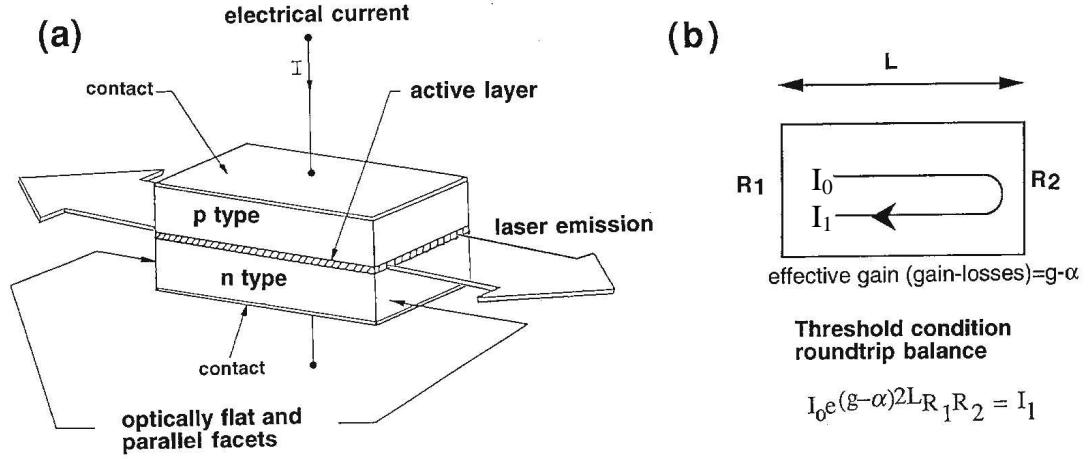
Figure 3.2. (a) Schematics of a semiconductor laser; **(b)** Balance equation for an optical wave completing a round trip in the cavity.

Figure 3.3 schematically depicts the formation of gain in a semiconductor structure. Under electrical injection of electrons and holes into the active region from the adjacent *n* and *p*-regions, one creates an inversion of excess carrier population near the band edge. If the injected carrier concentration becomes large enough, the stimulated emission can exceed the absorption so that optical gain can be achieved in the active region. The equilibrium condition between stimulated emission and absorption is referred to as transparency of the active medium. Since the Einstein coefficients describing these two processes are equal, the inversion condition is only determined by the occupancy factors f_c and f_v of the conduction and valence bands, respectively, via

$$f_c(1 - f_v) > f_v(1 - f_c) \tag{3.3}$$

Using the quasi Fermi levels E_{Fc} and E_{Fv} to express the occupancy factors, Eq.(3.3) becomes

$$E_{F_c} - E_{Fv} > h\nu \tag{3.4}$$

This is the well-known Bernard-Durrafourg equation, which shows that at least one quasi-Fermi level must penetrate one of the bands (conduction or valence) for the emitted photon energy *hv* to be the same or higher than the bandgap energy E_g.
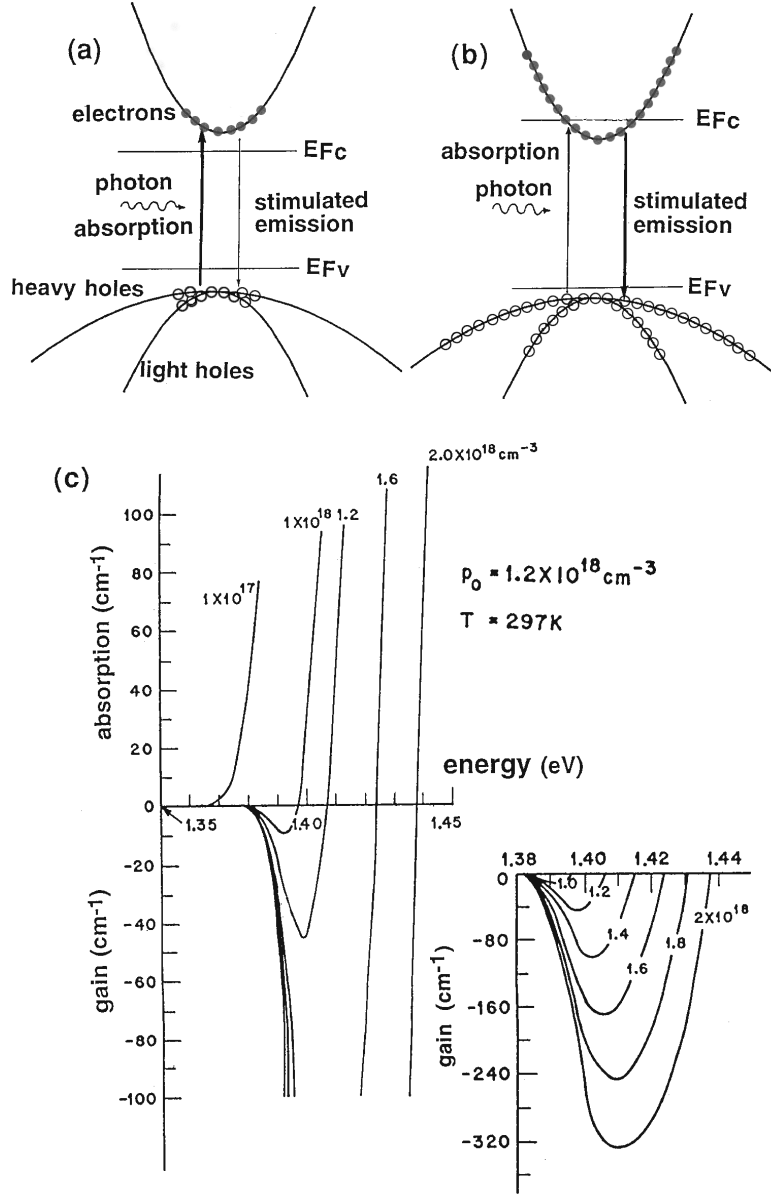
Figure 3.3. Schematics of gain formation in a semiconductor: absorption and stimulated emission transitions under weak **(a)** and strong **(b)** injection. Note the position of the quasi Fermi levels E_{Fc} and E_{Fv}; **(c)** absorption and gain under increasing excitation [8].

Charge neutrality dictates that the electron-hole densities are equal, which, expressed in terms of the equivalent densities of states N_c and N_v of the bands, takes the form

$$N_c f_c = N_v f_v \qquad (3.5)$$

From here it is easy to see that if N_c and N_v are equal, then $f_c = f_v = 0.5$ satisfies Eq.(3.3). However, in III-V group materials, $N_c \sim 0.25\, N_v$. Therefore one needs a much higher occupancy factor in the lower density band (here, the

46

conduction band) to satisfy Eq.(3.3). Indeed, to meet both Eqs. (3.3) and (3.5), one requires that $f_c \sim 0.8$ and $f_v \sim 0.2$. Due to the asymmetry between the bands, the fill factor for electrons needs to be increased considerably compared to a symmetric case. This need can be reduced by the use of strained quantum wells, which restores the symmetry between the valence and conduction bands by separating various hole sublevels and changing the dispersion of holes to light hole-like (for tensile strain).

Once transparency is reached, additional carriers create net gain. The standard calculation involves summation, for a particular photon energy, over the various transitions that can occur between all electron-hole pairs, whether inverted or not. The former give gain, and the latter absorption. A simpler model considers the electron-hole pair gas as a two-level system with a homogeneous linewidth $\Delta\nu$ given by the occupancy factor of carrier states. Then the gain is given by the standard formula [5]

$$g \simeq \Delta n \frac{c^2}{8\pi\nu^2 n_{opt}^2 \tau_{sp}} \frac{1}{\Delta\nu} \qquad (3.6)$$

where n_{opt} is the refractive index, Δn is the excess density above the inversion density (or transparency density) n_0:

$$\Delta n = n - n_0, \qquad (3.7)$$

and τ_{sp} is the spontaneous radiative lifetime. From relation (3.6) with $\tau_{sp} \approx 3 \cdot 10^{-9}$ s, one finds that for gain $g = 50$ cm^{-1}, $\Delta n \approx 4 \cdot 10^{16}$ cm^{-3}. This is within a factor of 5 of what was measured and calculated in the full manner [8], see Figure 3.3(c). Using the Casey-Panish [8] value of $\Delta n \approx 2 \cdot 10^{17}$ cm^{-3} and $n_0 \approx 10^{18}$ cm^{-3}, the threshold carrier density is found to be $1.2 \cdot 10^{18}$ cm^{-3}.

3.2.3. Optical confinement factor

In a real laser diode, only a fraction of the main optical mode overlaps the active region that provides gain. It is indeed only this fraction of the optical wave that is able to induce stimulated emission. However, the whole of the wave experiences absorption and loss. To account for this, Eq.(3.2) can be modified as follows:

$$\Gamma g = \alpha + \frac{1}{2L} \ln \frac{1}{R_1 R_2} \qquad (3.8)$$

where Γ is the optical confinement factor defining the overlap between the optical mode and the gain region.
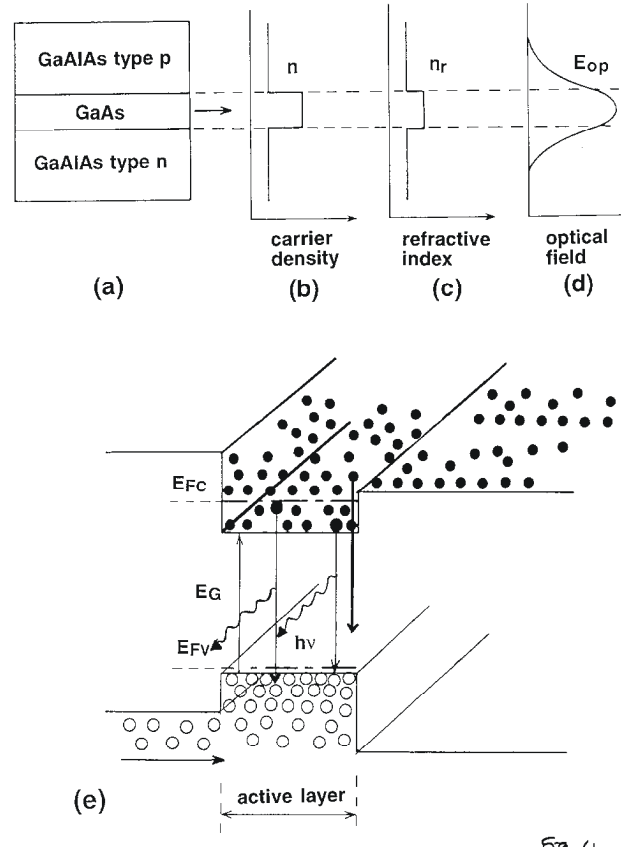
Figure 3.4. Schematics of a double heterostructure laser **(a)**, showing carrier density **(b)**, refractive index **(c)**, optical waveguiding **(d)** and spatial distribution of carriers **(e)**.

In the original *p-n* junction laser, the optical wave width is of the same order of magnitude as the carrier diffusion length, i.e., in the micron range. Therefore the overlap is nearly unity. In double heterostructures, the carriers are confined within the central active layer by the potential barriers, which are present at the hetero interfaces, as shown in Figure 3.4. The optical wave is guided by the higher index of refraction of the active, smaller bandgap material [5]. This waveguiding effect is present in active layers with thickness down to 0.1 μm, for which the optical confinement factor is still relatively large (> 0.1). Below this thickness, the active layer is too thin to have a strong waveguiding effect. This is similar to the poor electron confinement in thin quantum wells when the electron confining energy is comparable to the well energy depth, and the electron wave function penetrates deep

into the barrier material. In the optical waveguide context, the optical mode becomes wider with decreasing active layer thickness, which leads to a significant reduction in the confinement factor Γ. An approximate relationship for the refractive indices n_2 and n_1 of the waveguide core and cladding, respectively, wavelength λ and active layer thickness d is given in [8]:

$$\Gamma \approx 2\pi^2(n_2^2 - n_1^2)d^2/\lambda_0^2 \tag{3.9}$$

3.2.4. Progress towards present-day lasers

Semiconductor lasers have evolved over the past 40 years, and their threshold current, which is one of the main criteria for their suitability to real-life applications, has been reduced by several orders of magnitude. Compared to the first laser diode demonstrations of the 1960's with threshold current densities of 10^5 A $\cdot$ cm^{-2}, state-of-the-art devices operate at current densities of tens of A $\cdot$ cm^{-2}, as illustrated in Figure 3.5.
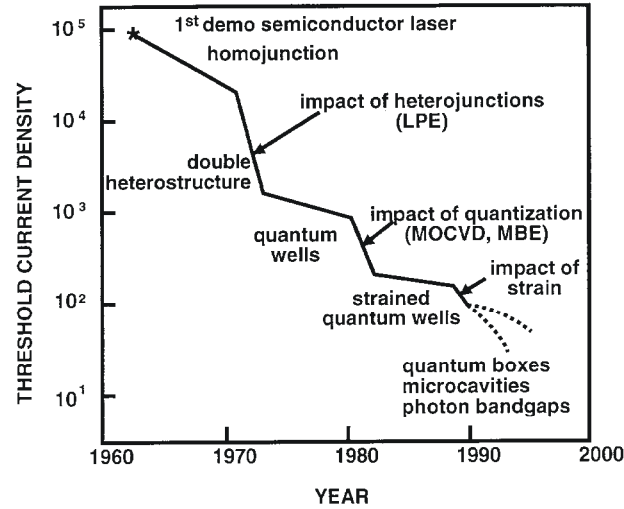
Figure 3.5. Evolution of threshold current density of semiconductor lasers (up to the year 1996, [4]).

An important breakthrough was made by the use of double heterostructures around 1970 (second generation lasers [9]), which enabled continuous operation of laser diodes through the reduction of threshold current density to the kA $\cdot$ cm^{-2} range. While they required an injected carrier density similar to that of junction lasers, the volume in which such carrier density must be created was greatly reduced, as was the threshold current.

The 1980's saw the impact of the new material growth techniques of MBE and MOCVD through the use of two-dimensional (2D) quantum wells (QW). Their key advantage is in the reduction of the carrier density required to achieve transparency. In quantum wells, the density of electron and hole states is much lower than in bulk (3D) material owing to the freezing of one degree of freedom. This reduces the transparency density by a factor of ten, while the more efficient utilisation of carriers above transparency improves gain per carrier by a factor of two, thanks to a step-like density of state function and discrete energy levels of a QW, as illustrated Figure 3.6.
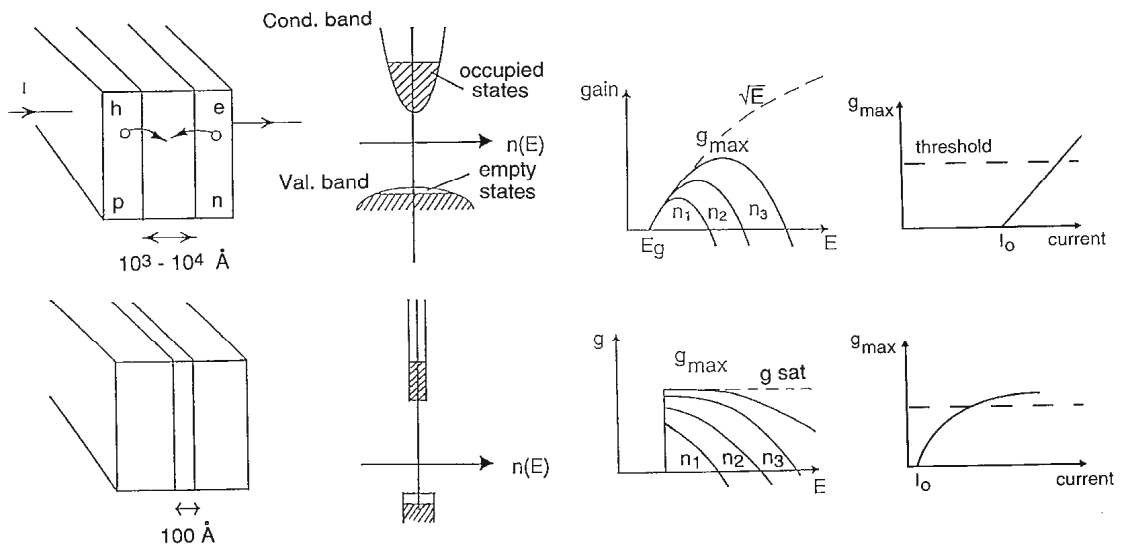
Figure 3.6. Schematic of gain formation in a 3D (bulk) double-heterostructure (top) and in 2D quantum well material (bottom). Due to the smaller density of states in QW's, the transparency current I_0 is reduced. Gain efficiency is also higher, which translates into a steeper gain-current curve at low injection levels.

There is, however, a difficulty in using QWs as active layers due to the small optical confinement factor Γ, see Eq.(3.9). An obvious solution would be to use more than one quantum well in the active region, but then the required transparency density is multiplied by the number of QW's.

However, it was the advent of separate confinement heterostructures (SCH) that made quantum-well lasers truly practicable. As the name suggests, such lasers rely on separate confinement for the guiding of carriers and photons. They circumvent the poor confinement factor Γ of Eq.(3.9) by confining photons in a wider optical cavity surrounding the active QW layer. This way, the optical wave is optimally compressed in a 1000 Å-wide optical cavity, and with a single quantum

well typically 100 Å thick, the confinement factor $\Gamma \approx 0.1$. Such lasers can have very low threshold current densities of ~ 100 A·cm^{-2}. This value can be further reduced by the use of strained QW's, with the best reported values for GaInAs/GaAlAs structures in the range of 60 A·cm^{-2}.

The advantage of a QW laser over a double-heterostructure laser stems mainly from the improvement in transparency current. Indeed, semiconductor lasers with a 3D electronic structure are very inefficient in that one needs to invert many more quantum states than required to reach the threshold gain. By contrast, the QW laser matches the number of inverted quantum states to the number needed to achieve the required gain. With its operation based on the freezing of one degree of freedom and on the step-like density of states dependence on energy, the QW laser is a truly quantum device. There are other advantages in using QWs such as the higher direct modulation frequency due to the larger differential gain near transparency current, and the slower temperature dependence of the threshold current.

Finally, the fourth generation of semiconductor lasers is in the making, powered by the search for full electron and photon quantisation and new device applications. Worth noting are quantum-dot lasers, which provide carrier confinement in all three directions, yet have a much wider gain bandwidth owing to the variation of dot sizes in the material. While still in early development stages, quantum-dot lasers offer a number of advantages, such as weaker temperature dependence of threshold current and reduced sensitivity to external feedback.

3.3.   High-frequency operation of semiconductor lasers

As shown in the previous chapters, the generation of short optical pulses at high repetition rates is of considerable interest in optoelectronic applications. Semiconductor lasers are especially suited for this purpose because of their wide gain bandwidth (~ several THz) and short carrier lifetimes.

Methods of producing ultrashort optical pulses (and high repetition frequencies) from semiconductor lasers rely on introducing short periods of net loss or gain. There are three generic ways of achieving this: gain switching, Q-switching, and modelocking, all of which can be applied to diode lasers. Of the three, only modelocking is capable of addressing THz frequencies, as the other two are

inherently limited by the bandwidth of the driving electrical circuit and also suffer from excessive frequency chirp and timing jitter.

Here, the principles of all three techniques, based on tutorial [10] and review [11], will be presented, with a specific emphasis on modelocking, while a more thorough treatment of the theory describing the ultrafast operation of THz-modelocked lasers will be presented in Chapter 4.

3.3.1. Gain-switching

The simplest of pulse generation techniques, gain-switching, was observed in the early days of the laser diode, but became of particular interest following the development of the double-heterostructure, which made possible high-repetition-rate pulse generation at high duty cycles and moderate drive currents [12]. Using this technique, large amplitude, short current pulses are applied directly to the laser. As the current is injected, the carrier concentration increases rapidly in the laser. Pulses are then formed from the transient oscillation in the photon output as the laser turns on. There is strong interaction between the populations of photons and injected electrons. The delay between the increased rate of photon generation due to carrier density increases and the build-up of the photon population, in part, enables the first spike to be much shorter than one might expect from small signal operation.

The generated photon population rapidly depletes the electron concentration to prevent further lasing so that a single resonance spike is generated. The current is abruptly terminated after the charge carrier concentration has exceeded threshold to ensure that no further relaxation oscillations occur. Pulses generated in this manner are found to be typically a few tens of picoseconds wide and have peak powers from a few tens to a few hundreds of milliwatts. However, the achievable frequency of modulation is still limited by the relaxation oscillation frequency of the laser being used.

The change in carrier density leads to a large refractive index modulation and a red shift in the lasing wavelength. This, in turn, leads to duration-bandwidth products that are considerably larger than the Fourier limit for single mode lasers [13]. Fabry-Pérot diode lasers under high-current driving conditions are prone to multi-longitudinal-mode pulse generation, which usually is most susceptible to mode

partitioning [14]. A range of techniques have therefore been exploited to achieve single-mode gain-switched operation. Short external cavities have been used to enhance the gain within a single longitudinal mode and successful monomode operation has been achieved even under high current injection. Injection locking of a pulsed laser by a CW-driven diode laser has also been successfully demonstrated.

The use of distributed feedback (DFB) and distributed Bragg reflector (DBR) devices has proved most effective in ensuring that single-mode output is generated. A gain-switched DFB laser with a 3 dB modulation bandwidth of 26 GHz has been reported [15].

Another technique for generating short optical pulses consists in switching gain in a laser diode using a pulse or sinusoidal injection current superimposed on a bias current below the threshold [16]. This method uses the first peak of the relaxation oscillation and can generate short pulses with pulsewidths of 20 – 30 ps and high peak power. The gain-switched pulses have large red-shift wavelength chirping and can be compressed to 6 – 2 ps by passing them through a normal dispersion medium [17]. Therefore, RF carriers with frequencies of approximately 100 GHz can be generated by selecting higher-order harmonics after direct detection of the pulses, although the repetition frequency of the pulse stream is limited to below the relaxation oscillation frequency [18].

As potential applications for high-repetition-rate picosecond pulses are being explored, it has become increasingly apparent that pulse-to-pulse amplitude and repetition frequency fluctuations can be important for certain diode laser applications. In terms of gain-switching, the spontaneous emission noise leads to a random turn-on time, commonly referred to as timing jitter. As the spontaneous emission levels increase with decreased bias current, timing jitter has been observed to decrease with increasing current in gain-switched lasers. In order to reduce jitter, optical feedback techniques have been introduced. Optical feedback requires either an external mirror, grating or a fibre loop to feed back light into the cavity. Hybrid feedback techniques have also been studied. These use the ability to control gain-switching pulse generation by feeding back information about the optical pulse train incident on the photodetector. The amplified photocurrent then directly modulates the laser.

However, all these techniques extend up to only a few gigahertz in pulse repetition frequency and are inadequate for ultrafast pulse train generation.

3.3.2. *Q*-switching

At an early stage in the development of the laser, trains of pulses or self-pulsations were observed, these being later found to be due to the presence of regions of saturable absorption in the laser devices. Rapidly it was recognised that such pulsations could have use, and hence research was initiated into the use of saturable absorbers in laser diodes to generate optical pulses by modulating the *Q*-factor of the Fabry-Pérot cavity, or *Q*-switching. It was suggested that if additional loss could be placed within the cavity prior to pulse generation, either by providing multi-contact sections with loss or gain or by specially introducing loss by irradiation or damage, then, according to the theoretical arguments described above for gain-switching, the carrier density can be significantly increased before lasing. If the loss was then reduced, the pulses generated could typically be expected to exhibit shorter pulsewidths and higher powers than in the gain-switched case.

Even single-contact diode lasers have been observed to produce self-sustained pulsation behaviour without the influence of externally modulated gain or loss [10]. For a passively *Q*-switched laser, the absorber region experiences the excitation of carriers to higher energy states and a resultant shift in the absorption edge until the material is bleached. With the higher absorption cross-section in the loss regime (below transparency), a significantly reduced perturbation of the carrier concentration in the loss section is required to increase the gain of the cavity compared to the gain-switched case. For the passive generation of *Q*-switched pulse trains, therefore, the differential absorption should be greater than the differential gain, and the gain section carrier lifetime should be greater than the carrier lifetime in the absorber section.

The most common ways of forming a saturable absorber are proton bombardment of the facets [19] and use of a segmented-electrode multi-contact structure [20]. The excited carriers should be recycled to take part in stimulated emission rather than vanish through spontaneous recombination. The pulse repetition frequency is not limited by the absorber spontaneous recombination lifetime but by the population transportation rate.

Passively *Q*-switched diode lasers thus can generate very high optical power pulse trains, whose repetition rates can be controlled over a significant range by the DC drive current. However, they do suffer from increased timing jitter and noise. To overcome this limitation, active or forced *Q*-switched techniques can be used, where the loss section is electrically modulated to define a recovery time-independent repetition rate. This has been shown to reduce the jitter of the generated pulses by modulating the stimulated absorption processes and to allow control of the pulse shape without affecting the peak power.

As jitter in *Q*-switched lasers has been of considerable importance, even in active *Q*-switching, optoelectronic feedback schemes have also been studied. These have proved successful, the uncorrelated jitter being reduced substantially. Here, rather than using photodiode detection, shot noise from a DC-biased gain section is coupled into the feedback loop through a microwave bias-tee. This causes repetitive pulse generation at frequencies determined predominantly by the electrical bandwidth of the feedback loop. With no microwave source or critical narrow-band filtering in the feedback loop system, costs are kept to a minimum. The signal is amplified and injected into a sub-threshold-biased absorber section. Stable self *Q*-switching at up to 80 GHz has been demonstrated with reduced jitter. But, as pointed out earlier, both *Q*-switching and gain-switching fall short of delivering the pulse repetition frequencies required for (near)-terahertz generation.

3.3.3. Modelocking in semiconductor lasers

Taken most generally, mode-locking (ML) is a regime of laser generation whereby the laser emits light in several modes with a constant phase relation, i.e., with constant and precisely equidistant frequencies. Usually, the term is used more specifically, referring to what is, rigorously speaking, amplitude-modulation modelocking, implying that the phases of the longitudinal modes are not only constant but may be considered approximately equal [11]. This picture corresponds to an optical pulse that is repetitively reshaped as it circulates in the laser cavity. The laser thus emits a train of pulses with a repetition frequency equal to an integer multiple (a harmonic) of the cavity round-trip frequency:

$$f = M \frac{v_g}{2L} \qquad (3.10)$$

where v_g is the group velocity of light in the laser waveguide, L is the cavity length, and M is the number of pulses coexisting in the cavity. From Eq.(3.10), a rough adjustment of the repetition frequency is possible either by modelocking a laser of desirable length, or, particularly, if high-frequency operation is required, using a construction, in which $M > 1$ pulses circulate in the laser cavity simultaneously (ML at a higher harmonic of the fundamental frequency). The standard methods of achieving ML are either modulation of one of the laser parameters at frequency f (active ML), or exploiting nonlinear properties of the medium, usually by introducing a saturable absorber (SA) into the laser cavity (passive ML). The combination of these methods is known as hybrid ML; in particular, if the external modulation is in the form of short pulses, the corresponding regime is referred to as synchronous ML. Physical and technological advantages of semiconductor lasers allow a broad combination of these routes and methods. Indeed, ML with an increasingly broad range of repetition frequencies and pulse characteristics has been realised with diode lasers in recent years.

Before proceeding with a discussion of ultrafast modelocking techniques, a brief review of the principles of modelocking would be appropriate.

3.3.4. Principles of the fundamental-frequency modelocking effect

While unlocked modes in a diode laser randomly related in phase result in irregular irradiance fluctuations on a steady optical level, locked modes induce an optical pulse to circulate back and forth inside the laser cavity. The difference between the two cases was illustrated in Figure 2.1(III-a & c). A modelocked laser therefore emits pulses separated by a time equal to the round-trip time of the laser cavity. The phase relation may be enforced by modulating loss or gain at a frequency equal to the intermode frequency separation, which corresponds to the reciprocal cavity round-trip time.

The longitudinal modes in a semiconductor laser are found from the standing wave condition, i.e., an integer number (k) of optical half-waves is to fit the cavity of length L:

$$L = k\,\frac{\lambda}{2n} \tag{3.11}$$

where λ is the wavelength of light, n is the effective index of refraction for a guided mode, which is wavelength-dependant due to dispersion: $n = n(\lambda)$. The spectral spacing between neighbouring longitudinal modes is given by

$$\Delta\lambda = \frac{\lambda^2}{2L\left(n - \lambda\dfrac{dn}{d\lambda}\right)} \quad \text{or} \quad \Delta v = \frac{c}{2Ln_g} \tag{3.12}$$

where n_g is the group refractive index: $n_g = n - \lambda\dfrac{dn}{d\lambda}$. This is a special case of Eq.(3.10) with $M = 1$, i.e., $f = \Delta v$.

In what follows, we shall neglect the dispersion of the group refractive index n_g and assume $\Delta v = \text{const}$. In a semiconductor with a wide enough gain curve, a large number of modes can be excited simultaneously. The aggregate electric field of laser radiation is the superposition of all the field strengths of individual modes:

$$E(t) = \sum_m E_m \exp\left[i\varphi_m + i(\omega_0 + m\Delta\omega)t\right] \tag{3.13}$$

We shall consider two extreme cases below.

The mode phases are statistically independent.

This is only the case if each mode has an independent source of energy. As a consequence, time averaging leads to the cancellation of electric fields from any two unrelated modes:

$$\overline{E_m \cdot E_{m'}} = 0 \quad (m \neq m') \tag{3.14}$$

The total intensity can be approximated as

$$I \sim \overline{E(t)^2} \sim \sum_m \left|E_m\right|^2 + \text{r.m.s.} \tag{3.15}$$

where r.m.s. is the root-mean-square intensity fluctuation. Consequently, in the case of statistically independent phases, the total intensity can be represented as the sum of intensities of each individual mode. If sum (3.15) contains N modes with identical intensities $|E_o|^2$, then

$$I_{non-ML} \cong N\left|E_0\right|^2 \tag{3.16}$$

Thus the total intensity equals the intensity of a single mode times N.

Correlated phases and frequencies

We assume that there are *N* modes with identical amplitudes, that the frequencies of neighbouring modes are equidistant, i.e., $\omega_m = \omega_o + m\,\Delta\omega$, and their phases meet the synchronism condition

$$\varphi_m - \varphi_{m-1} = \alpha = const \tag{3.17}$$

Then, in Eq.(3.13), we can substitute $(m\alpha + \phi_o)$ for ϕ_m. The resulting sum is a geometrical progression and is computed easily

$$E(t) = E_0 \frac{\sin\left[\frac{N}{2}(\Delta\omega t + \alpha)\right]}{\sin\left[(\Delta\omega t + \alpha)\right]} \exp i[\omega_0 t + \varphi_0] \tag{3.18}$$

Due to a specific correlation between the phases, the cavity modes interfere to produce short optical pulses. The pulse maxima occur at moments of time such that the denominator of Eq.(3.18) vanishes, i.e., when

$$\frac{(\Delta\omega t_q + \alpha)}{2} = q\pi \text{, where } q \text{ is an integer.}$$

The mode-locking effect implies that at instants t_q all modes make the maximum contribution to the aggregate electric field strength. The time interval between any two maxima is given by

$$T = \frac{2\pi}{\Delta\omega} = \frac{2L}{c} n_g \tag{3.19}$$

This happens to be exactly the time it takes light to make a round trip of the laser cavity. Therefore we find that there is only one pulse that travels back and forth. The pulse width can also be estimated from Eq.(3.18):

$$\tau_L = \frac{2\pi}{N\Delta\omega} = \frac{2\pi}{\delta\omega} \tag{3.20}$$

where $\delta\omega$ is the frequency interval containing the laser modes. The wider the gain curve and the higher the number of the locked modes, the shorter pulse width that can be obtained.

Apart from having very short widths, the phase-correlated pulses can also exhibit very high intensities. The peak intensity I_{ML} can be found from Eq.(3.18):

$$I_{ML} \cong N^2 |E_0|^2 \tag{3.21}$$

That is, the maximum intensity is proportional to the number of modes squared, whereas in the case of non-locked modes the intensity is proportional just to the number of modes. Therefore, for a given number of modes N, the maximum intensity is N times greater in the case of correlated phases than in the case where the mode phases are randomised with respect to one another. Thus a Type III spectrum, as defined in Figure 2.1 (III-a,c) of Chapter 2, can produce either a train of pulses as shown in Figure 2.1 (III-b), or random intensity spikes of Figure 2.1 (III-d), depending on the phase relationship between the lasing modes. In order to observe the mode-locking effect in a real laser, the excitation of three or more laser modes must take place with constant phase shift in an active medium with a sufficiently wide gain curve. The phase locking of laser modes can be achieved with either of the two techniques: active and passive ML.

Active ML requires direct electrical modulation at the pulse repetition frequency. As typical diode lasers have cavity lengths of only a few hundred microns, their round-trip frequencies are relatively large (tens of GHz). Therefore, some form of elongated (extended) cavity is usually required for actively modelocked lasers to allow modulation at electrically achievable frequencies.

Here, we shall only consider passive ML, as it offers the highest frequency performance and does not require (and is not limited by) external modulation. Passive ML takes place when a saturable absorber (SA) is introduced into the laser cavity. The SA is usually placed between the active medium and one of the end facets. In the case of diode lasers, the SA usually consists of an additional section to the laser waveguide, which is either reverse biased or is treated by ion implantation to create absorption centres. The un-pumped section of the diode has the same energy bandgap as the gain section and thus effectively absorbs the generated light. The absorber saturation is attributed to the band filling effect, whereby photo-generated electrons tend to fill the conduction band due to the low density of states therein, and thus push the absorption edge towards the short-wavelength end of the spectrum. In other words, the majority of states near the bottom of the conduction band become occupied and are therefore unable to accept any further electrons from the valence band.

The onset of ML creates an optical pulse, which, having bounced from the facets and passed through the gain section, will come back to the saturable absorber

in the round-trip time defined by Eq.(3.19). The pulse travelling back and forth inside the cavity will modulate the absorption at the frequency given by Eq.(3.12), which equals the spectral spacing between the adjacent modes of the laser's resonator.

By its nature, ML is a regime where an optical pulse circulating the cavity is repetitively reshaped, with its shape and parameters remaining constant, on average, due to a balance of pulse broadening and pulse shortening mechanisms, which include [11, 21]:

(a) Pulse shortening:

- Saturable absorption (for passive and hybrid ML)

- External modulation (for hybrid and active ML)

(b) Pulse broadening:

- Gain saturation

- Dispersion, including gain and group velocity dispersion, as well as dispersive cavity elements such as grating sections

(c) Self-phase modulation (SPM):

- Due to changes in the refractive index along the pulse (defines the degree of chirp in the pulse and may either shorten or broaden it by interacting with dispersion).

Mechanisms (a) and (b) are common to lasers of all types. However, there are some important properties that are peculiar to the semiconductor active media (amplifying sections and SA's) used in diode lasers, mainly due to the very high density of population inversion, of the order of 10^{18} electron-hole pairs per cm^3, and the broad energy spectra of these materials.

One such property is the strong coupling between gain/loss and refractive index changes, as a result of which changes in carrier density in the gain section are accompanied by strong SPM (c) leading to chirped ML pulses.

Another important point specific to semiconductor active media is that saturation of both gain and saturable absorption contains both "slow" components (with characteristic times longer than the ML pulsewidth), which are related to

changes in carrier population, and "fast" components associated with fast gain and saturable absorption nonlinearities. These nonlinearities include phenomena such as spectral hole burning, carrier heating and excitonic ionisation nonlinearities specific to quantum-well structures [22].

While the general principles of modelocking theory have long been established [22, 23], the complexity of the phenomena listed above merits further studies [11, 24, 25].

3.3.5. Multi-gigahertz and (sub)terahertz modelocking of diode lasers

A considerable body of work has been reported on achieving utrahigh (> 100 GHz) pulse repetition frequencies directly from a modelocked diode laser [11]. This invariably requires a passive SA because of unavailability of external modulation. Semiconductor lasers offer higher ML frequencies than any other type of laser, by virtue of their short cavity length. According to Eq.(3.10), a passive-modelocked monolithic semiconductor laser with a typical length of several hundred microns would have a pulse repetition frequency of several tens of gigahertz. Indeed, frequencies of over 100 GHz have been realised using monolithic cavities with an integrated SA [26, 27].

However, unlike the tens of GHz range, (sub)THz ML raises problems of physical, as well as technological, nature. In all other laser systems, including low-frequency semiconductor lasers, the SA is known to fully recover between consecutive pulses, a requirement that is difficult to meet in a short-cavity monolithic laser, where the absorber recovery time is the lifetime of non-equilibrium charge carriers in the SA section. Absorber recovery times of the order of picoseconds may be achieved by reverse biasing the absorber section or by ion implantation. In the latter case, it is believed that recombination centres, or clusters, are created in the implanted material, which result in a fall of the recombination time that is determined by the implantation dose. In the former case, an exponential decrease of the relaxation time with the absorber bias voltage down to picosecond values has been predicted theoretically and observed experimentally [28]. At the highest reported passive ML frequencies (~ 0.5 – 1.5 THz), it has been suggested that the absorption saturation is at least partly due to fast SA nonlinearities such as non-equilibrium effects in the carrier distribution function [11].

In order to achieve such ultrahigh frequencies, a number of techniques have been proposed. An obvious solution would be to minimise the cavity length L of Eq.(3.10) in order to maximise frequency f. Subpicosecond pulses at 240 GHz were obtained [29] using a short-cavity (160 μm) diode laser with a bulk GaAs active layer and a SA formed by implantation of heavy oxygen atoms into one of the facets, with the penetration depth estimated at 10 μm, which defines the SA length. Later, the same technique was used to obtain 0.65 ps pulses on a 110 GHz repetition rate from a bulk InGaAsP/InP laser at a wavelength of 1.535 μm [30]. However, practical constraints on the cavity length and low output power preclude further increase of pulse repetition frequency using this approach.

3.3.6. External pulse multiplication techniques

Pulse repetition frequency can be multiplied by external processing of the optical signal from a relatively low-frequency ML laser, as shown in Figure 3.7. The first technique, illustrated in Figure 3.7(a), is to increase the pulse repetition frequency by splitting the output of a modelocked laser into two paths, delaying one path, and then recombining them (the split–delay–recombine method). This is similar to the technique for generating ultrafast pulse trains in optical time-division-multiplexed (OTDM) systems [31], where individually modulated low-repetition rate pulses are combined optically to give a high bit-rate data stream. The key to the technique is for the original mark-to-space ratio of the pulses to be sufficiently small, so that the pulses can be interlaced without the optical fields in their tails mixing, as this would produce beat frequencies. The lack of mixing of the optical fields in the undelayed and delayed arms also means that the technique is insensitive to the input wavelength.

The second approach, see Figure 3.7(b), is to use a Fabry-Pérot interferometer with its free-spectral range set to the desired microwave output frequency. The interferometer can be used to select a comb of frequencies spaced by the spectral range of the interferometer. With careful adjustment of the ML laser and the RF drive frequency, the comb can be made to line up with the output spectrum of the ML laser, and thus select a set of equally spaced modes from the original spectrum. With an increased intermode spacing, the resulting pulse repetition frequency will also rise.
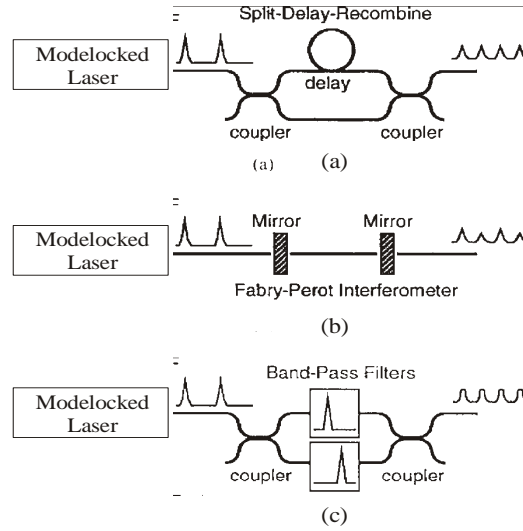
Figure 3.7. External processing methods for the generation of ultrafast optical signals from modelocked diode lasers [32].

The third method is shown in Figure 3.7(c) and consists in splitting the signal and inserting two bandpass filters to select two optical modes, followed by a recombination coupler. This method was mentioned in Section 2.2.2 in connection with fibre radio and is, effectively, a conversion of a Type-III spectrum into a Type-II one. The output is then a sinusoidal signal, with a period being the inverse of the frequency offset between the two selected spectral lines.

A feature common to all the external schemes described above is to store energy from a modelocked pulse, and to use this energy to fill in the gaps between the original pulses to increase the pulse repetition frequency of the optical pulse train, thus suppressing the output at the original drive frequency. However, the schemes described here require either high-Q optical filters, which are difficult to set up and keep in tune, or careful control of delay lines and splitting ratios [32].

3.3.7. Harmonic modelocking (HML)

Pulse multiplication, with a corresponding multiplication of the pulse repetition rate, can be performed within the laser cavity itself. This is a regime of laser operation, in which the laser is modelocked at a harmonic (integer multiple) of the fundamental (single pulse) repetition rate. This corresponds to a case where $M > 1$ in Eq.(3.10), with M pulses circulating in the cavity.

Colliding-pulse modelocking (CPM) is perhaps the best known embodiment of harmonic modelocking (HML) with $M = 2$. The CPM effect is created by placing

an SA in the middle of the cavity [Figure 3.8(b)], as opposed to the end of the cavity in the fundamental ($M = 1$) ML [Figure 3.8(a)]. A pulse passing through the absorber then automatically saturates the local loss not only for itself but also for light approaching the SA in the opposite direction. This means that two counter-propagating pulses coexist in the cavity and collide inside the absorber, hence the term CPM. ML is therefore achieved at the second harmonic of the fundamental (round-trip) frequency, and the pulse repetition rate is doubled. Such lasers are also believed to produce shorter and more stable pulses than the conventional ML construction of Figure 3.8(a), owing to the stronger bleaching of the absorber (incoherent colliding pulse effect). The shortening is assisted by the diffraction grating effect induced in the SA by the two counter-propagating pulses (coherent colliding pulse effect); however, it has been suggested that this effect is of relatively minor importance in diode lasers compared with dye lasers. Pulsewidths of about 1.1 ps have been reported [33] for purely passive CPM operation at 40 GHz ($L = 2.1$ mm) with InGaAsP lasers emitting at $\lambda = 1.5$ µm. CPM lasers in InGaAsP/InP and GaAs/AlGaAs material on a semi-insulating substrate were successfully modelocked at 36, 50 and 100 GHz by the author's colleagues at the University of Glasgow [1, 2]. Hybrid CPM modelocking was also achieved in a GaAs/AlGaAs laser at 60 and 120 GHz [34]. However, the mere doubling of the modelocking frequency with the CPM technique is still inadequate for attaining (sub)-THz speeds, for which higher harmonic numbers (M) are required.
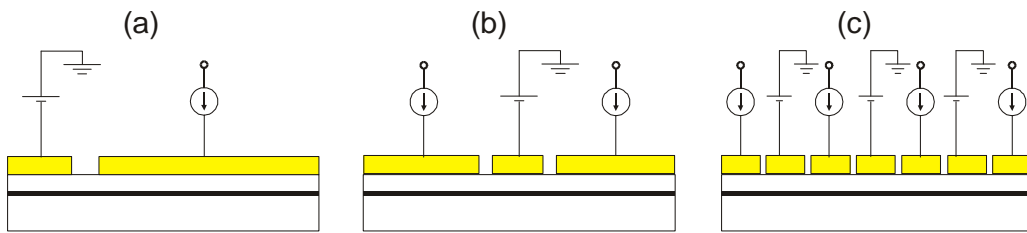
Figure 3.8. Diagrams of different types of modelocked semiconductor lasers: **(a)** standard (fundamental ML), CPM **(b)**, and MCPM **(c)**.

In Ref. [35], the CPM technique was generalised by using a structure with three individually addressable SA sections at ¼, ½, and ¾ of the cavity length [see Figure 3.8(c)]. By reverse biasing one of the side absorbers only, the central absorber only, the two absorbers at the sides, or all three absorbers, the laser was forced to operate in dynamic regimes with one, two, three and four pulses coexisting in the cavity, corresponding to harmonics $M = 1, 2, 3, 4$. With a cavity 600 µm long, the

multiple colliding pulse modelocked (MCPM) laser produced pulses with a pulsewidth not exceeding 1.6 ps at repetition frequencies of 60, 120, 180 and 240 GHz. A 400 μm long GaAs/AlGaAs laser with three reverse-biased SA's exhibited ML at about 375 GHz [35], with a pulsewidth of ~1 ps and a spectrum consisting of only three modes. A higher M has also been demonstrated, e.g., in Ref.[36], an InGaAsP ($\lambda = 1.56$ μm) laser with three SA's positioned at 1/6, 1/2 and 5/6 of the 450 μm cavity length, operated at 192 GHz ($M = 6$), with all side modes suppressed by at least 27 dB, generating an RF line about 1.1 MHz wide.

A similar effect was demonstrated at 380 GHz by means of asymmetric CPM (ACPM) [37]. ACPM is only different from standard CPM of Figure 3.8(b) in the positioning of the saturable absorber inside the cavity. The 380 GHz rate was achieved using an 800 μm-long InGaAs/InGaAsP laser with a single 20 μm SA located at 1/7 of the cavity length, with a pulsewidth of about 0.7 ps. A higher ACPM repetition frequency (up to 440 GHz) has been demonstrated [38] using an InGaAsP laser with a geometry similar to that of [35] [Figure 3.8(c)] and with only the side SA biased. Finally, the highest pulse repetition frequency by ACPM reported to date, of up to 860 GHz, was obtained from $\lambda = 1.5$ μm lasers [39], in which a single SA was located at a fraction $N : M$ of the cavity length, N and M being integer numbers without common factors, e.g., $N : M = 5 : 12$ was used to generate the 12th harmonic at 860 GHz.

However, the highest pulse repetition frequencies and harmonic numbers to date have been achieved with a different HML version known as compound-cavity modelocking, or CCM. It was first observed in the unusual behaviour of semiconductor laser structures incorporating an SA and a distributed Bragg reflector (DBR) section at high pumping currents [40]. For a DBR section 90 μm long, modelocking at 400, 800 and 1600 GHz was observed with increased pumping levels.

In a theoretical study [24, 25], a modification of this construction was proposed, which used a more strongly frequency-selective compound cavity (CC) with a lumped reflector within the cavity instead of the DBR section. The reflector may either be positioned at an integer fraction (1/M) of the cavity length or divide it into two parts with a length ratio of $N : (M – N)$ (N and M being integer numbers

without common factors), which is similar to the positioning of SA's in ACPM lasers. A similar principle was demonstrated in a non-integrated version [41], whereby pulses at 0.9 THz were produced by locking a long ML diode laser to a signal from a shorter laser.

Prior to the results obtained under the current project, the only observation of harmonic modelocking effects in a monolithic non-DBR CC construction had been made in a ring-geometry laser [25] modelocked at 250 GHz (8th harmonic of the fundamental ML frequency). Here, the compound cavity was formed by the reflections at the facets of the output waveguide. Unlike DBR HML lasers, this construction did not demonstrate ML at the fundamental frequency under any biasing conditions.

The present Thesis is concerned with the first realisation of the HML principle in a Fabry-Pérot CC laser, as proposed theoretically in Refs.[24, 25]. As shown above, this technique has allowed the highest multiplication of the fundamental pulse repetition frequency and is very promising for reaching into the terahertz range.

3.4. References

[1]   H.K. Lee, M.W. Street, I.G. Thayne, A.C. Bryce, and J.H. Marsh, "Efficient direct modulation of colliding pulse mode-locked lasers on semi-insulating substrate at 1.5 um," presented at 8th IEEE International Symposium on High Performance Electron Devices for Microwave and Optoelectronic Applications, Glasgow, UK, 13-14 Nov., 2000.

[2]   H.K. Lee, M.W. Street, S.D. McDougall, E.A. Avrutin, A.C. Bryce, and J.H. Marsh, "Colliding pulse mode-locked lasers on semi-insulating substrate at 1.5 um," presented at International Topical Meeting on Microwave Photonics MWP2000, Oxford, UK, 11-13 Sept. 2000.

[3]   H.K. Lee, V. Loyo-Maldonado, B.C. Qui, K.L. Lee, C. Shu, S. Pinches, I.G. Thayne, A.C. Bryce, and J.H. Marsh, "Efficient direct locking of colliding pulse mode-locked lasers on semi-insulating substrate at 1.5 um," *IEEE Phot.Techn. Lett.*, vol. 14, pp. 1049-1051, 2002.

[4]   C. Weisbuch, "The Development of Concepts in Light Emitting Devices," *Brazilian Journal of Physics*, vol. 26, pp. 21-42, 1996.

[5]   A Yariv, *Quantum Electronics*. New York: Wiley, 1989.

[6]   G.P. Agrawal and N.K. Dutta, *Semiconductor Lasers*. New York: Van Nostrand Rienhold, 1993.

[7]   J. Wilson and J.F.B. Hawkes, *Optoelectronics: An Introduction*: Prentice-Hall Int'l, 1983.

[8]   H.C. Casey and M.B. Panish, *Heterostructure Lasers*: Academic Press, New York, 1978.

[9]   Zh.I. Alferov and V.M. Andreev, "Investigation of the influence of the AlAs-GaAs Heterostructure Parameters on the Laser Threshold Current and the Realization of Continuous Emission at Room Temperature," *Soviet Physics-Semiconductors*, vol. 4, 1971.

[10]   I.H. White, "Picosecond optical pulse generation using semiconductor lasers," in *Laser Sources and Applications: Proceedings of the Forty Seventh Scottish Universities Summer School in Physics, 47*, A. Miller, Ed. St Andrews: NATO Advanced Study Institute, 1997, pp. 63-85.

[11]   E.A. Avrutin, J.H. Marsh, and E.L. Portnoi, "Monolithic and multi-gigahertz mode-locked semiconductor lasers: Constructions, experiments, models and applications," *IEE Proc. Optoelectron.*, vol. 147, pp. 251-278, 2000.

[12]   H. Ito, H. Yokohama, S. Murara, and H. Inaba, "Picosecond optical pulse generation from an R.F. modulated AlGaAs DH diode," *Electron. Lett.*, vol. 15, pp. 738-739, 1979.

[13]   C. Lin and J.E. Bowers, "Measurement of 1.3 um and 1.5 um gain-switched semiconductor pulses with a picosecond IR camera and a high-speed InGaAs PIN photodiode," *Electron. Lett.*, vol. 21, pp. 1200-1, 1985.

[14]   J.P. Van der Ziel, "Spectral broadening of pulsating AlGaAs double heterostructure lasers," *IEEE J. Quant. Electronics*, vol. 15, pp. 1277-9, 1979.

[15]   P. A. Morton, T. Tambun-Ek, R. A. Logan, N. Chand, K. W. Wecht, A. M. Sergent, and P. F. Sciortino, "Packaged 1.55 um DFB laser with 25 GHz modulation bandwidth," *Electron. Lett.*, vol. 30, pp. 2044-6, 1994.

[16]   C. Lin, C. A. Burrus, G. Eisenstein, R. S. Tucker, P. Besomi, and R. J. Nelson, "11.2-GHz picosecond optical pulse generation in gain-switched short cavity InGaAsP injection laser by high-frequency direct modulation," *Electron. Lett.*, vol. 20, pp. 238-240, 1984.

[17]   A. Takada, T. Sugie, and M. Saruwatari, "High-speed picosecond optical pulse compression from gain-switched 1.3-mm distributed feedback-laser diode (DFB-LD) through highly dispersive single-mode fiber," *J. Lightwave Techn.*, vol. LT-5, pp. 1525-1533, 1987.

[18]   E. Hashimoto, A. Takada, and Y. Katagiri, "High-Frequency Synchronized Signal Generation Using Semiconductor Lasers," *IEEE Trans. Microwave Th. and Techn.*, vol. 47, No.7, pp. 1206-1218, 1999.

[19]   L.A. Volkov, A.L. Guriev, V.G. Danil'chenko, A.G. Deryagin, D.V. Kuksenkov, V.I. Kuchinski, E.L. Portnoi, and V.B. Smirnitski, "Generation and detection of picosecond optical pulses in InGaAsP/InP lasers (1.5 - 1.6 um) with passive Q-switching," *Sov. Technol. Letters*, vol. 15, pp. 497-500, 1989.

[20]   D.Z. Tsang and J.N. Walpole, "Q-switched semiconductor diode lasers," *IEEE J. Quant. Electronics*, vol. 19, pp. 145-150, 1983.

[21]   D. Derickson, R.J. Helkley, A. Mar, J.R. Karin, J. Wasserbauer, and J.E. Bowers, "Short Pulse Generation using Multisegment Mode-Locked Semiconductor Lasers," *IEEE J. Quant. Electronics*, vol. 28, pp. 2186-2202, 1992.

[22]   H.A Haus and Y. Silberberg, "Theory of mode locking of a laser diode with a multiple-quantum-well structure," *J. Opt. Soc. Am. B, Opt. Phys*, vol. 2, pp. 1237-1243, 1985.

[23]   H.A. Haus, "Theory of mode locking with a fast saturable absorber," *J. Appl. Phys.*, vol. 46, pp. 3049-58, 1975.

[24]   E.A. Avrutin, J.H.Marsh, and J.M.Arnold, "Modelling of semiconductor laser structures for passive harmonic mode locking at terahertz frequencies," *International J. Optoelecron.*, vol. 10, pp. 427-436, 1995.

[25]   E.A. Avrutin, J.H. Marsh, J.M. Arnold, T.F. Krauss, H. Pottinger, and R.M. DeLaRue, "Analysis of harmonic (sub) THz passive mode-locking in monolithic compound cavity Fabry-Perot and ring laser diodes," *IEE Proc. - Optoelectron.*, vol. 146, pp. 55-62, 1999.

[26]   P.P. Vasil'ev and A.B. Sergeev, "Generation of bandwidth-limited 2 ps pulses with 100 GHz repetition rate from a multi-segmented injection laser," *Electron. Lett.*, vol. 25, pp. 1049-50, 1989.

[27]   S. Sanders, L. Eng, J. Paslaski, and A. Yariv, "108 GHz passive modelocking of multiple quantum well semiconductor laser with an intracavity absorber," *Appl. Phys. Lett.*, vol. 56, pp. 310-312, 1990.

[28]   A.V. Uskov, J.R. Karin, R. Nagarajan, and J.E. Bowers, "Dynamics of carrier heating and sweepout in waveguide saturable absorbers," *IEEE J. Sel. Top. Quantum Electron.*, vol. 1, pp. 552-561, 1995.

[29]   E.L. Portnoi and A.V. Chelnokov, "Passive mode-locking in a short-cavity laser," presented at Digest of the 12th IEEE Semicond. Conf, Davos, Switzerland, 1990.

[30]   A.G. Deryagin, D.V. Kuksenkov, V.I. Kuchinski, E.L. Portnoi, and Yu.I. Khrushhev, "Generation of 110 ps train of subpicosecond pulses in 1.535 um spectral region by passively modelocked InGaAsP/InP lasers," *Electron. Lett.*, vol. 30, pp. 309-310, 1994.

[31]   R. S. Tucker, G. Eisenstein, and S. T. Korotky, "Optical time-division multiplexing for very high bit rate transmission," *J. Lightwave Technol.*, vol. 6, pp. 1737–1749, 1988.

[32]   A. J. Lowery and P. C. R. Gurney, "Comparison of Optical Processing Techniques for Optical Microwave Signal Generation," *IEEE Trans. Microwave Th. and Techn.*, vol. 46, pp. 142-150, 1998.

[33]   Y.K. Chen, M.C. Wu, T. Tabun-Ek, R.A. Logan, and M.A. Chin, "Subpicosecond monolithic colliding-pulse mode-locked quantum-well laser," *Appl. Phys. Lett.*, vol. 58, pp. 1253-5, 1991.

[34]   M.W. Street, "Low-Jitter Optical Pulse Generation at Sub-THz Repetition Rates Using Hybrid Colliding Pulse Mode-locked Semiconductor Lasers," *Unpublished*, 2000.

[35]   J.F. Martins-Filho, E.A. Avrutin, C.N. Ironside, and J.S. Roberts, "Monolithic multiple colliding pulse mode locked quantum well lasers: experiment and theory," *IEEE J. Sel. Top. Quantum Electron.*, vol. 1, pp. 539-552, 1995.

[36]   Y. Katagiri and A. Takada, "A harmonic colliding-pulse mode-locked semoconductor laser for stable subterahertz pulse generation," *IEEE Phot.Techn. Lett.*, vol. 9, pp. 1442-4, 1997.

[37]   T. Shimizu, X. Wang, and H. Yokoyama, "Asymmetric colliding pulse mode-locking in InGaAsP semiconductor lasers," *Opt. Rev.*, vol. 2, 1995.

[38]   S.D. McDougall, C.N. Ironside, A.C. Bryce, J.H.Marsh, B. Vogele, and C.R. Stanley, "Harmonic modelocking at up to 440 GHz repetition rates InGaAs/InAlGaAs quantum well lasers," presented at CLEO, Glasgow, Scotland, 1998.

[39]   T. Shimizu, I. Ogura, and H. Yokoyama, "860 GHz Rate Asymmetric Colliding Pulse Modelocked Diode Lasers," *Electron. Lett.*, vol. 33, pp. 1868-1869, 1997.

[40]   S.Arahira, Y.Matsui, and Y.Ogawa, "Mode-locking at Very High Repetition Rates More than Terahertz in Passively Mode-locked Distributed-Bragg-Reflector Laser Diodes," *IEEE J. Quant. Electronics*, vol. 32, pp. 1211-1224, 1996.

[41]   M. Margalit, M. Orenstein, G. Eisenstein, E.L. Portnoi, E.B. Venus, and A.A. Khazan, "Two simultaneous wavelength and ultrahight repetition rate operation of a harmonically injection locked diode laser," presented at the 14th IEEE International Conference on Semiconductor Lasers, Haifa, Israel, 1996.

CHAPTER 4.

HARMONIC MODELOCKING

OF COMPOUND-CAVITY LASERS

It is hoped that a convincing case has been made in the previous chapters for the choice of modelocked semiconductor lasers as ultrahigh frequency sources in the optical domain and, in particular, for the use of pulse multiplication by harmonic modelocking to achieve modelocking frequencies in the (sub)-terahertz range. Indeed, harmonic-modelocked compound-cavity lasers have shown the highest pulse repetition frequencies reported so far [1], as noted at the end of Chapter 3. The laser devices that are the subject of this Thesis also employ a similar approach, although in a different cavity configuration.

In this Chapter, the theoretical basis for compound-cavity modelocking (CCM) will be presented and the CCM effect explained. But before that, a discussion of non-modelocked compound-cavity lasers and their principles of operation will be forthcoming.

4.1. Compound-cavity lasers

As the name suggests, compound-cavity (CC) lasers incorporate a superposition of two or more different Fabry-Pérot characteristics using parallel or series-coupled cavities that may be monolithically integrated or external to the semiconductor. The large family of CC lasers includes external cavity, cleaved-coupled cavity (Figure 4.1) and interference lasers [2]. Single-longitudinal-mode operation can usually be achieved by coupling light between the individual sub-cavities. It is the ability of CC lasers to generate single frequency output that has been the focus of much of the research interest in the field in the past 30 years.

4.1.1. External-cavity CC lasers

In external-cavity lasers, one cavity is formed by the laser itself and provides optical gain, while the external cavity provides additional wavelength-dependent optical feedback. In-phase feedback occurs only for those laser modes whose lasing wavelength coincides with one of the longitudinal modes of the external cavity. The longitudinal mode that is closest to the gain peak and has the lowest cavity loss becomes the dominant mode. A diffraction grating, an external mirror, and a Fabry-Pérot etalon can be used to provide feedback in external-cavity lasers. Although they have high side-mode suppression ratios and are often highly tuneable, these devices are difficult to integrate and, therefore, suffer from a lack of mechanical and thermal stability. Some work on realising a grating-loaded external cavity laser will be presented in Chapter 10.

4.1.2. Cleaved-coupled cavity lasers

Cleaved-coupled cavity ("C^3") lasers were the earliest realisation of the CC concept offering near-monolithic integration. A C^3 laser is shown schematically in Figure 4.1. It has two Fabry-Pérot sections that, although driven independently, are optically coupled through their mutual feedback. The coupling element is simply the air gap between them, which is usually not greater than 5 μm.
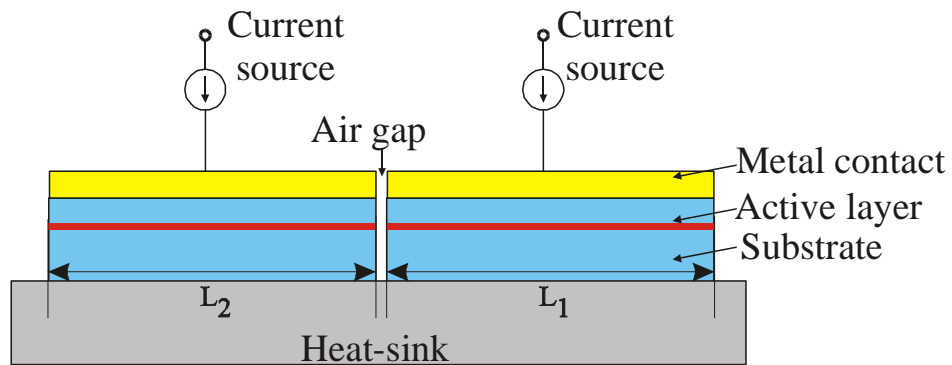
Figure 4.1. Schematic illustration of an all-active cleaved-coupled cavity laser.

A theoretical analysis of C^3 semiconductor lasers requires simultaneous consideration of the gain and loss in the multiple cavities after taking into account their optical feedback. In contrast to a single-cavity laser, for which the facet loss is wavelength-independent (and hence the same for all Fabry-Pérot modes), in a coupled-cavity laser the effective facet loss is different for different longitudinal

modes. A general analysis of such a system is extremely complicated (see, e.g., [3, 4]), with the principles of the mode selection therein most commonly explained by a combination of two mechanisms.

Fabry-Pérot mode selection

The first mechanism is responsible for periodic modal loss modulation as a function of mode number, with one of the sub-cavities acting as a Fabry-Pérot etalon. Thus only the modes supported by both sub-cavities and the overall compound cavity will experience minimum loss. The periodicity of modal loss modulation is dependent upon the ratio of the optical lengths of the two sub-cavities, $L_1:L_2$ (see Figure 4.1). It can be shown that when the ratio $L_1:L_2 = m:n$ forms a non-reducible fraction (i.e., m and n are integers without common factors), then the loss will have a period of $M = m + n$ modes. In other words, all but every M^{th} mode of the total cavity will experience some degree of loss, i.e., will be discriminated against. Examples of mode selection for cavity ratios of 1:2, 1:9 and 2:3 are illustrated in Figure 4.2(a-c). For the case of $L_1:L_2 = 1:2$ and a total cavity length $L = L_1 + L_2$, the two sub-cavities have lengths of $L_1 = 1/3\ L$ and $L_2 = 2/3\ L$. The respective mode patterns for cavities $L, L_2,$ and L_1 are shown in Figure 4.2(a). Here, every third mode of the compound cavity is supported. In the case of a cavity ratio of 1:9 [Figure 4.2(b)], the mode spacing is increased even further, with only every 10th mode supported.

The two cases of Figure 4.2(a & b) are representative of 1:n cavity ratios, where the resulting mode spacing is that of the shortest sub-cavity. In a more general case of $L_1:L_2 = m:n$, which is illustrated in Figure 4.2(c) for $L_1:L_2 = 2:3$, the CC mode spacing ($M = 5$) is an integer multiple of the mode spacing of each cavity.

Note that the width of the lines representing cavity modes in Figure 4.2(a-c) varies for cavities of different lengths, which signifies the spectral width of modes as cavity resonances. The modal spectral width is determined by the ratio of the mode spacing to the cavity finesse, the latter being a measure of the cavity's "idealness" (losslessness) (for a lossless passive cavity, mirror reflectivity). Therefore, modes of a shorter cavity compared to those of a longer one of identical finesse are spectrally broader, as the mode spacing of the former is larger. This suggests that the shorter subcavity might not fully suppress the nearest modes of the longer sub-cavity, unless

the finesse of the shorter subcavity is increased to match the increase in its mode spacing.
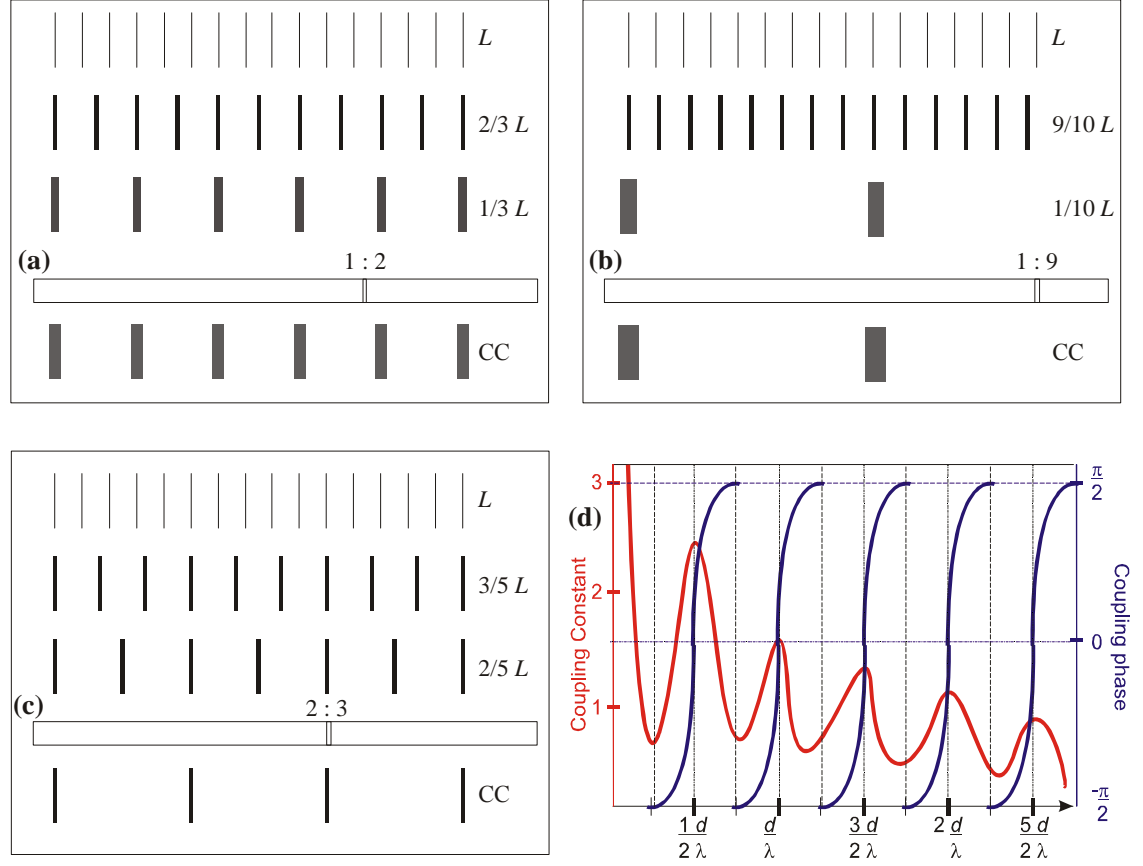
Figure 4.2. Cavity resonances in frequency space for compound cavities of different sub-cavity length ratios: **(a)** 1:2, **(b)** 1:9, and **(c)** 2:3. The top set of lines within each box **(a)-(c)** denotes eigenmodes of the unperturbed cavity of length L, followed by the individual mode sets of the longer and shorter sub-cavities; a schematic of the CC and its mode selection are then given. Mode linewidths are indicative of the spectral width of the resonances of the respective cavity.
(d) Dependence of the coupling constant (left-hand axis) and phase (right-hand axis) on the gap width d for a laser oscillating at a wavelength λ.

In the design of a CC laser, the cavity lengths are adjustable to some extent. The performance of such lasers depends on their *optical* lengths $n_1 L_1$ and $n_2 L_2$, where n_1 and n_2 are the mode indices of refraction for the respective sub-cavities. If one of the cavities is operated below threshold, a variation in its drive current significantly changes the carrier density inside the active region. Since the refractive index of a semiconductor laser changes along with the carrier density, the longitudinal modes will shift with a change in the drive current, and different Fabry-Pérot modes of the laser cavity can thus be selected.

The cases of Figure 4.2(b & c) are referred to as long-short and long-long geometries, respectively, based on the length relationship between the two sub-cavities. Although both geometries are capable of mode selection and wavelength tuning, they differ in one important aspect of wavelength stability. For the long-long geometry, even a relatively small shift of the Fabry-Pérot mode spacing can lead to "mode hopping". By contrast, a shift of about one mode spacing of the shorter sub-cavity is required to achieve mode hopping in the long-short geometry. Clearly, unintentional mode hopping because of temperature and current fluctuations is less likely to occur in the long-short case. By the same token, wavelength tuning would require larger current or temperature changes for a long-short than for a long-long device.

Effect of the inter-cavity gap

The second mode selection mechanism is associated with the diffraction loss in the air gap between the two cavities. The inter-cavity coupling is affected by the loss and phase shift experienced by the optical field while traversing the gap. In the relevant theory based on the scattering matrix approach [4], the coupling strength and phase are linked to the gap width, d, with the dependence shown in the graph of Figure 4.2(d). The in-phase (zero phase) coupling occurs whenever the gap width is a multiple of half-wavelengths, when the coupling constant also goes through a maximum. The interaction between the two sub-cavities is then at its highest, which may have a very strong effect on which mode(s) will be favoured by the CC. It is not surprising, then, that the operation of C^3 lasers is drastically affected by sub-micron variations in the gap width. The fabrication of reliable devices thus presents a considerable technical challenge.

Furthermore, the stability of C^3 lasers is very difficult to control, too, [5], with switching between single-mode and multimode operation under different pumping and temperature conditions and bistability being common behaviours. It has been observed that C^3 lasers exhibit two kinds of bistable behaviour. In one case, the bistability is associated with mode hopping due to changes in the driving current. In the other case, the output power in a single longitudinal mode displays bistability and hysteresis. Optical bistability of C^3 lasers may be useful for a number of signal-processing functions such as optical logic operations and switching.

4.1.3. Monolithic compound-cavity lasers

The C^3 devices were regarded as the "poor man's DFB laser" of the 1980s, as they were able to operate single-moded with a side-mode suppression ratio of 20-35 dB without the expense of a distributed-feedback (DFB) grating. However, they were plagued with alignment and reliability problems due to the inherent inability to maintain a constant gap between the two sub-cavities. The monolithic approach, by contrast, is less prone to stability problems as it keeps the original waveguide alignment intact, whilst relying on non-mechanical techniques to create a compound cavity.

The key challenge for the monolithic integration techniques is the controlled definition of the intra-cavity reflector (abbreviated "ICR" for future use), with which to create the CC effect. Early attempts included the definition of etched ICRs by reactive ion etching (RIE) [6], laser ablation [7] and, more recently, focused ion beam etching [8], which was particularly successful in obtaining reliable single-mode operation by carefully controlling the ICR position and size with minimum threshold penalty. In Ref.[9], single and multiple ICRs were employed to modify the Fabry-Pérot spectrum by "mode sculpturing", with the typical ICR reflectivity between 10^{-3} and 10^{-2}.

The device presented in this Thesis is essentially a monolithic CC laser with an etched ICR. With a different task in mind, the author used the "mode sculpturing" methodology of Ref.[9] to obtain desired spectral transformations, with ICRs defined by more mature RIE technology than that used in Ref.[6]. The author's objective was to controllably multiply the mode separation in the laser's spectrum, rather than obtain single-mode operation by suppressing all but one of the cavity modes (which was the primary focus of most published research in the field). The next challenge was to achieve modelocking with the few remaining modes and demonstrate a multiplication of the pulse repetition frequency. The relevant theory of high-frequency operation of such a device will be the subject of Section 4.2.

4.1.4. Compound-cavity lasers of non-linear geometry

In conclusion of this review, it should be mentioned that a CC can be created monolithically by combining sub-cavities in a non-linear geometry. In the ring laser

shown in Figure 4.3(a), for example, the main cavity of a racetrack geometry is coupled to an output waveguide, which is terminated by facets that provide optical feedback and outcoupling of light. The CC can be formed by reflections at the output facets as well as parasitic reflectances at the input/output ports of the coupler. Indeed, such a structure exhibited a mode spacing that was a multiple ($M = 8$) of that of the total cavity and was successfully modelocked at the 8th harmonic of the fundamental round-trip frequency [10].

Another embodiment of a non-linear CC was proposed in Ref.[11] in the form of a parallel compound cavity (PCC) , Figure 4.3(b), where light from two or more parallel waveguides is combined by means of a coupler (of either directional, Y-type, or multimode interference (MMI) type) into a single output waveguide. Here, each arm represents a sub-cavity, with their ratio determining the spectral properties of the total cavity in much the same way as that of a linear resonator.
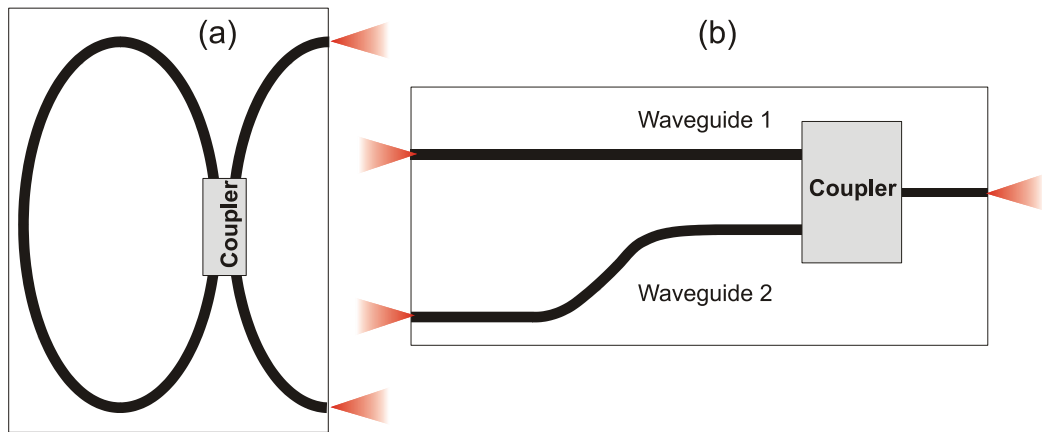
Figure 4.3. Schematics of non-linear CC lasers: **(a)** ring laser and **(b)** parallel coupled cavity (PCC) laser.

The advantages of these non-linear designs include the absence of sub-micron features (i.e., slots or air gaps) and increased tolerance to cleaving error. However, since only a relatively small length difference is achievable between the sub-cavities, both designs can only be used to create sub-cavity ratios of the *m:n* type (or "long-long" geometry). Furthermore, curved waveguides require deep etching and are more lossy than straight ones, leading to higher lasing threshold currents.

4.2. Modelling of hamonic-modelocked compound-cavity lasers

A theoretical model for a compound-cavity modelocked (CCM) laser should take into account two different mechanisms: compound cavity-induced spectral effects and passive modelocking (ML) due to the presence of an ultrafast saturable absorber (SA). Several theoretical approaches have been pursued recently, most of them in the time domain, ranging from approximations of the classical Haus theory of ML [12, 13] to accurate and powerful but computationally cumbersome distributed time-domain (DTD) models [14]. Dr E.A. Avrutin, who was the author's colleague at the University of Glasgow, has expended considerable effort into developing theoretical models for modelocked laser diodes, including CCM constructions [10, 11, 14-20]. Two main models have been developed, a full-scale DTD model for detailed simulations and a frequency-domain model, which allowed realistic diode laser constructions lasing in a limited number of modes to be simulated with much smaller computational effort. Both models have been shown to give good agreement for various experimentally-realised laser structures, with a combined time-frequency-domain approach that provided accurate, yet faster simulation results [14, 15, 18].

Before presenting a theoretical treatment of the device in question, it might be helpful to give a simplified explanation of compound-cavity modelocking.

4.2.1. Simplistic illustration of the CCM effect

The CCM approach consists in increasing the mode spacing of a cavity by placing an intermediate reflector (ICR) at a specific location within the cavity and then phase-locking the remaining modes with a saturable absorber (SA) located at one end of the resonator.

The principle of CCM is best described by its juxtaposition with fundamental ($M = 1$) modelocking of an unperturbed cavity with an SA. The spectrum of Figure 4.4(I-a) contains a complete set of Fabry-Pérot modes, separated by a spacing $\Delta\lambda_{F-P}$ and whose intensities reflect the shape of the gain curve as a function of wavelength (mode number). Passive modelocking can evolve from a random intensity spike of Figure 4.4 (I-b), which will be reshaped when it enters the SA [Figure 4.4(I-c)]. The

spike becomes a well-defined pulse as it is forced to re-circulate the cavity by being reflected from the facets [Figure 4.4(I-d & e)]. With each round-trip of the cavity, the pulse will be repetitively reshaped by a combination of pulse-shortening in the SA and pulse-broadening through dispersion in the rest of the cavity. The modal envelope of Figure 4.4(I-a) defines the transform-limited width of the shortest pulse that can be supported by the cavity, while the actual pulse width will be determined by the balance of pulse broadening and shortening mechanisms. Here, the pulse repetition frequency is determined by the cavity length with $M = 1$ through relation (3.10) of Chapter 3.
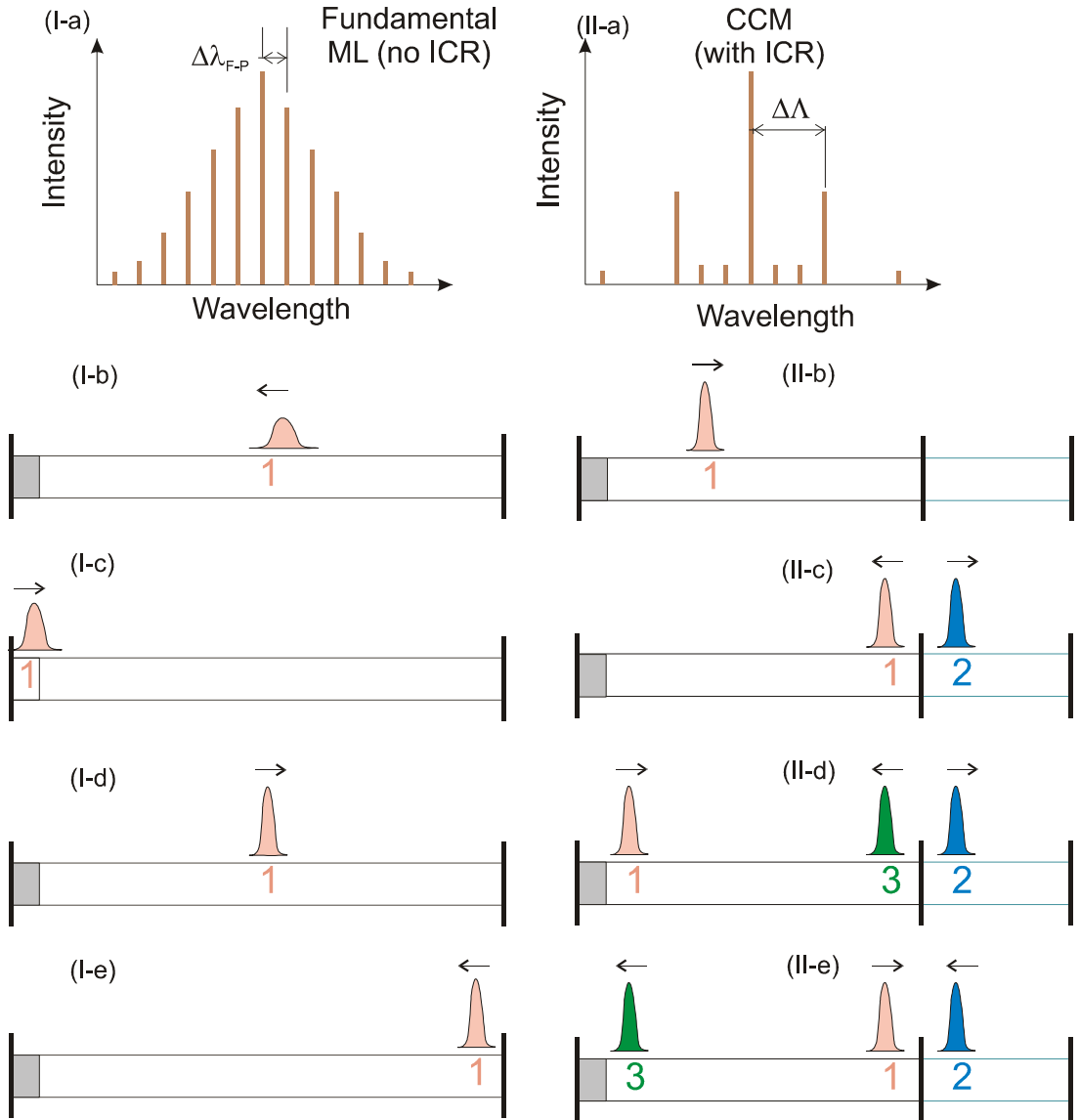
Figure 4.4. Evolution of modelocking in a conventional laser **(I)** and a CCM device with a 1:2 sub-cavity ratio **(II)**.

Now we shall consider the case of a CC having a sub-cavity length ratio of 1:2, which is illustrated in Figure 4.4(II-a – e). As already shown in Section 4.1.2, in such a geometry all but every 3rd mode of the total Fabry-Pérot cavity will be suppressed, which is reflected in the spectrum of Figure 4.4(II-a). Here, the resulting harmonic mode spacing $\Delta\Lambda = 3\ \Delta\lambda_{F-P}$. Assuming that harmonic ML is initiated in a similar manner to the fundamental case, with intensity fluctuations shaped into a pulse by the SA [Figure 4.4(II-b)], the primal Pulse 1 is split in two by being partially transmitted and partially reflected on reaching the ICR, thus creating Pulse 2, as shown in Figure 4.4(II-c). Having made a round-trip of the shorter sub-cavity, Pulse 2 returns to the ICR only to be split in two and give birth to Pulse 3 [Figure 4.4(II-d)]. If the shorter sub-cavity is indeed half the length of the longer one, then on its next return, Pulse 2 will collide with Pulse 3 at the ICR. The pattern will then repeat itself, with Pulse 2 colliding with Pulses 1 and 3 alternately and all three pulses supporting one another. This corresponds to ML at the third harmonic, with a threefold multiplication of the pulse repetition rate compared to that of the fundamental case. This case is described by Eq.(3.10) with $M = 3$. As before, the modal envelope of Figure 4.4(II-a) defines the shortest pulsewidth that the cavity can support.

Using the example of a 1:2 ratio CC cavity, it can be seen that similar harmonic CCM operation can be demonstrated for an arbitrary *m:n* ratio and harmonic number $M = m + n$.

4.2.2. CCM laser model

This Section presents the model and simulation results that were obtained by Dr Avrutin specifically for the type of devices realised in this Project and published in a joint paper [21], which is also attached in the Appendix. The theory of CCM used here is an extension of the approach developed in earlier work [10, 16]. The time-frequency domain model [15] is based on decomposition of the lasing light in terms of longitudinal modes of the active cavity:

$$E(\mathrm{r},t) = \varPhi(x,y)\sum_{k} \mathrm{E}_k(t)u_k(z)\exp(i\omega_k t) \qquad (4.1)$$

where $\varPhi$ is the profile of the (single) transverse-lateral mode,

$$E_k(t) = E_k(t)e^{i\varphi_k\,(t)} \tag{4.2}$$

represent complex modal amplitudes, with E and φ being the real amplitude and phase, respectively, $u_k(z)$ the instantaneous mode profiles, and ω_k equidistant frequencies. The time evolution of the complex mode amplitudes is then governed by equations

$$\frac{d}{dt}E_k(t) \approx \left[\gamma_k + i\left(\Omega_k - \omega_k \right) \right]E_k(t) + \sum_{m \neq 0} G_m(t)E_{k-m}(t) \tag{4.3}$$

Here, the parameter γ_k is the effective (amplitude) net gain of the k-th mode and Ω_k is the cold-cavity (i.e., calculated for uncoupled modes) modal frequency. The parameters G_m are responsible for passive modelocking and describe the strength of the interaction, via net gain pulsations caused by mode beating, between modes that are m fundamental modal intervals apart. These parameters also describe non-linear effects, including the ultrafast response of the SA section.

Single-reflector CCM configuration

The general formalism of Eqs.(4.1)-(4.3) applies to a broad variety of laser structures [14, 18], with a structure's geometry entering the model via the mode coupling parameters G_m and the modal eigenvalues:

$$\delta_k = \Omega_k - i\gamma_k \tag{4.4}$$

Here, we shall specifically consider the CCM laser of Figure 4.5(I-a) with a single intra-cavity reflector (ICR) separating the cavity of length L into two sub-sections of length $L_{1,2} = f_{1,2}L$, with $f_2 = 1 - f_1$. The longer subsection 2 includes a saturable absorber of the length $L_a = f_aL$, the remaining length $L_{g2} = f_{g2}L = L_2 - L_a$ being forward biased (amplifying). Then, it is convenient to write

$$2\gamma_k = (f_1g_1 + f_{g2}g_2 - f_aa - (a_i + a_{ck})) \tag{4.5}$$

Here, $g_{1,2}$ and a are the gain/saturable absorption coefficients (weak k-dependence due to material gain dispersion is omitted for simplicity), $f_{1,\ g2,\ a}$ are the length fractions of the corresponding sections, and a_i and a_{ck} are, respectively, the internal and outcoupling losses for each mode. It is the latter parameter that predominantly determines the harmonic operation of the CCM laser – the dependence of a_{ck} on k favours a fixed set of modes (those with the lowest losses) in the lasing spectrum. As noted earlier, [10], this predominantly linear selectivity mechanism is rather different

from the situation in multiple and asymmetric CPM constructions – there, the selectivity is provided solely by the nonlinear mode interaction parameters G_m so that the cavity geometry determines just the harmonic number, not the actual lasing modes, leading to an increased risk of supermode competition.

This selection mechanism is also different from that employed by the harmonic modelocked (HML) DBR lasers [Figure 4.5(II-a)] that demonstrated modelocking at 1.54 THz [22]. Both the experiment and theory of [22] lead to the conclusion that HML DBR lasers rely substantially on non-linear phenomena in the cavity to establish the harmonic character of the modelocking process; at low pumping currents those lasers operate at the fundamental ML frequency. With the CCM structures studied here, HML can be firmly established by the harmonic selectivity of the cavity. The difference in the selection rules is illustrated in Figure 4.5(I-b) and (II-b). It is clear that the CCM construction provides equal mode discrimination for any number of modal periods, whilst in the DBR design the spectral selectivity diminishes for modes that are distant from the Bragg frequency of the DBR section (corresponding to Mode 0 in Figure 4.5(II-b)). It is therefore useful to discuss the modal loss properties of CCM lasers in some more detail.
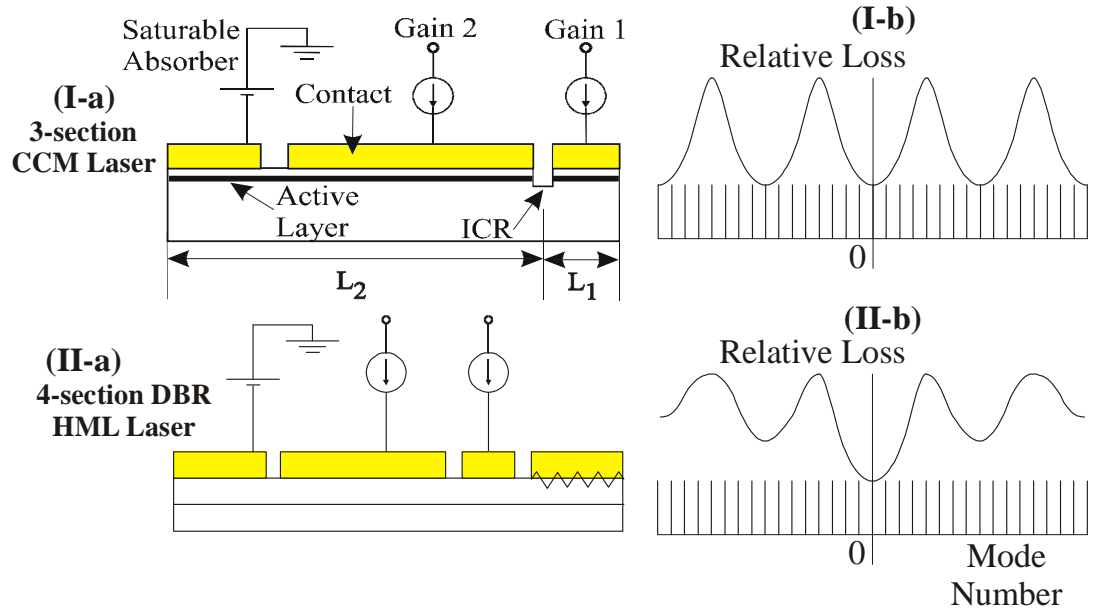
Figure 4.5. Schematic of the proposed CCM device **(I-a)** with a corresponding cavity selectivity **(I-b)** and schematic **(II-a)** and selectivity **(II-b)** of the DBR HML laser of Ref.[22].

Generally speaking, the expression (4.5) for the net modal gains γ_k should be used with some care, since the outcoupling losses a_{ck} may themselves depend on gain

and saturable absorption (and be therefore parametrically time-dependent), particularly due to the carrier-density-dependent refractive index. Most generally, γ_k should be calculated directly from the complex modal eigenvalues δ_k of Eq.(4.4). To find these eigenvalues (and, by the same token, the mode profiles u_k), we follow the procedure commonly used for threshold loss analysis in complex laser cavities. We express the mode profiles as linear combinations of forward- and backward-propagating waves with complex wave vectors

$$q_{g1(2)k}=\delta_k + \tfrac{1}{2} (-ig_{1(2)} +g''), \qquad q_{ak}=\delta_k+ \tfrac{1}{2} (ia+a'') \qquad (4.6)$$

inside the gain and SA sections respectively, with g'' and a'' describing the optical frequency chirp due to the carrier-density-dependent refractive index associated with gain g and saturable absorption a. We then require that these waves satisfy the usual reflectance/transmittance boundary conditions at the facets and the intermediate reflector, the latter being assigned phenomenological (amplitude) transmittance and reflectance coefficients t_{ICR} and r_{ICR}. This procedure yields a transcendental equation for δ_k :

$$\delta_k = \delta_k^{(0)} + \frac{i}{2L}\log\left[\left(1- r_{ICR}r_1 \exp(-i2q_{g1k}L_1)\right)\times\left(1- r_ir_2 \exp(-i2q_{g2k}L_{g2} -i2q_{ak}L_a)\right)\right] \qquad (4.7)$$

where $r_{1,2}$ are the *amplitude* reflectances of facets bordering the corresponding sections. Eq.(4.7) is a generalisation of formulae used in the literature for cleaved-coupled-cavity lasers; here, it is written in such a form that the first term

$$\delta_k^{(0)} = \frac{\pi k}{L} + \frac{1}{2}\left(f_a a''+ f_1 g_1 ''+ f_{g2} g_2 ''\right) + \frac{i}{2}\left[\ln\frac{1}{r_1 r_2 t_{ICR}^2} + f_a a - f_1 g_1 - f_{g2} g_2 \right] \qquad (4.8)$$

describes the solution for a simple, unperturbed Fabry-Pérot cavity, whilst the second term contains the effect of intermediate reflectance. This is particularly convenient in the (practically quite common) case of small ICR reflectance $r_{ICR} << 1$, $t_{ICR} \approx 1$, which results in relatively small differences between mode output losses. Then, Eq.(4.7) is easily simplified (see [10]) and may indeed be written in the form of Eq.(4.5), in which the values of cavity losses a_{ck} do not depend explicitly on gain/saturable absorption and may be estimated from a simple approximation:

$$a_{ck} = \frac{1}{L}\ln\frac{1}{r_1 r_2} + \Delta a_{ck}; \; \Delta a_{ck} \approx -\frac{r_{ICR}}{L}\left(\frac{r_1^{f_2}}{r_2^{f_1}} + \frac{r_2^{f_1}}{r_1^{f_2}} \right)\cos(2\pi f_1 k) \qquad (4.9)$$

(more precisely, the fraction of the *optical* rather than geometrical length of the shorter subcavity should be used in the argument of the cosine).

The cosine in expression (4.9) reaches its maximum value of one for certain discrete mode numbers k, separated by a multiple of $M = 1 / m f_1$, M and m being integers. With every M-th mode having a minimum loss, modelocking (ML) is predicted at the M-th harmonic whenever the sub-cavity length ratio L_1:$L_2 = m$:n with $M = m + n$ for integer m and n. More specifically, when $m = 1$, L_1:$L_2 = 1 : (M$-$1)$. In both the general ($m : M$-m) and the specific ($1 : M$-1) cases, all but every M-th mode have a higher loss and are therefore suppressed in the lasing output. The harmonic ML frequency is $f = M f_F$, f_F being the fundamental modelocking frequency. In spectral terms, this corresponds to an M-fold multiplication of the mode separation in the lasing spectrum, $\Delta\Lambda_{CCM} = M \Delta\lambda_{F\text{-}P}$, ($\Delta\lambda_{F\text{-}P}$ is the cavity's Fabry-Pérot mode spacing). For an $1 : (M$-$1)$ ratio, the harmonic mode spacing is effectively that of the shorter sub-cavity, as is the modelocking frequency. The exact degree to which all non-harmonic modes are suppressed is determined by the cavity discrimination, which can be quantified as the smallest loss difference between a harmonic mode and a non-harmonic one. In the special $1 : (M$-$1)$ case, the discrimination is given by

$$\delta a_c = a_{c1} - a_{c0} \qquad\qquad (4.10)$$

In the case of $r_{ICR} \ll 1$, the selectivity δa_c is defined by Eq.(4.9) and is thus proportional to r_{ICR}. In the general case, Eq.(4.7) has to be solved numerically. At $R_{ICR} = r_{ICR}^2 \sim 0.001 - 0.01$, the linear dependence of δa_c on r_{ICR} (4.9) holds well. A further increase in the intermediate reflection continues to improve the selectivity (in accordance with numerical time-domain simulations [23], which predicted more reliable harmonic operation with shorter pulses in lasers with highly reflective microstructures used as ICRs). However, the rate of selectivity improvement slows down considerably, and at $R_{ICR} \sim 0.6 - 0.9$, δa_c shows a broad peak and then falls as r_{ICR} approaches unity (with losses and scattering at the ICR taken into account by setting $R_{ICR} + t_{ICR}^2 < 1$, the maximum shifts to lower reflectances). This implies that there is a limit to the improvement of the quality of harmonic ML through the use of highly reflective ICRs. Unsurprisingly, equations (4.7) and (4.9) predict that the maximum cavity selectivity achievable with a single reflector falls drastically with the harmonic number M. In a particular case where the sub-section ratio is (1:M-1)

and $M = 1/f_1$, the series decomposition of the cosine term in Eq.(4.9) in the limit of $kf_1 = k/M << 1$, gives for large M an estimate

$$\delta a_c \approx -\frac{2r_{ICR}}{L}\left(\frac{r_1^{f_2}}{r_2^{f_1}}+\frac{r_2^{f_1}}{r_1^{f_2}}\right)\left(\frac{\pi}{M}\right)^2 .$$

The calculations presented in Figure 4.6 have been performed for $g_1 = g_2 = -a$, i.e., for a cavity homogeneously pumped below threshold. The selectivity δa_c can be increased by preferentially pumping the shorter subsection to ensure $g_1 > g_2$. However, as long as $g_1L << M$ and/or $r_{ICR} << 1$ (i.e., neither section approaches lasing individually), this improvement remains modest. Within these limits, we also found that the dependence of the mode losses a_{ck} (and hence of δa_c) on g_1, g_2, and a is nearly linear, as in Eq.(4.5), which speeds up the numerical integration of Eq.(4.3).
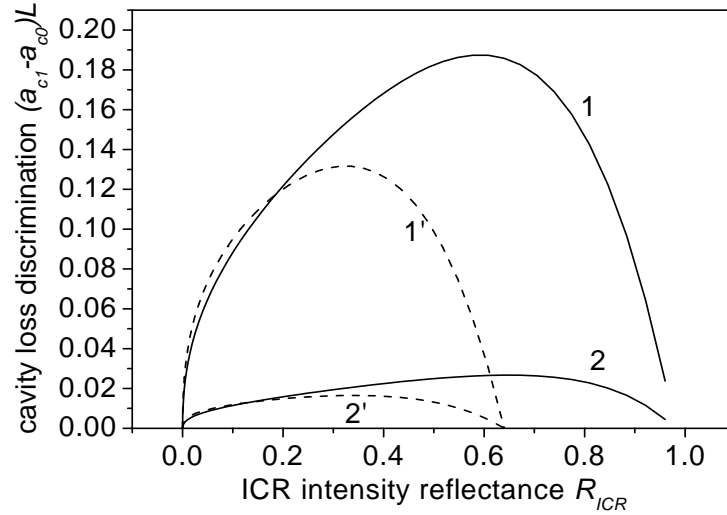
Figure 4.6. Calculated selectivity of the harmonic cavity versus ICR reflectance. ICR position $f_1 = 1$:$M = 1$:11 (**1, 1'**) and 1:30 (**2, 2'**). Solid curves (**1,2**): $r^2_{ICR} + t^2_{ICR} = 1$ (no scattering or losses at ICR); Dashed curves (**1', 2'**): $r^2_{ICR} + t^2_{ICR} = 0.64$

Twin-reflector CCM configuration

An alternative method of improving mode selectivity at high M is to use more than one ICR, as was done in [9] to achieve single-frequency lasing. Whilst the general expression for the modal loss a_{ck} in the case of two or more ICRs is very cumbersome, in the case of $r_{ICR} << 1$, the contributions from individual reflectors to Δa_{ck} can be treated additively, with each individual term calculated via Eq.(4.9). Particularly promising is the use of two reflectors positioned at different fractions of the cavity length, as each of them is then responsible for suppressing a different

subset of "non-harmonic" modes, leading to a much stronger overall selectivity. The first slot, which divides the cavity into an *m:n* ratio, provides suppression for the Fabry-Pérot modes nearest to the harmonic modes, whereas the second slot at a ratio of 1:*k* offers discrimination against the fundamental modes located towards the middle of the intervals between the adjacent harmonic modes (here, *m, n,* and *k* are integers without common factors). With $(m + n)$ being equal to or a multiple of $(1 + k)$, both ICRs will select the same harmonic $M = m+n$, one ICR complementing the spectral selectivity of the other. Alternatively, $(1 + k)$ can be a multiple of $(m + n)$ or vice versa. This idea is illustrated in the schematic of Figure 4.7 for the case of $(m + n) = 4 (1 + k)$, with $k = 2$, $m = 5$ and $n = 7$, where enhanced selection for every 12th mode is demonstrated.

Fabry-Perot modes of unperturbed cavity

**Mode selectivity of a
1:2 reflector cavity**

**Mode selectivity of a
5:7 reflector cavity**

**Combined selectivity
from both reflectors**
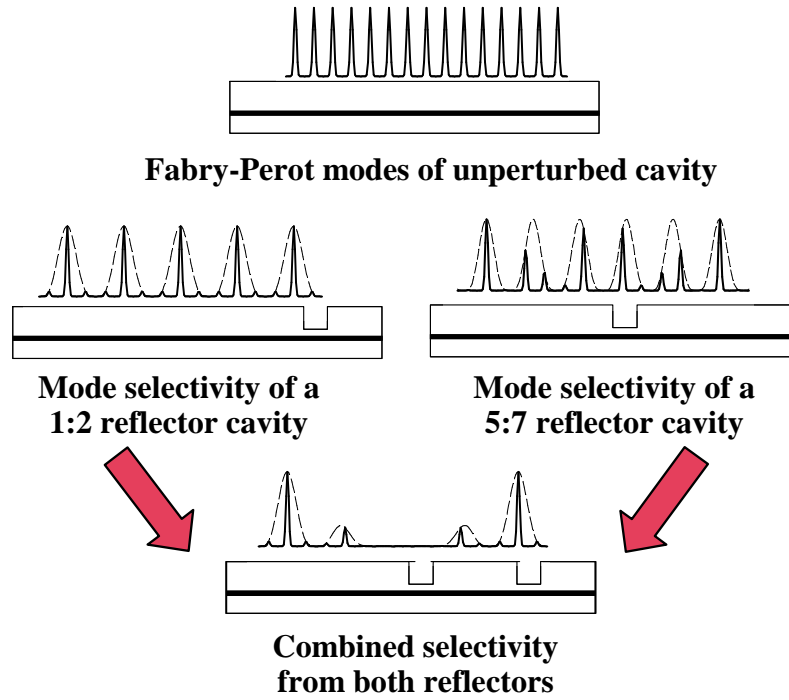
Figure 4.7. Illustration of the principle of mode selection by twin ICRs. Two ICRs (one with a ratio of 1:2 and the other with 5:7) provide enhanced selectivity for every 12th mode only.

4.2.3. Saturable absorber model

As explained in Chapter 3, the SA must provide intensity-dependent non-linearity that is indispensable for passive modelocking operation. Furthermore, the nonlinearity must recover sufficiently quickly to be able to support light modulation at (sub)-THz rates. However, the absorption recovery times in reverse-biased QW

SA's, where the photo-generated carriers are swept out by the applied electric field (see the diagram of Figure 4.8), are on the multi-pico–nanosecond time scale, which is clearly inadequate for supporting ML at these high frequencies.
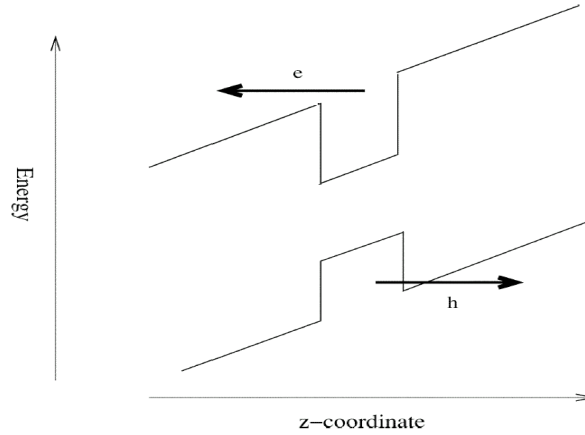
Figure 4.8. Schematic band structure for a quantum well under reverse bias [24].

Recently, Avrutin *et al.* have developed a microscopic model [24] for the sweep-out process in a GaAs/AlGaAs QW SA that includes both thermionic and tunnelling carrier escape mechanisms. The main escape mechanism at room temperature was established to be thermally-assisted tunnelling/emission through near-barrier-edge states. For a low electric field, the thermionic component was found to be the main contributor, since the tunnelling is slow, whereas for a higher field, the tunnelling becomes dominant. The calculated escape times as a function of the applied field are plotted in Figure 4.9 and show a more complex dependence than the often-postulated exponential, but can be reduced down to several picoseconds at high enough fields. Further reduction of sweep-out time can be achieved by optimising the QW design [19]. In a practical device, however, the field itself is reduced by the photo-carrier screening, so the sweep-out time becomes carrier-density dependent.

Cleary, then, the SA must have much faster recovery mechanisms than electrical carrier sweep-out to enable harmonic ML at THz frequencies. Indeed, the semiconductor laser itself is a highly non-linear system, with a number of microscopic processes that can have sub-picosecond timescales [14]. Such nonlinearities can be caused by the dynamic deviation of the energy distribution of electrons and holes from quasi-equilibrium and include phenomena such as spectral hole burning [25], dynamic carrier heating [26, 27] and non-equilibrium of the

carrier distribution between the well and the barrier. Another mechanism that is specific to QW structures is excitonic absorption and ionisation [13]. The characteristic relaxations times are 300–700 fs for carrier heating nonlinearities, and ~100 fs for spectral hole burning [18]. While such nonlinearities are relatively weak and are incapable of fully recovering the SA between ultrafast pulses, they may prove sufficient for establishing ML where the SA provides only a partial intensity modulation. Carrier heating, for example, is predicted to play a major role in the ultrafast dynamics in bulk semiconductor absorbers, favouring the generation of sub-picosecond pulses over longer ones [28]. A fully microscopic model is required to investigate the effect of these nonlinearities on the laser behaviour and quantify their parameters.
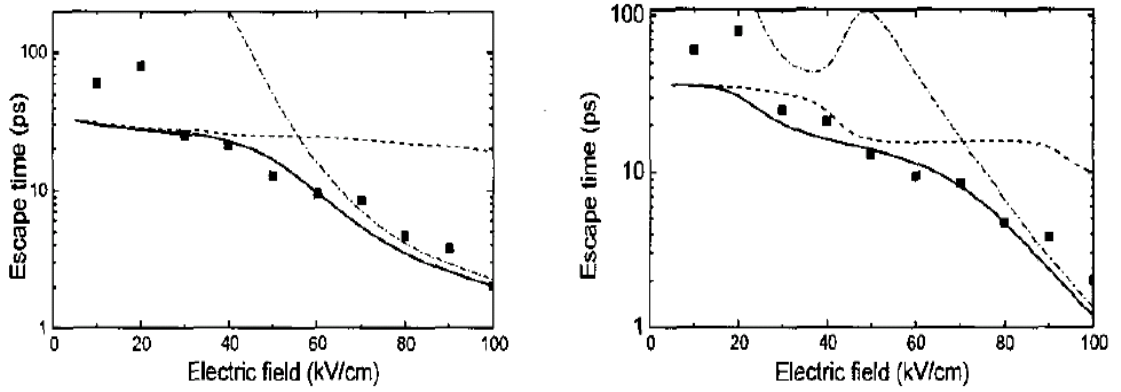
Figure 4.9. Electron (left) and hole (right) sweep-out times in GaAs/AlGaAs QW SA vs. applied electric field: solid – total, dashed – thermionic, dash-dotted – tunnelling, dots – experimental from literature [17].

In the distributed time-domain model [14, 16, 20], the absorption due to fast nonlinearities in the SA section is approximated with a characteristic relaxation time $\tau_{nl}^{(a)}$ and nonlinearity coefficient ε_A using the phenomenological relaxation equation:

$$\frac{da}{dt} = \frac{a_L - a(1 + \varepsilon_A S)}{\tau_{nl}^{(a)}}; \quad a_L(N) = -A_A(N - N_0) \tag{4.11}$$

where A_A is the absorption cross-section, the subscript L denotes "linear", N and N_0 are the instantaneous and equilibrium carrier densities in the SA section, respectively, and S is the intensity of light.

In the time-frequency-domain model used for the simulation of CCM devices and formulated by Eqs.(4.1)-(4.3), the fast nonlinearities are included in the mode interaction parameters G_m that were introduced in Eq.(4.3):

$$G_m = (\sum_k E_k E_{k+m}^*) \cdot \left\{ \xi_m^{(a)} a \left[\frac{v_g(1+i\alpha_A) \cdot A_G \cdot \tau_{\Sigma a}}{1 - im\Delta\Omega\tau_{\Sigma a}} + \frac{\varepsilon_A}{1 - im\Delta\Omega\tau_{nl}^{(a)}} \right] \right.$$
$$\left. - \xi_m^{(g)} g \left[\frac{v_g(1+i\alpha_G) \cdot A_A \tau_{\Sigma g}}{1 - im\Delta\Omega\tau_{\Sigma g}} + \frac{\varepsilon_G}{1 - im\Delta\Omega\tau_{nl}^{(g)}} \right] \right\}$$

(4.12)

where the key parameters are: a and g denote saturable absorption and gain, $\Delta\Omega = \pi c / n_g$, $L = 2\pi\Delta F$ is the intermodal interval, $\tau_{\Sigma a,g}$ are the inverse total recombination rates, $A_{g,a}$ are the gain and absorption cross-sections, $\xi_m^{(g,a)}$ are the spatial overlap factors defined by the laser geometry, $\alpha_{G,A}$ are the Henry factors, and $\varepsilon_{G,A}$ are the gain and SA nonlinearity coefficients. In Eq.(4.12), the first factor is the component of the light intensity oscillation due to the beating between the modes. The terms circled in orange and green denote the response of the SA and gain sections, respectively, to these intensity pulsations. The group of terms enclosed in the blue box describes the response of the active medium to carrier density changes ("slow" terms), while the red box captures the effect of gain and absorber nonlinearities ("fast" terms). It is these fast terms that are crucial to simulating harmonic ML at ultrahigh frequencies.

In Eq.(4.12), the parameters of gain sections of ML lasers are largely the same as those of other laser types and, as such, are widely analysed and relatively well known. By contrast, the characteristics of QW SA's have not been studied as extensively, and ambiguity remains over parameters such as the nonlinearity coefficient ε_A and effective recovery time. The value of ε_A is the least well-known parameter in the model and may be used as a fitting parameter. In Ref.[20], the nonlinearity was estimated to be $\varepsilon_A \geq 10^{-17} \text{cm}^{-3}$, which is a reasonably modest value and is often quoted for gain nonlinearity coefficients. Values for nonlinearity relaxation time $\tau_{nl}^{(a)}$ were chosen phenomenologically at below 0.5 ps. Such a short recovery time was observed in pump-probe experiments in reverse-biased multiple QW material [29], but has not been fully understood. It was found no ML could be simulated for longer nonlinearity relaxation times at THz frequencies and that changes in $\tau_{nl}^{(a)}$ strongly affected the boundaries of the harmonic ML regime and the relative amplitudes of the multiple pulses in the cavity [20]. Ultimately, ML frequencies achievable with laser diodes are limited by: the magnitude of the

nonlinearity coefficients (which depend on the absorber structure and applied voltage), nonlinearity recovery times and the spectral width of the gain curve of the active medium [14].

4.2.4. Modelling results

The above model was employed to simulate the lasing spectra of Figure 4.10(I-a –V-a), which were obtained by full numerical solution of the complex rate equations (4.3) complete with rate equations for the carrier density in the gain and saturable absorber sections [15]. The method has been demonstrated to give good agreement, for different laser structures, with the more generic but much slower DTD approach employed in earlier work, and only requires use of a single model throughout the present study without recourse to DTD modelling.

The graphs of Figure 4.10(I-b – V-b) have been produced by summation of the Fourier series (with modal phases provided by calculations along with the amplitudes) and represent a fragment of the pulse train within the timeframe of a single round-trip of the long cavity, registered at 20 ns after turn-on to allow the transients to settle down. The geometry of the laser approximates that of a fabricated device, and the parameters of the material were chosen within the limits quoted in the literature and are similar to those used in earlier work [18, 20, 30].

In the case of an unperturbed cavity with no ICR, Figure 4.10(I), the usual picture of fundamental frequency ML is simulated, with the spectrum being shifted and asymmetric due to self-phase modulation. A single ICR at 1/3 of the cavity length, with an intensity reflectance of $R_{ICR} = 0.01$, provides a very good quality 3rd harmonic ML shown in Figure 4.10(II) (the intermediate modes for this value of R_{ICR} are suppressed by over 60 dB). However, for a higher harmonic number of $M = 12$, the selectivity of a single reflector is insufficient to achieve uniform harmonic operation in the relatively long cavity, whether the ICR is positioned at 1/12 [Figure 4.10(III)] or 5/12 [Figure 4.10(IV)] of the cavity length. Nonetheless, the combined effect of two identical ICRs, in this case at $L/3$ and $5L/12$, clears the spectrum of intermediate modes, resulting in good-quality harmonic ML with $M = 12$ [Figure 4.10(V)]. This is due to the fact that both ICRs simultaneously select every 12th mode only.
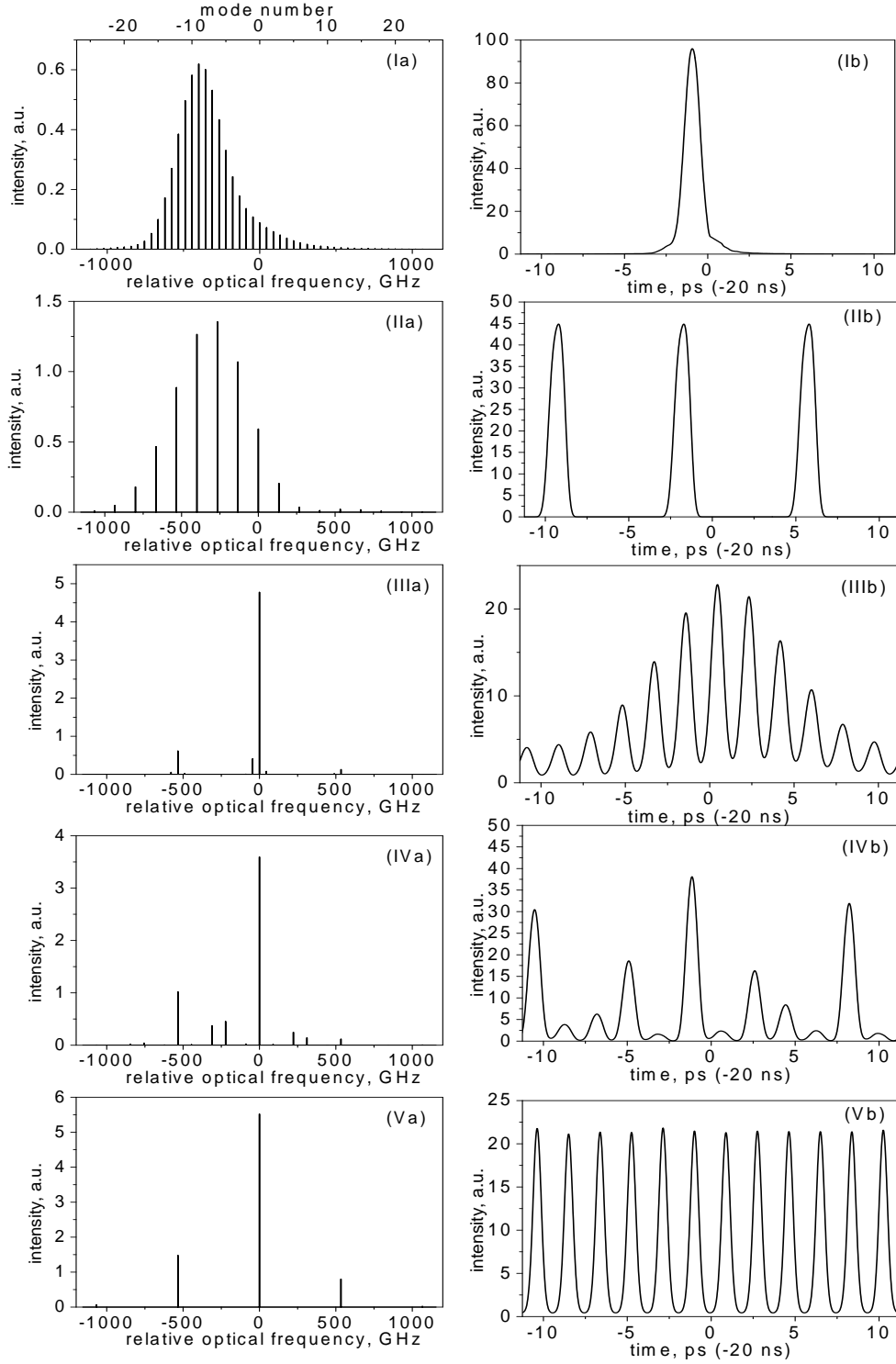
Figure 4.10. Typical simulated lasing spectra **(a)** and corresponding pulse trains **(b)** for a laser with $L = 900$ μm (fundamental repetition rate = 44 GHz) and L_a=30 μm. **(I)**: Fundamental frequency mode-locking with no ICRs; **(II)**: Harmonic ML (M=3) with an ICR at L/3; **(III-IV)**: incompletely rendered harmonic ML (M=12) with single ICRs at L/12 **(III)** and 5L/12 **(IV)**; **(V)**: good quality harmonic ML (M=12) with the combined effect of two ICRs at L/3 and 5L/12. Assumed $R_{ICR} = 0.01$.

In conclusion, we note that a similar analysis has been applied to CC devices of non-linear geometries. CCM has been successfully observed and modelled in ring lasers [10] and predicted in parallel-cavity lasers [11]. The simulation results presented here provide strong grounds for the experimental realisation of CCM lasers in purpose-designed configurations.

4.3.   References

[1]   S. Arahira, Y. Matsui, and Y. Ogawa, "Mode-locking at Very High Repetition Rates More than Terahertz in Passively Mode-locked Distributed-Bragg-Reflector Laser Diodes," *IEEE J. Quant. Electronics*, vol. 32, pp. 1211-1224, 1996.

[2]   T. Kunii and Y. Matsui, "Narrow spectral linewidth semiconductor lasers," *Opt. & Q. Electronics*, vol. 24, pp. 719-735, 1992.

[3]   M.J. Adams and J. Buus, "Two-segments cavity theory for mode selection in semiconductor lasers," *IEEE J. Quant. Electronics*, vol. QE-20, No.2, pp. 99-103, 1984.

[4]   L.A. Coldren and T.L. Koch, "Analysis and design of coupled cavity lasers-Part I: threshold gain analysis and design guidelines," *IEEE J. Quant. Electronics*, vol. QE-20, No.6, pp. 659-670, 1984.

[5]   C.H. Henry and R.F. Kazarinov, "Stabilisation of single frequency operation of coupled cavity lasers," *IEEE J. Quant. Electronics*, vol. QE-20 (7), pp. 733-744, 1982.

[6]   L.A. Coldren, B.I. Miller, K. Iga, and J.A. Rentschler, "Monolithic two-section GaAsP/InP active-optical-resonator devices formed by reactive ion etching," *Appl. Phys. Lett*, vol. 38 (5), pp. 315-318, 1981.

[7]   L.F. Dechiaro, "Spectral width reduction in multi-longitudinal mode lasers my spatial loss profiling," *J. Lighwave Tech*, vol. LT-9, pp. 975-989, 1991.

[8]   J.S. Young, D.A. Kozlowski, J.M.C. England, and R.G.S. Plumb, "Spectral perturbation and mode suppression in 1.3 um Fabry-Perot lasers," *Elec. Lett.*, vol. 31, pp. 290-292, 1995.

[9]   D.A. Kozlowski, J.S. Young, J.M.C. England, and R.G.S. Plumb, "Longitudinal mode control in 1.3 mm Fabry-Perot lasers by mode suppression," *IEE Proc.-Optoelectron.*, vol. 143 (1), pp. 71-76, 1996.

[10]   E.A. Avrutin, J.H. Marsh, J.M. Arnold, T.F. Krauss, H. Pottinger, and R.M. De La Rue, "Analysis of harmonic (sub) THz passive mode-locking in monolithic compound cavity Fabry-Perot and ring laser diodes," *IEE Proc.-Optoelectron.*, vol. 146, pp. 55-61, 1999.

[11]   E.A. Avrutin, F. Camacho, A.C. Bryce, C.J. Hamilton, D. Yanson, J.M. Arnold, and J.H. Marsh, "Analysis of monolithic parallel-compound-cavity semiconductor lasers for high brightness, single-frequency, and short-pulse

operation," presented at The Conference on Lasers and Electro-Optics (CLEO"99), Baltimore, 24-29 May 1999, paper CTuK55.

[12]   H.A. Haus, "Theory of mode locking with a fast saturable absorber," *J. Appl. Phys.*, vol. 46, pp. 3049-58, 1975.

[13]   H.A Haus and Y. Silberberg, "Theory of mode locking of a laser diode with a multiple-quantum-well structure," *J. Opt. Soc. Am. B, Opt. Phys*, vol. 2, pp. 1237-1243, 1985.

[14]   E.A. Avrutin, J.H. Marsh, and E.L. Portnoi, "Monolithic and multi-gigahertz mode-locked semiconductor lasers: Constructions, experiments, models and applications," *IEE Proc. Optoelectron.*, vol. 147, pp. 251-278, 2000.

[15]   E.A. Avrutin, J.H. Marsh, and J.M. Arnold, "Static and dynamic modal analysis of monolithic mode-locked semiconductor lasers," presented at 12th LEOS Annual Meeting, San Francisco, CA, 8-13 November 1999, paper CThF4.

[16]   E.A. Avrutin, J.H.Marsh, and J.M.Arnold, "Modelling of semiconductor laser structures for passive harmonic mode locking at terahertz frequencies," *International J. Optoelecron.*, vol. 10, pp. 427-432, 1996.

[17]   E. A. Avrutin, J.M. Arnold, J. H. Marsh, V.V. Nikolaev, C. Xing, and D. Gallagher, "Modelling monolithic mode-locked semiconductor lasers," presented at IEEE Conf. on Numerical Simulation of Semiconductor Optoelectronic Devices (NUSOD '03), Paper ThB1 (Invited), Tokyo, Japan, 2003.

[18]   E.A. Avrutin, J.H. Marsh, and J.M. Arnold, "Dynamic modal analysis of monolithic mode-locked semiconductor lasers," *IEEE J. Sel. Top. Quantum Electron.*, vol. 9, pp. 844-856, 2003.

[19]   E. A. Avrutin and V.V. Nikolaev, "Quantum-well design for monolithic optical devices with gain and saturable absorber sections," *IEEE Phot. Tech. Lett.*, vol. 16, pp. 24-25, 2004.

[20]   J.F. Martins-Filho, E.A. Avrutin, C.N. Ironside, and J.S. Roberts, "Monolithic multiple colliding pulse mode locked quantum well lasers: experiment and theory," *IEEE J. Sel. Top. Quantum Electron.*, vol. 1, pp. 539-552, 1995.

[21]   D. A. Yanson, M. W. Street, S. D. McDougall, L. G. Thayne, J. H. Marsh, and E. A. Avrutin, "Ultrafast harmonic mode-locking of monolithic compound-cavity laser diodes incorporating photonic-bandgap reflectors," *IEEE J. Q. Elec.*, vol. 38(1), pp. 1-11, 2002.

[22]   S. Arahira, Y. Matsui, and Y. Ogawa, "Mode-locking at very high repetition rates - more than Terahertz - in passively mode-locked distributed-Bragg-reflector laser diodes," *IEEE J. Quant. Electronics*, vol. 32, pp. 1211-1224, 1996.

[23]   B.D. Allan, E.A.Avrutin, J.M.Arnold, R.M. DeLaRue, and J.H. Marsh, "Modelling deep etched optical waveguide step discontinuities," presented at the 1998 International Symposium on Information Theory, CLEO/EUROPE, Glasgow, Scotland, Sep 14-18, 1998.

[24] V.V. Nikolaev and E. A. Avrutin, "Photocarrier escape time in quantum-well light-absorbing devices: effects of electric field and well parameters," *IEEE J. Q. Elec.*, vol. 39, pp. 1653-1661, 2003.

[25] G.P. Agrawal, "Gain nonlinearities in semiconductor lasers: theory, and appications to distributed feedback lasers," *IEEE J. Q. Elec.*, vol. QE-23, pp. 860-868, 1987.

[26] B. Gomatam and A.P. Defonzo, "Gain suppression in semiconductor lasers: the influence of dynamic carrier temperature changes," *IEEE J. Q. Elec.*, vol. 26, pp. 1689-1704, 1990.

[27] A Plyavenek, "Gain nonlinearities in semiconductor lasers: the combined effect of the modulation of the carrier density and the electron temperature at the beat frequency of interacting optical fields," *Opt. Comms.*, vol. 100, pp. 278-288, 1993.

[28] A.V. Uskov, J.R. Karin, J.E. Bowers, J.G. McInerney, and J.L. Bihan, "Effects of carrier cooling and carrier heating in saturation dynamics and pulse propagation through bulk semiconductor absorbers," *IEEE J. Q. Elec.*, vol. 34, pp. 2162-2171, 1998.

[29] A.V. Uskov, J.R. Karin, R. Nagarajan, J.E. Bowers, and J. Mork, "Ultrafast dynamics in waveguide saturable absorbers," presented at 14th International IEEE Semiconductor Laser Conference, Maui, HI, 1994.

[30] E.A. Avrutin, J.H.Marsh, and J.M.Arnold, "Modelling of semiconductor laser structures for passive harmonic mode locking at terahertz frequencies," *International J. Optoelecron.*, vol. 10, pp. 427-432, 1995.

CHAPTER 5.

DESIGN OF HARMONIC MODELOCKED

COMPOUND-CAVITY LASERS

The results of theoretical modelling presented in Chapter 4 substantiated the feasibility of realising an ultrahigh-frequency source using modelocked compound-cavity semiconductor lasers. In the present Chapter, the design of these devices will be presented and their parameters discussed, while all material and waveguide design issues and material characterisation will be the subject of Chapter 6.

In this Project, the conventional "theory → design → fabrication → test" cycle was not always adhered to, with many changes being made "on the fly" as a result of feedback at the fabrication and testing stages. Numerous approaches, variations and optimisations have been attempted in the course of the Project, with 14 major device generations and mask redesigns. No "frozen" design was ever achieved, and some parameters were even varied among devices within a single sample. Despite the poor repeatability and limited resources, this approach has nonetheless enabled to author to arrive at a device design that was adequate for the successful demonstration of the principle of harmonic compound-cavity modelocking (CCM) at ultrahigh frequencies.

5.1. CCM device design

In this Section, the geometrical layout of CCM devices and their design parameters will be discussed. Only the most significant design versions will be presented and final or near-final device parameters will be used.

5.1.1. Overall device concept

The compound-cavity harmonic mode-locked lasers are essentially ridge-waveguide devices with one or two etched intracavity reflectors (ICR), an electrically isolated saturable absorber section and two gain sections, *Gain 1* and

Gain 2, of lengths L_1 and L_2, respectively, that allow the fine tuning of the optical length of the cavity through differential pumping. The schematics of cross-sections of single-ICR and twin-ICR device versions are shown in Figure 5.1(a, b).
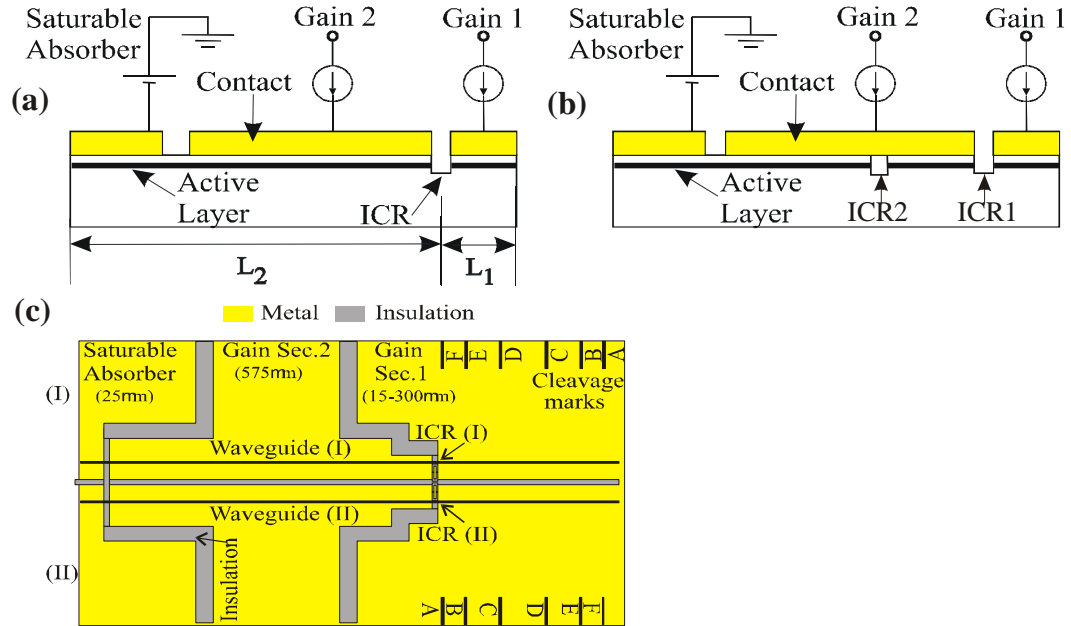
Figure 5.1. Cross-sections of single-ICR **(a)** and twin-ICR **(b)** CCM lasers and planar view **(c)** of device **(a)**.

To allow direct comparison between different types of ICR, two symmetric lasers (I & II) with different ICRs (or with one having none at all) were placed on a single chip, with the two waveguides electrically and optically isolated from each other by a 50 µm gap, as illustrated in Figure 5.1(c). Besides doubling the yield of devices, such integration offered a straightforward way of characterising different types of ICR in otherwise identical lasers, as both lasers were cleaved to precisely the same length. In earlier versions of the chips, only one device had an ICR so that it could be referenced against the identical unperturbed waveguide of the other device.

The waveguide width was chosen to be 3 µm with a height of 0.75 µm, which was established from numerical simulations using a mode solver, as will be explained in Chapter 6. Within each device, the metal isolation was staggered in order both to form contact pads of a similar size and to ensure a near-uniform pump current distribution along the active part of the cavity, which can be seen in Figure 5.1(c).

To allow testing of the device with a single current probe, narrow metal interconnects were created in the isolation between the two gain sections, with a view to mechanically removing the interconnects by scratching them with a probe tip following an initial test. However, it proved very cumbersome to do so with every single device, therefore the interconnect idea was later abandoned.

One of the first versions of the chip utilised etched facet technology to define precisely both the cavity length and sub-cavity ratio. With this approach, the positioning imprecision associated with facet cleaving is eliminated, and the laser facets are defined by lithography and dry-etching. All device dimensions are then "frozen" into the mask design, with no allowance for subsequent adjustment of the cavity length. However, initial trials showed that such devices suffered from catastrophic optical damage failures of the facets under low pumping levels and were generally very unreliable. The etched facet approach was then abandoned in favour of the reliable, yet imprecise, facet definition by wafer cleaving.

5.1.2. Design of sub-cavity ratios for cleaved-facet devices

In laying the laser chips out on a wafer, it was desirable to have the option of deciding on a chip's cavity length/ratio at the cleaving stage, rather than rigidly defining it in the mask design. This would allow flexibility in cleaving devices of various cavity lengths/ratios based on their initial test data. To preserve as much uniformity in the device design as possible, the lengths of the SA and *Gain 2* sections were kept constant, and only the length of *Gain 1* was varied to obtain different cavity ratios.

A reciprocal device layout was designed with two lasers facing each other, as shown in Figure 5.2, so that when one laser was cleaved to length *OA* (implying a given *m:n* ratio), the other one would be automatically cleaved to length *O'F' = OF* (with a different *l:k* ratio), the next pair being lengths *OB* and *O'E' = OE*, etc. Other ratios could be obtained by deviating from the designated cleavage markers *A - F*.

Earlier generations of the chip used fairly symmetric geometries with a range of *m:n* ratios (a "long-long" configuration as defined in Section 4.1.2). However, after those lasers failed to demonstrate the expected performance (see the discussion of Section 9.1.2, Chapter 9), only 1:*m* ratio devices were used.
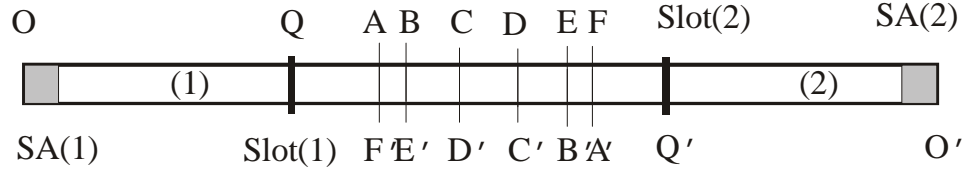
Figure 5.2. Reciprocal device layout allowing two lasers with exact 1:*m* and 1:*k* cavity ratios to be cleaved simultaneously at any of the points *A - F*.

To describe a system of 1:*m* reciprocal ratios mathematically, we shall use the diagram of Figure 5.2 with the following identities:

$$AB = A'B' = EF = E'F'; \quad BC = B'C' = DE = D'E';$$

$$QA = Q'A'; \quad OQ = O'Q'; \quad CD = C'D'.$$

For a set of six possible cavity ratios

$$1{:}a = QA/OQ = Q'A'/O'Q'; \quad 1{:}b = QB/OQ = Q'B'/O'Q';$$

$$1{:}c = QC/OQ = Q'C'/O'Q'; \quad 1{:}d = QD/OQ = Q'D'/O'Q';$$

$$1{:}e = QE/OQ = Q'E'/O'Q'; \quad 1{:}f = QF/OQ = Q'F'/O'Q',$$

and corresponding harmonic numbers $(a+1) > (b+1) > (c+1) > (d+1) > (e+1) > (f+1)$, we can write a system of five equations

$$1/a + AB/OQ = 1/b; \quad 1/b + BC/OQ = 1/c; \quad 1/c + CD/OQ = 1/d;$$

$$1/d + BC/OQ = 1/e; \quad 1/e + AB/OQ = 1/f$$

in integer unknowns *a, b, c, d, e, f* and real *AB, BC, CD, OQ*. By substitution, we reduce the above to

$$1/a + (2\,AB + 2\,BC + CD)/OQ = 1/f$$

Specifically for variables *a...f,* further substitution yields

$$1/e = -1/b + 1/c + 1/d; \qquad 1/f = -1/a + 1/c + 1/d \tag{5.1}$$

for independent positive integers $a > b > c > d$. Purpose-written code was used to perform a numerical search over all permitted combinations of *a, b, c, d* to satisfy Eq.(5.1) for positive integers *e* and *f* and modest harmonic numbers under 45. The search has produced two sets of solutions for [*a, b, c, d, e, f*]:

[24, 18, 15, 10, 9, 8] and [42, 18, 15, 10, 9, 7]

However, neither set was deemed suitable for use in the CCM laser design due to the non-uniform distribution of values within either set (i.e., the absence of lower

harmonics between 2 and 8). Attempts to reduce the number of cleavable ratios of Figure 5.2 to five have encountered a similar problem (best fit [*a, b, c, d, e*] = = [24, 18, 12, 9, 8]). Suitable ratio distributions were only found for a set of four cleaving ratios (i.e., [*a, b, c, d*] only), or fewer.

Low-asymmetry device layout

A different approach was adopted instead, using two different layouts, one suitable for low-harmonic devices and the other for high-harmonic ones. The former included low-asymmetry devices with ratios of 1:2, 1:3, 1:5 and 1:10. It also contained one high-harmonic ratio of 1:30 for comparison. As these numbers are not compatible with Eq.(5.1), one "sacrificial" ratio of the *m:n* type was added with *m:n* = 13:30. This is the 6-point layout illustrated in Figure 5.2, with the design data given in Table 5.1.

Table 5.1. Design parameters for low-asymmetry CCM devices. The length of the SA section is 25 μm in all devices.

Total cavity length μm	HML Freq- uency, GHz	Fundam'l ML freq., GHz	HML mode spacing, nm	Fabry-Pérot mode spacing, nm	Sub- sectio n ratio	Harmonic No.	*Gain. 1* section μm	*Gain 2* section, μm (inc. SA)	Device marking
620	1943	63	4.846	0.156	1:30	31	20	600	*A*
660	648	59	1.615	0.147	1:10	11	60	600	*BB*
720	324	54	0.808	0.135	1:5	6	120	600	*CCC*
800	194	49	0.485	0.121	1:3	4	200	600	*DDDD*
860	1943	45	4.846	0.113	13:30	43	260	600	*EEEEE*
900	130	43	0.323	0.108	1:2	3	300	600	*FFFFFF*

The above data were calculated using Eq.(3.12) (see Chapter 3) for a wavelength $\lambda = 860$ nm with a group refractive index $n_g = 3.861$, which was inferred from the mode spacing of reference single-section ridge-waveguide lasers of known cavity lengths.

The low-asymmetry CCM devices were laid out in such a way that the length of the longer sub-cavity *(Gain 2)* was kept constant at 600 μm, whilst the length of the shorter one *(Gain 1)* was varied from 300 μm down to 20 μm, resulting in sub-cavity ratios from 1:2 to 1:30 (with design harmonics $M = 3 \div 31$), as specified in Table 5.1. Note that multiplication of the absolute repetition frequency was achieved both by an increased harmonic number through more asymmetric ratios and the reduction of the total cavity length. Interestingly enough, the devices with 1:30 and 13:30 ratios are expected to exhibit the same harmonic mode spacing and modelock

at the same HML frequency despite the different harmonic numbers and cavity lengths. Another reason for including an *m:n* ratio device in this layout was to investigate its performance as a function of ICR type, as will be discussed in Section 9.2.3.

Some of the devices in this layout also had a second ICR positioned at 375 µm from the facet of the *Gain 2* section, with a view to creating a 5:7 ratio within the device cleaved to a 1:2 ratio (marked *FFFFFF* in Table 5.1). This is the twin-ICR configuration illustrated in Figure 5.1(b) and Figure 4.7 and modelled in Figure 4.10(V).

High-asymmetry device layout

The high-asymmetry layout, by contrast, was designed with high-harmonic devices in mind. It is a reduced version of the low-asymmetry layout, with only 3 cleavable ratios, as specified Table 5.2. For device dimensions as in the case above, the 3 cleavage markers are only separated by 20 µm, yet such small variations in the cavity length result in vastly different sub-section ratios and harmonic numbers ($M = 11 \div 31$). Furthermore, the 20 µm separation is comparable to the cleavage inaccuracy ($\pm$ 10 µm) of the facet cleaving process, thus precluding the exact definition of cavity lengths within the $620 \div 640$ µm range. The purpose of this layout, therefore, was to allow for the cleaving of devices on a best effort basis, where no two similar cleavages were guaranteed to produce identical cavity ratios due to the much tighter length tolerances.

Table 5.2. Design parameters for high-asymmetry CCM devices. The length of the SA section is 25 µm in all devices.

Total cavity length µm	HML freq-uency, GHz	Fundam'l ML freq., GHz	HML mode spacing, nm	Fabry-Pérot mode spacing, nm	Sub-section ratio	Harmonic No.	*Gain. 1* section µm	*Gain. 2* section, µm (inc. SA)	Device marking
620	1943	63	4.846	0.156	1:30	31	20	600	*A*
640	972	61	2.423	0.151	1:15	16	40	600	*B-*
660	648	59	1.615	0.147	1:10	11	60	600	*BB*

High-asymmetry 1:*m* devices are more prone to "harmonic snapping" (i.e., deviation from the design harmonic number) due to imprecise cleaving than low-asymmetry ones. Indeed, the length tolerance and its effect on harmonic number can be estimated from the following formula:

$$\Delta M = \frac{\varepsilon(M-1)^2}{\varepsilon(M-1)+1}$$

where M is the design harmonic number, ΔM is the mismatch between the design and actual harmonic numbers, and $\varepsilon = \Delta L / L_2$ is the relative length error measured against the length of the longer sub-cavity, L_2, which is kept constant in this layout.
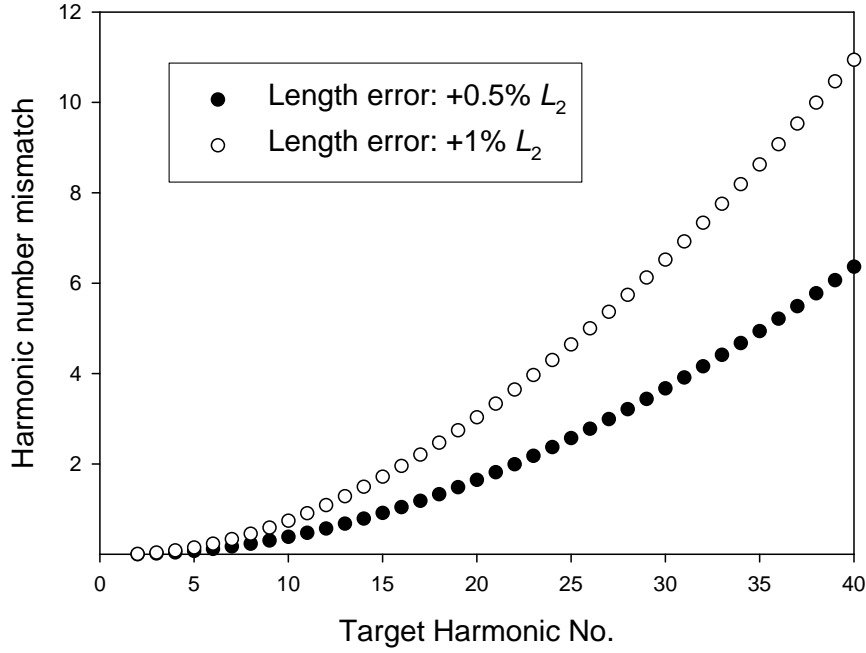
Figure 5.3. Increase in the mismatch between actual and target harmonic numbers for two levels of cleavage error (represented as percentage of the longer *(Gain 2)* sub-cavity length L_2) in 1:*m* ratio CCM devices. As before, different harmonics are achieved by varying the length L_1 of the shorter *(Gain 1)* sub-cavity only, with $L_2 =$ *const*.

The plot of Figure 5.3 illustrates the deviation from the design harmonic number with increasing asymmetry (design harmonic) for two values of length error: $\varepsilon = 0.5\%$ and 1%. For the design parameters of Table 5.2, these would correspond to a random increase of the length of the shorter sub-cavity by only 3 μm and 6 μm, respectively. It can be seen that such a degree of error can result in a deviation from design harmonic numbers in devices cleaved to the 10th harmonic and higher. At the same time, the devices are much less susceptible to variation in the length of the longer sub-cavity *(Gain 2)*, with errors of the order of tens of microns required to shift a harmonic number by one.

As devices cleaved from both low and high-asymmetry layouts are likely to have imprecise cavity lengths resulting in deviation from their design 1:*m* ratios, the

devices can still be "snapped" to the nearest 1:($m \pm 1$) ratio by adjusting the optical lengths of the two sub-cavities. The split contact configuration, as shown in Figure 5.1, allows for the differential pumping of the two active sub-sections to control their carrier-induced refractive indices and, consequently, their optical lengths.

5.1.3. Mask design

The masks for the CCM devices in the above layouts along with some control features and test lasers were designed using the *WaveMaker 4.32* software. The package allows the user to design the layout of semiconductor/optoelectronic components and circuits on a hierarchal basis, whereby the final layout is made up of smaller units, or cells, which are used as building blocks and can be nested and arrayed as required. This way, changes to any of the constituent cells (e.g., alteration of a ridge waveguide width) are automatically reflected in the global layout, without the need to redesign other cells of higher hierarchy or their arrays. Independent of their grouping in cells, different device features can be assigned to different layers, with each layer corresponding to a separate lithography stage.
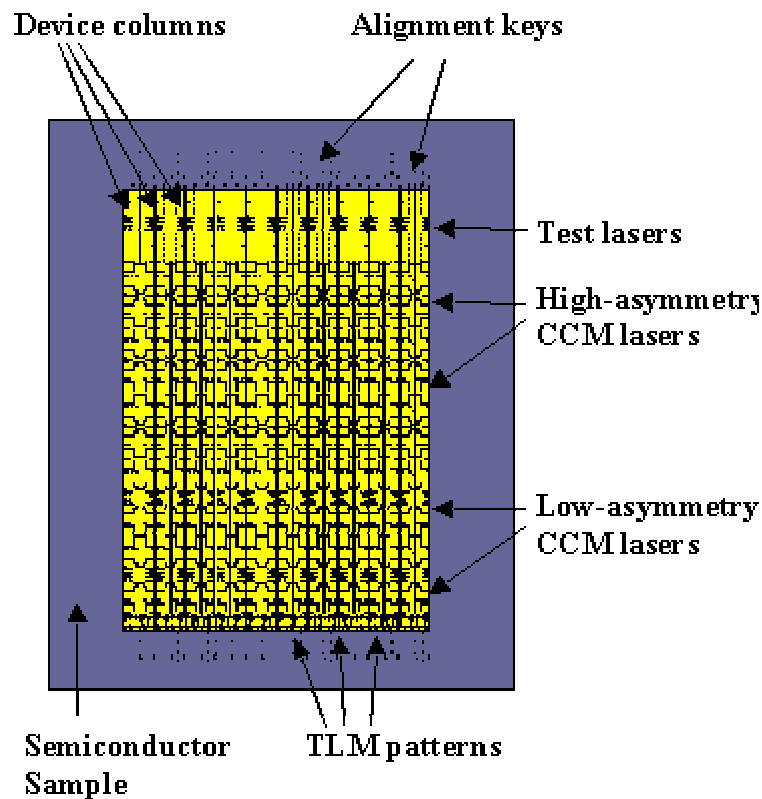
Figure 5.4. Plan view of CCM laser mask layout shown against a typical sample.

The low-asymmetry version of the CCM laser mask for a single device was shown in Figure 5.1(c). For ease of presentation, the image of Figure 5.1(c) overlays masks for all the different layers (lithography stages) used in the fabrication of the device. The cell containing a single device is then replicated and arrayed (with only identical devices in each row), yielding some 120 CCM devices on a ~1.5 cm^2 sample, as shown in Figure 5.4 (here, waveguide ridges run in the vertical direction). Special test features are also added, such as standard ridge-waveguide lasers (with no ICRs in them) to be used as reference devices, and TLM patterns for the electrical characterisation of the semiconductor material and metal contacts (these will be discussed in Chapter 6). The layout of Figure 5.4 also shows the location of the main pattern on a typical sample. The pattern is surrounded by alignment keys, which are used for layer-to-layer registration at various lithography stages.

The *WaveMaker* package stores layout data in the so-called GDSII format, which is interpreted by pattern fractionation software that prepares exposure data for electron beam writers. Beamwriters are used to transfer the pattern data onto chrome mask plates, with one data layer corresponding to one mask plate, or direct onto a resist-coated semiconductor surface. The former method then relies on photolithography to transfer a pattern onto a semiconductor wafer using ultra-violet irradiation of the resist-coated wafer through the mask plate. This approach is suited for large-scale production, where mask plates can be re-used many times to define the same pattern at a minimum cost. The "direct-write" approach, by contrast, allows much greater flexibility in design changes, as digital pattern data are transferred directly onto the wafer surface. At the same time, it is much more expensive on a per-sample basis. It also has much higher resolution capability (several nanometres) than photolithography. E-beam lithography was used for most of the CCM device fabrication in this Project. The key consideration in the choice of lithography was the requirement for the definition of sub-micron ICR features, with the added benefit of design flexibility and an accelerated feedback loop at the design, fabrication and testing stages. The specific aspects of e-beam lithography will be discussed in Chapter 7.

5.2. Intracavity reflector (ICR) design

The ICR design evolved concurrently with iterations of the overall device design. Initial experimental results obtained from the fabricated lasers suggested that the effect of the ICR on device performance was very weak, therefore several increasingly more reflective ICR features were fabricated in order to augment their effect. The ICRs of different types exhibited different performance in devices of different sub-cavity ratios. It is thus appropriate to present the different ICR designs employed and discuss their characteristics.

5.2.1. Shallow-etched single-slot ICR

This is the simplest type of intra-cavity reflector, which consists of a slot, or notch, etched across the waveguide ridge. The term "shallow-etched" implies that the etch depth is less than the depth of the active layer, so that the quantum wells are intact within the etched region. The slot feature thus presents a weak perturbation to the waveguide. The preferred definition of such a slot would be to etch it to the same depth as the waveguide ridge, so that both can be etched together in one step.

Although such a slot does create a compound cavity, the analysis of C^3 lasers as discussed in Section 4.1.2 of Chapter 4 cannot be directly applied in this case. The reason is that the air gap between the two sub-cavities of a C^3 laser is now replaced with a partially etched section of the same waveguide, so the refractive index perturbation is not as drastic as in the C^3 case.

A waveguide model suitable for such a slot feature was developed by the author's fellow Ph.D. student, Bruce Allan, who kindly carried out numerical simulations for the specific structures used in this Project. The model [1] was based on coupled-mode theory and employed a mode matching technique to examine the behaviour of a step discontinuity in a multi-layer waveguide. Light in a guided mode is scattered by a step discontinuity into a finite number of radiation modes, as well as transmitted and reflected guided modes, as illustrated in Figure 5.5(a). The model uses a step-down discontinuity (waveguide 1 / waveguide 2) and a step-up discontinuity (waveguide 2 / waveguide 3) to form a notch in a multi-layer waveguide, which is shown in Figure 5.5(b) [2]. An arbitrary number of layers can

be used in this model. It is important that the cover and substrate refractive indices are always different, and that there is a guided mode in the etched waveguide section.
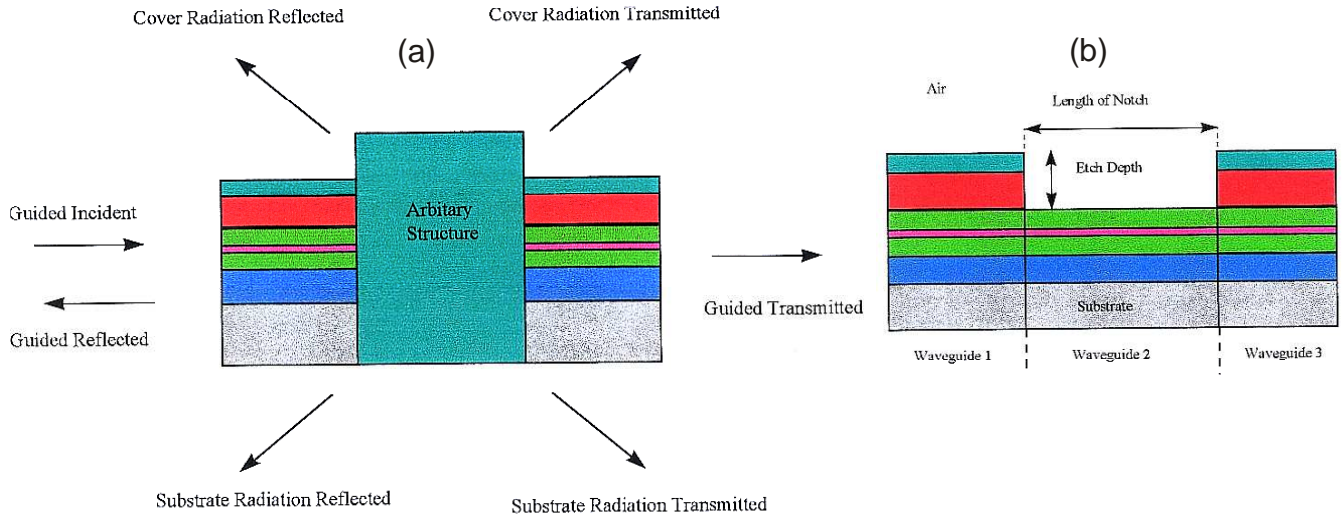
Figure 5.5. (a) Modes considered in model [2] and **(b)** representation of the notch structure. See Section 6.1.2 (Chapter 6) for a description of the waveguide structure used.
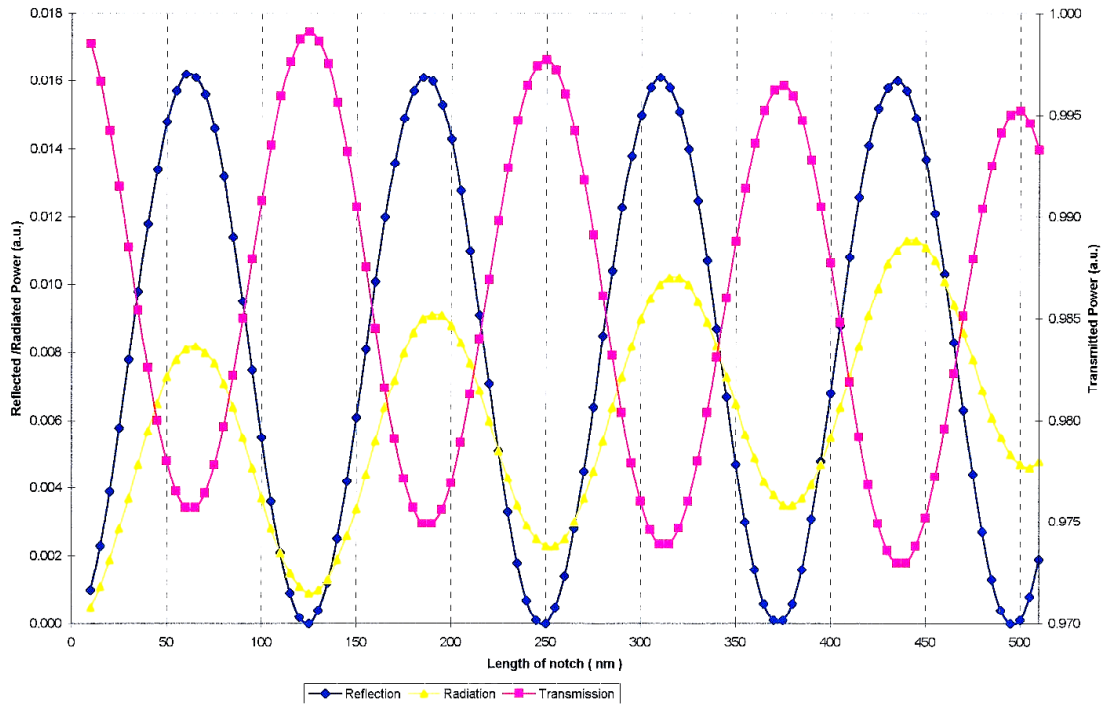
Figure 5.6. Reflected, transmitted and radiated power as a function of notch width.

The modelling results showing the dependence of the reflected, transmitted and radiated power on slot width for the material structures described in Chapter 6 are shown in Figure 5.6. As expected, the dependence is periodic, with a period approximately equal to half the wavelength in the semiconductor material (GaAs

104

refractive index $n \approx 3.5$). It can be seen that a variation of about 60 nm in the slot width results in a minimum to maximum shift in reflected power. To define the feature's reflectivity reliably, one would need to control the slot width to within several nanometres. Such a tight size tolerance is very difficult to meet technologically, therefore a large spread in performance was to be expected from shallow-etched single-slot CCM devices.

To allow the shallow-slot feature to be defined simultaneously with the waveguide ridge, the slot was etched inside a lateral bow-tie extension to the waveguide (see the SEM photograph of Figure 7.6). The slot dimensions were 0.3 µm (gap width) by 25 µm (etch length across the 3 µm waveguide). The model [1] predicted sub-1% values for the slot's reflectivity, of the order of $R \sim 0.001$.

5.2.2. Short-grating ICR

The ICR reflectivity value $R_{ICR} \sim 0.001$ achievable with a single shallow-etched slot was found to affect the modal pattern of a CCM laser only marginally, therefore an attempt was made to create a more reflective ICR feature by cascading the single slots to form a retro-reflecting Bragg diffraction grating.

In waveguides, a Bragg resonance occurs when

$$\Lambda = m \frac{\lambda_0}{2n_{eff}},$$
(5.2)

where Λ is the grating period, λ_0 is the wavelength of the guided light in a vacuum, n_{eff} is the effective refractive index of the corrugated waveguide, and $m = 1, 2, 3\ldots$ is the diffraction order. The grating effect is imparted by periodic corrugation of the waveguide, which can be achieved by etching groove features into the surface layers. A well-developed theory of periodic waveguides based on coupled-mode formalism [3, 4] describes the corrugation in terms of the variation $\Delta n = n_u - n_e$ of the refractive indices in the unetched (n_u) and etched (n_e) regions of the waveguide. Then the effective index n_{eff} of Eq. (5.2) and the grating's coupling strength κ can be written as

$$n_{eff} = \frac{2}{1/n_u + 1/n_e}; \quad \kappa = \frac{\pi n_{eff}}{\lambda_0} \Delta n.$$
(5.3)

The coupling strength κ is then used to approximate the amplitude transmittance t and reflectance r for a grating length L:

$$t = \frac{1}{\cosh \kappa L}; \quad r = \tanh \kappa L. \tag{5.4}$$

The corresponding intensity transmittivity T, reflectivity R and grating bandwidth $\Delta\lambda$ (reflectance peak width) are given by

$$T = t^2; \quad R = r^2; \quad \Delta\lambda = \frac{3\lambda_0^2}{2\pi n_{eff} L}. \tag{5.5}$$

To design a diffraction grating for use as an ICR, one needs to take into account several requirements. First, its bandwidth must be sufficiently broad to provide near-equal reflectivity to all frequency components within the lasing spectrum. Second, it must be relatively short so that it can still be considered as a near-singular perturbation of the cavity. At the same time, it must not be etched so deep as to destroy the waveguide confinement and create too high a loss. Furthermore, the equations above assume that the grating corrugation is relatively weak so that the etched sections of the waveguide still support a guided mode.

For a specific GaAs/AlGaAs waveguide structure and a lasing wavelength $\lambda_0 = 865$ nm, a mode-solver was used to find the fundamental modes in the unetched and etched waveguides with their respective refractive indices n_u and n_e, assuming an etch depth that is the same as the height of the waveguide ridge (0.75 µm). The data were then used with Eqs.(5.2)-(5.5) to model a third-order [$m = 3$ in Eq.(5.2)] diffraction grating, as the small feature sizes of first and second order gratings in a semiconductor are very difficult to define technologically. With a third-order period $\Lambda = 388$ nm and a length of 13 periods (4.8 µm), the designed grating was to provide a reflectivity $R = 73\%$ across a bandwidth $\Delta\lambda = 22$ nm.

Unfortunately, the fabricated gratings had virtually no effect on the behaviour of CCM devices, which is thought to be due to the under-etching of the grating grooves, resulting in a different value of the effective index that that assumed in Eq.(5.3).

5.2.3. Deep-etched ICRs

The experimentally realised shallow-etched ICR features having failed to deliver the high reflectivities required for the CCM effect, despite the predictions of the modelling results, a natural way forward was to try to increase the etch depth of

ICR features, even though this would entail a number of difficulties. Firstly, a special etch process would have to be developed for the deep etching of sub-micron slot features. Secondly, the increased etch depth would require additional patterning and etch steps, thus further complicating the fabrication process. Finally, the notch and grating models described above would not be applicable, as they assume the existence of a guided mode inside the etched regions.
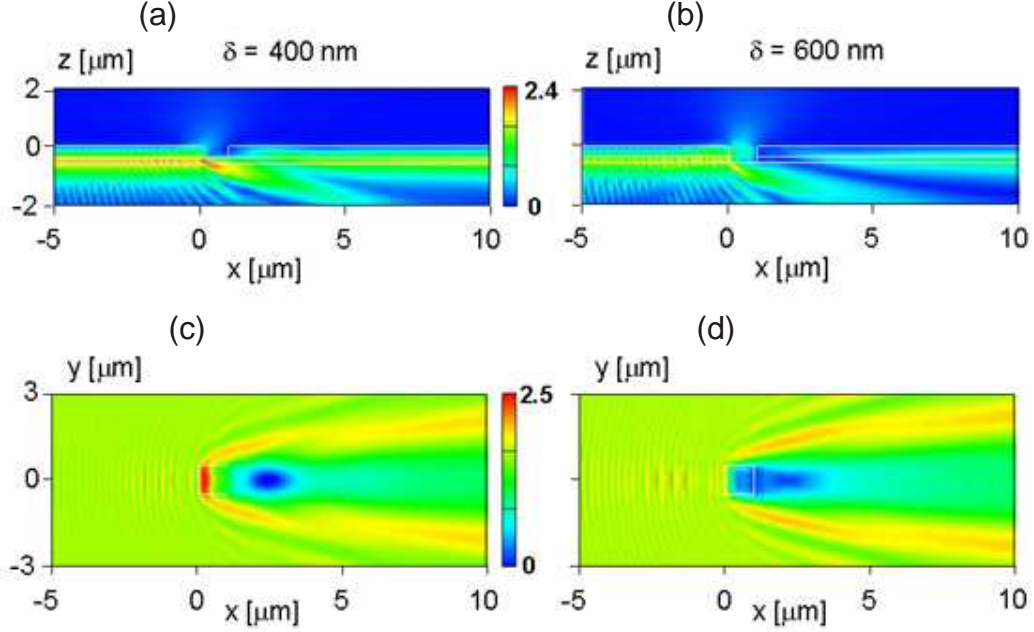
Figure 5.7. Cross-sectional **(a,b)** and plan views **(c,d)** of optical field amplitude distributions created by a shallow **(a,c)** and deep-etched **(b,d)** slot feature of $0.5 \times 0.5 \ \mu m^2$ in a slab InGaAsP/InP waveguide (after [5]).

Some modelling work on shallow and deep-etched slot features was carried out in Ref.[6] using the Green's tensor technique. The fully vectorial model can provide a self-consistent and accurate solution for the electric field distribution near a waveguide singularity. The results of a full 3D modelling [5, 6] of a slab InGaAsP/InP waveguide perturbed by a slot feature of two different etch depths are given in Figure 5.7. It can be seen that compared to the shallow-etched feature of graphs **(a,c),** the deep-etched slot **(b,d)** penetrating the waveguide core presents a much stronger perturbation, with the associated scattering, radiation and reflection, and with the fundamental mode re-establishing itself in the waveguide over a much longer distance. However, Ref. [6] does not consider the case of a slot in a ridge waveguide nor provides formulae for quantifying the feature's reflectivity.

5.2.4. Photonic Band-gap (PBG) structures

Deep-etched perturbations can also be described by the mathematical apparatus usually applied to a rather different class of structures called photonic crystals. Photonic crystals are formed by artificially created lattices in one, two, or all three dimensions and can be used to engineer unique waveguiding and wavelength-selective properties. In particular, they are capable of creating photonic bandgaps (PBG) to selectively suppress or enhance the propagation of light within a specific wavelength band.

For the case in question, a series of periodic deep-etched features can be thought of as a 1D photonic crystal, with the light confinement in the vertical and lateral planes provided by the host semiconductor and the shallow-etched waveguide ridge, respectively. Indeed, such structures have been successfully used to create waveguide microcavities [7, 8] and short-cavity DBR lasers [9].
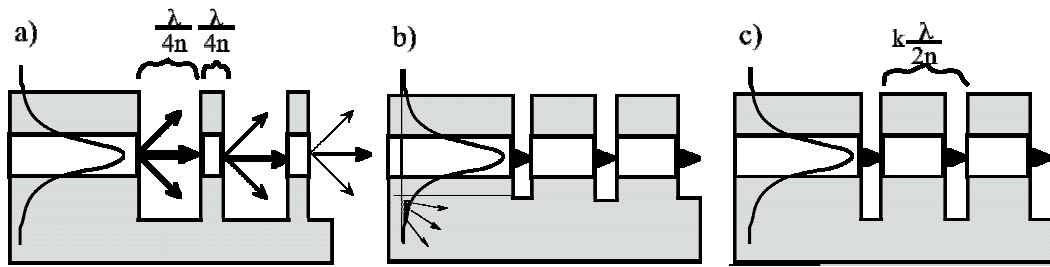
Figure 5.8. (a) A deep-etched waveguide, designed according to "conventional wisdom" for maximum reflectivity with the high and low index layers $\lambda/4n$ thick. This configuration suffers from diffraction losses, because light is not guided in the low index region and diffracts out of the waveguide plane. **(b)** Another source of loss is an insufficient etch depth. If the microstructure is not etched deep enough, the tail of its guided mode does not interact with the microstructure and radiates away. **(c)** If the air-gaps are small and etched deep enough, there is very little loss so long as the fundamental criterion for obtaining photonic bandgap effects, i.e., the Bragg condition, is fulfilled by designing the optical length of the structure as an integer multiple of half-wavelengths (after [10]).

When designing deep-etched PBG structures, conventional wisdom would dictate adherence to the "$\lambda/4$" rule used, e.g., in the design of multilayer mirrors, that requires the optical path in both the low (etched) and the high (unetched) index regions to be a quarter-wavelength long for maximum interaction. Light is then only confined within the semiconductor but is unguided while travelling through the air gaps, so diffraction losses and scattering into the third dimension (i.e., out of the

plane of the waveguide) are inevitable. This configuration is illustrated in Figure 5.8(a).

The losses can be minimised by increasing the fill-factor of the semiconductor, i.e., creating a semiconductor-rich 1D PBG lattice. The principle of this approach is that light can "hop" across the narrow air gaps without suffering excessive loss, whilst still experiencing the full refractive index contrast between the semiconductor and air. The author's colleagues Dr T. F. Krauss and Prof R. M. De La Rue have expended considerable effort into the modelling and fabrication of intra-waveguide PBG structures [7, 8, 10]. One of the findings was the conclusion that the etch depth was critical and that, surprisingly, PBG structures not etched deep enough experienced a higher radiation loss than those etched all the way through the waveguide core [10], as explained in Figure 5.8(b). It was shown that, contrary to the "conventional wisdom $\lambda/4$" rule, an etched photonic structure having a high semiconductor fill factor supported the low-loss guiding of light while acting as a highly reflective mirror to those wavelengths that fell within the structure's stopband. The "$\lambda/4$" rule is then superseded by the generic Bragg condition that the optical path length of each individual semiconductor-air cell be a multiple of half-wavelengths, which is illustrated in Figure 5.8(c).

The 1D transfer-matrix routine, derived from the multilayer stack theory [4, 11, 12], has been successfully used to estimate the transmission and reflection characteristics of such PBG structures. The method consists in assigning a characteristic matrix M_i to each layer $i = 1 \ldots N$ in a stratified medium of N layers, and then taking the matrix product of all the layer matrices traversed by incident light. The resulting matrix $M = M_1 \cdot M_2 \cdot \ldots \cdot M_N$ contains the cumulative effect of the whole layer stack and, when applied to the input electromagnetic field vector, can be used to obtain the stack's reflection and transmission characteristics.

In terms of periodic PBG microstructures etched into a semiconductor waveguide, the above definition would take on the following meaning. Matrix M_1 represents the initial section of the semiconductor waveguide with its characteristic length (measured along the direction of wave propagation) and refractive index; matrix M_2 represents the initial air gap, also with its characteristic length and refractive index. Their product $M^{(1)} = M_1 \cdot M_2$ represents the effect of the first PBG

period, while the matrix $M^{(N)} = [M^{(1)}]^N$ accounts for the combined effect of N periods.

Computational code implementing the above procedure was written using the *MatLab* and *Derive* packages. The code allowed the reflectivity of an arbitrary stack of periodic, infinitely deep PBG features to be computed. Initially, the lengths of the unetched and etched sections of the waveguide, as well as that of the PBG period, were established from the half-wavelength Bragg condition, as explained earlier [see Figure 5.8(c)]:

$$a\lambda_0 n_u + b\lambda_0 = k\frac{\lambda_0}{2}, \tag{5.6}$$

where k is an integer, and a and b are the length fractions occupied by the semiconductor and air sections, respectively; the index of the air gap is assumed to be unity; other parameters as in Eqs.(5.2)-(5.3). For a semiconductor-rich PBG lattice, a semiconductor fill-factor of 80%, was chosen, with $a / b = 80\% / 20\% = 4$. Equation (5.6) is then easily solved to find the geometrical lengths $L_a = a\lambda_0$ and $L_b = b\lambda_0$ of the semiconductor and air sections, respectively. The bar chart representing the length of each section, and their sum (total bar height) as the PBG period, is shown in Figure 5.9 for a range of integer values of parameter k. With technological limitations in mind, the shortest manufacturable optical period is 1½ wavelengths ($k = 3$), with $L_a = 361$ nm and $L_b = 90$ nm on a period $L_a + L_b = 451$ nm.

Having established the dimensions of the first period and its characteristic matrix $M^{(1)}$, the matrices can then be cascaded to obtain the stack's reflectivities for any number of periods. The computed data for PBG stacks containing up to 4 periods are plotted Figure 5.10. It can be seen that starting with only two periods, the stack's reflectivity assumes a resonance nature, while the peak reflectivity quickly approaches unity with increasing number of periods. For a PBG structure containing 4 periods (slots), the reflectance bandwidth is still larger than 150 nm, which is more than adequate for supporting the broad modelocked spectrum of a CCM laser.
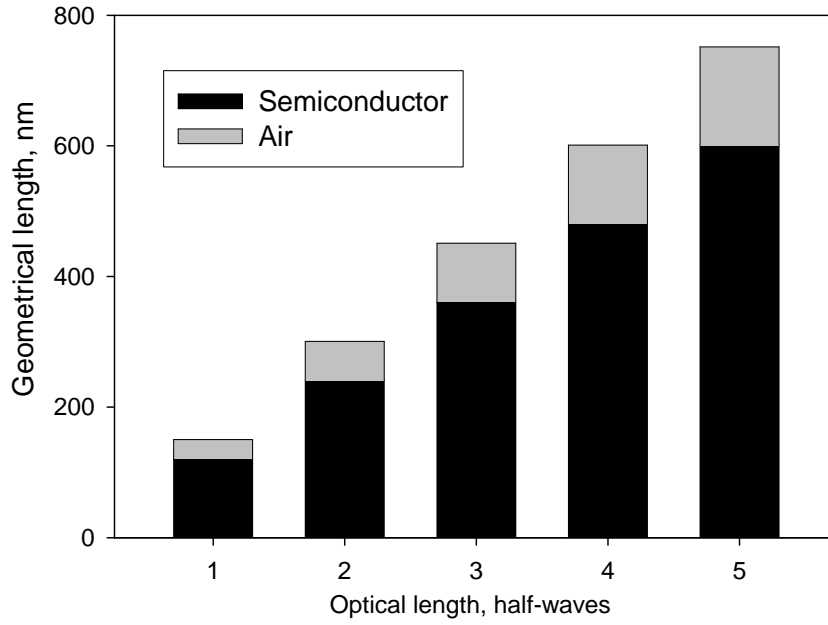
Figure 5.9. Bar chart showing the geometrical lengths of the unetched and etched PBG sections, their sum being the geometrical period, as a function of the optical length (in half-wavelengths) of one PBG period.
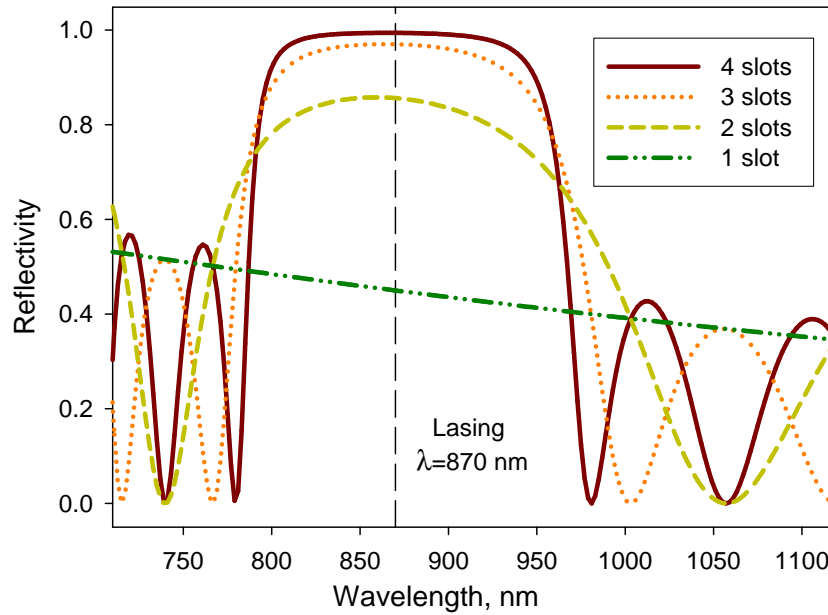
Figure 5.10. Computed reflectivity of PBG stacks as a function of wavelength for different numbers of periods (slots).

PBG microstructures incorporating 1, 2, 3 and 4 slots were included in the final design of CCM masks. As can be seen from Figure 5.10, the resulting reflectivities would be well above the target value of $R = 0.6 - 0.7$ predicted in Figure 4.6. The excess reflectivity created by the high number of slots was a redundancy in case the sizes of the fabricated features might be at variance with the

design ones, as a fabricated structure's period is likely to be defined more precisely than the sizes of its component features. Note that the actual reflectances are likely to be smaller than the computed values because of the scattering of light at the ICR.

Finally, recalling the analysis of C^3 lasers in Chapter 4, one would hope that by employing a periodic PBG structure instead of a single air gap, it should be possible to greatly improve the stability and control of a CC device. The periodic nature of the PBG feature renders it more robust by averaging out the fabrication errors across several slots and thus reduces the variability associated with a one-off etched feature.

5.3. Design of non-linear geometry lasers

While the main focus of the current Project was on the experimental realisation of straight-cavity CCM lasers, some work was also done on bent-waveguide CCM devices. Although no operational devices have been obtained, it may still be beneficial to present a brief summary of the design activity in that direction.

5.3.1. Parallel-cavity lasers

Parallel-cavity CCM devices were briefly mentioned in Sec. 4.1.4 of Chapter 4, with a schematic of the device shown in Figure 4.3(b). The device concept was proposed in a joint paper [13]. The original construction, although somewhat more tolerant to cleaving error, suffers from the limited freedom in changing the relative lengths of the two arms (sub-cavities), which limits the choice of cavity ratios to values close to 1:1. Therefore, the device geometry has been modified to look as shown in Figure 5.11, which is capable of providing cavity ratios from nearly 1:1 to possibly 1:5 (for realistic device lengths). Careful minimisation of the stretch common to both cavities (including the coupler) and sharper bends may allow higher asymmetry ratios to be realised. One obvious drawback of this design is that two adjacent chip sides will have to be cleaved with optical quality, which would make the cleaving and handling of these devices rather difficult.
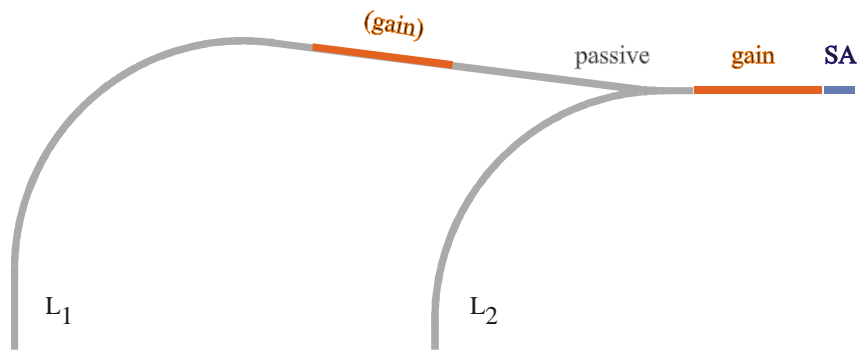
Figure 5.11. Modified geometry parallel-cavity CCM laser.

The curved passive sections of the device as well as the coupler would ideally be made less absorbing through the quantum well intermixing technique. Tapers would have to be used to ensure a smooth transition between shallow-etched straight waveguides and deep-etched curved ones. Part of the (longer) arm can be made active to enable fine optical length control over the cavity ratio by varying the pumping current.

5.3.2. Coupler modelling

Some design activity was undertaken to optimise the coupler for the CCM device described above. Two types of coupler, multimode interference (MMI) and Y-junction, have been considered. A 1x2 MMI coupler comprises an input single-mode waveguide, a widened mode conversion section of an appropriate length, where the single input mode is transformed into a two-lobe intensity profile, and two output waveguides. A Y-junction uses two waveguides branching out at a very small angle ($< 1^o$) to split the optical input in two. There exists a sizeable body of research into the theory and design of both MMI [14-17] and Y-junction [18-20] waveguide splitters. The most commonly used modelling tool is the beam propagation method (BPM).

In this Project, couplers of both MMI and Y-type have been simulated using BPM-based BEAM-Prop software, with examples shown in Figure 5.12 and Figure 5.13. The coupler length is critical for reducing CCM device dimensions, therefore both couplers were optimised for minimum size with tolerable losses. Simulations showed that both the MMI and the Y-junction splitters had similar characteristics for similar lengths, as shown in Figure 5.14, with a minimised length of about

110 - 120 µm. However, due to relative ease of fabrication, the MMI coupler would be the preferred option for CCM devices.
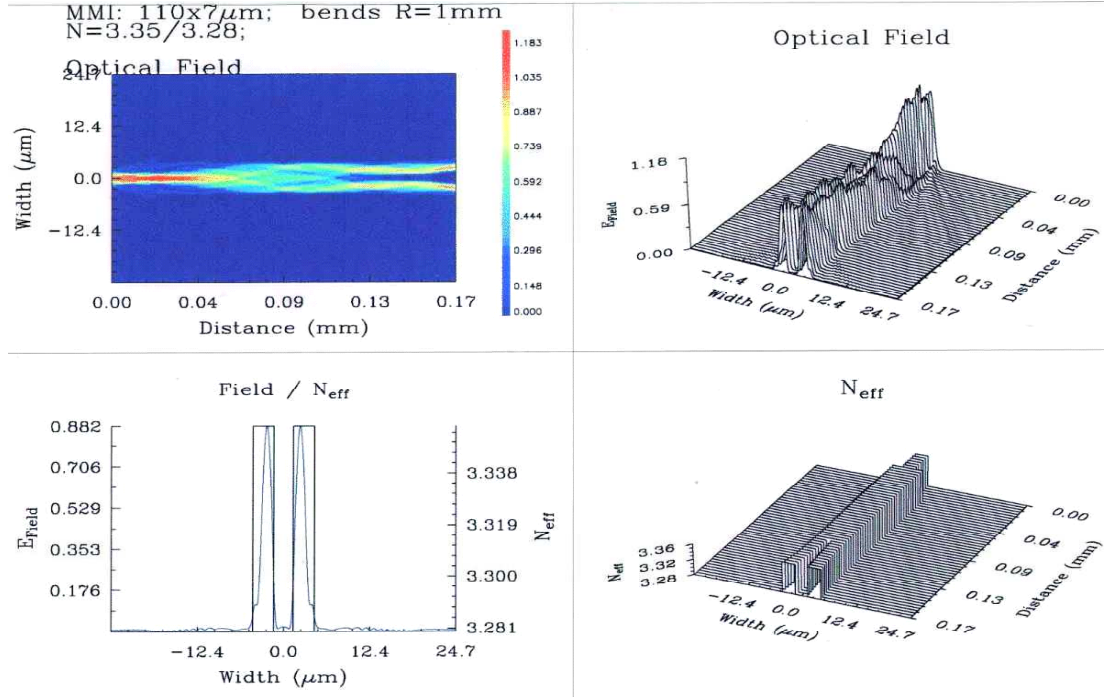
Figure 5.12. BPM simulation results of an MMI coupler. Clockwise from top left: optical field in 2D (planar view), and in 3D; refractive index in 3D, and cross-section of optical field/refr. index at coupler exit.
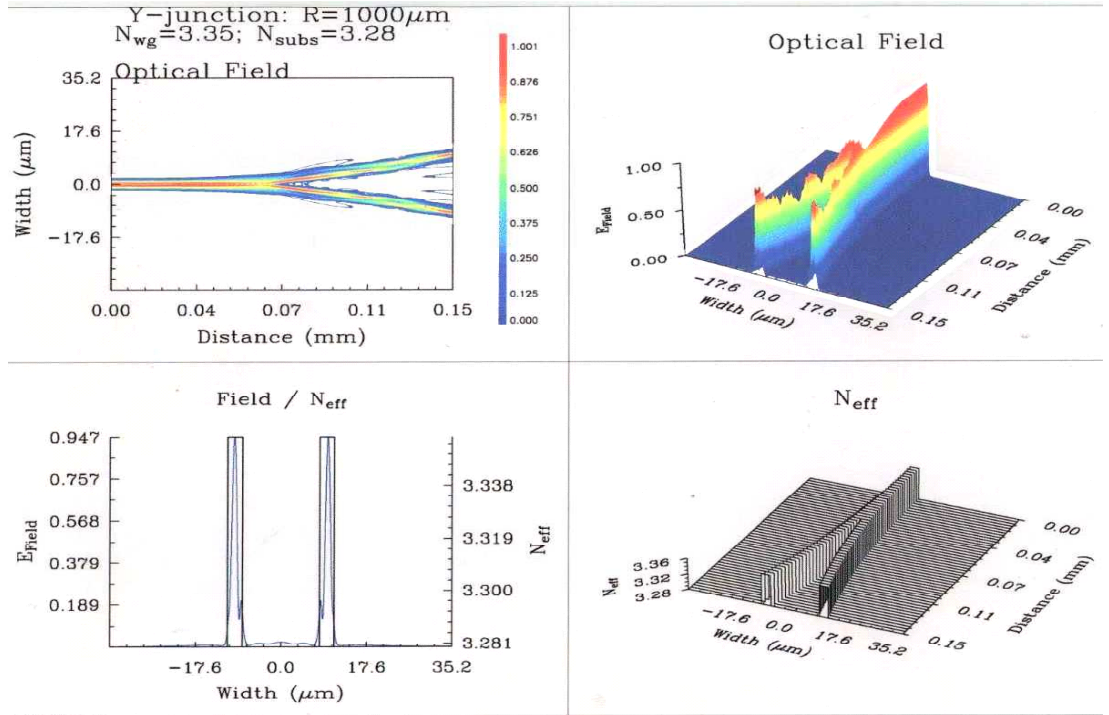
Figure 5.13. BPM simulation results for a Y-junction. Legend as in Figure above.

Normalised Power in 1-to-2 MMI & Y-couplers

MMI coupler: 110 x 7 µm, access bend R = 1500 µm
Y-junction: R = 1000 µm
Refractive index difference Δn = 0.07 (3.35/3.28) was assumed for both couplers
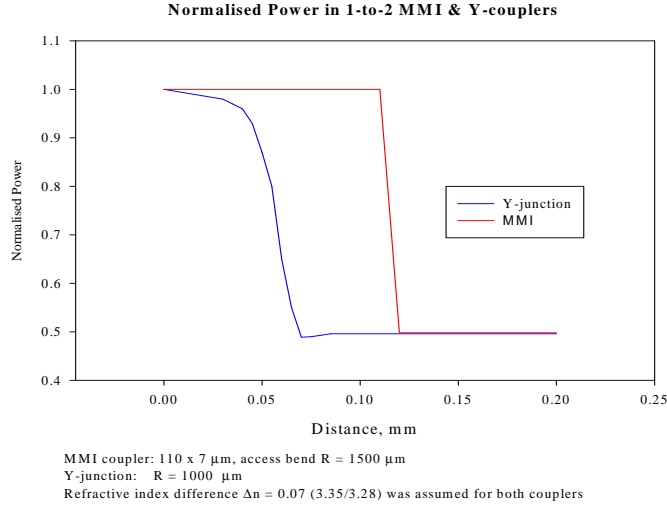
Figure 5.14. Simulated power division per arm for MMI and Y-junction couplers

5.3.3. Design of bent-waveguide lasers

While no parallel cavity CCM lasers have been designed or fabricated, preliminary experimental work was done to develop the technology for non-linear laser cavities. To this end, a test structure incorporating arc waveguide lasers of varying radii was designed. It is shown in Figure 5.15, with the final chip to be quartered using the axes drawn. Each quarter would then produce a set of 4 different arc lasers, which are individually addressable by probing the adjacent metal stripe. It was hoped that, from the threshold data of the 4 lasers, one would be able to infer the waveguide losses associated with each bend radius (100, 200, 300 and 400 µm). The outer ring also contains a device having a Y-junction at one end (two facets) and a conventional facet at the other end. Such a laser, which is, in fact, a 1:1 ratio parallel compound cavity device, would be useful for evaluating the effect of a Y-splitter on the device performance. Furthermore, all devices had a common saturable absorber (SA) section, which, when reverse biased, could be used to attempt modelocking operation.

Furthermore, a dedicated mask, shown in Figure 5.16, was designed for the comparison of the two coupler types (MMI and Y-junction). Upon quartering, the four sub-chips would each contain a parallel cavity device with either an MMI or a Y-coupler. By evaluating the threshold and spectral data from the two, it should be possible to make a comparative analysis of the two coupler types.
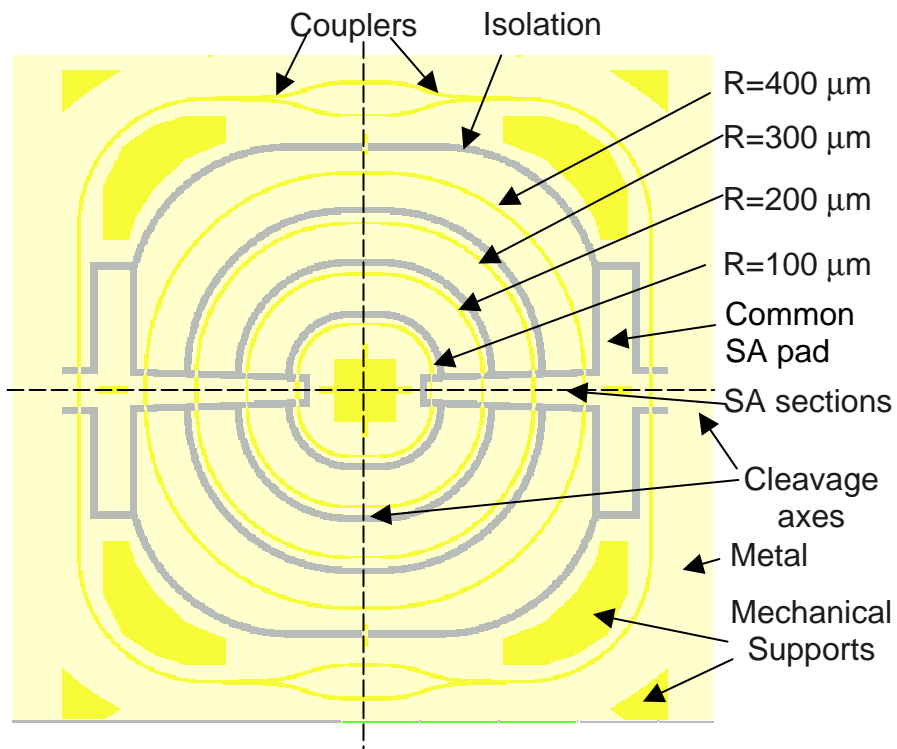
Figure 5.15. Design of test structure incorporating arc lasers of 4 different radii and a Y-junction laser (outer ring).
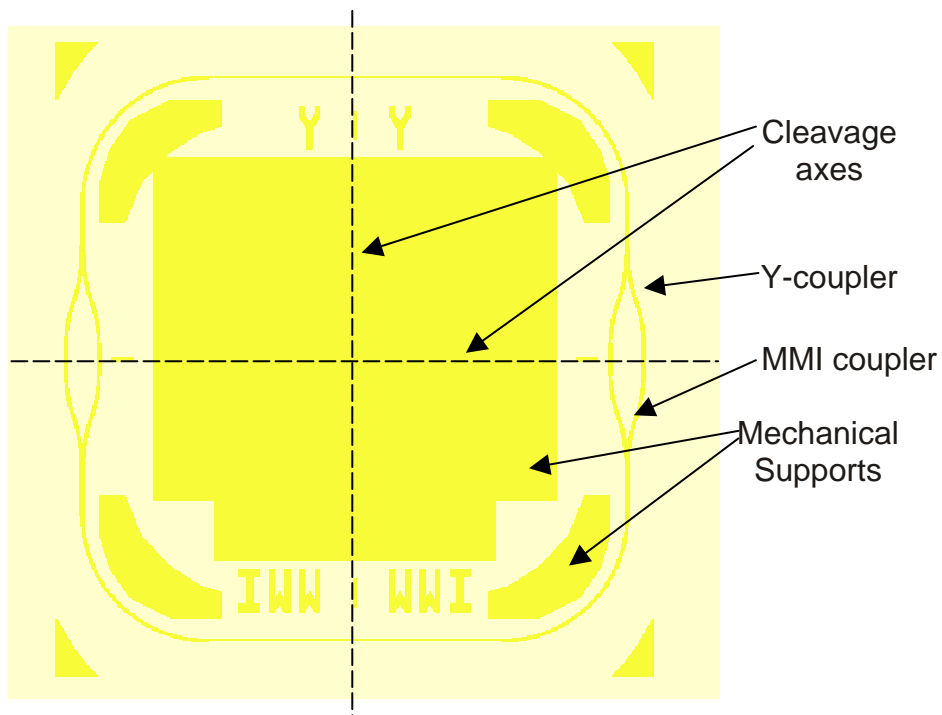
Figure 5.16. Test structure for comparison of MMI and Y-junction couplers.

The test results obtained from these structures were poor and will be discussed in Chapter 9.

5.4. References

[1] B.D. Allan, E.A.Avrutin, J.M.Arnold, R.M. DeLaRue, and J.H. Marsh, "Modelling deep etched optical waveguide step discontinuities," presented at the 1998 International Symposium on Information Theory, CLEO/EUROPE, Glasgow, Scotland, Sep 14-18, 1998.

[2] B.D. Allan, "Notch Model Notes," Dept. of Electronics & Electrical Engineering, University of Glasgow, 1998.

[3] H. Kogelnik, "An introduction to integrated optics," *IEEE Trans. Microw. Th. & Tech.*, vol. 23 (1), pp. 2-16, 1975.

[4] H. Kogelnik, "Theory of optical waveguides (Ch. 2)," in *Guided-Wave Optoelectronics*, T. Tamir, Ed. New York: Springer, 1990, pp. 7-88.

[5] O.J.F. Martin, "Photonics: a 3D scattering defect," http://www.ifh.ee.ethz.ch/~martin/res41.en.html, (Web page).

[6] Michael Paulus and Olivier J. F. Martin, "How to tap an innocent waveguide," *OPTICS EXPRESS*, vol. 12, pp. 644-648, 2001.

[7] T.F. Krauss and R.M. De La Rue, "Optical characterization of waveguide based photonic microstructures," *Appl. Phys. Lett.*, vol. 68 (12), pp. 1613-1615, 1996.

[8] T.F. Krauss, B. Vogele, and R.M. De La Rue, "Waveguide microcavity based photonic microstructures," *IEEE Phot. Tech. Lett.*, vol. 9 (2), pp. 176-178, 1997.

[9] Y. Yuan, T. Brock, P. Bhattacharya, C. Caneau, and R. Bhat, "Edge-emitting lasers with short-period semiconductor/air distributed Bragg reflector mirrors," *IEEE Phot. Tech. Lett.*, vol. 9 (7), pp. 881-883, 1997.

[10] T.F. Krauss, "Photonic Crystals For Integrated Optics," presented at The Summer School on Nanoscale Linear and Non-linear Optics, Erice (Sicily), 2000.

[11] M. Born and E. Wolf, "Wave propagation in a stratified medium," in *Principles of Optics*. Cambridge: Cambridge University Press, 1999, pp. 70-74.

[12] J.M. Bendickson and J.P. Dowling, "Analytic expressions for the electromagnetic mode density in finite, one-dimensional photonic band-gap structures," *Physical Rev. E*, vol. 53 (4), pp. 4107-4121, 1996.

[13] E.A. Avrutin, F. Camacho, A.C. Bryce, C.J. Hamilton, D. Yanson, J.M. Arnold, and J.H. Marsh, "Analysis of monolithic parallel-compound-cavity semiconductor lasers for high brightness, single-frequency, and short-pulse operation," presented at The Conference on Lasers and Electro-Optics (CLEO"99), Baltimore, 24-29 May 1999, paper CTuK55.

[14] A. Ferreras, F. Rodriguez, E. Gymez-Salas, J.L. de Miguel, and F. Hernбndez-Gil, "Useful formulas for multimode interference power splitter/combiner design," *IEEE Phot. Tech. Lett.*, vol. 5, pp. 1224-1227, 1993.

[15] P.A. Besse, M. Bachmann, H. Melchior, L.B. Soldano, and M.K. Smit, "Optical bandwidth and fabrication tolerances of multimode interference couplers," *IEEE J. Lightw. Techn.*, vol. 12, pp. 1004-1009, 1994.

[16] G.M. Berry and S.V. Burke, "Analysis of optical rib self-imaging multimode interference (MMI) waveguide devices using the discrete spectral index method," *Opt. & Q. Elec.*, vol. 27, pp. 921-934, 1995.

[17] L.B. Soldano and E.C.M. Pennings, "Optical multi-mode interference devices based on self-imaging: Principles and applications," *IEEE J. Lightw. Techn.*, vol. 13, pp. 615-627, 1995.

[18] K-Y Liou, U. Koren, E.C. Burrows, M. Young, M.J.R. Martyak, M. Oron, and G. Raybon, "Y-junction power divider in InGaAsP-InP photonic integrated circuits," *IEEE J. Quant. Elec.*, vol. 26, pp. 1376-1383, 1990.

[19] M.L. Osowski, R.M. Lammert, and J.J. Coleman, "A dual-wavelength source with monolithically integrated electroabsorption modulators and Y-junction coupler by selective-area MOCVD," *IEEE Phot. Tech. Lett.*, vol. 9, pp. 158-160, 1997.

[20] R.S. Burton, T.E. Schlesinger, and M. Munowitz, "Imporved Y-junction splitter for ring waveguides," *Elec. Lett.*, vol. 30, pp. 956-957, 1994.

CHAPTER 6.

MATERIAL DESIGN AND CHARACTERISATION

In this Chapter, the design of the semiconductor material used for the fabrication of CCM lasers will be presented along with the modelling results describing its waveguiding properties. Characterisation of the material using broad area lasers and evaluation of its electrical properties using transmission line measurements will also be discussed.

6.1. Material design

Some concepts relating to the material composition and light confinement in laser diodes were introduced in Chapter 3 (Sec. 3.2.1). Here, these concepts will be developed a little further and then applied to specific semiconductor structures.

6.1.1. Semiconductor waveguides

Optical waveguides are commonly formed by layers of dielectric materials and are used to confine and guide light in guided-wave devices and circuits of integrated optics. In classical theory (see, e.g., [1, 2]), an elementary waveguide is represented as a thin film of dielectric material with a high refractive index n_f and a thickness t that is sandwiched between two layers of dielectrics (substrate and cover) with lower refractive indices (n_s and n_c, respectively). A schematic of such a waveguide, also referred to as a slab waveguide, is shown in Figure 6.1. Light can then propagate inside the thin film layer by multiple zig-zag total internal reflections at the two interfaces. A waveguide having specific combinations of n_s, n_f, n_c, and t, may support several guided modes, each with its own propagation constant, effective refractive index n_{eff} and reflection angle ϑ.
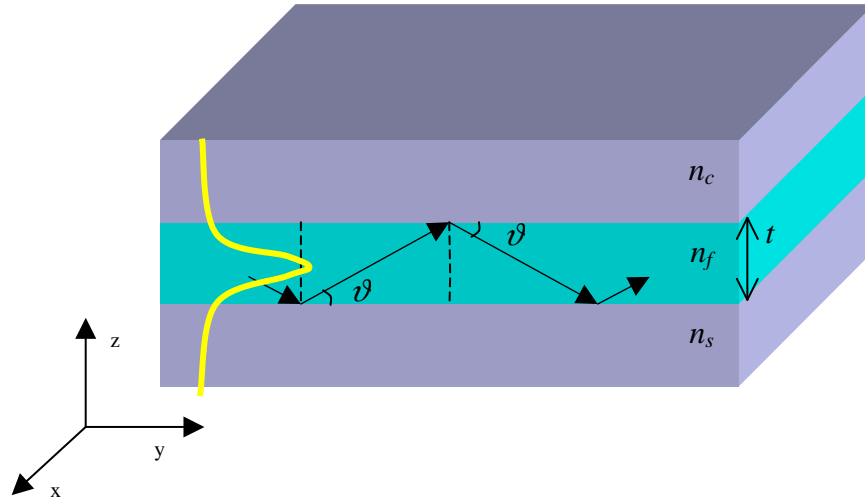
Figure 6.1. Schematic representation of a slab dielectric waveguide.

1D confinement

An epitaxially grown semiconductor laser wafer is a good example of the planar waveguide: on top of a substrate lies a carefully grown stack of epitaxial layers, each with a different refractive index determined by the layer's composition. In the AlGaAs/GaAs material system, the index of the $Al_xGa_{1-x}As$ alloy can be controlled by varying the fraction x of aluminium, with increasing values of x corresponding to lower indices for a given wavelength. There exist semi-empirical models [3, 4] for estimating the refractive index from the material composition. Numerical code was written using model [4] to find the refractive index of $Al_xGa_{1-x}As$ material as a function of wavelength and Al fraction x below the band edge. The plot of Figure 6.2 shows the computed wavelength dependence of the refractive index for several Al concentrations.

The GaAs quantum wells, which provide gain, usually lie in the middle of the higher-index AlGaAs active layer, with the overlap of the guided mode with the gain layers per well expressed by the optical confinement factor Γ_w, as defined in Sec. 3.2.3. The GaAs quantum wells themselves, however, have virtually no effect on the waveguide confinement due to their very small thickness (~10 nm each).

Optical modes of such waveguides can be found numerically by 1D mode solvers that are available commercially, e.g., using the waveguide modelling tool that is part of the *BEAMProp CAD* package by Optiwave Corp. In order to perform a mode search, it requires data on the layer thickness and pre-computed index for each

layer as well as the incident optical field profile. The layer indices were found from model [4]. The computed values for the effective refractive index of the fundamental (zeroth order) mode in the material structures described in Section 6.1.2 were of the of the order of 3.36 – 3.38.
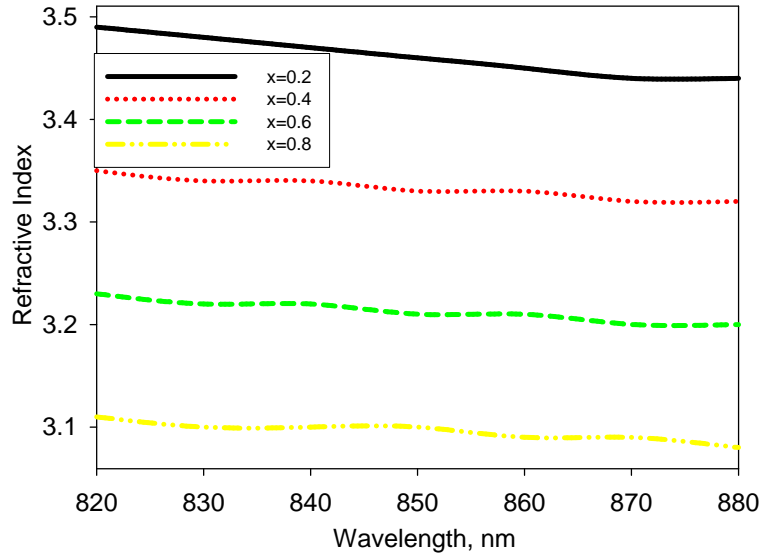
Figure 6.2. Dependence of the refractive index on wavelength for several Al fractions *x* in AlGaAs material (computed using model [4]).

2D confinement

In a slab waveguide, light is only confined in one (vertical) direction; to make a laser one also needs to confine light in a lateral direction. The simplest way of achieving such confinement is to electrically pump a contact stripe along the cavity, with light generated only in underlying areas. This is called gain guiding, as light propagation is defined by the geometry of the electrical contact that provides gain. It is used primarily in broad-area and oxide-stripe lasers, with a contact stripe often tens of microns wide. A schematic of an oxide-stripe laser device is shown in Figure 6.3(a).

This type of confinement is rather weak and fails to suppress the appearance of multiple lateral modes. The emergence of lateral modes with increasing stripe width in a typical broad-area laser is illustrated in Figure 6.3(b) [5]. Such lasers are also prone to filamentation, i.e., lasing in several self-organised narrow channels, or filaments.

Another type of 2D confinement, known as index guiding, is obtained by spatially modifying the refractive index of the material to create a waveguide in the lateral sense. A common way of doing this is by partially etching areas of the planar semiconductor waveguide to form a ridge structure, as illustrated in Figure 6.4. By varying the ridge width and depth, the degree of lateral confinement can be controlled and the lateral waveguide engineered to support only a single (fundamental) guided mode.
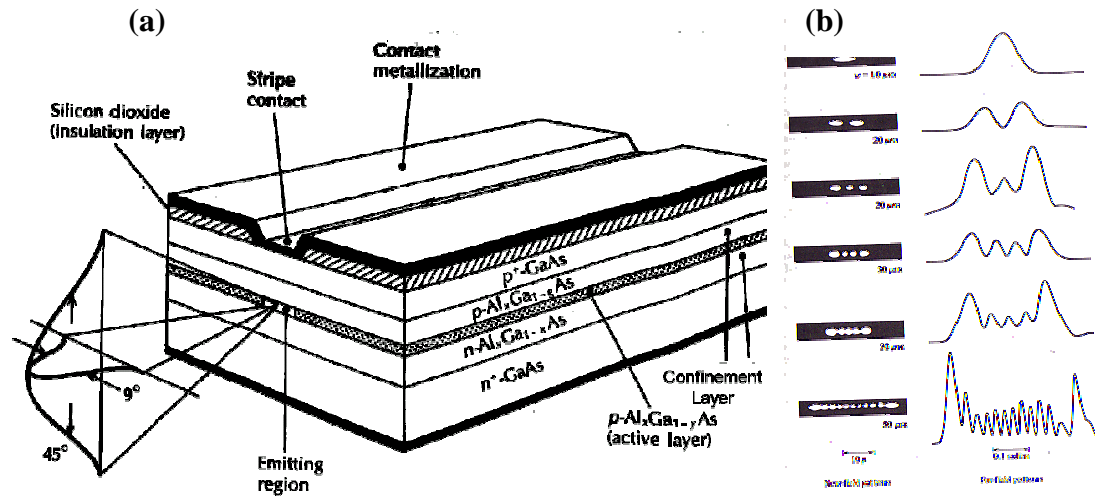
Figure 6.3. (a) Schematic of an oxide-stripe laser.
(b) Near-field (left) and far-field (right) patterns showing the emergence and evolution of lateral modes as a function of stripe width (after [5]).
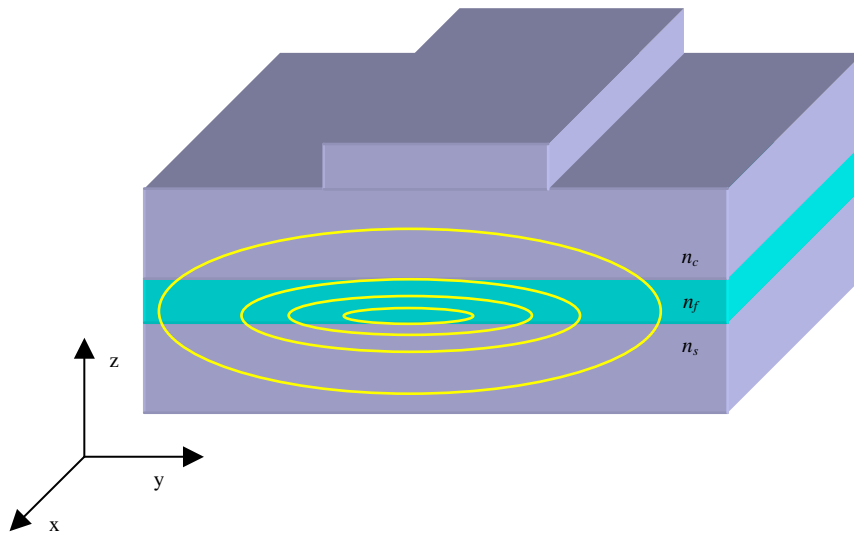
Figure 6.4. Schematic of 2D confinement of light by etching a ridge structure.

Such waveguides can be modelled using 2D mode solvers, which can find optical modes supported by both the vertical (as-grown) and lateral (ridge)

waveguides. Two software packages were used: *BEAMProp CAD* for Windows and *F-Wave* for Macintosh, with both producing similar results for the structures studied.

6.1.2. Description of GaAs/AlGaAs material

GaAs/AlGaAs double-quantum-well (DQW) separate confinement heterostructure (SCH) material of two different designs has been used within this Project. The material was supplied by the EPSRC National Centre for III-V Technologies at the University of Sheffield. Wafers of the first type, coded QT1147, had a "wide waveguide" design, with relatively thick active and cladding layers. The material was designed with high-power applications in mind and also with a view to reducing the vertical far field to improve fibre coupling efficiency. Material of the second type, QT1243 (and its replica QT1269), had a more conventional design commonly used by the Optoelectronics Research Group at the University of Glasgow. The material structures for the QT1147 and QT1243 designs are given in Table 6.1 and Table 6.2, respectively. A comparison of their refractive index profiles, shown in Figure 6.5, illustrates the differences both in the waveguide widths and depths. The computed normalised 1D intensity profiles of the fundamental TE mode for both structures are plotted in Figure 6.6 [6].
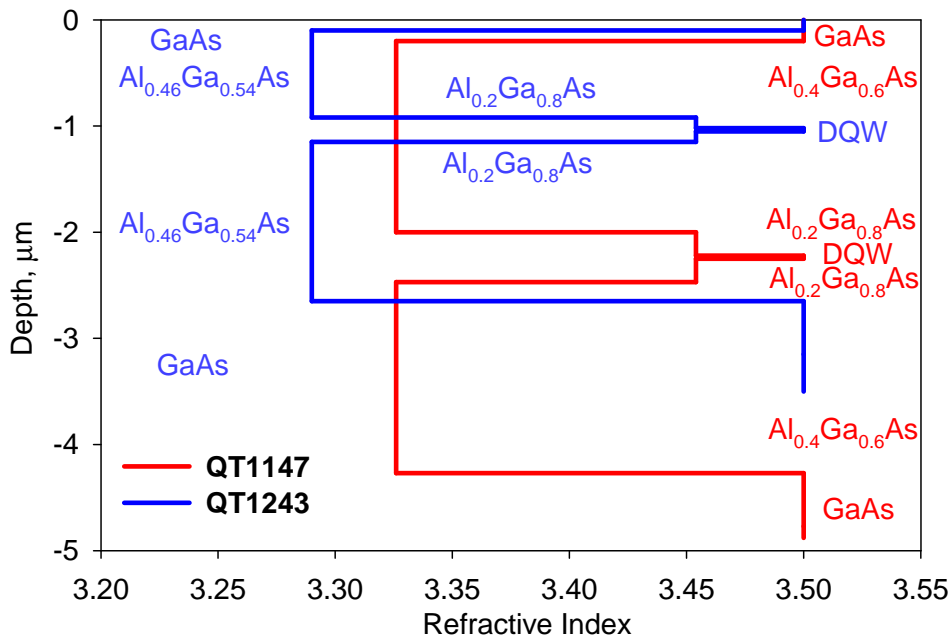
Figure 6.5. Refractive index profiles as a function of position below the surface for the QT1147 (red) and QT1243 (blue) GaAs/AlGaAs DQW SCH laser structures.

Table 6.1. QT1147 GaAs/AlGaAs DQW SCH Laser Structure.

Material	Thickness	Doping
GaAs	0.2 μm	p+
Al0.40	1.8 μm	p
Al0.20	0.22 μm	undoped
GaAs QW	100 Å	undoped
Al0.20	100 Å	undoped
GaAs QW	100 Å	undoped
Al0.20	0.22 μm	undoped
Al0.40	1.8 μm	n
GaAs	0.5 μm	n+
Si doped GaAs substrate 3 deg off (100) to (110)		n+

Table 6.2. QT1243/QT1269 GaAs/AlGaAs DQW SCH Laser Structure.

Material	Thickness	Doping
GaAs	0.1 μm	p+
Al0.46	0.82 μm	p
Al0.2	0.1 μm	Undoped
GaAs QW	100 Å	Undoped
Al0.2	100 Å	Undoped
GaAs QW	100 Å	Undoped
Al0.2	0.1 μm	Undoped
Al0.46	1.5 μm	n
GaAs	0.5 μm	n
Si doped GaAs substrate 3 deg off (100) to (110)		Si doped
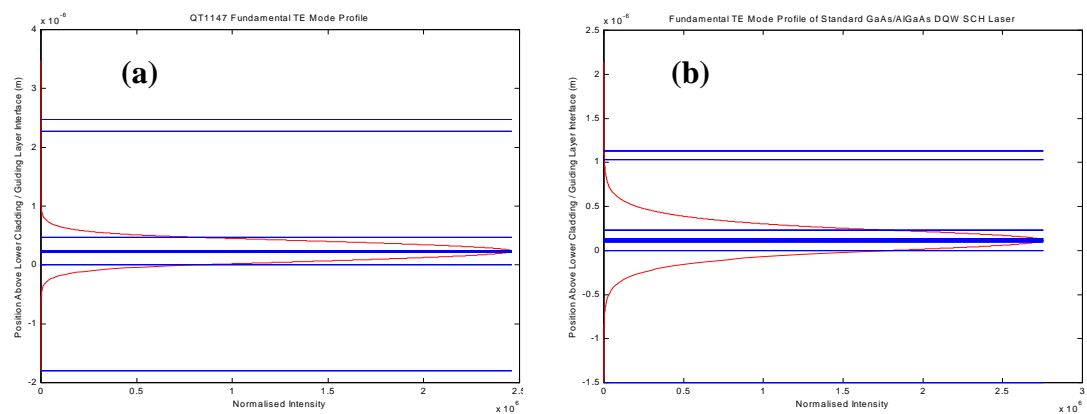
Figure 6.6. Fundamental TE mode profiles for the QT1147 **(a)** and QT1243 **(b)** GaAs/AlGaAs DQW SCH laser structures with layer interfaces indicated. The origin of the ordinate axis lies at the interface of the guiding layer with the lower cladding. Intensity is normalised such that integrated intensity is equal to unity [6].

For the QT1147 structure, the overlap factors calculated from the data of Figure 6.6(a) are $n_w\Gamma_w = 0.049$ and $\Gamma_{clad} = 0.139$. These are the overlap integrals with the DQW active layers and the non-guiding highly doped layers, respectively, and $n_w = 2$ is the number of quantum wells. For a low threshold current and a high external quantum efficiency, Γ_w should be as large as possible (large overlap of the carrier population with the optical field), while Γ_{clad} should be as small as possible (to reduce the overlap with the dopants and hence reduce the free carrier absorption).

To estimate the loss coefficient α, a similar analysis to that of Ref.[7] may be performed. Assuming negligible scattering losses at all heterointerfaces, and neglecting free carrier absorption in the intrinsic guiding layers either side of the QWs, α is given by:

$$\alpha = n_w\Gamma_w\alpha_w + \Gamma_{clad}\alpha_{clad} \qquad (6.1)$$

Here, α_w is the free carrier absorption loss in the QW active layer and at threshold is ~50 cm^{-1}, while α_{clad} is the free carrier absorption loss in the cladding layers and for a doping concentration of ~10^{18}/cm^3 is ~10 cm^{-1}. It should be noted that the carrier concentrations in the intrinsic confinement layers may be significant, especially for a step-like SCH, but that any free-carrier absorption associated with these carriers has been neglected in Eq.(6.1). One may then estimate α for the QT1147 GaAs/AlGaAs DQW SCH laser structure to be approximately 4 cm^{-1}.

The calculated overlap factors for the QT1243 structure are $n_w\Gamma_w = 0.055$ and $\Gamma_{clad} = 0.445$ [see Figure 6.6(b)]. These values compare with $n_w\Gamma_w = 0.049$ and $\Gamma_{clad} = 0.139$ for the QT1147 laser structure. Clearly, Γ_{clad} for the QT1147 wider waveguide structure is approximately a third of Γ_{clad} for the QT1243 structure. This is to be expected since the optical mode is better confined in the wider waveguide layer and has a smaller overlap with the cladding layers. Correspondingly, $n_w\Gamma_w$ for the QT1147 wider waveguide structure is marginally smaller than $n_w\Gamma_w$ for the QT1243 structure, as the peak intensity in the QT1147 structure is higher. From Eq.(6.1) it is possible to estimate the loss coefficient for QT1243 to be 7 cm^{-1}.

Ridge waveguides, with a width of 3 μm in both structures, were then modelled using 2D mode solvers. For the QT1147 material, waveguide ridges must be etched to a depth of 1.6 μm to provide sufficient lateral confinement for the optical field due to the thick upper cladding and wider guiding layer. For the QT1243 material, an etch depth of only 0.75 μm was required to achieve the guiding of a single lateral mode. The number of modes found by the 2D mode-solver for several etch depths in QT1243 is plotted in Figure 6.7. Due to the practical difficulty with the deep etching of QT1147 and metallisation of the high sidewalls, the QT1243 material and its repeat growth QT1269 were used for the fabrication of all but the first three generations of CCM lasers. The broad-area lasers used for the external cavity experiments of Chapter 10, however, were fabricated from the QT1147 wafer. The reduced far field of the QT1147 material was thought to be more appropriate for the coupling of light from and into the fabricated lasers in an external cavity configuration.
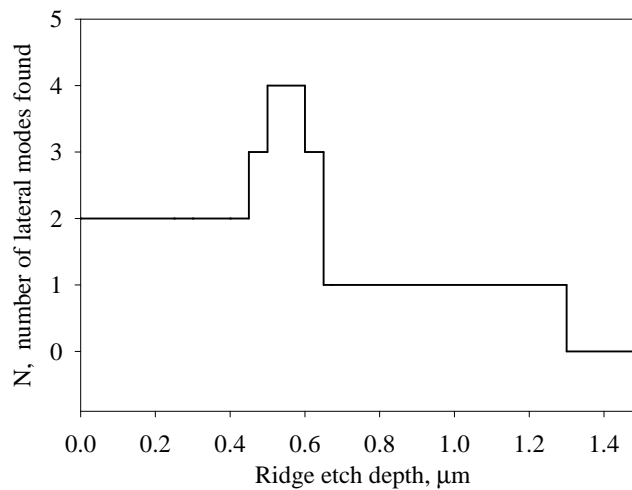
Figure 6.7. The number of lateral modes supported by a 3 μm wide ridge waveguide etched into the QT1243 material as a function of etch depth.

6.2. Material characterisation

Prior to using the above semiconductor materials to make CCM devices, it was important to ascertain the material quality and obtain an estimate for the expected performance of lasers that would be fabricated from this material. This was done both optically and electrically, i.e., by evaluating the performance of test broad-

area lasers and analysing the sheet resistance of the material and the metal contacts formed thereon.

6.2.1. Broad area laser analysis

A common way of assessing material quality is by fabricating and testing broad-area lasers. Indeed, broad-area devices are the simplest type of laser diode, as they do not require any etching of semiconductor material. They can be fabricated simply by defining metal contact stripes on the semiconductor surface, or by depositing a layer of insulator (silica) and etching contact window stripes followed by blanket metallisation. In the latter case, such devices are usually referred to as oxide-stripe lasers, with the device geometry illustrated in Figure 6.3(a). In this section, a brief theory [6, 8] for analysing the test data obtained from broad-area lasers is presented.

Theory

The approximate expression for the threshold current density J_{th} of broad-area QW lasers used here was originally applied in Ref.[9] and is given by:

$$J_{th} = J_{\infty} \cdot \exp\left(\frac{L_0}{L}\right)$$

(6.2)

where J_{∞} is the threshold current density for an infinite cavity length laser and is found from:

$$J_{\infty} = \frac{n_w J_t}{\eta_{inj}} \exp\left(\frac{\alpha}{n_w \Gamma_w G_0}\right)$$

(6.3)

and

$$L_0 = \frac{\ln(1/R)}{n_w \Gamma_w G_0}$$

(6.4)

In the above equations, n_w is the number of quantum wells, Γ_w is the optical confinement factor per well, J_t is the transparency current density per well, α is the loss coefficient, G_0 is the QW gain parameter as defined originally in Ref.[10], and R is the reflectivity of the laser facets. η_{inj} is an "injection efficiency", which is defined as the fraction of the total carriers injected into the laser that recombine in

the active layer. In Ref.[9], it is further assumed that all carriers recombining in the active layer do so radiatively, i.e., the analysis assumes that no non-radiative recombination takes place in the active layer. From Eq.(6.2) we then have

$$\ln(J_{th}) = \frac{L_0}{L} + \ln(J_\infty) \tag{6.5}$$

i.e., by plotting $\ln(J_{th})$ as a function of $1/L$ one can determine L_0 (and hence G_0) and J_∞ from the gradient and the intercept, respectively.

In the same model (i.e., assuming that a fixed proportion η_{inj} of the total carriers injected into the laser recombine in the active layer), the external quantum efficiency η_{ext} obtained from the slope of the light-current (L-I) curve above threshold is given by:

$$\eta_{ext} = \eta_{inj} \frac{\frac{1}{L}\ln(1/R)}{\frac{1}{L}\ln(1/R) + \alpha} \tag{6.6}$$

which may be re-arranged to give:

$$\frac{1}{\eta_{ext}} = \frac{\alpha}{\eta_{inj}\ln(1/R)}L + \frac{1}{\eta_{inj}} \tag{6.7}$$

Hence from a plot of $1/\eta_{ext}$ as a function of L, η_{inj} can be determined from the intercept. The loss α may then be determined from the gradient by assuming a value for R. The values for η_{inj} and α thus determined can, in theory, then be fed back into Eq.(6.3) to obtain J_t once Γ_w has been calculated from knowledge of the waveguide structure.

In practice, there is a statistical spread in both the J_{th} and η_{ext} values measured for a given device length. Variations in the η_{ext} values for a given device length can arise through the practical difficulties associated with collecting and measuring all the optical power from a given laser facet. It is for this reason that very little emphasis is placed on the η_{inj} and α results derived from the plots of $1/\eta_{ext}$ as a function of L. The measurement of J_{th}, however, tends not to suffer from such experimental errors; rather, the spread observed in the J_{th} values may be attributed to non-uniform current injection along the device due to localised imperfections in

the device contacts, and to imperfections of the cleaved facets. Any localised reduction in the current density can result in a large decrease of the localised gain due to the logarithmic form of the QW gain curve. This, in turn, can manifest itself as a significant increase in the laser threshold current. Facet imperfections will also result in increased threshold currents. Due to the nature of these errors, the analysis of the broad-area lasers has been performed as follows:

1. Several broad-area devices are fabricated for each of several different lengths, and J_{th} and η_{ext} are measured for all devices.

2. For each device length, all the $\ln(J_{th})$ values are plotted against $1/L$ and two linear best fits are performed: the first is a best fit of *all* the $\ln(J_{th})$ data at each length, while the second is a best fit of the *minimum* J_{th} value at each length

3. For each device length, all the $1/\eta_{ext}$ values are plotted against L and two linear best fits are performed: the first is a best fit of *all* the $1/\eta_{ext}$ data at each length, while the second is a best fit of the $1/\eta_{ext}$ value corresponding to the laser with the *minimum* J_{th} value at each length

By selecting the devices with the lowest threshold data at each length, it is hoped that one can extract the most accurate values for J_{∞}, G_0, η_{inj} and α possible within the assumptions of the model used. In what follows, the values of these parameters extracted from the best fits for the minimum threshold device data are denoted by the suffix "(min)", while the parameters extracted from the best fits for all the device data are denoted by the suffix "(all)". The emphasis is placed on J_{∞}(min), as this parameter is thought to provide the best measure of material quality for the reasons discussed above. The η_{inj} and α values extracted from the experimental data are listed, but no real significance is attached to them because of the experimental errors associated with their measurement.

MatLab code was written by the author's colleague Dr M. Street to extract threshold current and external quantum efficiency data from the light-current curves. The code's algorithm relies upon identifying the point on the light-current curve with the maximum gradient. The threshold current and external quantum efficiency are

then given by the current axis intercept and the gradient of the straight line which passes through the maximum gradient point, respectively.

Finally, it should also be noted that the contact resistance was not measured for any of the broad-area lasers used. The devices fabricated from different wafers were simply annealed at the same nominal temperature. Contact resistance is likely to have an effect on the performance of broad-area lasers as determined from pulsed light-current curve measurements. Electrical characterisation of material on a sample-to-sample basis was only adopted in the final stages of the Project and will be discussed in Section 6.2.2.

Results

Every incoming wafer of material was characterised by fabricating and testing broad-area lasers of the oxide-stripe type. A 75 µm stripe width was used, with devices on a 500 µm pitch. The lasers were then cleaved to a range of cavity lengths, from 500 to 2000 µm. Several devices for each cavity length were tested in pulsed regime (current pulsewidth 0.5 µs, duty cycle 0.1%) to avoid heating effects. The optical power-current-voltage (L-I-V) data were acquired using an automated measurement set-up, with the photodetector triggered by the current source. The data were then analysed using the *MatLab* code, which extracted the material parameters of interest.

Table 6.3. Material parameters extracted from broad-area laser analysis

Material ID	J_∞, A/cm^2		G_0, cm^{-1}		η_{inj}		α, cm^{-1}	
	(min)	(all)	(min)	(all)	(min)	(all)	(min)	(all)
QT1147	326	334	1150	827	0.503	0.473	5.91	5.66
QT1243	332	342	1160	1190	0.484	0.474	4.17	3.81
QT1269	223	235	1310	1380	0.495	0.538	7.92	9.47

The data for the 3 wafers studied (QT1147, QT1243 and QT1269) are plotted in the graphs of Figure 6.8. The values of material parameters J_∞, G_0, η_{inj} and α extracted from these plots are summarised in Table 6.3
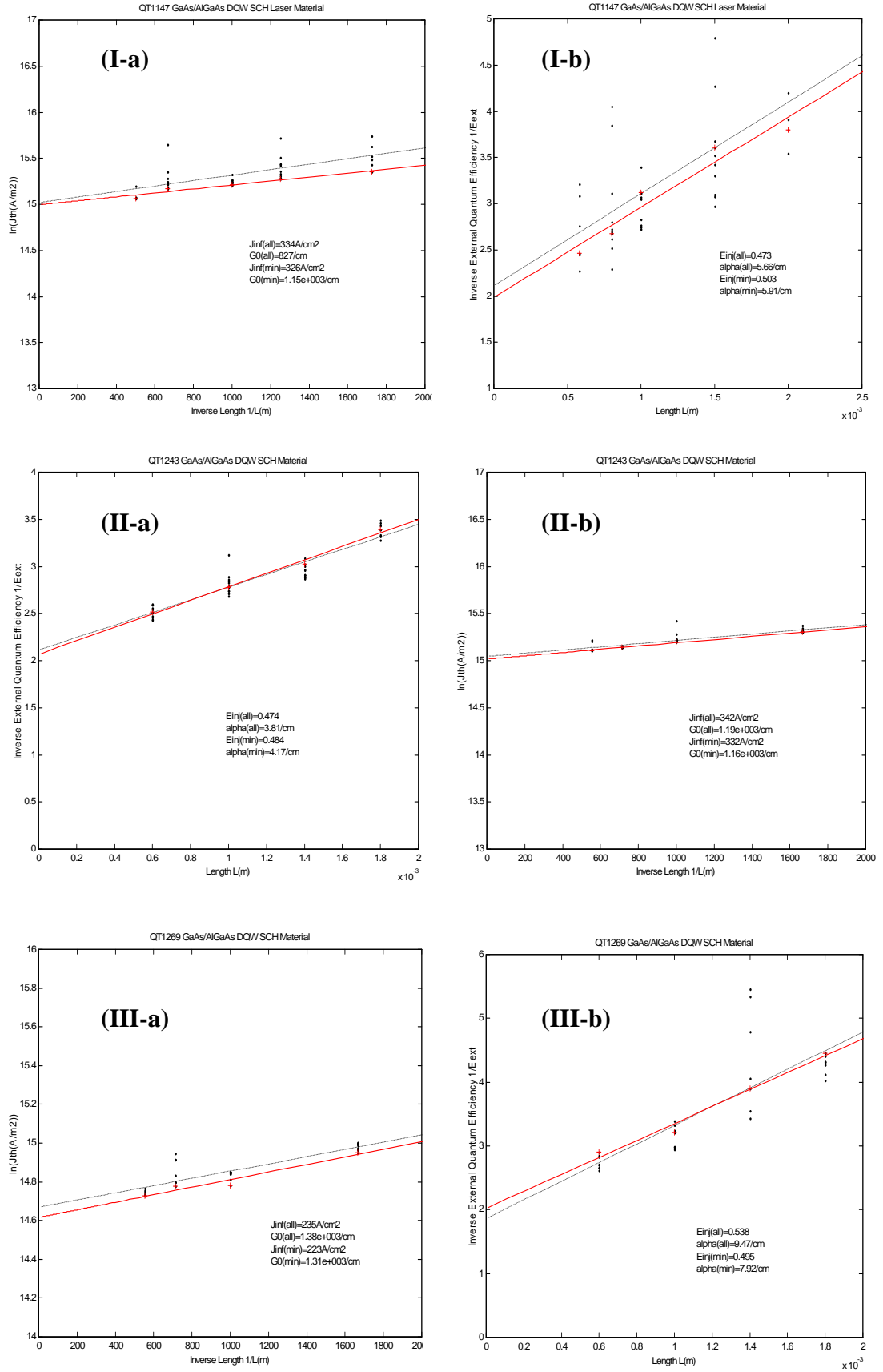
Figure 6.8. Broad-area laser analysis for wafers QT1147 **(I-a,b)**, QT1243 **(II-a,b)** and QT1147 **(III-a,b)**:

(I-a), (II-a), (III-a): $\ln(J_{th})$ as a function of inverse length. Minimum $\ln(J_{th})$ values are indicated by red crosses. Dashed black curve represents best fit through all data points for a given laser length. Solid red curve represents best fit through minimum $\ln(J_{th})$ data points for a given laser length.

(I-b), (II-b), (III-b): Inverse external quantum efficiency η_{inj} as a function of length. η_{inj} values corresponding to minimum threshold lasers of a given length are indicated by red crosses. Dashed black curve represents best fit through all data points for a given laser length. Solid red curve represents best fit through data points corresponding to minimum J_{th} lasers.

It can be seen from the summary of Table 6.3 that the analysis of broad-area laser data from the QT1147 and QT1243 material suggests very similar characteristics for both structures despite the different waveguide design. For example, the optical loss α in QT1147 appears to be even higher than in QT1243, contrary to the theoretical prediction otherwise, as discussed in Sec. 6.1.2.

The threshold current densities $J_{\infty}(\text{min})$ for an infinitely long laser for both structures are greater than 300 A/cm^2, suggesting that CW operation of ridge waveguide lasers fabricated from these materials may be more difficult than for lasers fabricated from the QT1269 material, for which $J_{\infty}(\text{min}) = 223$ A/cm^2. The QT1269 wafers were grown to the same design as QT1243 but at an elevated substrate temperature. The different growth conditions of QT1269 appear to have improved the material quality, with significantly reduced threshold currents and higher gain values G_0. At the same time, the loss coefficient seems to be higher, with a value of 7.92 cm^{-1} that is very close to the theoretical estimate. It can therefore be concluded that, on the basis of the threshold current data, the QT1269 material is superior to both QT1147 and QT1243 and is more suitable for the fabrication of CCM lasers

6.2.2. Electrical characterisation

Electrical characteristics of a laser diode are known to have a very strong effect on its optical performance. There are two key parameters that are used to evaluate the electrical "health" of a semiconductor device: the sheet resistance of the highly-doped contact layers (p++ or n++) and the semiconductor-metal contact resistance. The former is responsible for the uniform distribution of pump current to

the active layer, while the latter should have an ohmic behaviour (i.e., a linear I-V characteristic) and contribute as little parasitic resistance as possible.

High contact resistance causes higher voltage to be applied to obtain the same current, which results in excessive heating and possibly electrical breakdown. The seemingly simple task of creating an ohmic contact represents an extraordinary amount of solid-state physics and experimental development. This is because simply placing a metal in contact with a wide-bandgap semiconductor such as GaAs generally results in a rectifying contact (a diode) rather than an ohmic one. Achieving a stable, low-resistance ohmic contact has been as much of technical art as science, and this problem has generated a large amount of research over the past few decades [11-13].

It is also important to be able to measure contact resistance reliably in order to assess both the material quality and monitor the fabrication process. In general, very low values of contact resistance R_C should be achievable. More specifically, a good n-type contact (11nm Au / 11nm Ge / 11nm Au / 14nm Ni / 150nm Au) evaporated onto a 0.5 µm thick layer of n-GaAs (doping ~ 2×10^{18} Si) should have $R_C \sim 0.1$ Ω·mm. A good p-type contact (33nm Ti / 33nm Pd / 150nm Au) evaporated onto a 0.1 µm thick layer of p-GaAs (doping ~ 1.2×10^{19} Zn) may have $R_C \sim 0.2$ Ω·mm.

Transmission line measurements

Transmission line model (TLM) measurements have been widely used to characterise metal contacts to planar semiconductor devices [11, 14]. The TLM method allows one to measure the resistance across several different gaps between metal contact pads on a highly doped semiconductor layer [15].

To perform a TLM measurement of the contact resistance, several identical rectangular metal pads must be deposited (evaporated or sputtered) onto a clean, de-oxidised semiconductor surface. The pads are separated by gaps of varying sizes, as shown in Figure 6.9. The total resistance R_T across the gaps between each pair of adjacent pads should be measured using a 4-probe technique to ensure an accurate resistance measurement. The total resistance R_T as a function of the gap length L is given by:

$$R_T = \frac{R_{SH}}{W} L + 2R_C \qquad (6.8)$$

where R_{SH} is the semiconductor sheet resistance (assumed to be the same in the regions both underneath and between the contact pads), and W is the width of the contact pads. Therefore, by plotting the graph of R_T as a function of L and performing a linear fit, the value of R_C in ohms (for the specific geometry of the metal pad used) is readily determined from the intercept with the R_T axis and is precisely half the intercept value. To convert R_C into $\Omega \cdot$mm, it is then a simple matter of multiplying R_C in Ω by the width of the contact pads W expressed in mm.
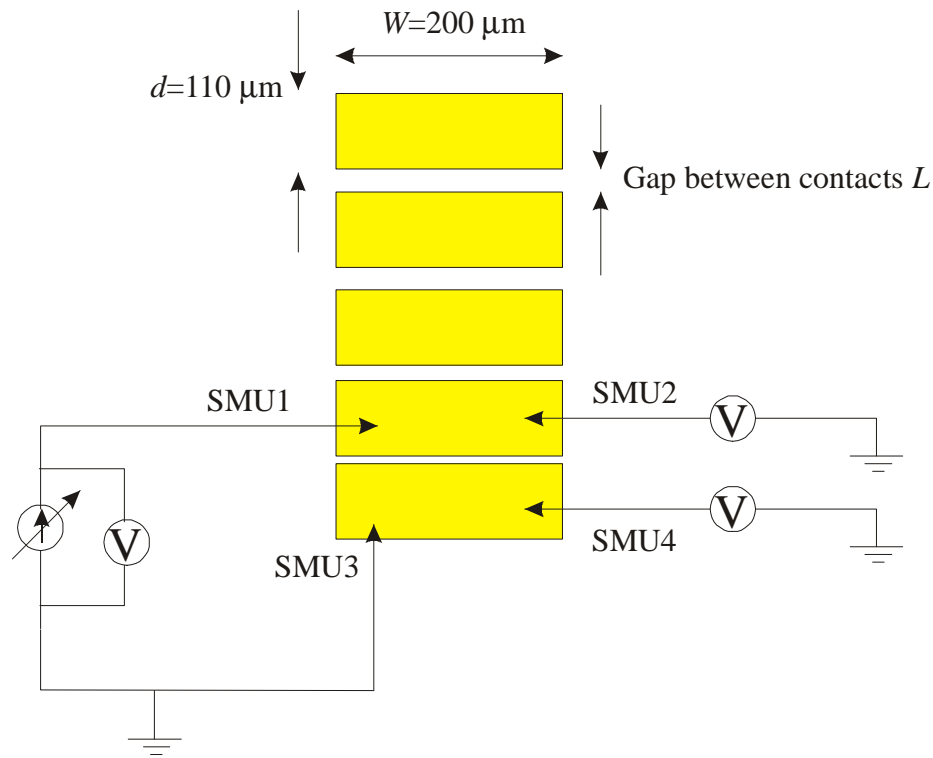
Figure 6.9. 4-probe measurement of the total resistance across the gap between 2 metal contact pads.

From Eq,(6.8) it may also be seen that R_{SH} may be determined from the slope of the graph of R_T as a function of L: R_{SH} in $\Omega/\square$ (ohms per square) is equal to the slope in Ω/μm multiplied by the width W in μm. A typical value of R_{SH} for a 0.5 μm thick layer of n-type GaAs (doping $\sim 2 \times 10^{18}$ Si) is 20 $\Omega/\square$, while for a 0.1 μm thick layer of p-type GaAs (doping $\sim 1.2 \times 10^{19}$ Zn), $R_{SH} \sim 250$ $\Omega/\square$.

TLM measurements according to the above model were carried out on fabricated CCM samples using the HP4145B Semiconductor Parameter Analyser.

The standard 2-probe measurement technique is generally inaccurate for evaluating resistances below 20 Ω, as the resistance of the interface between the probe tip and the contact pad is then proportionally large and can also vary drastically. A 4-probe technique, which eliminates this uncertainty, was used instead to measure the TLM resistance R_T between adjacent metal contact pads, as illustrated in Figure 6.9. The source and measurement units (SMU) of the HP4145B analyser were configured in such a way that the SMU1 and SMU3 probes formed the drive circuit, while the SMU2 and SMU4 probes were operated as voltmeters. The total resistance R_T is then equal to the gradient of the plot of the voltage offset between SMU2 and SMU4 versus the drive current through SMU1.

Results

TLM patterns consisting of contact pads spaced by gaps of varying size were included in most CCM laser samples fabricated. Electrical characteristics of the p-type contacts only were measured. A recipe of Ti/Pd/Au layers with thicknesses of 30/30/150 nm was used, with a further Ti/Au stack of 20/180 nm thicknesses being evaporated while rocking the sample to ensure continuous ridge sidewall coverage. The contacts were annealed at 360$^{\text{o}}$C for 60 sec. A typical I-V characteristic of a fabricated CCM laser diode having a 2 μm wide, 800 μm contact on top of a 3 μm wide waveguide ridge, is shown in Figure 6.10. An R_C value of 10.1 Ω can be inferred from the gradient of the linear part of the measured I-V curve.
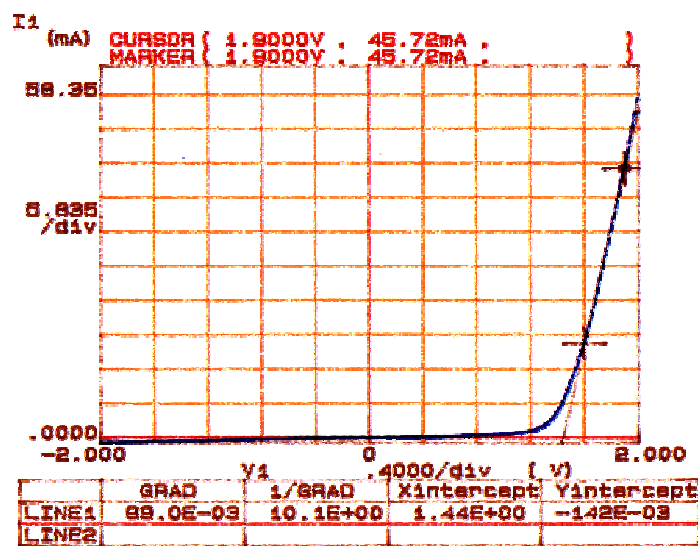
Figure 6.10. A typical I-V characteristic of a CCM laser diode showing $R_C \cong 10.1 \, \Omega$.

A typical graph of the measured resistance in the QT1269 material as a function of the gap width between two adjacent pads is shown in Figure 6.11. The inferred values of contact resistance and sheet resistance obtained by a linear best fit were $R_C = 2.9\ \Omega$ and $R_{SH} = 344\ \Omega/\square$, which was representative of the average values measured. However, because of the poor repeatability of the contact metallisation process and the curve-fitting nature of the method employed, a large variation in TLM data was observed even in samples fabricated from the same material. A summary of the TLM results obtained from a series of CCM laser samples fabricated from each material structure, is presented in Figure 6.12.
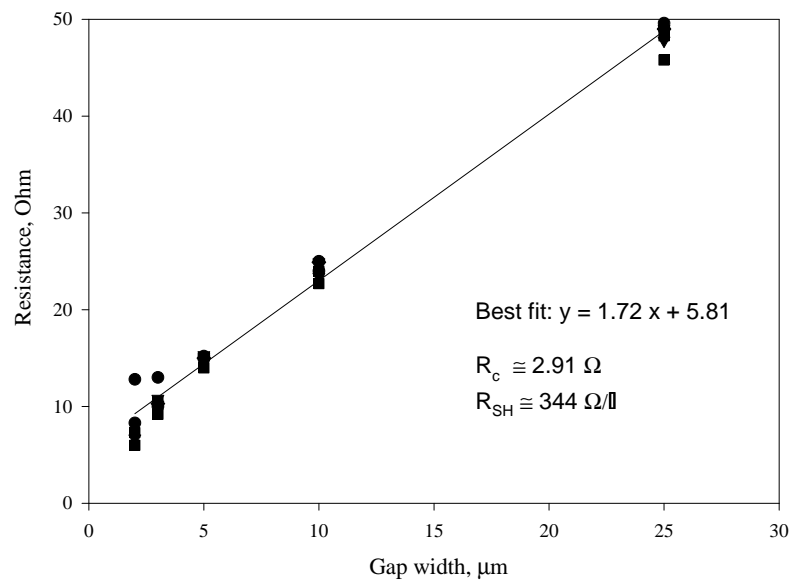
Figure 6.11. Results of TLM measurement on a CCM laser sample from the QT1269 material using 200 µm x 110 µm contact pads with gaps of 2, 3, 5, 10, 25 µm.
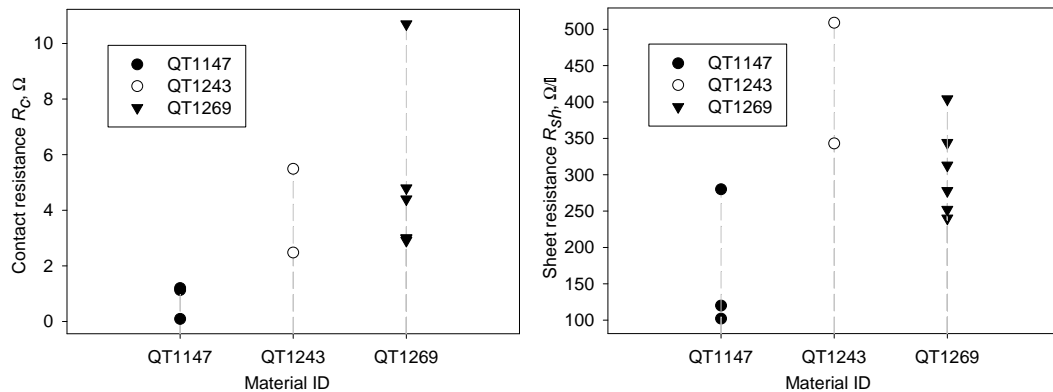
Figure 6.12. Summary of R_C and R_{SH} data from TLM measurement of several fabricated CCM laser samples in different materials.

It can be seen from the summary of Figure 6.12 that, on average, the QT1147 material appears to have the best electrical characteristics, both in terms of contact resistance and sheet resistance. While there are not enough data to make a rigid comparison between QT1243 and QT1269, both seem to be rather similar in electrical terms.

In summary, it was established that the QT1269 material offered the best laser performance from the analysis of Sec. 6.2.1, whilst the QT1147 material showed the best electrical characteristics based on TLM measurements. A possible explanation is that QT1147 had a 0.2 μm-thick p++ contact layer, while that of QT1269 was 0.1 μm thick, which could have possibly been damaged during the multiple fabrication steps applied to CCM laser samples.

6.3.   References

[1]   H. Kogelnik, "Theory of optical waveguides (Ch. 2)," in *Guided-Wave Optoelectronics*, T. Tamir, Ed. New York: Springer, 1990, pp. 7-88.

[2]   H. Kogelnik, "An introduction to integrated optics," *IEEE Trans. Microw. Th. & Tech.*, vol. 23 (1), pp. 2-16, 1975.

[3]   D. W. Jenkins, "Optical constants of AlxGa(1-x)As," *J. Appl. Phys.*, vol. 68, pp. 1848-1853, 1990.

[4]   R. J. Deri and M. A. Emanuel, "Consistent formula for the refractive index of Al(x)Ga(1–x)As below the band edge," *J. Appl. Phys.*, vol. 77, pp. 4667-9, 1995.

[5]   J. Kelliher, "Course EE/3351 Fundamentals of Optical Communications," Centre for Telecommunications Research, King's College London, http://www.ctr.kcl.ac.uk/lectures/Johnk/2003%20Course/.

[6]   M. W. Street and D. A. Yanson, "Quantum Well SCH Laser Material: Feedback and Request for New Material," Univ. of Glasgow, Report 1999.

[7]   W. T. Tsang, "Extremely low threshold (AlGa)As graded-index waveguide separate-confinement heterostructure lasers grown by molecular beam epitaxy," *Appl. Phys. Lett.*, vol. 40, pp. 217-218, 1982.

[8]   S. Ayling, "Follow-up on characterisation of old MBE laser material grown by A. Kean and tested by T. Krauss," Univ. of Glasgow, Memo 1992.

[9]   A. Kurobe, H. Furuyama, S. Naritsuka, N. Sugiyama, Y. Kokubun, and M. Nakamura, "Effects of well number, cavity length, and facet reflectivity on the reduction of threshold current of GaAs/AlGaAs multiquantum well lasers," *IEEE J. Quant. Elec.*, vol. 24, pp. 635-640, 1988.

[10]   P. W. A. McIlroy, A. Kurobe, and Y. Uematsu, "Analysis and application of theoretical gain curves to the design of multi-quantum-well lasers," *IEEE J. Quant. Elec.*, vol. 21, pp. 1958 - 1963, 1985.

[11]   H. H. Berger, "Models for Contacts to Planar Devices," *Solid State Electronics*, vol. 15, pp. 145-158, 1972.

[12]   G. Stareev and H. Kunzel, "A controllable mechanism of forming extremely low-resistance nonalloy ohmic contacts to group III-V compound semiconductors," *J. Appl. Phys.*, vol. 74, pp. 7344-7356, 1993.

[13]   K. S. Sandhu, A. E. Staton-Bevan, and M. A. Crouch, "Electrical and micro-structural investigation of Au/Pt/Ti ohmic contacts for AlGaAs/GaAs heterojunction bipolar transistors," *Materials Sc. & Techn.*, vol. 11, pp. 1083-1088, 1995.

[14]   G. K. Reeves and H. B. Harrison, "Obtaining the Specific Contact Resistance from Transmission Line Model Measurements," *IEEE Electr. Device Lett.*, vol. 3, pp. 111-113, 1982.

[15]   M. W. Street, "Contact Resistance Measurement Using the Transmission Line Model," Notes, Univ. of Glasgow 1998.

CHAPTER 7.

FABRICATION OF HARMONIC MODELOCKED

COMPOUND-CAVITY LASERS

The fabrication of CCM lasers was the most arduous and time-consuming part of the current Project. To produce operating laser devices, a thorough familiarisation with, and hands-on experience of, state-of-the-art semiconductor technology proved indispensable for the success of the Project. Standard fabrication processes such as photo and e-beam lithography, wet and dry etching and contact metallisation and patterning, were heavily used, with many requiring further optimisation and development to meet specific device requirements.

GaAs/AlGaAs material emitting at a wavelength of 850 nm was used, as this is a well-understood material system, which also offers ease of fabrication. The structure and design of the material were discussed in Chapter 6. The core fabrication cycle employed was that of the standard ridge-waveguide laser, involving the stages of ridge definition and etching, deposition of an insulation layer (silica), opening of contact windows on top of the ridge, p-contact metallisation, wafer thinning, back-side (n-contact) metallisation, contact annealing and device cleaving and chipping. However, additional stages had to be developed specifically for CCM devices, such as contact patterning (lift-off), precision cleaving and, most importantly, dry-etching to define the deep-etched intra-cavity reflector (ICR) features and, in early devices, etched facets. It is the development of these additional processes that will be discussed first, followed by a description of the final process flow documenting the fabrication of CCM laser diodes and a presentation of the fabricated devices.

7.1. Technology development

The fabrication of CCM lasers was heavily reliant upon both e-beam lithography (EBL) and reactive ion etch (RIE) technology in order to define the sub-

micron ICR features. The development of the deep-etch ICR process and of its special case, the etched facet process, is discussed below.

7.1.1. Dry-etched facets

CCM lasers were initially designed to have etched facets, as this was thought to provide better control over the cavity length and reduce the uncertainty associated with facet cleaving. In the literature, the etched facet approach has been investigated as part of full-wafer technology [1], and laser devices with both facets etched have demonstrated similar characteristics to those with cleaved facets [2]. Etched-facet lasers require extremely deep trenches ($> 3 - 4 \mu m$) to enable lossless outcoupling of light from the facet, which presents a difficult technological challenge.

To allow preliminary characterisation of the reactive ion etching (RIE) process, oxide-stripe lasers with dry-etched facets were fabricated and the etching process was optimised to produce smooth vertical sidewalls. The process involved depositing a layer of SiO_2 or Si_3N_4, patterning it with resist and etching in CHF_3 gas to produce an oxide or nitride hardmask, and then etching GaAs/AlGaAs in $SiCl_4$ + O_2 gas [3]. The oxygen was added to improve sidewall verticality in the etched trenches, as suggested in Ref.[4].

Both photolithography and e-beam lithography were attempted for mask definition purposes. Shown in Figure 7.1 are scanning electron microscope (SEM) images of the etched sidewalls obtained by photo and e-beam lithographically defined hardmasks. It can be seen that EBL (with a small beam spot size of 15 nm) appears to produce a smoother sidewall surface than photolithography. It is also evident from Figure 7.1 that deep etching leaves unetched pillars of material, also known as micromasking. This was linked to the localised under-etching of the hardmask layer and chamber contamination of the RIE machine. In most cases, the micromasking effect was corrected by increasing the hardmask etch time and reducing the O_2 fraction in the gas flow. Wet-etching was also used to reduce the micromasking after the dry-etch step, however, it adversely affected the sidewall smoothness, as is clear from the SEM image of Figure 7.2, which shows an etched facet of a fabricated CCM ridge-waveguide device.
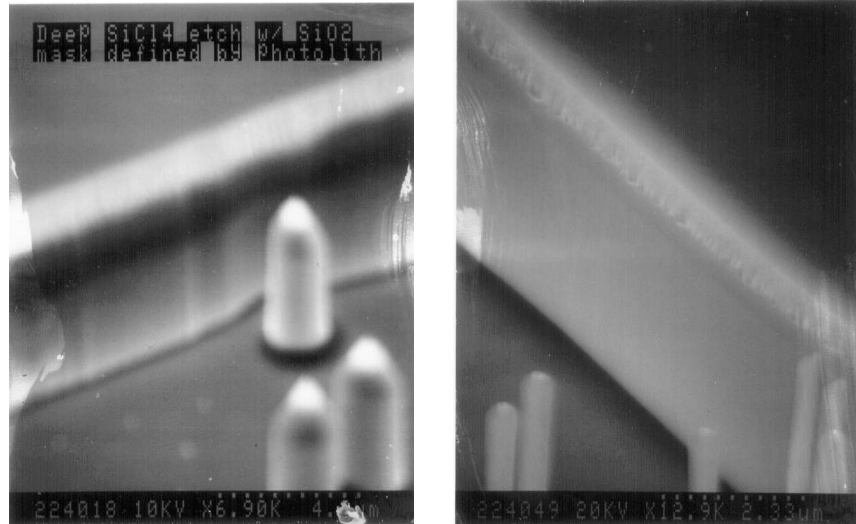
Figure 7.1. Comparison of sidewall quality obtained by use of photolithographically defined hardmask (left) versus that defined by e-beam lithography (right).
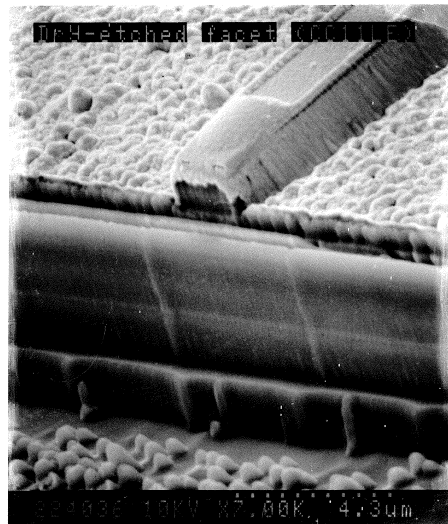
Figure 7.2. SEM image of an etched facet in a CCM laser. The damage is due to the prolonged exposure to wet etch in an attempt to eliminate micromasking.

7.1.2. ICR definition

To further optimise the slot definition and etching process, a number of trials were performed writing slots of various sizes across ridges in scrap GaAs material and then dry-etching the resulting patterns. Optimum EBL process parameters (resist composition, exposure dose and beam spot size) were thus established. The SEM pictures of Figure 7.3 show some of the results for different slot geometries.
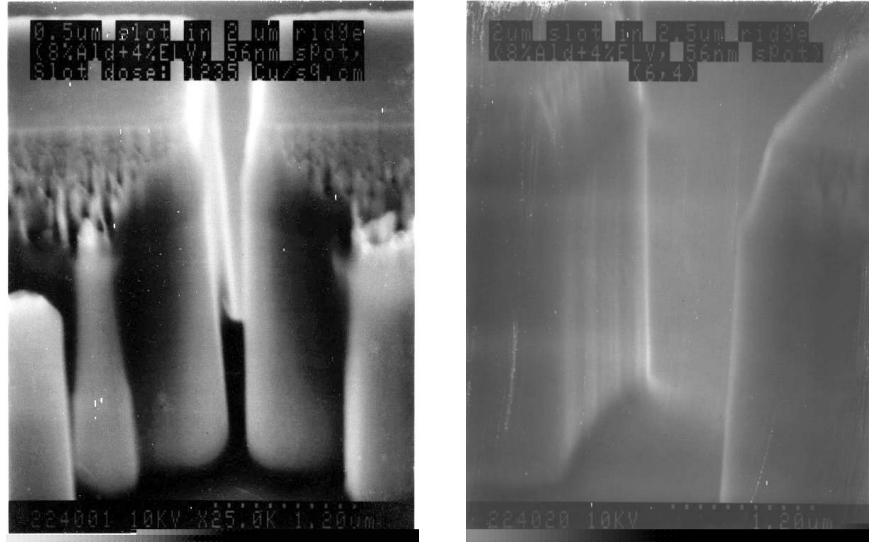
Figure 7.3. Slots of different widths (left: 0.5 μm, right: 2 μm) defined by EBL in 2 ÷ 2.5 μm wide, 3 μm tall ridges.

Low-resolution ridge exposure   High-resolution slot exposure
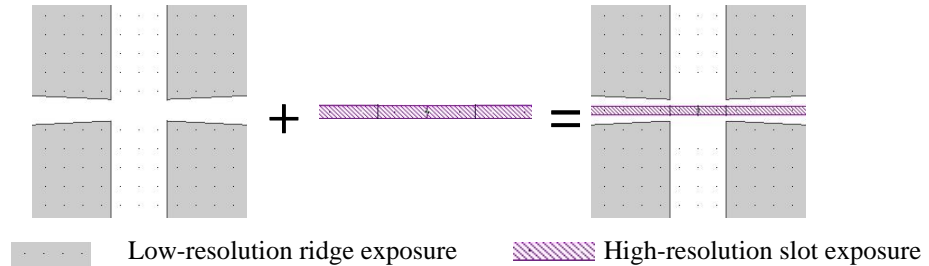
Figure 7.4. Definition of a high-resolution slot inside a bow-tie ridge extension.

Considerable effort was expended into the definition of a shallow-etched slot that could be written in one EBL step along with the waveguide ridge. In EBL, there exists a trade-off between resolution (beam spot size) and writing time, i.e., the smaller the spot size, the longer the time taken to expose a given area. Therefore, for reasonable exposure times (minutes rather than hours), the ridge pattern (i.e., all the large areas outside the 3 μm ridge) must be exposed using a large spot size (200 ÷ 300 nm), whereas the slot feature can only be written with a high-precision beam focused to a spot of at least 15 nm. This was achieved by writing the ridge and slot patterns in two different exposures (known as "matrices") overlaid in a single beamwriter job. However, this resulted in a wider, non-uniform slot due to the overexposure of ridge corners caused by proximity effects. The problem was solved by including a bow-tie extension to the ridge pattern, inside which the high-resolution slot was written, as explained in the schematic of Figure 7.4. The resulting slot images taken by the SEM are presented in Figure 7.5, which show a uniform slot width and sharp corners at the ridge-slot intersection.
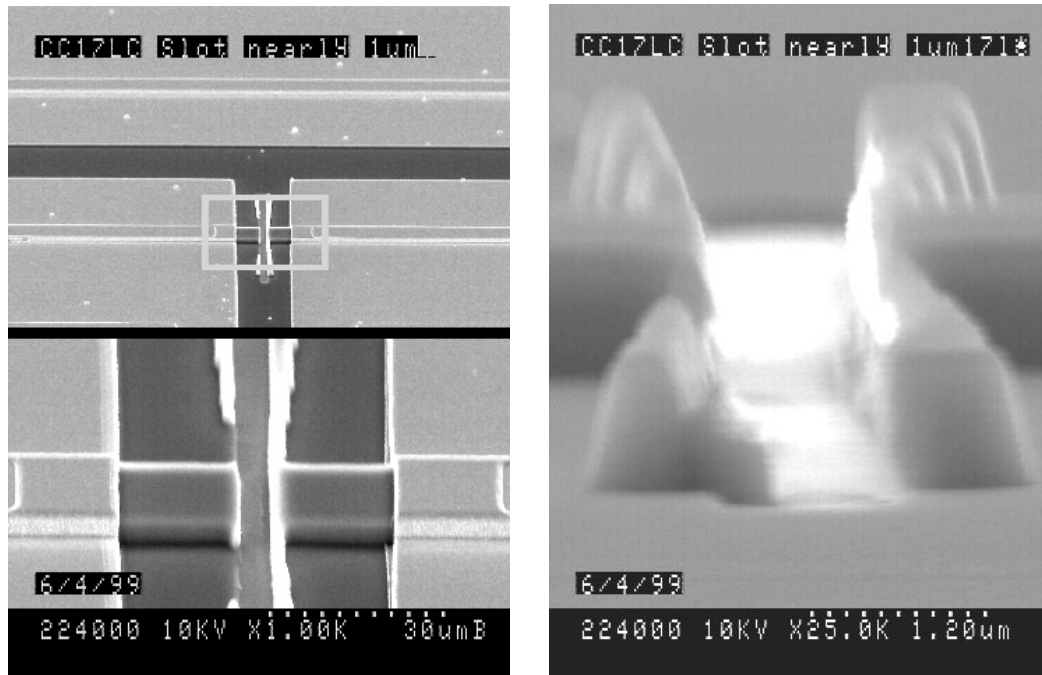
Figure 7.5. Plan (left) and side (right) SEM views of a fabricated shallow-etched slot using a bow-tie extension to reduce corner overexposure.
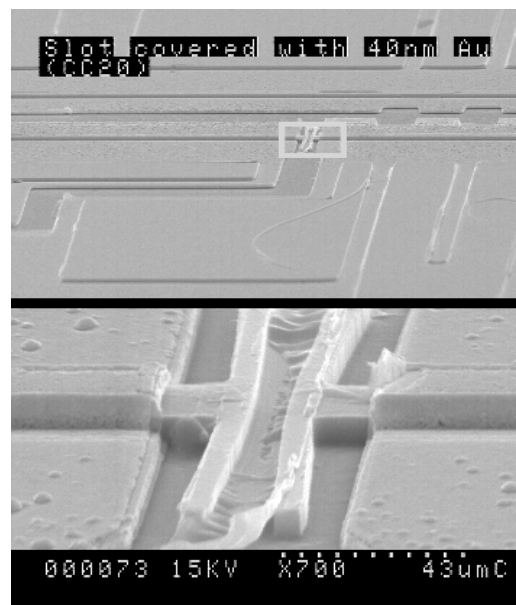
Figure 7.6. SEM image of magnified bow-tie slot covered with a 40 nm thick layer of gold.

One of the ideas for increasing the reflectivity of a single shallow-etched ICR feature was to use metallisation to cover up the etched slot. Indeed, metal would act as a highly reflective mirror, e.g., with gold having a "skin depth" (characteristic distance over which the amplitude of an electromagnetic wave falls by a factor of e inside the metal, see [5]) of several nanometres at the wavelength of interest

(λ = 850 nm). A SEM picture of a shallow-etched slot covered with 40 nm of sputtered gold is shown in Figure 7.6.

In another attempt to increase the ICR reflectivity, periodic structures containing multiple shallow-etched slots were fabricated. The design of these structures was discussed in Section 5.2.2. They were particularly difficult to define, as trade-offs between resolution, exposure dose and resist thickness resulted in a very narrow process window. To characterise the definition process, test structures containing single bow-tie slots as well as 3rd and 4th order grating features etched into a mock waveguide ridge were fabricated. A process suitable for the concurrent definition of both a standalone slot feature and a 3rd period grating ICR was established, with a SEM photograph being shown in Figure 7.7.

As it became evident from the performance of the fabricated CCM devices that the shallow-etched ICR features had failed to provide sufficient reflectivity, effort was directed towards developing a process suitable for deep-etched ICRs (see Sections 5.2.3 and 5.2.4 for design and modelling). As the etch depth required was much larger than the height of the waveguide ridge, such features had to be fabricated in separate lithography and etch steps. After a few unsuccessful attempts to define the deep ICRs post ridge-etch, it was decided to fabricate them in the very first step on a virgin sample. Indeed, owing to their small width ($\sim$ 100 nm), they would have little effect on the subsequent processing of the host material. A suitable combination of hardmask thickness (300 nm), resist, exposure and etch conditions was established to etch the ultra-narrow ICR features to a depth of at least 2 μm, both as a single slot and a photonic bandgap structure of up to four periods. SEM photographs confirming the successful implementation of this approach are shown in Figure 7.8 for the cases of 1 and 4 periods.

However, upon inspection of the cleaved profile of the deep-etched ICR slots, it was established that their effective width was approximately 60 nm at the waveguide core level, with a 100 nm opening width at the top. Therefore the predicted reflectivities of Figure 5.10 had to be re-calculated using the actual gap width. The corrected reflectivity estimates at λ = 860 nm were 8% for a single deep-etched slot, and 70% for a PBG microstructure of four slots.
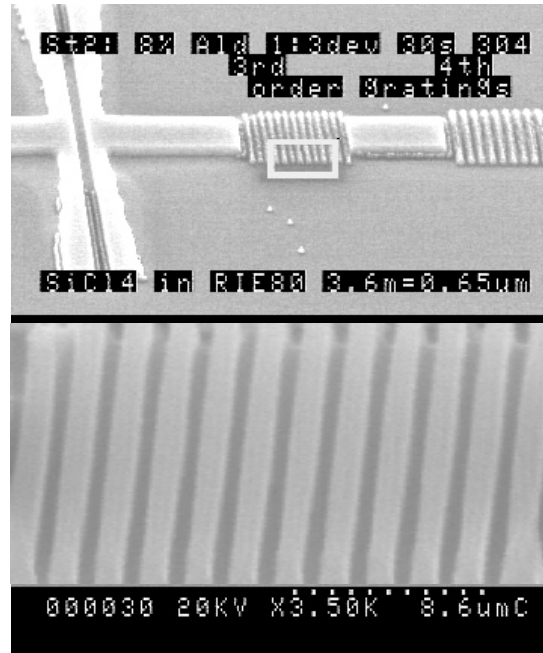
Figure 7.7. SEM image of a test structure containing a bow-tie slot and 3rd and 4th order ICR gratings. The bottom part of the image shows the magnified area marked by the white box above.
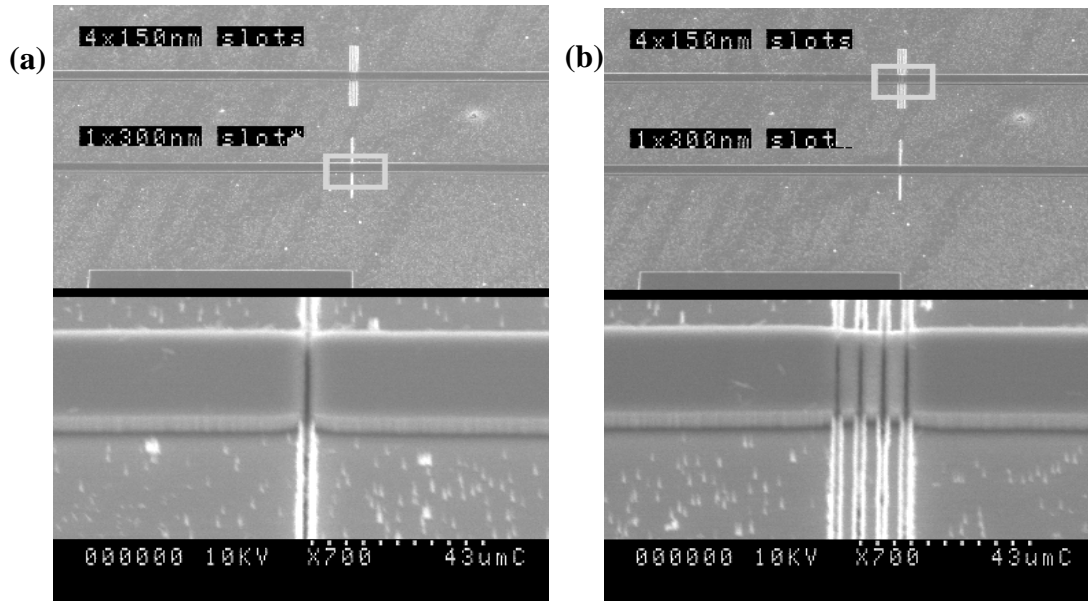
Figure 7.8. SEM images of deep-etched ICRs etched into 3 µm waveguides: **(a)** single slot; **(b)** a PBG structure of 4 slots. The bottom part of each image shows the magnified area marked by the white box above.

7.1.3. Precision cleaving

Accurate sub-cavity length ratios are essential if harmonic effects are to occur in CCM lasers. They are particularly important in high-harmonic devices, where an

error of only a few microns can result in modelocking at a different harmonic. The ideal solution would be to employ etched facet technology, where the cavity length is defined lithographically to a very high precision. However, due to the early optical failure of the fabricated etched-facet CCM devices, the standard facet cleaving approach had to be adopted. The problem with this approach was that the accuracy of the conventional wafer scriber used to cleave the devices was only about ±15 μm, which was inadequate for reliably defining sub-cavity ratios, especially in high-asymmetry (high-harmonic) devices.

As an alternative way forward, a special, wet-etch facilitated cleaving process was developed. It relied on the use of a fast anisotropic wet-etch to produce ~70 μm deep triangular pits from lithographically-defined seed windows along the sample edges. After thinning, these pits were used, in place of scribe nicks, to define cleavage lines.

Wet-etch process development

Wet etch recipes based on solutions of H_2SO_4, H_2O_2 and H_2O are known to etch GaAs in an anisotropic manner [6], with sidewalls having a positive slope along one crystallographic direction and a negative slope along the orthogonal one. By selecting an appropriate wafer orientation, V-shape grooves can be etched from seed windows, with the slope angle defined by etch composition and crystallographic properties of the material. In Ref.[7],V-shape valleys having [111] sidewalls were produced in GaAs grown on a [100]-oriented substrate using a H_2SO_4:H_2O_2:H_2O solution (1:8:40 by volume).

A series of simple experiments was carried out to assess the wet etching process. Both thick photoresist (S1828) and silicon dioxide (silica) were successfully used as mask materials and were found to withstand long exposure to the etch solution. A fairly arbitrary mask plate containing linear features in both X and Y directions was used to pattern samples for the etch trials. Typical etch profiles can be seen in Figure 7.9. The etch rate was found to be approximately 2 μm/min at ambient temperature for etch times under 10 minutes, after which the rate seemed to fall in a non-linear fashion, possibly due to ageing/saturation of the etch solution. The rate of etching also appeared to be dependent on the feature size and mask undercutting. It was established that an etch time of 80 minutes produced ~70 μm deep triangular

valleys with [111]-oriented sidewalls and a slope angle of 33°. Increasing the etch time beyond 1½ hours resulted in mask undercutting and non-uniform sample thinning on the back side with no significant increase in the etch depth, thus the 80 minute process was adopted as standard for the cleavage technique under study.
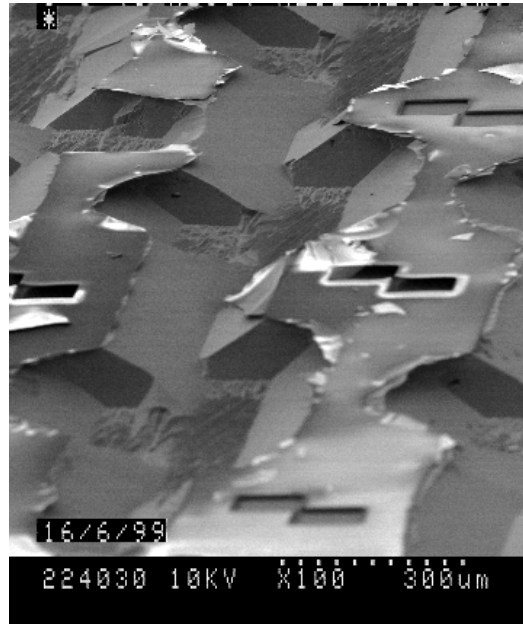
Figure 7.9. SEM image of resulting profiles of a wet-etch trial sample.

The effect of the etched pits on wafer cleaving was then investigated in terms of pit length and sample thickness. Figure 7.10 presents the pit profile in a test sample which was thinned to 120 μm, causing the sample to disintegrate along the defined axes. It was found that 2 mm long nicks across the longer edges of a 15 x 10 mm^2, 180 μm-thick sample were adequate for the reliable definition of cleavage planes. An enlarged optical microscope image of an etched nick in a cleaved sample is shown in Figure 7.11. Here, the etched nick was obtained from a seed window just a 3 μm-wide, which, after etching, broadened to some 240 μm by undercutting the silica mask in the directions orthogonal to the cleavage line.

Figure 7.10. Profile of etched cleavage pits in a test sample as seen in an optical microscope.
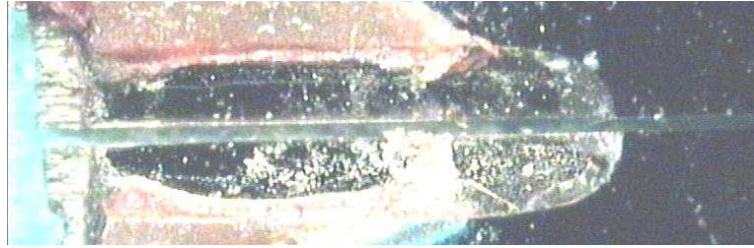
Figure 7.11. Etched pit in the edge of a cleaved sample with the cleavage gap in the centre.

Precision cleaving process

After the suitability of the wet-etched defined cleaving process had been ascertained and its parameters established, the following procedure was incorporated in the CCM laser process flow.

The seed windows for etching the cleavage nicks were defined and etched in the silicon dioxide mask at the same time as the contact windows on top of the waveguide ridge. If the seed windows were to be defined by photolithography, this would require a special mask plate to be made up, which would have to be specific both to the sample size and device layout. Since all other lithography stages were carried out using the beamwriter, which allowed for "on-the-fly" design changes and device modifications, it was desirable to direct-write the seed window pattern as well. It was also important that the windows extend to the very edges of the sample to facilitate cleaving, as shown in Figure 7.11.

However, it being a registration job, the beamwriter could only align the window pattern to pre-defined registration keys within the sample, with the pattern entirely contained within the markers used for registration. Thus it would not normally be possible to extend the windows to the sample edges owing to a clearance of some 2-3 mm between the edges and the alignment markers. Nonetheless, a loophole in the beamwriter software was exploited to achieve registration to a set of only two markers (as opposed to four) in the middle of the sample, which allowed the pattern to be written across the sample edges. A plan view of the sample showing the main device pattern, alignment keys and the seed windows is given in Figure 7.12 (a).
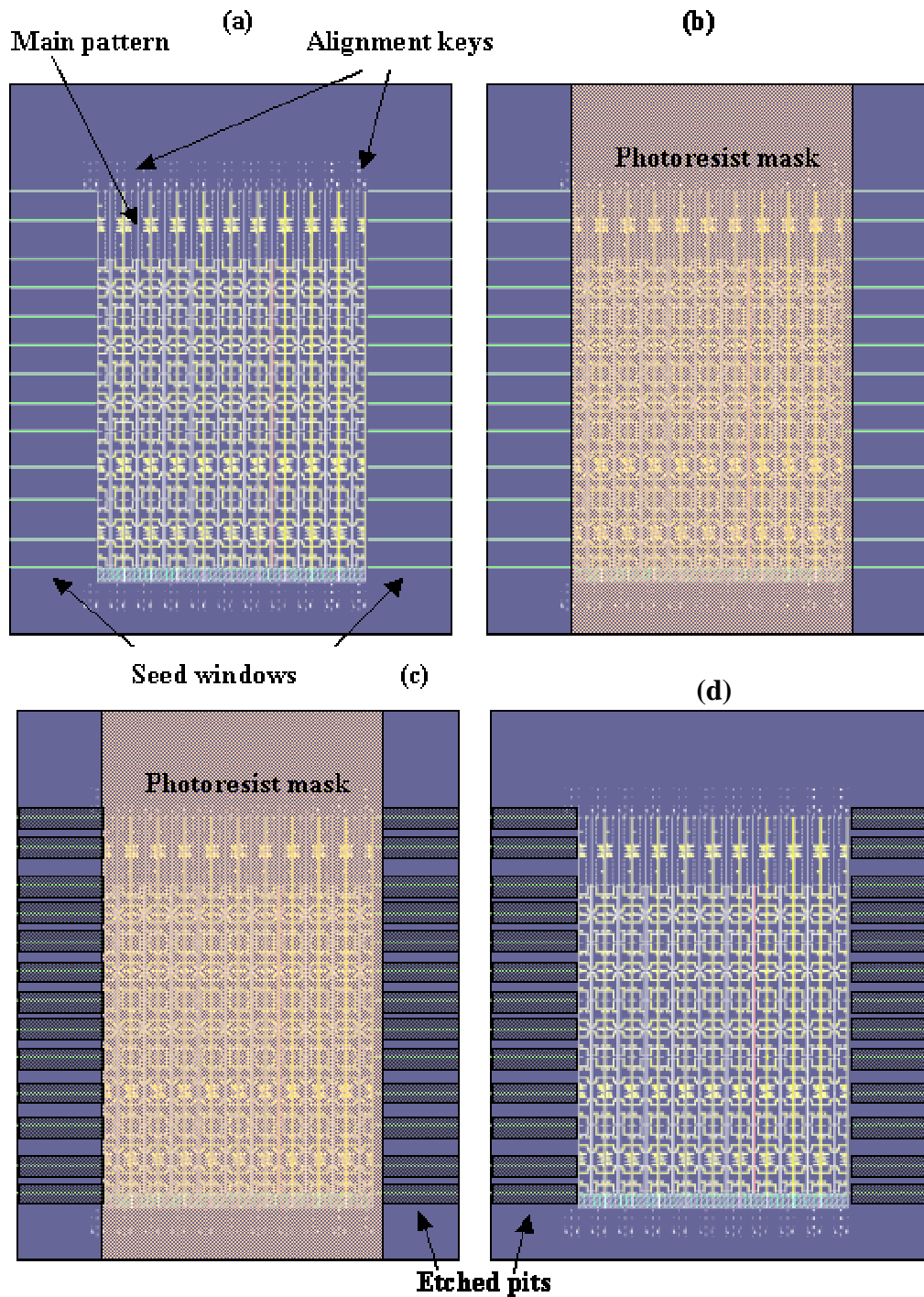
Figure 7.12 (a) Plan view of sample layout with seed windows for etching cleavage nicks; **(b)** Photolithography stage masking the main pattern;
(c) Cleavage nicks following the wet etch step; **(d)** View of the resulting pattern.

The next stage was to protect the main device pattern containing areas of unprotected semiconductor from the highly aggressive nick etch. This was best done by photolithography, as it only required a simple mask plate containing a broad light-field and a dark-field area. The sample was spun with S1828 photoresist, with a layer

thickness of ~2.8 μm. The resist was baked at 90°C for 30 minutes. Two exposures were then made in the mask aligner, each exposing a longer sample edge containing the seed windows in silica, as illustrated in Figure 7.12 (b). After development, the resist was post-baked at 120°C for 60 minutes.

The sample was then wet-etched in a $H_2SO_4:H_2O_2:H_2O$ solution (1:8:40) for 80 minutes to define the cleavage nicks from the seed windows [Figure 7.12 (c)]. The resist mask was stripped in acetone, with the resulting pattern as shown in Figure 7.12 (d).

After thinning to 180 μm, the sample was cleaved by positioning the nicks over a razor blade and applying slight pressure, without any need for scribing whatsoever. The resulting cleavage accuracy was estimated at ±4 μm and was largely limited by the initial misalignment of the main pattern with respect to the crystallographic axes of the sample. Thus an accurate wet-etch facilitated cleaving technique has been developed, which relies on the lithographic definition of cleavage positions and does not require any mechanical scribing.
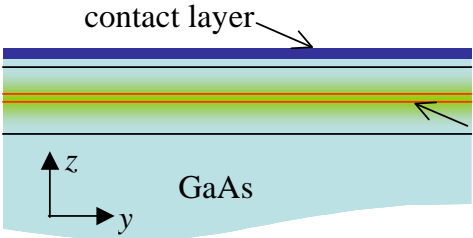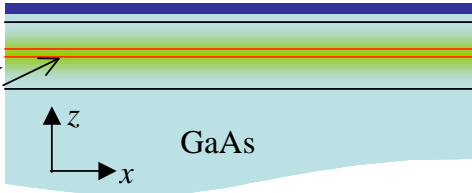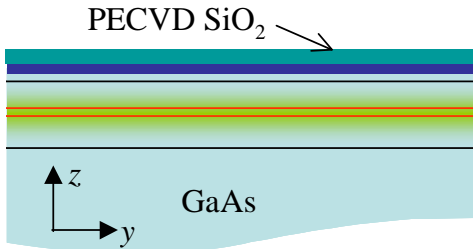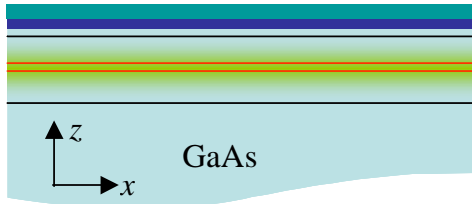
7.2. CCM laser process flow
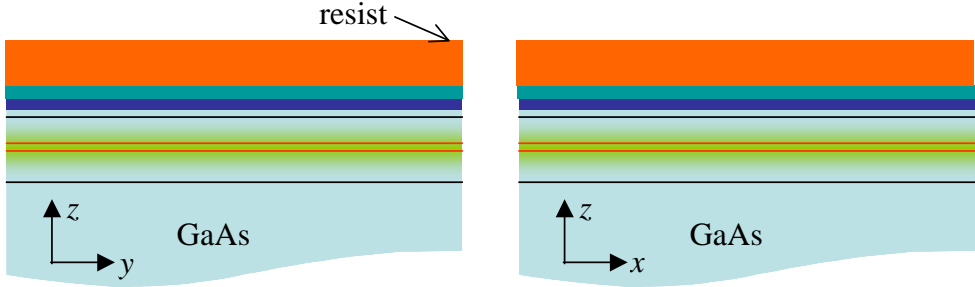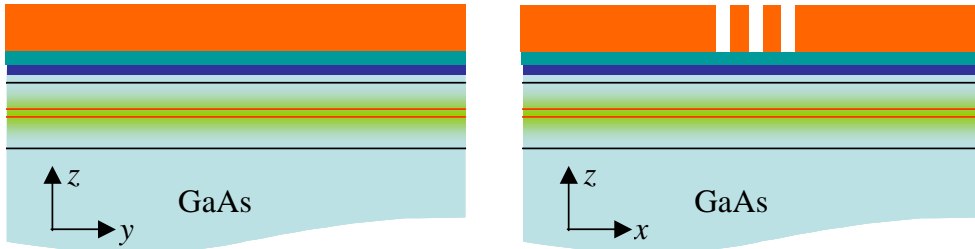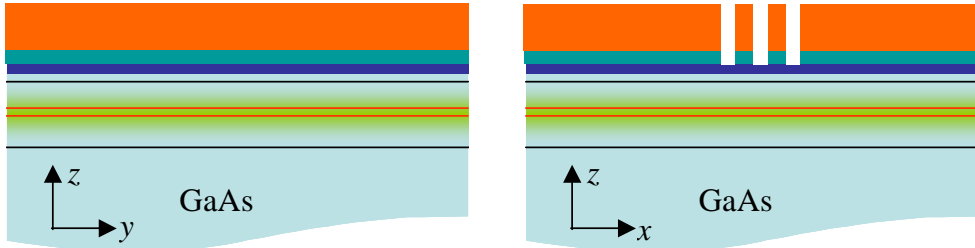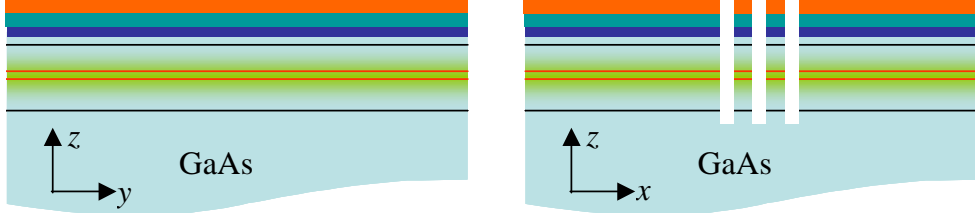
In this Section, the final version of the step-by-step process flow for the fabrication of cleaved-facet CCM lasers will be presented. Due to the special definition of ICR features and the etching of cleaving nicks, the overall process requires five lithography stages. Each step will be illustrated with a schematic showing the wafer profile as seen from the two virtual cross-sections (Cut *A* and Cut *B*) as defined in Figure 7.13. Cut *A* shows the material profile across an area that will evolve into one of the two waveguide ridges, while Cut *B* is made along the top of the ridge and across the deep-etched ICR feature. The simultaneous illustration of the two profiles will hopefully clarify the changes occurring at each step. The illustrated fabrication flow can be found in Table 7.1, while the complete Process Sheet containing process parameters is attached in the Appendix.
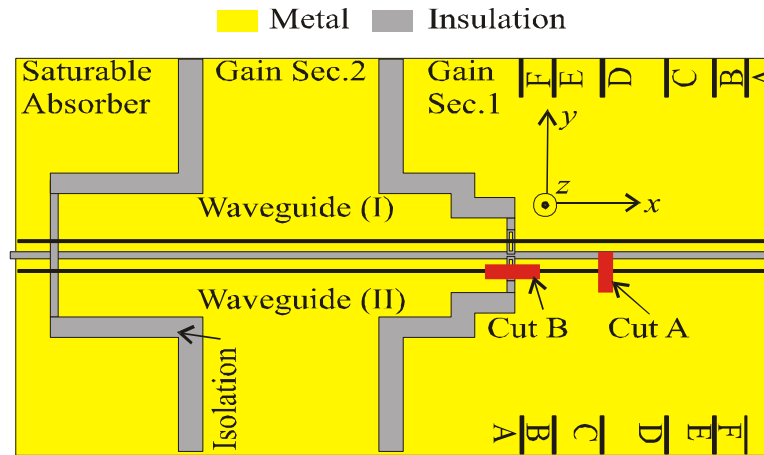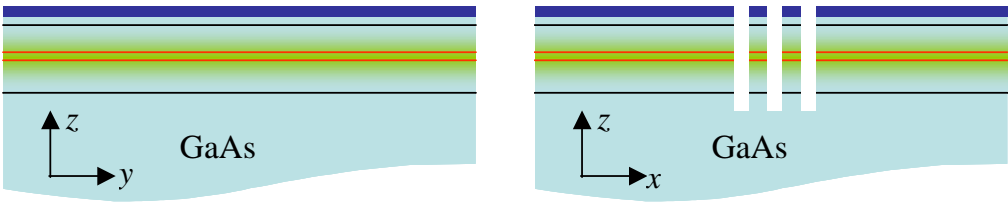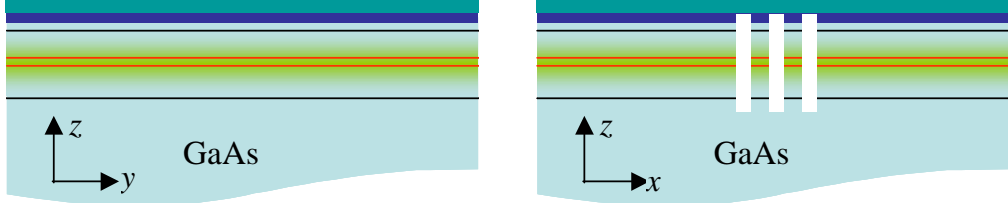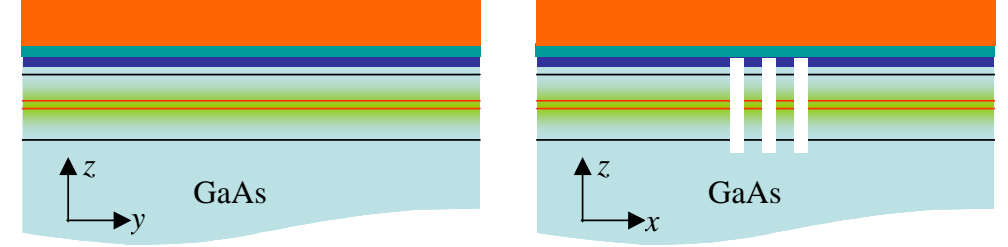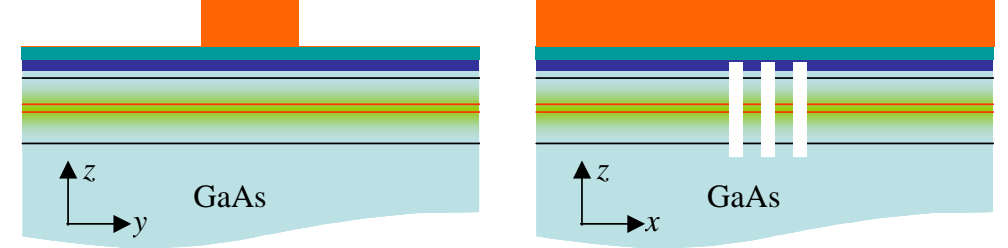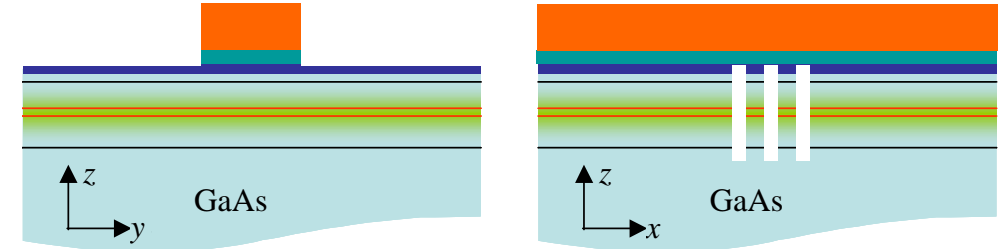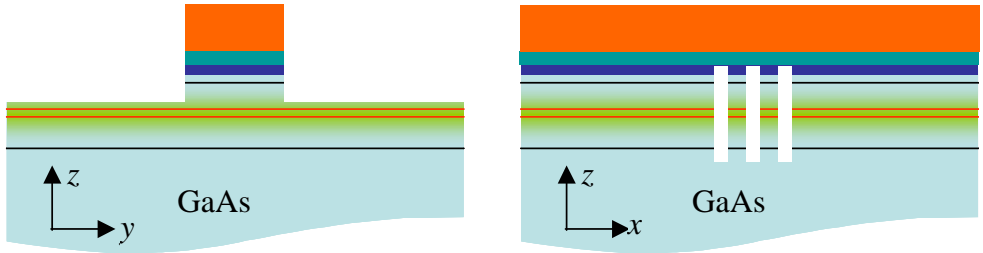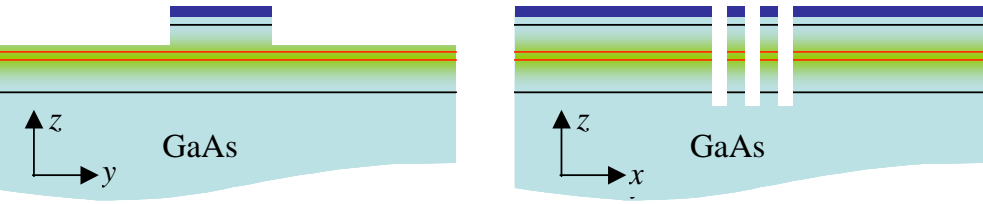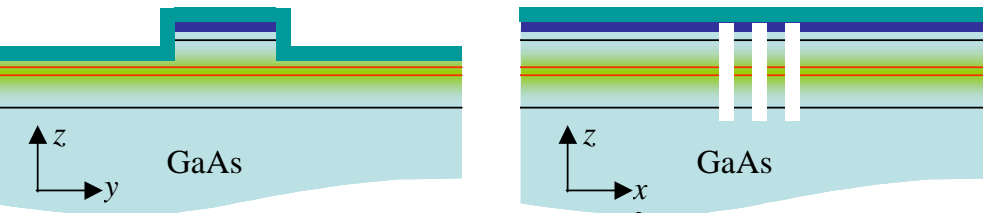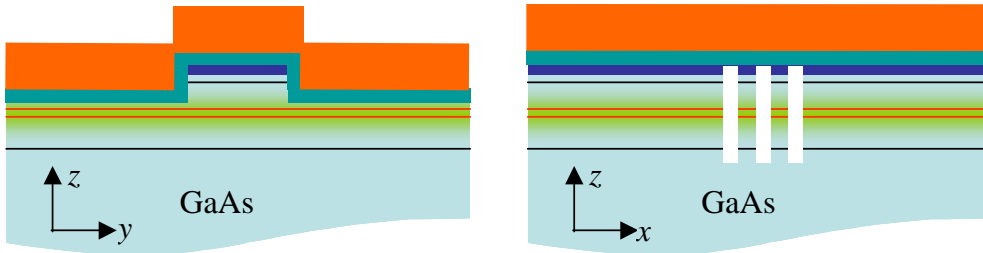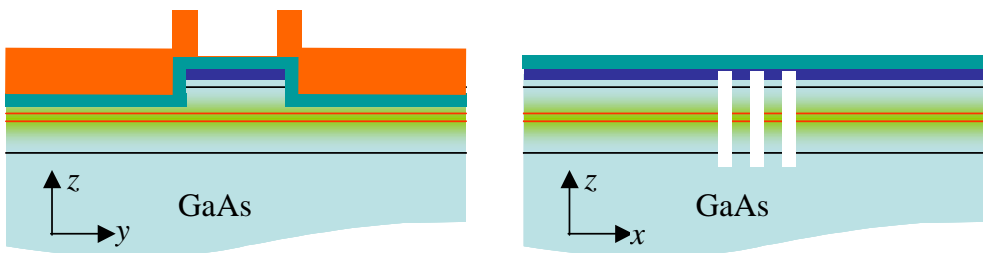
Figure 7.13. CCM device schematic showing two cross-sections, one across the ridge (Cut *A*) and one along the ridge but across the ICR (Cut *B*), which will be used to illustrate the wafer profiles at each processing step in Table 7.1.

Table 7.1. Illustrated process flow for the fabrication of CCM lasers.
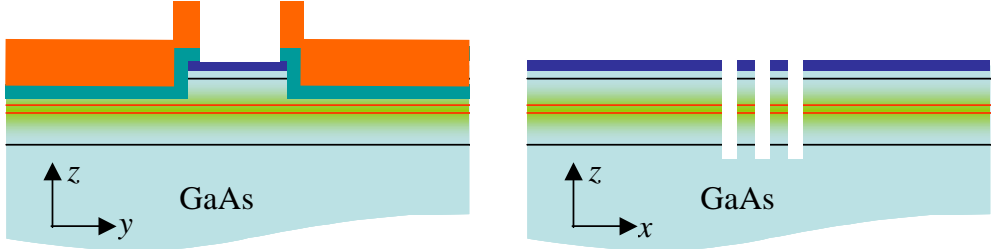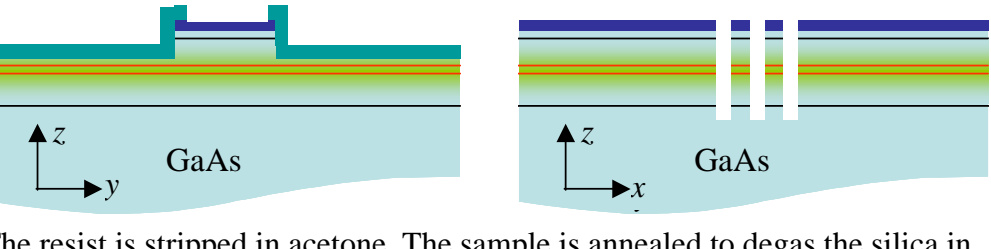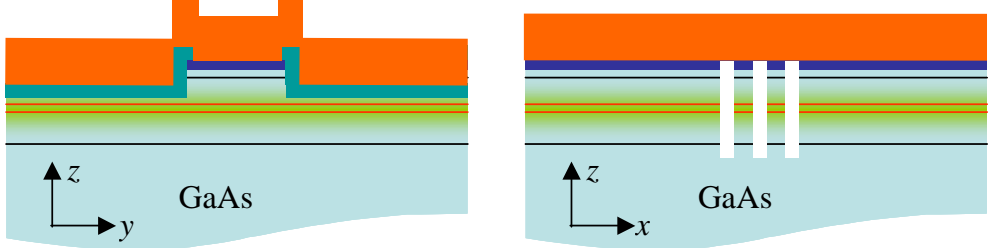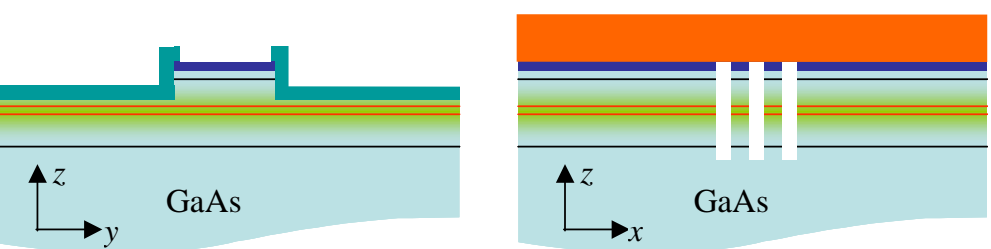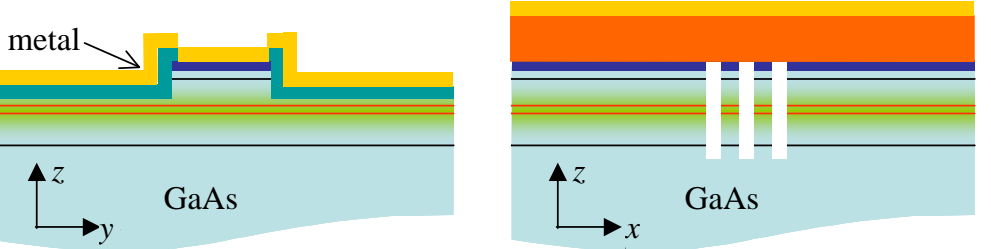
No	Cut *A*	Cut *B*
1.	A sample is cleaved to size from a 2-inch wafer of semiconductor material. The sample is then cleaned in acetone, methanol and water. The as-grown material has an identical profile in all directions, with two quantum wells (red lines in the schematics above) buried inside cladding layers that are capped by a highly-doped p++ contact layer. The curved bottom denotes the near-infinite GaAs substrate, which is more than two orders of magnitude thicker (~ 500 µm) than the epitaxial waveguide shown.	
2.	A thin layer of silica is deposited everywhere on the sample using plasma-enhanced chemical vapour deposition (PECVD). This will be used as a hardmask for the ICR etch of Step 6.	
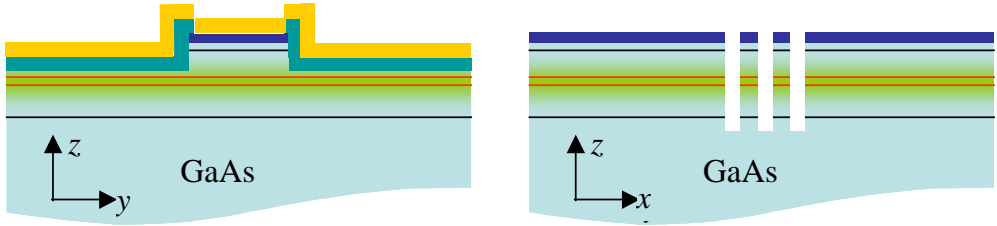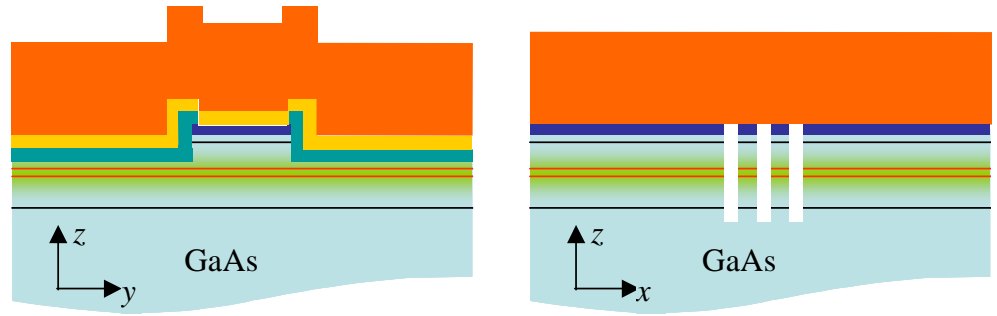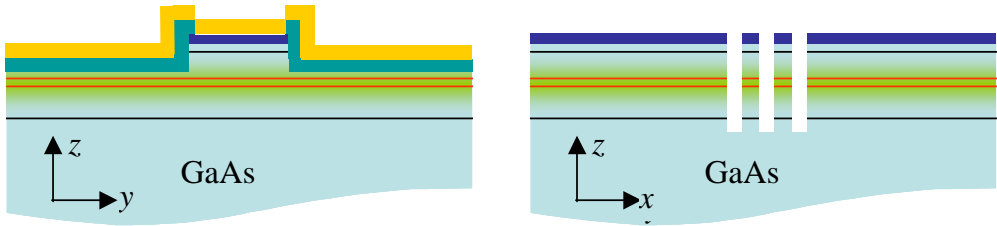
3.	A layer (in fact, a bi-layer recipe) of Aldrych PMMA e-beam resist is spun on the surface and hard-baked.
4.	A pattern containing multiple-slot PBG ICR features along with squares to be used as registration keys is exposed by the beamwriter. The resist is developed, with the ICR pattern shown above.
5.	The resist pattern is transferred into the silica hardmask using a dry-etch step with CHF_3 gas.
6.	The ICRs and registration keys (not shown) are etched deep inside the semiconductor in a prolonged dry-etch step using $SiCl_4/O_2$ gas. The resist and the hardmask are eroded during the etch.
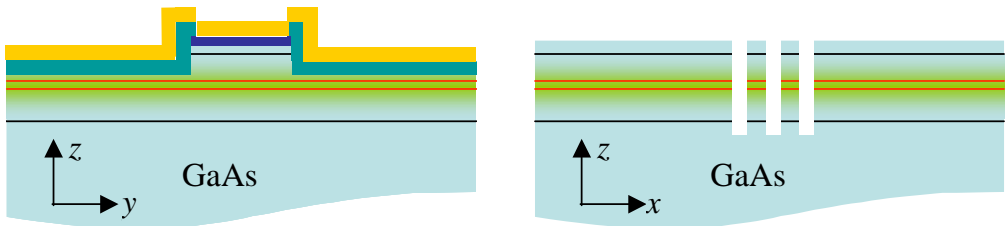
7.		Any remaining resist and silica hardmask are stripped using acetone and buffered hydrofluoric acid.
8.		A new layer of PECVD silica is deposited. It will be used as a hardmask for the ridge etch of Step 12. Due to the smallness of the ICR slots, they get closed up with the silica at the top.
9.		E-beam resist is spun and baked.
10.		The ridge pattern is exposed by the beamwriter; the resist is developed.
11.		The silica hardmask is dry-etched using CHF_3 gas.

12.	
	The ridge is dry-etched using SiCl$_4$ gas to required depth, which is monitored *in-situ* with a laser-based interferometer.
13.	
	The resist and silica hardmask are stripped using acetone and buffered hydrofluoric acid.
14.	
	A new layer of PECVD silica is deposited. It will be used as an insulation layer between the p++ contact layer and metal pads.
15.	
	E-beam resist is spun and baked.
16.	
	The contact window pattern and the seed nick window pattern for precision cleaving (not shown) are exposed by the beamwriter; the resist is developed.

17.	
	The contact and seed nick windows in silica are wet-etched using a buffered HF solution.
18.	
	The resist is stripped in acetone. The sample is annealed to degas the silica in order to avoid contact metal peeling at the contact anneal stage (Step 29).
19.	
	E-beam resist (lift-off recipe) is spun and baked.
20.	
	The lift-off pattern is written and developed, leaving resist in isolation areas (between device sections) and removing resist in areas requiring metallisation. The sample is then ashed in oxygen to purge the surface.
21.	
	A stack of metals with gold as the topmost layer is evaporated. A second evaporation step is performed while rocking the sample to ensure the metal covers the ridge sidewalls.

22.	 Unwanted metal is lifted off with the resist in acetone.
23.	 A thick layer of photoresist is spun and hard-baked.
24.	See Figure 7.12(b) Edges of the sample containing the seed nick windows are exposed in the mask aligner. The resist is developed away in these areas.
25.	See Figure 7.12(c) A prolonged wet-etch step is used to define the cleaving nicks.
26.	 The photoresist is stripped in acetone. See also Figure 7.12(d)
27.	*(Image as above)* The sample is mounted p-side down on a glass cover slip and thinned by lapping against alumina grit on a glass plate. The sample is then removed from the slip and cleaned in acetone.
28.	*(Image as above)* The sample is again mounted p-side down on a glass cover slip and the back side of the sample is metallised with evaporated n-contact metal.
29.	*(Image as above)* The sample is removed from the slip and annealed in a rapid temperature cycle to form ohmic contacts between GaAs and the evaporated metal.

30.	An isolation wet etch is performed to remove the highly-doped GaAs layer on top of the ridge and obtain high electrical isolation between the different sections of the device.
31.	Contact resistance measurements are performed using the TLM patterns on the sample.
32.	The sample is cleaved into bars using the wet-etched nicks. Each bar is then diced to obtain individual CCM laser chips.
33.	The chips are bonded onto gold-plated copper heatsinks using indium balls. The indium is heated to melting point and spread over the heatsink surface, with solder flux being used to prevent oxidation. A laser chip is then placed on the heatsink, aligned and allowed to cool. As the placement and alignment of individual chips proved very difficult, whole bars of undiced devices were mounted on some heatsinks.
34.	Flux residues are removed by solvent clean.

No wire bonding was used, as the mounted devices were tested using needle probes.

7.3. Fabricated devices

A total of 33 straight-waveguide CCM laser samples was fabricated in the course of the Project, with 14 major design changes. Four samples of bent-cavity lasers were also processed. Shown below are some photographs of the fabricated devices.

7.3.1. CCM lasers

Initially, *m:n*-type cavity ratio lasers were fabricated. They utilised cavities defined both by etched and cleaved facets, as shown in the photographs of Figure 7.14. These early devices had single-slot, shallow-etched ICR features. Cleaved facets were used in all subsequent device generations.
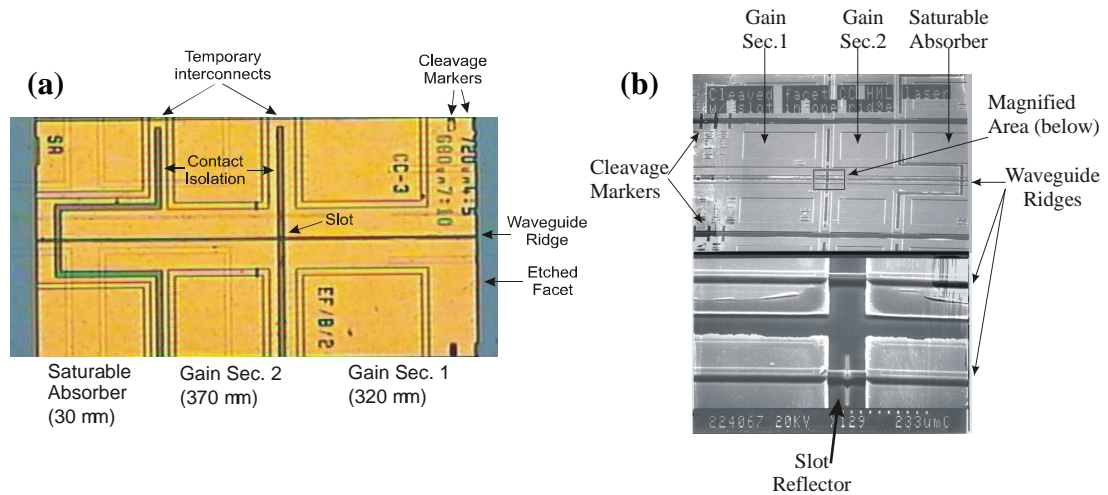
Figure 7.14. Photographs of early *m:n* cavity ratio CCM lasers. **(a)** Plan view of an etched-facet device as seen under an optical microscope. **(b)** Scanning electron microscope image of a cleaved facet device.

To assess the performance of different types of ICR, a reference ridge waveguide laser with no ICR feature was included in the same chip as the CCM laser. An optical photograph of such a twin laser chip is given in Figure 7.15.
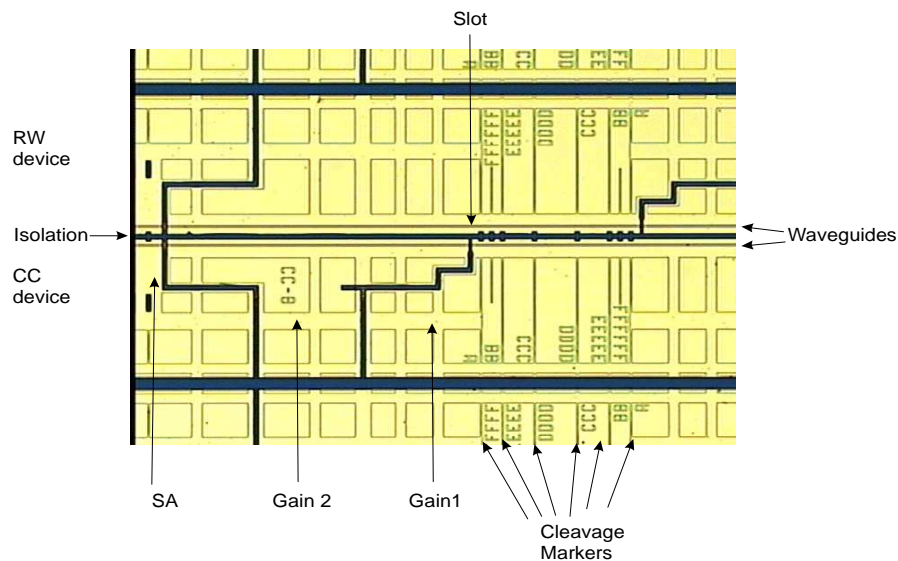
Figure 7.15. Plan view photograph of a complete 1:*n* ratio twin laser chip. Lower and upper halves form two electrically and optically independent devices (a CCM laser and an identical ridge waveguide laser).

The wet-etch-facilitated precision cleaving technique described in Section 7.1.3 has proven very successful for the accurate definition of cavity lengths. Photographs of a final fabricated sample are shown in Figure 7.16 both in plan **(a)** and side **(b)** views. The vertices at the bottom of the etched pits run opposite the cleavage markings on the CCM devices.

158
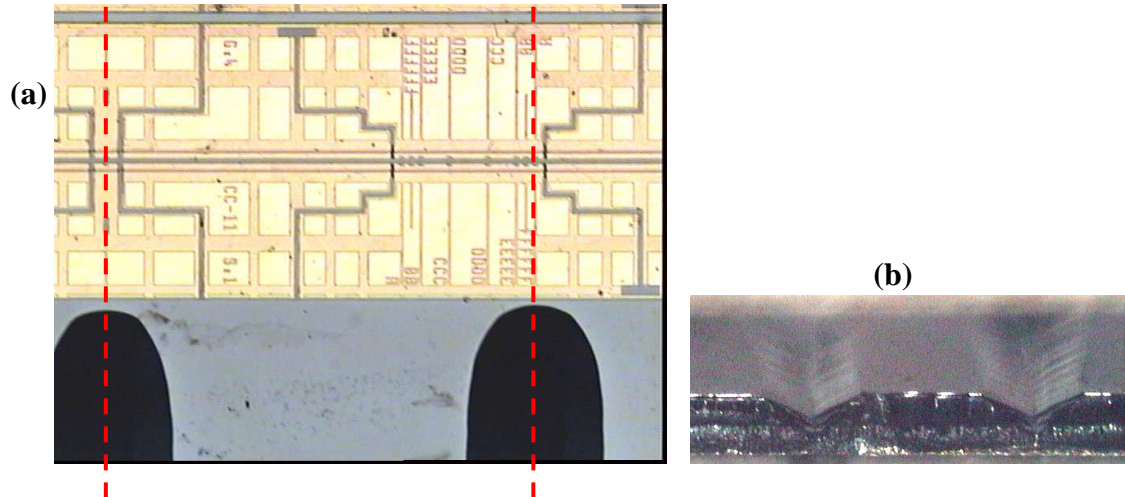
Figure 7.16 Plan view **(a)** of etched nicks opposite cleavage markings separating CCM devices, and corresponding profile of the fabricated sample **(b)**.

Finally, a SEM image of a mounted high-asymmetry CCM laser chip is shown in Figure 7.17. The magnified ICR features in both waveguides are shown in the bottom part of photograph **(a)**, with an image of the facet and the ridge profile given in inset **(b)**.
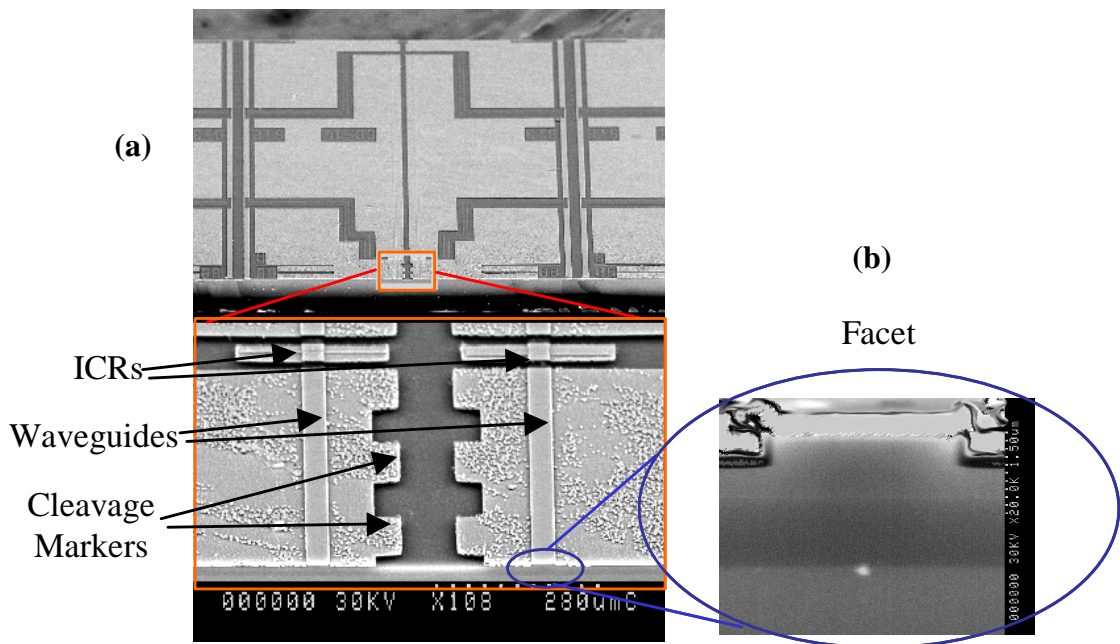
Figure 7.17. SEM image of a mounted 1:30 ratio CCM chip. The bottom part of photograph **(a)** shows a magnified view of the shorter sub-cavity including the PBG ICR features. The inset **(b)** is an enlarged image of the front facet.

7.3.2. Bent-cavity lasers

Only four samples of bent cavity-lasers were fabricated to the designs of Section 5.3.3. As this work was carried out at a relatively early stage in the Project,

the fabricated devices suffered from a range of processing issues, particularly the difficulty with the deep etching of the bent waveguide ridges and metal coverage of the sidewalls. Due to the limited resources and tight timescales, this type of CCM laser was not developed beyond the four trial samples.

A plan-view photograph of a cleaved quarter of a fabricated arc-cavity CCM laser array is presented in Figure 7.18. The chip incorporates four lasers of varying curvature and a Y-junction laser, all having a common saturable absorber section. Furthermore, a sample containing couplers of Y and MMI types was fabricated. A photograph of the sample just after cleaving, with a different type of coupler on either side of the cleave line, is shown in Figure 7.19(a). The Y-junctions were particularly difficult to fabricate, owing to the narrow split region between the two waveguides. The small split feature had to be written in a separate step by the beamwriter using the technique developed for the bow-tie slot as described in Section 7.1.2. This, however, led to alignment problems and caused asymmetry and stitching issues in the fabricated Y-couplers, which are visible in the magnified SEM image of Figure 7.19(b). Due to these technological challenges, the MMI-type coupler would be the preferred solution for future bent-cavity CCM lasers.
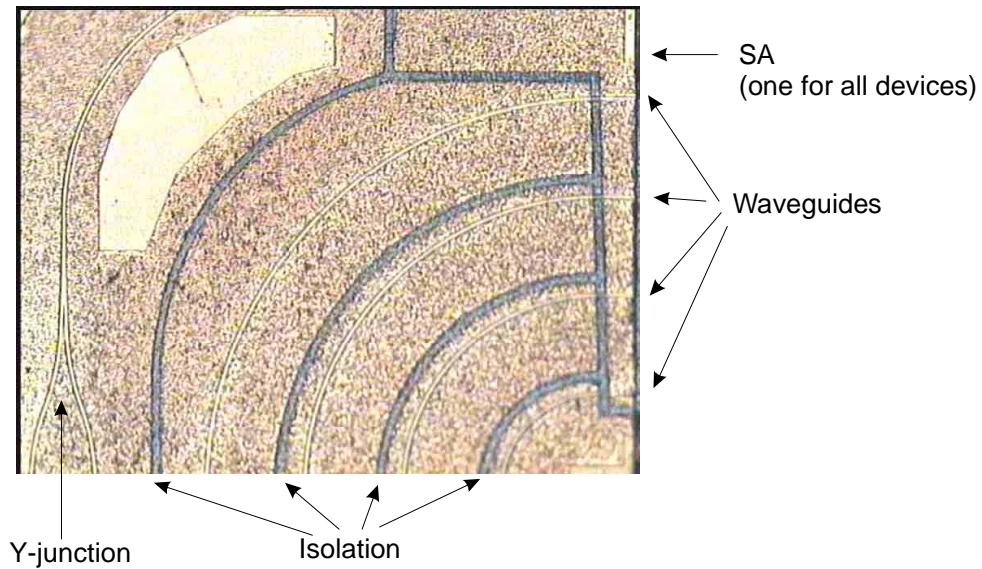
Figure 7.18. Bent waveguide lasers with varying curvature radii.
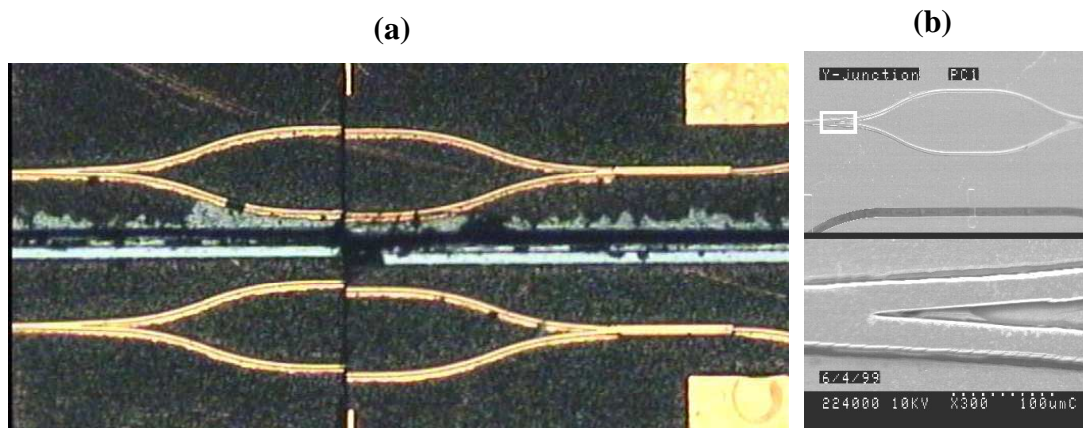
Figure 7.19. (a) Y-junction (left) and MMI coupler (right) on either side of a cleaved trial sample; **(b)** SEM image of a fabricated Y-junction showing an alignment error in the magnified area.

7.4. References

[1]   P. Vettiger, M. K. Benedict, G. L. Bona, P. Buchmann, E. C. Cahoon, K. Datwyler, H. P. Dietrich, A. Moser, H. K. Seitz, O. Voegeli, D. J. Webb, and P. Wolf, "Full-Wafer Technology - A new approach to large-scale laser fabrication and integration," *IEEE J. Quant. Elec.*, vol. 27, pp. 1319-1331, 1991.

[2]   H. Saito, Y. Noguchi, and H. Nagai, "High-performance InGaAsP/InP 1.3um laser structures with both facets etched," *Elec. Lett.*, vol. 22, pp. 1157-1158, 1986.

[3]   S. K. Murad, C. D. W. Wilkinson, P. D. Wang, W. Parkes, C. M. Sotomayor-Torres, and N. Cameron, "Very low damage etching of GaAs," *J. Vac. Sci. Technol. B*, vol. 11, pp. 2237-2243, 1993.

[4]   T. F. Krauss, B. Vogele, and R. M. D. L. Rue, "Waveguide microcavity based photonic microstructures," *IEEE Phot. Tech. Lett.*, vol. 9 (2), pp. 176-178, 1997.

[5]   G. R. Fowles, "Propagation of light in conducting media," in *Introduction to Modern Optics*: Dover Pubns, 1999, pp. 160-163.

[6]   R. Williams, "Wet etching," in *Modern GaAs processing methods*: Artech House, Boston, London, 2nd ed., 1990, pp. 95-114.

[7]   T. G. Kim, S. M. Hwang, E. K. Kim, S. K. Min, J. Jeon, S. Leem, J. Jeong, and J. Park, "Fabrication of V-Grooved Inner Stripe GaAs-AlGaAs Quantum-Wire Lasers," *IEEE Phot. Techn. Lett.*, vol. 9, pp. 135-8, 1997.

CHAPTER 8.

MEASUREMENT OF MODELOCKED

OPTICAL PULSE TRAINS

Following the fabrication of compound-cavity modelocked (CCM) lasers, the next challenge was to demonstrate their modelocking operation at terahertz frequencies and assess the quality of their pulses. With pulse widths on a picosecond time scale and pulse separation of the order of the pulse width itself, the task of characterising such pulse trains can actually prove more exacting than generating them! Indeed, as the bandwidth of commercially available photodetectors extends to only tens of gigahertz, no direct measurement is possible that would confirm the pulsed nature of a CCM laser beam, let alone extract its pulse characteristics, at (sub)terahertz frequencies. Therefore, other, indirect measurement techniques, such as autocorrelation, have to be used to obtain pulse information of interest.

In this Chapter, an overview of common pulse characterisation methods will be given, followed by a brief primer on autocorrelation theory and a description of the experimental set-up and of the different types of autocorrelator detectors used.

8.1.   Overview of ultrafast optical pulse characterisation techniques

There are two main instruments for directly characterising the output of modelocked lasers in the time domain: fast photodiodes and streak cameras. For a full characterisation, such techniques must be able to obtain a value for the repetition frequency and the temporal width and shape of the modelocked laser pulses. Ultrafast photodetectors, when used with fast sampling oscilloscopes, allow time-modulated signals to be characterised with frequencies of up to tens of gigahertz. With special designs, such as uni-travelling-carrier photodiodes, the frequency limit can be pushed to 300 GHz, as was already mentioned in the discussion on direct detection in Section 2.3.1 of Chapter 2. As noted above, this approach is not suitable

for the direct assessment of ultrafast CCM lasers, with (sub)-terahertz modelocking frequencies and pulse widths of the order of 1 ps.

Another possibility would be to use electron-optical streak cameras. The method of studying rapidly varying luminous phenomena by electro-optical chronography was originally proposed in the 1960's [1]. Streak cameras have the ability to determine directly the profile of optical pulses combined with two-dimensional analysis, such as time-resolved spectroscopy, i.e., measurement of time variation of incident light with respect to its wavelength. However, the instrument typically has a resolution limited to around 2 ps, which, again, would be inadequate for the measurement of CCM laser pulses. Furthermore, streak tubes have a low sensitivity in the near-infrared region, so the generally low power in modelocked semiconductor laser pulses makes them difficult to detect with a streak camera. Synchroscan operation (rather than a single shot) is required [2], where the detected signal is integrated over a large number of periods to obtain sufficient signal-to-noise discrimination. To achieve this, the camera must be triggered by a sub-multiple of the modelocked laser repetition frequency, which presents an issue for ultrafast CCM lasers. The author's colleague Dr M. Street attempted the use of a streak camera to characterise the output of 850 nm CPM laser diodes modelocked at 40 – 100 GHz. His conclusion was that the low optical power available from the CPM lasers precluded their analysis using this instrument.

Ultrashort pulses can also be characterised by inferring pulse information from indirect measurements. The most commonly used indirect pulse characterisation methods involve interferometer-based autocorrelation measurements. In interferometers, light beams are split and optical path differences are introduced between them so that, on analysis of the recombined beams, information about the original signal can be deduced. By using interferometers, timescales on the order of femtoseconds are converted into path length differences of micrometres, easily obtainable with precision translation stages. The interference signals produced can also be processed using low-speed electronics.

Other correlation techniques can be used that rely on a non-linearity to create a shorter pulse than the one being measured and use the former as a gate to probe the latter. An example of such a technique is frequency-resolved optical gating (FROG) [3], where a shutter based on the Kerr effect is employed. In FROG, a tandem

combination of autocorrelation and spectrum are used to extract shape and pulse information from ultrashort pulses. The measurement provides directly a representation of the pulse as a two-dimensional function of frequency and time. In Ref.[4], the FROG technique was successfully applied to the measurement of modelocked laser diodes. Other methods rely on the determination of pulse shape from the distortion of the pulse spectrum in a non-linear material. Ultrafast optoelectronic sampling techniques [5], similar to the pump-probe configurations described in Section 1.3.2 of Chapter 1, can also be used for ultrafast pulse characterisation, however, they themselves require femtosecond-scale pulses to probe the (sub)picosecond pulses of interest.

8.2.   Principles of autocorrelation measurements

Autocorrelation studies have been chosen as the preferred method for the characterisation of ultrafast CCM lasers. Of all the correlation techniques, autocorrelation is the easiest to implement experimentally, as the pulse under study is probed with multiple replicas of itself, with no separate probe pulse required. As a result, however, autocorrelations are always symmetric and can only deliver limited information about the pulse of interest, with data on the pulse phase, coherence, chirp and timing jitter obtainable through deconvolution only by assuming a specific pulse shape.

Autocorrelations are obtained by splitting the pulse in two and introducing a controlled delay between the original pulse and its replica before recombining them in a photodetector. This can be achieved by a Michelson-type interferometer or another arrangement, e.g., a Wallaston prism [6]. The photodetector response is then measured as a function of the delay between the two pulses. In the case of a train of modelocked pulses, instead of a single pulse, the ensemble-averaged autocorrelation function $G(\tau)$ of pulse delay τ is usually measured:

$$G(\tau) = \frac{1}{N} \sum_{j=1}^{N} G_j(\tau)$$

(8.1)

where $G_j(\tau)$ is the autocorrelation of the j-th pulse in a train of N pulses. If the pulse characteristics, such as pulse width, are fluctuating during the train, the averaged

autocorrelation $G(\tau)$ will reflect the train statistics rather than the properties of individual pulses.

Since the seminal work by Weber [7] in 1967, pulse characterisation through autocorrelation methods has been the subject of continuing research. A well-developed theoretical apparatus now enables the experimentalist to deconvolve pulse characteristics from measured autocorrelation and spectral data. For an in-depth treatment of autocorrelation theory, the reader is referred to reviews [8-12]; a rigorous theory of ultrashort pulses and their measurement in terms of Fourier-transform formalism can be found in book [3]. In this Section, only a concise summary of the pertinent theory will be given.

Two types of pulse measurement techniques will be discussed here: linear (field) and non-linear (intensity and interferometric) autocorrelations. Both require a Michelson-type interferometer set-up, which will be described in detail in Section 8.3.2, but differ in the type of detector used.

8.2.1. Linear (field) autocorrelation

The linear autocorrelation, also referred to as field correlation, uses the Michelson interferometer with a conventional square-law detector. The signal generated by such a detector is proportional to the square of the electrical field of incident electromagnetic waves. The detector output thus depends linearly upon the time-averaged intensity of the incoming signal. Consider a pulse having a field envelope $E_0(t)$, which is split into two pulses of equal amplitude $E_0(t)/\sqrt{2}$. The interferometer introduces a time delay τ between the pulses, so their real field amplitudes can be represented as

$$E_1(t) = \frac{E_0(t)}{\sqrt{2}}\exp(i\omega t) \; ; \;\; E_2(t) = \frac{E_0(t+\tau)}{\sqrt{2}}\exp[i\omega(t+\tau)] \tag{8.2}$$

where $E_0(t)$ is assumed to be a slowly-varying pulse envelope with respect to the optical angular frequency ω. Neglecting any phase difference, the instantaneous signal intensity $I(t,\tau)$ becomes

$$I(t,\tau) = c\varepsilon_0 \left\langle [E_1(t)+E_2(t)]^2 \right\rangle_{time} \cong \frac{c\varepsilon_0}{4}[E_0(t)+E_0(t+\tau)]^2 \tag{8.3}$$

where ε_0 is the electric permittivity of vacuum, c is the speed of light, and time-averaging is performed over a few optical cycles but still on a timescale much smaller than delay τ. For an ultrafast pulse train, whose repetition frequency exceeds the detector bandwidth (i.e., the detector response is slow compared to τ), the linear photo-response $J_1(\tau)$ is proportional to

$$J_1(\tau) \propto \int_{-\infty}^{+\infty} I(t,\tau)dt \propto WG_1(\tau) \qquad (8.4)$$

In the above expression, W is the pulse energy and $G_1(\tau)$ is the amplitude autocorrelation function:

$$W = \int_{-\infty}^{+\infty} E_0{}^2(t)dt \; ; \quad G_1(\tau) = 1 + \frac{\int_{-\infty}^{+\infty} E_0(t)E_0(t+\tau)dt}{\int_{-\infty}^{+\infty} E_0{}^2(t)dt} \qquad (8.5)$$

When the path lengths of the two interferometer arms are equal, i.e., $\tau = 0$, the linear autocorrelation function $G_1(\tau)$ of Eq.(8.5) is at its maximum value of 2. For the case where τ is such that no overlap occurs between the two pulses, $G_1(\tau)$ approaches unity, which results in a signal-to-background ratio of 2:1 in the measured photo-response signal of Eq.(8.4).

Thus the output signal of a linear autocorrelator is proportional to the first order, or linear, correlation function of the electric field. However, the practical use of such an instrument as a pulse characterisation tool is quite limited. Indeed, the Wiener-Khintchine Theorem (also known as the Autocorrelation Theorem) states that the linear autocorrelation function and the power spectral density are related through the Fourier transform. Since the power spectral density contains no phase information, a linear correlation cannot, in principle, offer a measurement of the actual pulse width. The linear autocorrelator, therefore, can only provide as much information about a pulse train as a spectrometer. With the convenience afforded by modern spectrum analysers, the use of such an interferometer for spectral measurements would be superfluous.

The instrument, however, can still be used as a tool for measuring the coherence time of a laser output [13]. A semiconductor laser modelocked at the fundamental harmonic gives out a pulse train with a repetition frequency determined

by the photon cavity round-trip time (CRT). However, an incoherent multi-mode laser (non-modelocked) will also exhibit a general pulsation behaviour at this frequency. The pulsation arises from the modes beating together as they chaotically drift in and out of phase with one another. The pulses emitted by an incoherent multi-mode laser vary significantly in amplitude, phase and width, with many sub-peaks and satellite pulses. Thus, it should be expected that, owing to the averaging effects in a linear correlation of such a device, a correlation signal should be observed not only at zero delay, but also at delays equal to multiples of the CRT of the laser. Due to the increase in the drift of the mode phases as time passes, it is also reasonable to expect the magnitude of the correlation peaks to decrease with increasing delay.

In practice, the output of a linear autocorrelator consists of a series of peaks, or coherence spikes, at delays corresponding to the inverse modal frequency separation of the laser spectrum, with amplitudes exponentially decreasing with increasing delay. The width of the coherence spikes represents the transform-limited pulse width, i.e., the shortest possible pulse width attainable with the given spectrum. The average time over which a laser mode is self-coherent is called the coherence time τ_c and is defined as the time over which the correlated signal falls to $1/e$ of its value at zero delay. Thus a linear autocorrelator can be used to study the coherence properties of semiconductor lasers [14, 15].

Obviously, the presence of coherence spikes alone in a linear autocorrelation of a laser beam is not sufficient to indicate the presence of modelocking. For an incoherent multi-mode laser diode, the coherence time and cavity round-trip time are very close, resulting in a rapid fall-off in the magnitude of the coherence spikes [14, 15]. However, in an ideal modelocked laser diode, the coupling of the modes prevents their phases from drifting, with the coherence time approaching infinity. Even for the practical non-ideal modelocking case, where some broadening of the pulse is present, the extension of the coherence time beyond the CRT leads to a high level of inter-pulse coherence. Thus observation of the coherence time of the output of a laser can allow one to distinguish between modelocked and incoherent multi-mode operation in laser diodes. To this end, the linear autocorrelator is used with long time delays (several CRT's) to enable correlation between consecutive pulses. In contrast to autocorrelation, which is performed at interferometer path differences of around zero, this mode of cross-pulse measurement is called cross-correlation.

Cross-correlation studies were successfully used by the author's colleague Dr S.D. McDougall to corroborate the modelocking operation of CPM laser diodes [13]. It should be noted that the measurement of enhanced coherence in modelocked lasers can only be used as supporting, but not sufficient, evidence of modelocking. Intensity autocorrelation measurements should be carried out to obtain pulse information as well as to confirm modelocking operation beyond dispute.

8.2.2. Non-linear autocorrelations

As explained in the previous section, the linear auto/cross-correlation, whose output is proportional to the correlation function of the electric field, can only serve as an indirect verification of the modelocked nature of a laser beam via change in the coherence time against the non-modelocked output of the same laser. The only pulse width information that can be derived is that of the transform-limited value (which will be formally defined in Section 8.2.3), which can easily be estimated from a measurement of the power spectrum of the laser output, as the two are linked via the Fourier transform. In other words, even if modelocking is assumed, a linear correlation of the pulse electric field will not differentiate between chirped and transform-limited pulses.

This problem can be solved by using the Michelson interferometer with a non-linear detector. It can be shown that the higher the order of the non-linearity being used, the more accurately it is possible to characterise a pulse train [3]. In the simplest case, a second-order non-linearity is used, so that the output of a detector is proportional to the square of incident intensity. Detectors based on second-order non-linear processes, such as second-harmonic generation (SHG) and two-photon absorption (TPA), are commonly employed for autocorrelation measurements. These detector types will be discussed in more detail in Section 8.4.

Slow (intensity) autocorrelation

Using the same formalism as in Eqs.(8.2)-(8.3), the photo-response signal $J_2(\tau)$ of a second-order non-linear intensity detector can be expressed as

$$J_2(\tau) \propto \int_{-\infty}^{+\infty} I(t,\tau)^2 \, dt \propto \int_{-\infty}^{+\infty} \left[\left| E(t) + E(t+\tau) \right|^2 \right]^2 dt \propto W G_2(\tau) \tag{8.6}$$

where W is the pulse energy and $G_2(\tau)$ is the intensity autocorrelation function. The expression for $G_2(\tau)$ can take different forms depending on the resolution and measurement speed of the interferometer set-up. If the measurement system does not have the sensitivity to resolve the interference pattern formed by the two beams, or the detector lacks the speed to respond to the fast-varying interferometric fringes, the autocorrelation is referred to as slow, or simply intensity autocorrelation, with the function $G_2(\tau)$ obtained by time-averaging Eq.(8.6) [8]:

$$G_2(\tau) = 1 + \frac{2\int_{-\infty}^{\infty} E^2(t) E^2(t+\tau)\, \mathrm{d}t}{\int_{-\infty}^{\infty} E^4(t)\, \mathrm{d}t} = 1 + 2\frac{\int_{-\infty}^{+\infty} I(t) I(t+\tau)\, dt}{\int_{-\infty}^{+\infty} I^2(t)\, dt} \tag{8.7}$$

Analysis of Eqs.(8.6)-(8.7) shows that the intensity autocorrelation can distinguish clean, well-defined modelocked pulses from periodically modulated noise. In both cases, at zero delay $G_2(\tau) = 1+2 = 3$ by definition. For well-defined modelocked pulses, the modulation depth is 100%, so as delay τ increases, $G_2(\tau) \rightarrow 1+0 = 1$. This gives an intensity autocorrelation peak-to-background ration of 3:1 for the modelocked case. For the modulated noise of an incoherent multi-mode laser, the average modulation is statistically half the peak value, so in this case the contrast ratio is 3:2.

Fast interferometric autocorrelation

We will now consider the full form of the autocorrelation function of Eq.(8.6) without simplification by time-averaging. The full time-resolved expression is

$$G_2(\tau) = 1 + \frac{2\int_{-\infty}^{\infty} E^3(t) E(t+\tau)\, \mathrm{d}t + 2\int_{-\infty}^{\infty} E(t) E^3(t+\tau)\, \mathrm{d}t + 3\int_{-\infty}^{\infty} E^2(t) E^2(t+\tau)\, \mathrm{d}t}{\int_{-\infty}^{\infty} E^4(t)\, \mathrm{d}t} \tag{8.8}$$

With field amplitude $E(t)$ having the form of Eq.(8.2), the above equation will contain terms that rapidly vary with τ. Resolution of these fast variations requires a high degree of accuracy in each path length step, which must be better than around 1/10 of the smallest wavelength present [8]. Autocorrelations, where these requirements are adhered to, are known as interferometric, or fringe-resolved. Providing that the central wavelength of the pulse is known, and there is not excessive chirp present, the fringe spacing enables interferometric autocorrelation traces to be self-calibrating. In this case, the contrast ratio between the measured

signals when the pulses overlap ($\tau = 0$) and when they do not (background signal) is 8:1, as can be seen from Eq.(8.8).
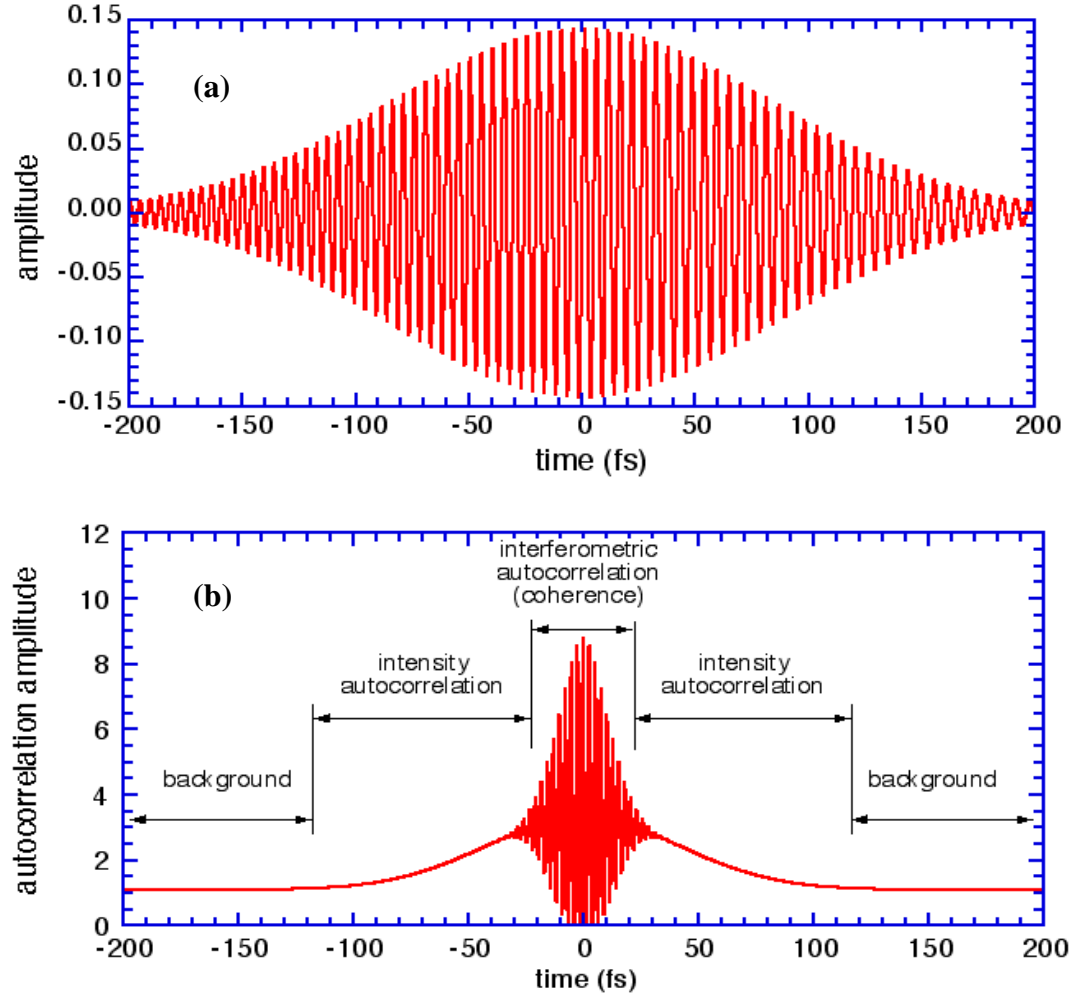
Figure 8.1. Example of an optical pulse in the time domain **(a)** and corresponding intensity autocorrelation **(b)** as a function of time delay [16].

When the two interferometer arms differ in length by only half a wavelength, the two *E(t)* fields will cancel, producing zero signal. Where they put the two copies of the pulse in phase, the *E(t)* field will be double, with the non-linear detector signal 8 times the background signal. So as long as the pulses are coherent, there will be deep fringes that oscillate every wavelength of path-length difference. Eventually, as the pulses overlap but are not coherent, the signal will be twice the background; finally, for widely different arm-lengths, there will be only a constant-level background signal from the two uncorrelated pulses. An example of such an autocorrelation is shown in Figure 8.1(b) for an optical pulse of Figure 8.1(a).
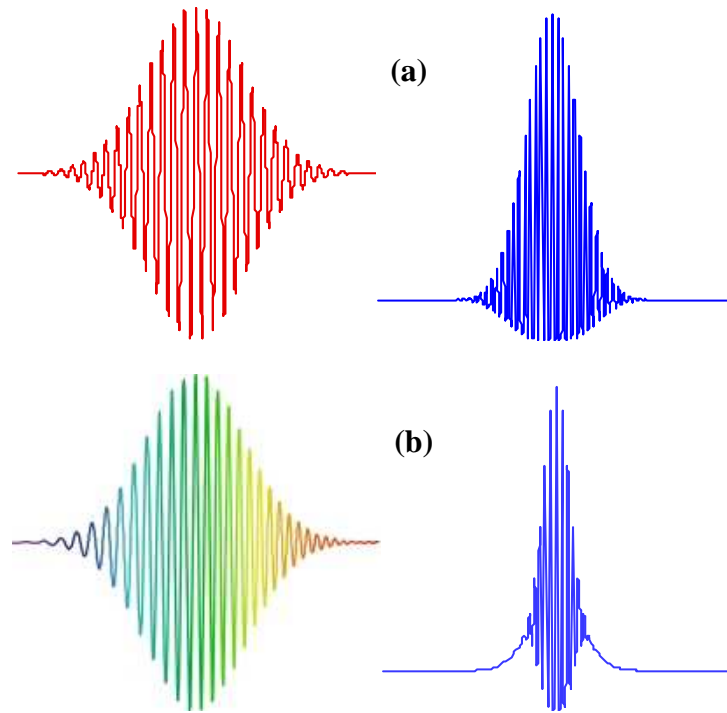
Figure 8.2. Temporal profile (left) and corresponding interferometric autocorrelation function (right) for unchirped **(a)** and chirped **(b)** pulses [17].

Since the interferometric autocorrelation, in contrast with the "slow" intensity autocorrelation, resolves individual optical cycles, it is also sensitive to frequency chirp. Frequency chirp in the pulse can be detected, because changes in instantaneous phase (and hence in carrier frequency) over the duration of the pulse will reduce the visibility of the fringes in the "wings" of the autocorrelation trace [18]. The effect of pulse chirp on the shape of interferometric autocorrelation is illustrated in Figure 8.2. For an ideal transform-limited chirp-free pulse of Figure 8.2(a), the autocorrelation shows well-defined interference fringes in the "wing" regions. However, one can observe a loss of coherence in the "wings" of the autocorrelation function of the chirped pulse of Figure 8.2(b), thus giving a false reading of the pulse width. The true pulse shape – in amplitude and phase – can be determined by simultaneously fitting the slow intensity autocorrelation, interferometric autocorrelation and optical spectrum [3].

8.2.3. Interpretation of autocorrelation data

Interpretation of measured autocorrelation traces can prove a challenging task owing to the inherent ambiguity of the measurement. Since second-order autocorrelation functions (both intensity and interferometric) are symmetric, the

measured autocorrelation trace $J_2(\tau)$ of Eq.(8.6) is also symmetric in time delay τ. The Fourier transform of a symmetric function is real, hence little information about the pulse shape can be extracted from the Fourier deconvolution of such a measurement. Furthermore, the intensity autocorrelation of Eq.(8.7) contains no explicit information about the pulse phase or its coherence.

There exist a number of definitions for key characteristics of short pulses [19], therefore it is important to adopt a single standard for assessing pulse width, both in the time and spectrum domains. Most commonly, pulse duration τ_p is defined as the full width at half-maximum (FWHM) of the intensity profile, and spectral width Δv_p as the FWHM (bandwidth) of the spectral intensity. Precisely because of the difficulty in asserting an exact pulse shape, standard waveforms have been selected as best approximations. The normalised profiles of most common pulse shapes, both in frequency and time domains, are shown in Figure 8.3.

——————— Gaussian pulse	$\mathcal{E}(t)$	$\propto$	$\exp[-1.385(t/\tau_p)^2]$
– – – – – – – sech - pulse	$\mathcal{E}(t)$	$\propto$	$\mathrm{sech}[1.763(t/\tau_p)]$
· · · · · · · · · Lorentzian pulse	$\mathcal{E}(t)$	$\propto$	$[1 + 1.656(t/\tau_p)^2]^{-1}$
——————— asymm. sech pulse	$\mathcal{E}(t)$	$\propto$	$[\exp(t/\tau_p) + \exp(-3t/\tau_p)]^{-1}$
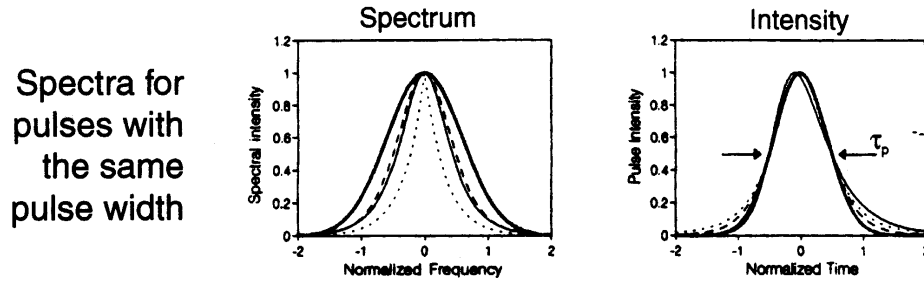
Figure 8.3. Spectra and temporal pulse profiles (normalised) for common pulse envelopes. τ_p denotes the FWHM of the pulse's intensity profile [19].

As the temporal and spectral characteristics of the electromagnetic field are related via Fourier transforms, pulse bandwidth Δv_p and duration τ_p cannot vary independently of each other. This fact is formulated by the Uncertainty Principle, which states that there is a minimum time-bandwidth product (TBP):

$$\Delta v_p \Delta \tau_p \geq K \qquad (8.9)$$

where K is a numerical constant of the order of unity, depending on the actual pulse shape. Examples of pulse shapes and corresponding relationships between temporal and spectral widths, along with their minimum TBPs, are given in Table 8.1.

Table 8.1. Relationship between pulse characteristics and minimum time-bandwidth product (TBP) for common pulse envelopes. $\Delta \omega_p = 2\pi \, \Delta \nu_p$ denotes the FWHM of the spectrum profile [19].

Field envelope	Intensity profile	τ_p (FWHM)	Spectral profile	$\Delta \omega_p$ (FWHM)	TBP
Gauss	$e^{-2(t/\tau_G)^2}$	$1.177\tau_G$	$e^{-(\omega\tau_G)^2/2}$	$2.355/\tau_G$	0.441
sech	$\text{sech}^2(t/\tau_s)$	$1.763\tau_s$	$\text{sech}^2(\pi\omega\tau_s/2)$	$1.122/\tau_s$	0.315
Lorentz	$[1+(t/\tau_L)^2]^{-2}$	$1.287\tau_L$	$e^{-2|\omega|\tau_L}$	$0.693/\tau_L$	0.142
asymm. sech	$\left[e^{t/\tau_a}+e^{-3t/\tau_a}\right]^{-2}$	$1.043\tau_a$	$\text{sech}(\pi\omega\tau_a/2)$	$1.677/\tau_a$	0.278
rectang.	1 for $|t/\tau_r| \leq \frac{1}{2}$, 0 else	τ_r	$\text{sinc}^2(\omega\tau_r)$	$2.78/\tau_r$	0.443

The TBP of Eq.(8.9) is only equal to pulse-specific constant K for ideal pulses without frequency modulation (chirp), which are often called "bandwidth-limited" or "transform-limited". Such pulses exhibit the shortest possible duration at a given spectral width and pulse shape. If there is a frequency variation across a pulse, its spectrum will contain additional frequency components. Consequently, such a pulse possesses a spectral width that is larger than the Fourier limit given by Eq.(8.9).

Despite the ambiguity in estimating the above pulse characteristics from autocorrelation measurements, further information can be obtained by simultaneously measuring the optical spectrum of the signal. Simple pulse shapes can be fitted to autocorrelations and pulse spectra, with analytical expressions and constants available in the literature [3, 11]. For complex pulse shapes, a systematic fitting algorithm has been developed [20], which converges to the final signal amplitude and phase function without any *a priori* knowledge of pulse parameters. Another method that has been used is to record the spectrum of the non-linear signal generated in the autocorrelator, for each value of delay τ. The amplitude and pulse shape of the pulse can be reconstructed from these sets of measurements [21]. The

disadvantage of this method is in the large amount of data that has to be processed. Other methods involve insertion of a block of glass of known dispersion and thickness in order to break the symmetry of the autocorrelator and measure the asymmetry in the recorded interferometric traces [3].

The pulse characterisation procedure adopted for this Project is a fairly basic one and involves the simultaneous fitting of pulse shapes both to the spectral envelope of the lasing spectrum and the measured intensity autocorrelation trace. The procedure includes the following steps:

1. Select a spectral profile from the library of standard waveforms of Table 8.1 and try to obtain a best fit to the measured laser spectrum by varying the assumed pulse width.

2. After the best-fit standard pulse shape has been chosen, the autocorrelation trace is modelled using Eq.(8.6) and the theoretical autocorrelation peak width τ_{ac} obtained. Alternatively, analytical expressions for the autocorrelation peak profile and its width for each pulse form can be found in the literature [3, 11]. E.g., see Table 9.1 for information on the $sech^2$ pulse shape.

3. The theoretical autocorrelation peak width is compared with the measured one and Step 2 is repeated with different pulse widths until agreement is reached.

4. Time-bandwidth product is computed using the best-fit pulse width and the experimental spectrum bandwidth. Data in the literature can also provide the relationship between the measured autocorrelation peak width and pulse duration for a given pulse shape.

5. The TBP thus obtained is compared with the theoretical limit (constant K) listed in Table 8.1. The difference between the computed and transform-limited TBP's is indicative of the amount of chirp and phase modulation present in the pulse.

8.3.   Description of the autocorrelator measurement system

The Michelson interferometer is the most commonly used instrument for autocorrelation studies. It allows the delay τ to be scanned on a femtosecond timescale in order to record the autocorrelation trace for various degrees of temporal overlap between the two pulse trains. A general review of the implementation of intensity autocorrelation systems for laser diode pulse measurements can be found in Ref.[9]. In this Section, the experimentally realised autocorrelator system comprising a free-space optical delay set-up and measurement and control electronics will be described; the specific types of non-linear detectors introduced into this system will be the subject of Section 8.4. Initially, the laser characterisation part of the overall measurement system will be described.

8.3.1.   CW and pulsed laser characterisation

The measurement set-up for the characterisation of heatsink-mounted CCM lasers was built on a vibration-isolated optical bench with a total area of 2.5 m x 1.5 m. Copper heatsinks with bars of bonded CCM devices were screwed onto a Peltier-cooled mount on a lateral translation stage, allowing easy transition from one device to the next. For continuous-wave (CW) measurements, the CCM laser under test was pumped using a Newport 8000 twin laser driver, with the two current source modules used to independently drive the two gain sections of the CCM device. The bias on the saturable absorber section was applied using a protected voltage source.

In order to minimise heating effects, the CCM devices were also tested in pulsed current regime (not to be confused with ultrafast operation or modelocking; modelocked pulses have repetition frequencies several orders of magnitude higher, and equally shorter pulse widths, than the current pulses used here). As the pulsed laser characterisation rig used for the assessment of broad-area lasers described in Chapter 6 (see "Results", Section 6.2.1), was not suitable for the CCM devices due to their split contact configuration, a bespoke pulsed current set-up was built on the autocorrelator bench. An Avtec AVO-6D-B Laser Diode Pulser was used to generate 0.8 µs-wide current pulses on a duty cycle of around 0.3%. Three DC probes were used to bias each device section individually, with the length of the leads minimised

to reduce their inductance. Parasitic inductance can distort square current pulses, increasing their rise time and possibly causing inductive current spikes. A high-frequency SMA cable with a bandwidth of 1 GHz was used to deliver the pulses from the Avtech source to the probe heads. The cable was terminated by a resistor in series with the laser diode to create a combined 50 Ω load. The current through each gain section was controlled by placing a resistor into one of the probe arms. Such a crude current divider proved very inflexible, so in high-asymmetry CCM devices with a *Gain 1* section less than 60 μm long, only the longer *(Gain 2)* section was pumped by the current pulser, while the shorter one *(Gain 1)* was DC biased using one module of the CW laser driver. Large inductors were inserted in all DC bias circuits to protect them from the current spikes generated by the pulse source.

Optical output from one facet (SA side) was coupled into a lensed single-mode fibre and fed into the Advantest Q8381 or Anritsu MS96A optical spectrum analyser (depending on instrument availability) or a Melles-Griot power meter. The current pulse profile was obtained from a current probe (voltage drop across a known resistor) displayed on a Tektronix oscilloscope that was triggered by the current source. The trigger signal was also used to lock the optical power meter to the current pulses. The current pulser and oscilloscope were calibrated against the broad-area laser set-up of Section 6.2.1 by measuring the threshold current of a reference laser in both set-ups. The system was controlled by a PC running custom-written software, as will be explained in Section 8.3.3. The measurement system thus allowed the measurement of output optical power and spectrum of CCM lasers as a function of drive current, both in CW and pulsed regimes. The system in the CW regime configuration is illustrated in the left-hand part of Figure 8.4.

8.3.2. Autocorrelator set-up

Output from the other facet (i.e., opposite to the one used for the L-I/spectrum measurements above) was collected to characterise the modelocking behaviour of the CCM device by intensity autocorrelation studies. The complete measurement system is illustrated in the schematic of Figure 8.4, with a photograph of the optical delay (interferometer) set-up shown in Figure 8.5.
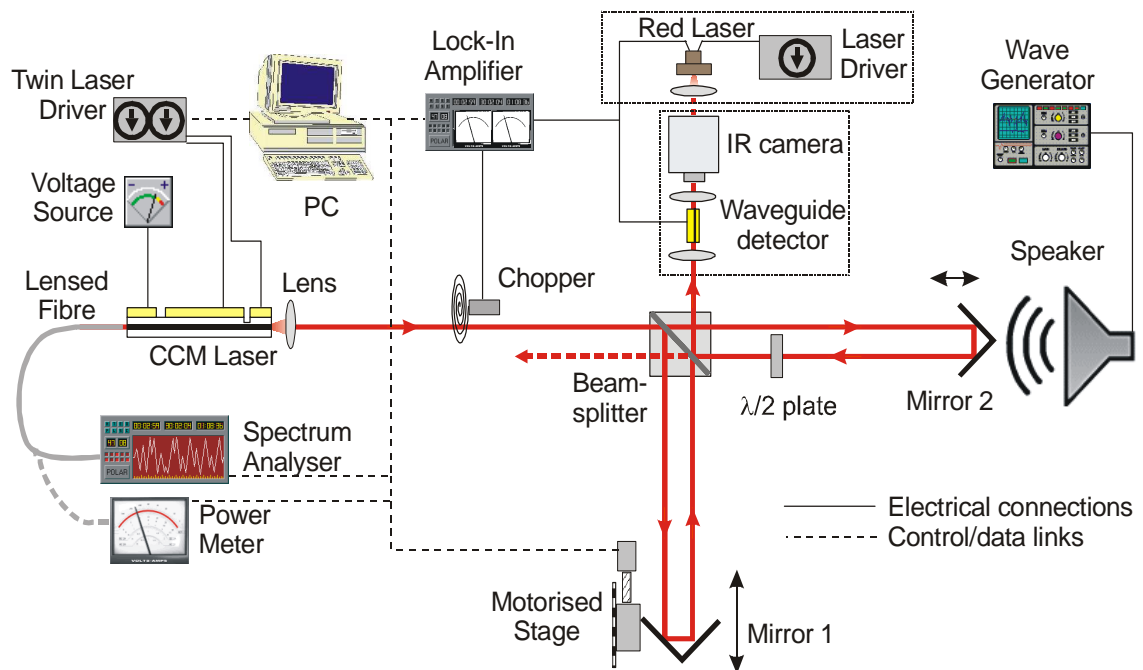
Figure 8.4. Diagram of the experiment set-up allowing simultaneous spectrum and autocorrelation measurements (CW configuration). Either a waveguide detector with an IR camera or a commercial red laser was used as a non-linear detector.
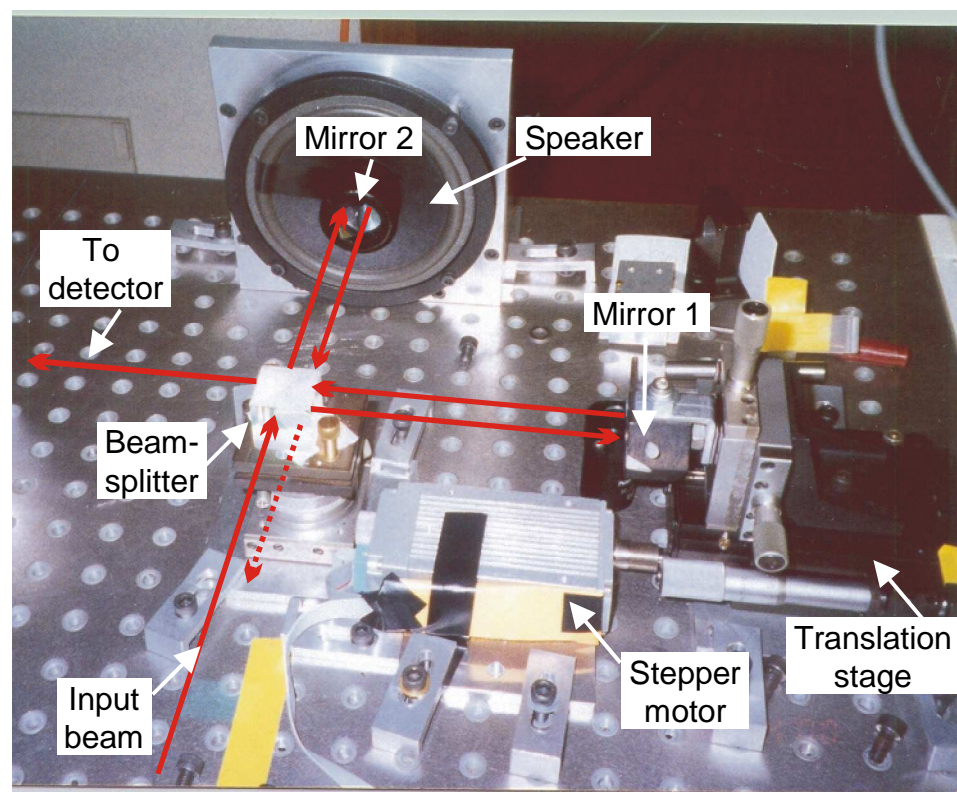
Figure 8.5. Photograph of the optical delay set-up within the autocorrelator system of Figure 8.4. The thick red arrows are superimposed to show the beam paths in the system.

The autocorrelator set-up comprised a Michelson-type interferometer, with one corner cube retroreflector (Mirror 1) positioned on a computer-controlled translation stage and the other one (Mirror 2) mounted on a an audio speaker. The choice of retro-reflecting corner cubes as Mirrors 1 and 2, rather than plane mirrors, was particularly appropriate for several reasons. First, the incident and reflected beams travel along different paths, which eliminates any reflection-related feedback into the laser. The unwanted beam returning from the beam-splitter (shown as a dotted line in Figure 8.4 and Figure 8.5) is sufficiently separated from the path of the incident beam not to be coupled back into the laser. Secondly, by the same virtue, the polarisation of the beam in one of the arms can be rotated by inserting a half-wave-plate, with the beam traversing the plate only once rather than twice, as would be the case with a plane mirror. Finally, corner cubes are much more tolerant to alignment errors than plane mirrors (especially in view of the fast oscillation of the loudspeaker), as the angle of the returning beam always follows that of the incident beam regardless of the small changes in the tilt of the reflector [9].

A StepperMike M10 stepper motor used to drive the translation stage had a positioning error of ±2 μm and a minimum step size of 1 μm. The translation stages of Mirror 1 and of the beam-splitter also had manual precision 3D controls to facilitate the optical alignment of the system. A non-polarising beam-splitter was used to both split and recombine the CCM laser pulse train, with variable delay introduced either by slowly translating Mirror 1 or rapidly sweeping Mirror 2 at the frequency of the loudspeaker, or both, depending on the type of measurement. The Philips audio speaker was specially selected to have a large sweep linearity as a function of bias and was driven by a sine-wave generator with an audio amplifier. The speaker with the mounted Mirror 2 had a resonance at 42 Hz, which was the sweep frequency used in interferometric experiments.

Due to the extremely small signal levels available from the non-linear detectors studied, a lock-in amplifier (EG&G 5210) had to be employed to improve the signal-to-noise discrimination. To achieve this, the instrument required an input signal modulated at some reference frequency and electrical trigger pulses at the same frequency to allow it to "lock in" to the signal of interest. In the CW configuration (i.e., when the CCM laser under test was biased with the DC current source), a Scitec optical chopper set at 290 Hz (i.e, away from the AC frequency of

the mains and harmonics of the loudspeaker frequency) was used to impart modulation to the CCM laser beam, with the reference signal fed into the lock-in amplifier. In the pulsed current configuration, the trigger signal of the current source at a frequency of around 4 kHz was used to lock the amplifier, with the chopper removed from the system.

8.3.3. Measurement automation

Automated experiment control and data acquisition proved to be indispensable to the successful realisation of autocorrelation measurements. An initial attempt at manually translating Mirror 1 to control the optical delay and recording the instrument readings had failed due to the sheer volume of data to be collected and the time required to do so. Furthermore, commercial data acquisition software (LabVIEW 6.0) was unable to run on the low-specification 200 MHz Pentium II PC available to this Project.

It was then decided to write a bespoke software package, codenamed MULINREC (MULti INStrument RECorder), in order to interface all relevant equipment to the PC and automate the experiment. The code was written in Turbo Pascal 6 using low-level control procedures obtained from Keithley Instruments, the manufacturer of the GPIB card installed in the PC. The GPIB (General Purpose Interface Bus) interface allows multiple instruments to be linked to a computer using one cable, with each instrument addressable via its selectable address cell. All instruments, except for the stepper motor and pulsed current source, had GPIB connectivity. The stepper motor was controlled via a serial (COM) port, while the magnitude of current pulses from the Avtec source could only be controlled by application of an external bias to its voltage sensor terminals, which was achieved by connecting the pulser sensor to the independently programmable voltage (DAC) output of the lock-in amplifier. The DAC voltage was set by the PC via GPIB control. As equipment control and measurements had to be performed in real time, critical timing issues had to be resolved to allow the PC to send commands to and poll the individual instruments in the correct order and with appropriate delays.

Table 8.2. Instruments controllable with the MULINREC program and possible types of measurement.
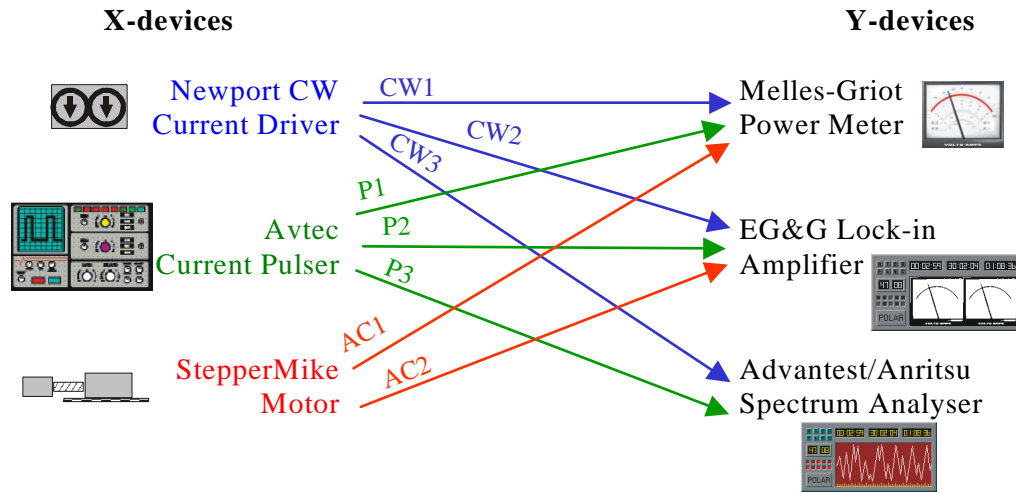
Measurement	Description
CW1	Linear detector power vs. DC current (L-I) characteristic
CW2	Non-linear detector power vs. DC current (L-I) characteristic
CW1+CW2	Combined measurement: non-linear vs. linear detector power (CW)
CW3	Spectrum vs. DC current
P1	Linear detector power vs. pulsed current (L-I) characteristic
P2	Non-linear detector power vs. pulsed current (L-I) characteristic
P1+P2	Combined measurement: non-linear vs. linear detector power (pulsed)
P3	Spectrum vs. pulsed current
AC1	Linear autocorrelation (Power meter must be used instead of non-linear detector)
AC2	Non-linear autocorrelation
AC1+AC2	Non-linear autocorrelation while monitoring average output power (Power meter must be connected to the output fibre from SA facet).

In the MULINREC program, each instrument (or its function) was classed either as Master (X-device) or Slave (Y-device). The program would ask the user to input the scan range for the Master device (e.g., a current range for a current source or a position range for the stepper motor) and record the readings from the Slave device (e.g., a detector) while performing the scan. The full device classification along with possible types of measurement is given in Table 8.2. For example, in order to measure an L-I curve from a laser (optical power versus pump current), one should select the DC current source as an X-device, and the power meter as a Y-

device, so that the measured dependence is Y = f(X) (measurement CW1 in Table 8.2). In another example, in an autocorrelation scan, the stepper motor will act as an X-device, and the lock-in amplifier measuring the non-linear detector signal, as a Y-device. Multiple Y-devices can be selected, e.g., one may want to read both the amplified autocorrelation signal and the average optical power from the power meter simultaneously during the scan (combined measurement AC1+AC2 in Table 8.2). In the latter case, MULINREC has the option of providing a feedback loop between the measured average power and pump current in order to stabilise the laser during long autocorrelation scans.

The MULINREC program stored the recorded data in a file with an extension corresponding to the type of measurement. In autocorrelation scans, the Mirror 1 position data were automatically converted from microns to picoseconds (1 μm ≅ $2 \times 3.33 \cdot 10^{-3}$ ps; the factor 2 accounts for the doubling of the optical delay for every change in the mirror position). Autocorrelation scans were performed in both directions (to and fro), so that the start stage position was the same as the finish one; both scans were then compared to eliminate the presence of any measurement artefacts. As some scans took a long time to complete (up to one hour), the program had some added functionality, e.g., switching off the laser source on completion of a scan and uploading the measurement data file on a remote server.

8.3.4. Intensity autocorrelation measurement

As explained in Section 8.2.2, an intensity autocorrelation trace is obtained using a "slow" non-linear detector, i.e., by averaging out any interferometric signal variation on a wavelength scale. To eliminate the interference effects, the two beams were cross-polarised by inserting a half-wave plate into one of the arms (see Figure 8.4), as suggested in Refs.[22, 23]. However, the interference was not completely suppressed, resulting in a very noisy non-linear signal. The fast-varying interferometric fringes could only be averaged out by "dithering" the loudspeaker at 85 Hz with an amplitude of several wavelengths at each position of the Mirror 1 translation stage.

The measurement was performed by dividing the scan range into a required number of delay points and performing an accurate reading with a long integration time in the lock-in amplifier (0.5 – 2 s) at each point. This resulted in prolonged scan

times, depending on the accuracy and number of points required. The MULINREC program was operated in the AC1+AC2 mode (see Table 8.2) and maintained constant average optical power throughout each scan by creating a feedback loop between the power meter and the laser driver. Prior to each scan, the non-linear detector was calibrated to only extract the non-linear component of the measured signal, as will be explained in Section 8.4.4.

8.3.5. Interferometric autocorrelation measurement

Interferometric autocorrelation is more challenging to realise than the intensity one due to the much higher measurement speed required. This is further complicated by the low level of the non-linear detector signal, which requires long integration times for the lock-in amplifier to be able to make a reliable measurement.

In the context of the autocorrelator set-up of Figure 8.4, a fast fringe-resolved autocorrelation can be recorded with either of the two methods: a slow scan of Mirror 1 or fast repeated sweeps of Mirror 2. In the first method, the measurement was limited by the positioning precision of the stepper motor (± 2 μm in contrast to the < 0.1 μm accuracy required by the "1/10 wavelength rule" [8]). A trade-off solution was to set the motor in motion at the lowest speed possible (5 μm/s) and continuously record the lock-in amplifier signal with the shortest time constant (10 ms) without stopping the motor for each reading. However, only a limited contrast between the fringes was thus obtained due to a high noise level.

The second method was implemented in Ref.[24] for the real-time characterisation of a modelocked Nd:YLF laser. The amplified signal from a non-linear detector was applied to the Y-input of a storage oscilloscope, while the X-channel was driven by the signal from the sine-wave generator that also controlled the loudspeaker-mounted mirror. A full interferiometric autocorrelation trace could thus be plotted after a sufficient number of speaker sweeps have been made. In Ref.[24], it was found that the acquisition time of the lock-in amplifier was not short enough to measure the rapidly varying signal, hence a regular (audio) amplifier was used instead.

A similar arrangement was attempted with the set-up of Figure 8.4 and a CCM laser, however, no meaningful signal was obtained, most probably due to the

low optical power available from the CCM device under CW pumping compared to the Nd:YLF laser. Eventually, it became possible to discern interference fringes by running the CCM laser in pulsed regime and operating the lock-in amplifier with the shortest integration time and the fastest lock-in frequency (10 kHz) from the trigger of the current pulser. The fringe pattern recorded at a speaker sweep frequency of 42 Hz is shown in the photograph of Figure 8.6. While it still proved impossible to obtain an autocorrelation trace with this method, it allowed the movement of the speaker to be calibrated against the number of optical cycles in a sweep.

Figure 8.6. Interferometric fringes on the oscilloscope display.

8.4. Autocorrelator detectors

It was stated in Section 8.2.2 that intensity autocorrelations (both slow and fast interferometric) can only be performed using a detector whose output is proportional to (at least) the square of the intensity of the incident light. In this Section, detectors utilising different non-linear processes will be reviewed and the results of their performance in the autocorrelator system of Figure 8.4 will be presented.

It is worth noting that the autocorrelation measurements of CCM laser diodes with any non-linear detector are particularly difficult for at least two reasons. First of all, the power levels available from laser diodes are generally low, while most non-linear processes are very inefficient at low optical powers. This is aggravated by the fact that about 75% of the ex-facet laser power is lost in the autocorrelator set-up.

Secondly, the peak pulse power in a CCM laser output is considerably less than in other types of laser due to the ultrahigh pulse repetition frequency. For example, the pulse power of a CCM laser modelocked at 1 THz is at least 4 orders of magnitude smaller than that of a Nd:YLF laser pulsing at 80 MHz for an identical average power in the beam.

8.4.1. Second harmonic crystal

Second-harmonic generation (SHG) is by far the most commonly used non-linear detection technique. While the use of an SHG detector was only contemplated in this Project but never actually implemented, it is nonetheless appropriate to outline its principles. SHG detectors are crystals of non-linear optical materials such as KDP and Lithium Iodate ($LiIO_3$), the latter being particularly suitable for SHG with laser diodes thanks to a high non-linear coefficient in the appropriate wavelength band. Light at the second harmonic (twice the frequency, or half the wavelength) of the incident light is generated through the interaction between the induced electric field and non-linear material susceptibility, which induces polarisation at the second harmonic of the incident light. Phase matching requirements make SHG very sensitive to the wavelength, polarisation, intensity and orientation of the input beams with respect to the crystal.

Intensity autocorrelation studies of CPM laser diodes modelocked at 175 GHz were performed by the author's colleague Dr S.D. McDougall [13] using an SHG crystal detector. In order to selectively detect the weak SHG signal, the crystal was followed by a filter to remove any remaining light at the incident frequency, and a sensitive photo-multiplier tube to amplify the signal. Due to the low pulse powers, the detector efficiency was also very low, with the signal recorded close to the detectability limit. As a result, the autocorrelations were performed in complete darkness, with a long integration time in the lock-in amplifier. With the CCM devices expected to modelock at frequencies higher than the CPM lasers of Ref.[13] and correspondingly lower pulse powers, other types of non-linear detector were deemed to have more promise than SHG.

8.4.2. Photoconductive switch-based detector

This is a novel type of ultrafast non-linear detector originally proposed in Ref.[25]. It was decided to fabricate such a detector because of its relevance to the work on THz photomixers described in Chapter 10. The detector incorporates a metal transmission line fabricated on low-temperature grown GaAs material, which is known to have a fast photoresponse with a short (~ ps) carrier lifetime. Inside the transmission line lies a small interdigitated structure (switch) similar to the one used in the photomixer devices (see Section 2.3.2 and Chapter 10). In the autocorrelator, the interdigitated structure is illuminated with the train of ultrashort pulses of interest combined with its time-delayed replica. The structure's photoconductance is modulated by the fast-varying optical signal in a sub-linear manner, with the non-linearity resulting in a variable time-averaged current in the slow external DC circuit as a function of the delay between the two pulse trains. Pulses from a modelocked Ti:sapphire laser were successfully characterised using this type of detector [25].
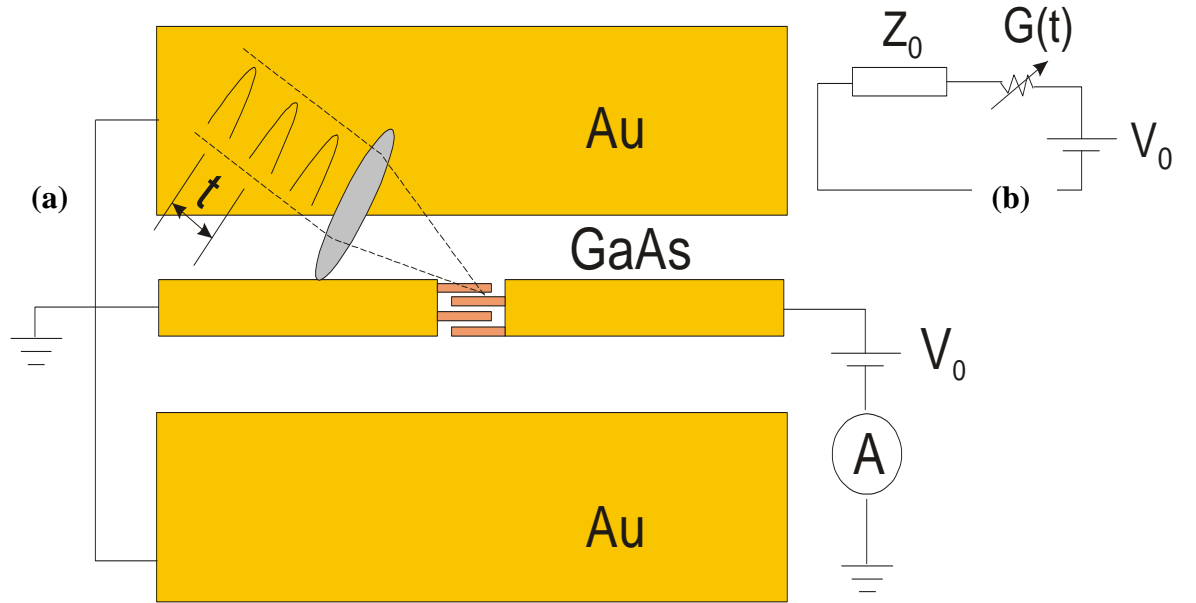
Figure 8.7. Schematic of the photoconductive switch detector **(a)** and its equivalent circuit **(b)**.

Principle of operation

The detector schematic is shown in Figure 8.7(a) along with its equivalent electrical circuit of Figure 8.7(b). On illumination of the structure with an intensity envelope $I(t)$, its photoconductance $G(t) = \alpha \cdot I(t)$ is modulated by $I(t)$ (here, α is the

absorption coefficient). The induced photocurrent $i(t)$ in response to $I(t)$ is then approximately:

$$i(t) = \frac{V_0}{Z_0 + 1/G(t)} \tag{8.10}$$

where V_0 is the external DC bias and Z_0 is the embedding impedance presented by the transmission line. For a range of incident intensities where $Z_0 \sim 1/G(t)$, the photoresponse $i(t)$ can be approximated as

$$i(t) \sim \alpha V_0 I(t) - Z_0 \alpha^2 V_0 I(t)^2 \tag{8.11}$$

The output of an autocorrelator is a train of pulses $I(t) = I(t) + I(t + \tau)$. As the circuit outside the switch is too slow to respond to the ultrafast modulation in t, the photocurrent is averaged to a DC level. The corresponding photoresponse $i(t)$, after time averaging, reduces to

$$\langle i(t) \rangle_t = 2S^{(2)} \langle I(t)I(t + \tau) \rangle_t + const \tag{8.12}$$

where $S^{(2)} \cong -Z_0 \alpha^2 V_0$ is the second-order non-linearity. Therefore, intensity modulation can be detected by measuring the DC photocurrent in the external circuit as a function of time delay τ.
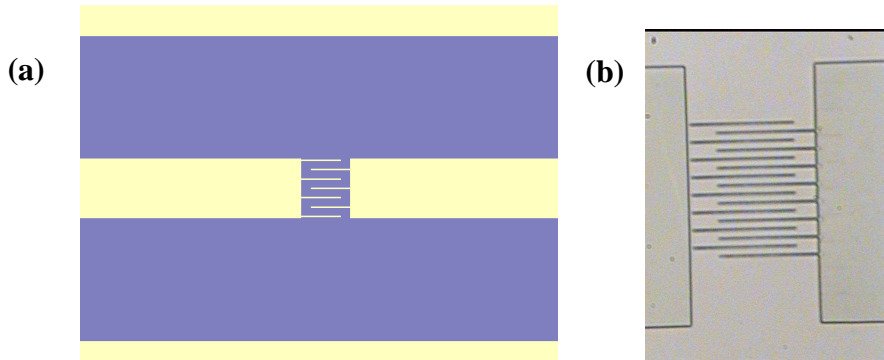
Fabrication

Figure 8.8. **(a)** Fabricated photoconductive switch inside the electrical transmission line; **(b)** SEM image of the interdigitaged structure defined in e-beam resist. The electrode size is 0.2 μm x 10 μm on a 1.7 μm period.

Several types of photoconductive switch autocorrelators with different finger sizes and microstrip lines were fabricated on a single low-temperature-grown GaAs sample using e-beam lithography. The processing steps involved defining a metal isolation pattern in resist, metallisation and metal lift-off. Images of a fabricated

device and of the interdigitated region are shown in Figure 8.8(a,b). A bespoke printed circuit board was made to mount the GaAs sample, so that each switch device on the sample was individually addressable with short wire bonds.

Testing

The fabricated devices were tested electrically and their resistance was found to be dependent upon the level of optical illumination. Their dark resistance measured 80 Ω, which was reduced to 65 Ω when the sample was illuminated with a bright microscope light.

Unfortunately, these devices were never used for autocorrelation studies, as another type of detector (commercial red laser diode, see Section 8.4.4) had proven adequate for the autocorrelation measurements of CCM lasers. It was not possible to assess the performance of the fabricated switch devices within the timescale of the Project, as these would require special (vertical) mounting and alignment arrangements to be made in order to focus the two beams in the small interdigitated region.

8.4.3. Two-photon absorption waveguide detector

Principle of operation

Another non-linear process commonly utilised for autocorrelation studies is two-photon absorption (TPA), which occurs for photons with energy $\hbar\omega_0$ that is less than the semiconductor energy gap E_g but greater than $E_g/2$. In wavelength terms, this condition holds for detector material, in which the wavelength of the absorption peak lies between $\lambda_0/2$ and λ_0, where λ_0 is the emission wavelength of the laser under study. For the range of photon energies with $E_g/2 < \hbar\omega_0 < E_g$, there is very little fundamental absorption of light, i.e., the absorption of single photons. However, when a semiconductor is irradiated by an intense beam of light, an electron can be excited from the valence band to the conduction band by the absorption of two photons. Because of the two-photon nature of the interaction, the induced photocurrent will be a quadratic function of the incident light intensity, as opposed to fundamental (single-photon) absorption, which exhibits a linear dependence. Therefore, the second-order non-linearity of the TPA mechanism can be employed as

the basis for autocorrelation. For example, a standard *p-i-n* semiconductor photodiode can be used as the non-linear element in an autocorrelation measurement. By measuring the TPA photocurrent as a function of the time delay between the two pulses, the laser pulses can be characterised.

Autocorrelation studies with a TPA detector have been carried out by a number of researchers [6, 22-24, 26-31]. A particularly attractive solution was offered in Ref.[23], which was to use a *p-i-n* waveguide detector. Indeed, such a device has all the advantages of the photodiode detector (e.g., low cost and a broad wavelength range) with a greatly improved efficiency thanks to the tight confinement of the incident signal in the waveguide and the increased interaction length afforded by the waveguide structure.

In Ref.[23], a relationship was deduced between the intensity *I* of the incident light and the measured photocurrent J_{cw}. When the detector is illuminated with a CW beam,

$$J_{cw}(I) = e\Omega\left(\frac{\alpha}{\hbar\omega}I + \frac{\beta}{2\hbar\omega}I^2\right)$$
(8.13)

where *e* is the electron charge, Ω is the volume in which the photo-generated carriers are created, $\hbar\omega$ is the photon energy, and α and β are the one and two-photon absorption coefficients, respectively. Note that for small intensities the contribution from residual single-photon absorption may be comparable to that of TPA. For the case of illumination with a pulsed beam, Eq.(8.13) is modified to obtain the averaged photo-response $J_p(I)$

$$J_p(I) = e\Omega\left(\frac{\alpha}{\hbar\omega}I + \frac{\beta\Delta t}{2\sqrt{\pi}\hbar\omega T}I^2\right)$$
(8.14)

where Δt is the time between the pulses, and *T* is the pulse duration. It can be seen that the linear terms in Eqs.(8.13) and (8.14) are identical for both CW and pulsed beams. However, the quadratic terms vary by a constant factor determined by the mark-to-space ratio (or the duty cycle) of the pulse train.

The contrast ratio of intensity autocorrelation peaks recorded with a TPA detector depends upon the relative polarisations of the two pulsed beams being correlated. When the beams are co-linearly polarised, the contrast ratio for perfectly modelocked pulses is 3:1 (see Section 8.2.2 and Refs. [23, 32]). However, there is

disagreement in the literature as to the value of the contrast ratio for the case of orthogonally polarised beams. According to Refs.[22, 23], the ratio is 2:1, while in thesis [30] and note [33], a value of (5/3):1 is derived from the anisotropy of the TPA coefficient in semiconductors. In Ref.[30], it is argued that, based on the results of Refs.[34, 35], the dependence of TPA non-linearity on the polarisation of input light can be used to increase the observed contrast ratio to nearly 2:1. In any case, it can still be concluded that by using cross-polarised beams to suppress interference effects, one should expect to measure a reduced autocorrelation contrast ratio compared to the case of co-linearly polarised beams.

Design and fabrication

TPA waveguide detectors were designed to be similar to the devices used in Refs.[23, 24, 30]. In essence, they had almost the same structure as a conventional ridge-waveguide laser, save for a longer ridge (up to 3 mm), a range of ridge widths (3 - 5 µm) and an extra 20 µm-wide mesa etched in order to reduce the reverse dark current of the device. It is important that the dark current is as small as possible in order to increase the detector's sensitivity. The device cross-section across the ridge is shown in the schematic of Figure 8.9(a).
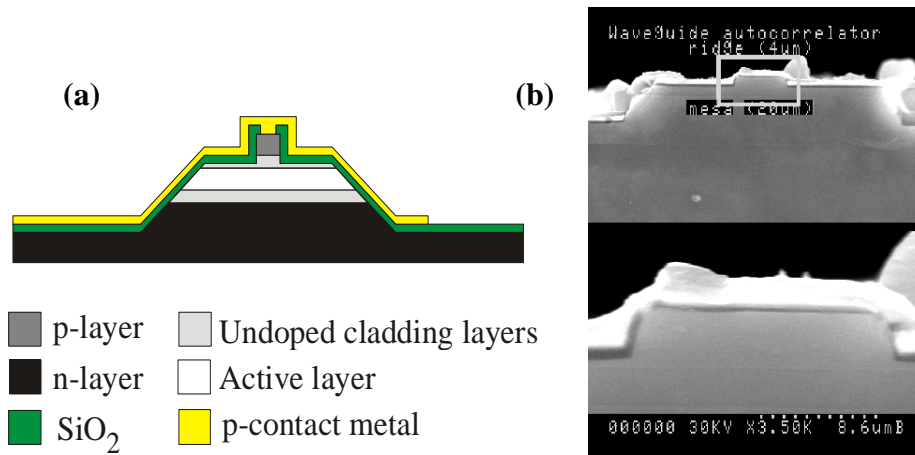
Figure 8.9. Profile **(a)** and SEM image of a fabricated waveguide detector **(b)** (courtesy of Dr M. Street)**.** The bottom part of image **(b)** contains a magnified view of the ridge facet.

The detector devices were fabricated jointly with Dr M. Street from the purpose-grown QT1363 material, with the layer structure shown in Table 8.3. The material was designed to have a bandgap of 1.66 eV corresponding to a wavelength of 750 nm, which is well below the CCM laser emission wavelength of 860 nm. The

etch depth of the ridge was modelled using the methods of Chapter 6 in order to obtain guiding in a single lateral mode. An end-on SEM photograph of a fabricated 4 μm ridge detector is shown in Figure 8.9(b).

Table 8.3. TPA PIN Waveguide Autocorrelator Structure (QT1363)

Material	Thickness, μm	Doping
GaAs	0.1	3E18 C
Al0.39	0.51	1E18 C
Al0.39	0.35	UD ~5E15
Al0.20	0.68	UD ~5E15
Al0.39	0.34	UD ~5E15
Al0.39	3.6	7E17 Si
GaAs	0.1	1.5E18 Si
VFG N+ GaAs Substrate (100) with 3º misorientation towards (110)		

Device assessment

The waveguide TPA detectors were mounted on a translation stage and inserted in the autocorrelator set-up. Two bias options were used. The first one was to apply a reverse bias of -3 to -6 V using a battery and measure the voltage drop across a known resistor, with the lock-in amplifier operated in voltage measurement mode, as illustrated in the equivalent circuit of Figure 8.10(a). A dark current of -280 nA was measured for a bias of –5 V. The other option was to connect the waveguide detector to the current input of the lock-in amplifier, operated in current measurement regime, to register the induced photocurrent directly. The input port of the lock-in amplifier had an input impedance of virtual zero, so the connected device was effectively short-circuited. The second bias option, shown in Figure 8.10(b), proved more sensitive than the first and was used for all subsequent measurements.

The autocorrelator output was end-fire coupled into one facet of the TPA waveguide using a microscope objective, while the unabsorbed light from the other facet was collected with another objective lens and imaged on an infrared camera, as shown in Figure 8.4. With this arrangement it was possible to ensure that output from both arms of the autocorrelator was aligned and coupled into the detector waveguide. This was, however, very difficult to achieve due to the low power available from CCM lasers and the extremely tight alignment tolerances. A visible He-Ne laser was used to facilitate the initial alignment of the optical system.
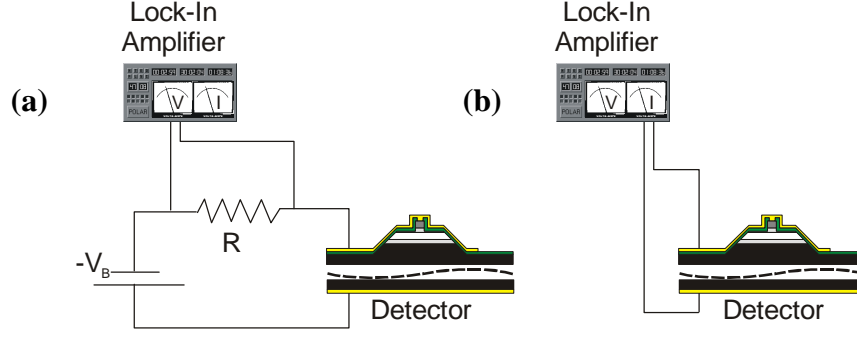
Figure 8.10. Bias schemes for TPA waveguide detectors. **(a)** Voltage measurement under reverse bias $-V_B$; **(b)** Current measurement under zero bias.

The TPA devices were assessed by measuring the $J_{cw}(I)$ characteristic of Eq.(8.14), with intensity I substituted by average power P measured with a power meter. Both Eqs.(8.13) and (8.14) can be approximated with a fitting parabola containing linear $J_1(P)$ and quadratic $J_2(P)$ photocurrent terms with a background C

$$J(P) \cong J_1(P) + J_2(P) + C \cong aP + bP^2 + C \tag{8.15}$$

It is also helpful to define the non-linearity factor $\gamma = \dfrac{b}{a^2}$, which will be used as a "figure of merit" to assess the quality of the TPA detector. The higher γ, the stronger the TPA behaviour of the detector. For a purely quadratic detector, $\gamma \to \infty$.

The non-linearity assessment measurements were performed with one arm of the autocorrelator blocked to avoid any interference effects. An optical power meter was placed in the blocked arm to measure the optical power per arm and estimate the power incident upon the detector facet. A reference ridge-waveguide laser with an SA section was used as the optical source. As the laser was part of the fabricated CCM devices but had no ICR etched, it will also be referred to as a CCM laser for convenience. The MULINREC program was used to sweep the laser driver through a range of currents above the threshold of the CCM laser. The laser power was recorded using the Melles Griot power meter, while the TPA detector response was measured by the lock-in amplifier (combined measurements CW1+CW2 or P1+P2 of Table 8.2, depending on the current source). For CW measurements, the chopper was used both to modulate the beam and trigger the amplifier. The recorded TPA detector readings were then plotted against the concurrently recorded power meter readings, and the curve of Eq.(8.15) was fitted to the resulting chart.

Results

For the CW pump case, the plots obtained were very linear (in some cases, even sub-linear), as shown in Figure 8.11. When a TPA detector is illuminated with a pulsed beam, Eq.(8.14) predicts a larger quadratic term than in the pure CW case [Eq.(8.13)]. Therefore, a reverse bias was applied to the saturable absorber section of the CCM laser to induce modelocking, however, no change was observed the slope of the plot of Figure 8.11(b) (nor was there a way of knowing whether the CCM laser was modelocked under those bias conditions). Such behaviour would suggest the dominance of the linear absorption at the small optical powers available from the CCM laser in CW mode.
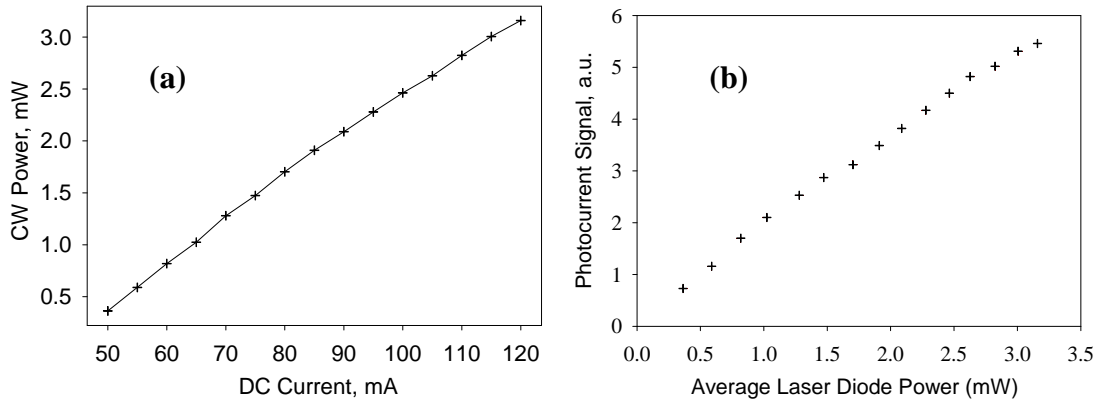
Figure 8.11. A linear part of a CCM laser's L-I characteristic (above threshold) **(a)**, and corresponding readings from the TPA detector **(b)** measured in CW mode. The ordinate of plot **(a)** is used as the abscissa of plot **(b)**.

By contrast, when the CCM laser was operated in pulsed regime, a pronounced non-linearity was observed in the TPA readings with increasing laser power, as is evident in Figure 8.12(a) (the peak power within the current pulse was used for the abscissa values). An excellent fit with the parabola of Eq.(8.15) was obtained, albeit with a very small non-linearity factor $\gamma \sim 5.5 \cdot 10^{-4}$. The non-linear behaviour was further confirmed by measuring the output power from the TPA waveguide as a function of laser power, concurrently with the non-linear signal. One can see from the plot of Figure 8.12(b) that the transparency of the waveguide decreases with increasing input power, which indicates the dominance of TPA over linear absorption at high input intensities.
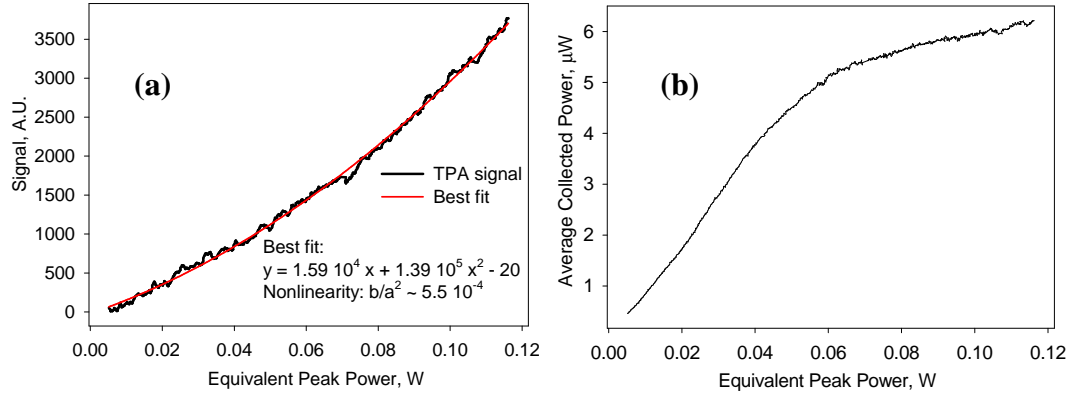
Figure 8.12. Pulsed measurement of the non-linear response of the TPA waveguide detector as a function of peak power measured inside the autocorrelator arm **(a)** and corresponding average power at the output of the waveguide **(b)**. Square 350 ns current pulses on a 2 kHz repetition rate were used to drive the CCM laser source.

However, it was still not possible to observe any change in the slope of the curve of Figure 8.12(a) when the SA section of the CCM laser was reverse biased, whereas the changes obtained by varying the duty cycle and pulse width of the laser current source while maintaining constant average power were very marginal. A possible explanation for the poor non-linearity of the TPA waveguides is that the absorption peak at 750 nm of the QT1363 material, from which these devices were fabricated, lay too close to the CCM laser wavelength of 860 nm, with some residual linear absorption in the absorption tail due to donor levels, defects, etc. In the published reports [23, 24, 30], TPA waveguides with a similar bandgap were used to characterise pulsed lasers having wavelengths in excess of 1 μm, so the separation between the absorption peak of the detector material and the emission wavelength of the laser was greater than that used in this Project.

Such low detector non-linearity had little promise for the feasibility of intensity autocorrelation studies of CCM laser diodes using the fabricated TPA waveguides. Indeed, with the amount of effort invested, it was not possible to obtain meaningful autocorrelation traces using these TPA devices. A large part of the problem was the instability of the overall free-space autocorrelator set-up and the extreme difficulty with maintaining both the accurate optical alignment of the system and good coupling of light into the TPA waveguide.

8.4.4.   Red laser diode detector

Due to the poor non-linear performance of the fabricated TPA waveguide detectors, it was decided to attempt autocorrelation measurements with another type of TPA detector, which would offer a larger separation between its absorption peak and the lasing wavelength of CCM devices. A simple solution was to use commercially available visible light emitters in the 600 – 700 nm wavelength region as TPA detectors for CCM laser radiation at 860 nm. Indeed, such an approach was suggested in Refs.[6, 27, 28]. For enhanced sensitivity, it was also desirable that such a detector should have a waveguide geometry, the ideal candidate being a visible laser diode.

Device assessment

A range of inexpensive packaged red laser diodes manufactured by Fuji and having emission wavelengths between 650 – 670 nm were acquired. The T-can package contained the laser with an integrated photodiode for power monitoring. The devices were connected using the zero-bias current measurement scheme of Figure 8.10(b), while the photodiode connectors were intentionally shorted as the photodiode was found to interfere with the measurement.

The position of the red laser in the measurement set-up is shown in Figure 8.4 (the TPA waveguide, outcoupling lens and IR camera were removed). The light from the output of the autocorrelator was coupled using a microscope objective, as in the case of the TPA waveguides fabricated earlier, however, due to the packaging, it was not possible to use the IR camera to check the coupling efficiency into the red laser. At the same time, the optical alignment and coupling were both enormously simplified and improved by the fact that, by forward-biasing the red laser with a DC current source, its bright red beam could be used as an excellent alignment guide. The added benefit of using red light for alignment was that it was strongly absorbed by the material of the CCM laser, and the measurement of the photocurrent thus induced in the CCM laser indicated the quality of the coupling of the red light into the waveguide. Hence, for alignment purposes, the autocorrelator set-up was operated in a reciprocal configuration, where the functions of the CCM and red lasers as source/detector were reversed and the electrical connections of the two lasers changed over.

Results

     The red laser detectors were assessed using the same methods as the fabricated TPA waveguides of Section 8.4.3. Like the TPA waveguides, the red lasers produced near-linear $J_{cw}(P)$ characteristics of Eq.(8.15) in the CW pump case. However, higher signal levels with much larger non-linearities were observed when the CCM laser was driven with pulsed current, with the non-linearity factor γ strongly dependent upon the current pulse width and duty cycle for the same average beam power. The $J_p(P)$ curve, plotted in blue in Figure 8.13, was taken under the same pump conditions as that of Figure 8.12 and fitted with Eq.(8.15) to give $\gamma \sim 1.7$. When the fundamental-harmonic (non-ICR) CCM laser was modelocked, the non-linearity rose to $\gamma \sim 4.8$ (red curve, Figure 8.12), which is consistent with the larger non-linear term expected from Eq.(8.14) for the modelocked case (the actual peak pulse power is higher than the average power registered by the power meter). Several red laser-based detectors were tested with a view to selecting those having the highest γ values. The tests revealed that, even in the best-performing devices (*Fuji 670/5S* with $\lambda = 670$ nm), the contributions from the linear $J_1(P)$ and non-linear $J_2(P)$ photo-current components of Eq.(8.15) were comparable for the power levels used.
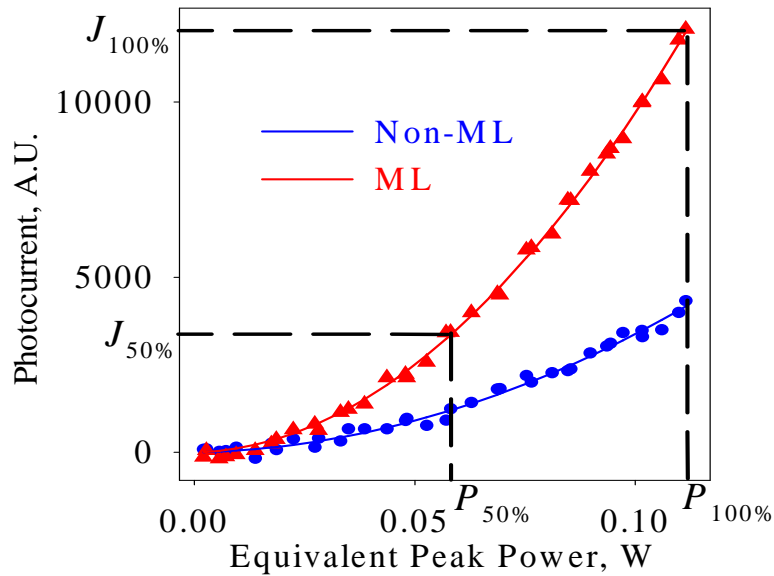
Figure 8.13. Response of the red laser detector where the source laser is mode-locked and unlocked [upper (red) and lower (blue) curves, respectively]. The photo-current data are fitted with parabolas (thin lines), with corresponding non-linearities $\gamma_{ML} \sim 4.8$ and $\gamma_{NonML} \sim 1.7$. In autocorrelation data, the contribution of the linear absorption and noise floor were cancelled out by calibrating the signal at points $P_{100\%}$, $P_{50\%} = \frac{1}{2} P_{100\%}$ and $P_{0\%}$ (blocked beam).

Intensity autocorrelation traces from CCM lasers were successfully obtained using the red laser-based TPA detectors. However, the observed contrast ratios of the autocorrelation peaks obtained with co-linearly polarised beams were much smaller than the theoretical value of 3:1 for co-linearly polarised beams. This was attributed to the presence of unwanted single-photon absorption, which leads to a linear component – the photocurrent that is proportionally large at low optical powers – and reduces the height of the correlation peaks. The effect of linear absorption on the contrast ratio in autocorrelation peaks was investigated in Ref.[22].

To eliminate the linear component $J_1(P) \sim aP$ and the noise floor from the measured signal, the following calibration procedure was performed immediately before each autocorrelation scan. With the CCM laser running at full power $P_{100\%}$, (whether modelocked or not) and the translation stage positioned at a delay in between correlation peaks, three detector readings, $J_{100\%}$, $J_{50\%}$ and $J_{0\%}$ were taken at powers $P_{100\%}$, and $P_{50\%} = \frac{1}{2} P_{100\%}$ obtained by placing a 50% filter in the beam, and $P_{0\%}$ by blocking the beam entirely, see Figure 8.13. Assuming the parabolic dependence of Eq.(8.15), the detector non-linearity factor γ' for the beam under study can be easily found from the three points:

$$
\left.\begin{array}{c}
J_{100\%} = aP_{100\%} + bP_{100\%}^2 + C \\
J_{50\%} = a\dfrac{P_{100\%}}{2} + b\left(\dfrac{P_{100\%}}{2}\right)^2 + C \\
J_{0\%} = C
\end{array}\right\} \Rightarrow \gamma' = \frac{bP_{100\%}^2}{(aP_{100\%})^2} = 2\frac{J_{100\%} - 2J_{50\%} + J_{0\%}}{(J_{100\%} - 4J_{50\%} + 3J_{0\%})^2}
\tag{8.16}
$$

Assuming that γ' stays the same throughout the autocorrelation scan, the measured photocurrent data J_k can then be modified by extracting their non-linear component bP_k^2 only:

$$
\left.\begin{array}{c}
J_k = aP_k + bP_k^2 + J_{0\%} \\
\gamma = \dfrac{bP_k^2}{(aP_k)^2} = \gamma'
\end{array}\right\}
\begin{array}{l}
\Rightarrow J_k = \sqrt{\dfrac{bP_k^2}{\gamma}} + bP_k^2 + J_{0\%} \Rightarrow \\
\Rightarrow bP_k^2 = \dfrac{\left(\sqrt{4\gamma'(J_k - J_{0\%}) + 1} - 1\right)^2}{4\gamma'}
\end{array}
\tag{8.17}
$$

The resulting data therefore approximate the autocorrelation trace that would be registered with a purely quadratic detector. This calibration and data processing procedure was implemented in the MULINREC code and was found to work accurately only for relatively high peak pulse powers (specifically, for CCM devices modelocked at harmonics $M \leq 7$). Therefore a change in the contrast ratio with and

without bias on the saturable absorber (SA) was also registered as evidence of modelocking. This change was appreciable only when the lasers were driven in pulsed mode, which also helped to maintain lasing stability throughout the scan.

However, at the very high frequency end, where the peak power of modelocked pulses was very low due to the high repetition rate, it was impossible even to register any definite change in the contrast ratio by reverse-biasing the SA section, so measurements of the coherence time of a laser were used to corroborate its modelocking operation. Indeed, due to the significant linear photocurrent component present in the output of a red laser detector, linear cross-correlations can be carried out as described in Section 8.2.1.

In summary, the autocorrelator system described in this Chapter allowed the following measurements to be made:

1. L-I characteristics, both in CW and pulsed regimes

2. Spectral measurements

3. Slow intensity autocorrelation

4. Partially resolved interferometric autocorrelation

5. Linear auto/cross-correlation

The autocorrelation measurement results from the fabricated CCM laser diodes using the red laser TPA detectors with the autocorrelator set-up of Figure 8.4 will be presented in Chapter 9.

8.5. References

[1]   E. K. Zavoiskii and S. D. Fanchenko, "Image converter high-speed photography with 10^{-9} to 10^{-14} time resolution," *Appl. Opt.*, vol. 4, pp. 1155-1167, 1965.

[2]   H. Photonics, "Universal streak camera C5680," User manual, 1994.

[3]   J.-C. Diels and W. Rudolph, "Diagnostic techniques," in *Ultrashort pulse phenomena*. San Diego: Acad. Press, 1996, pp. 365-400.

[4]   P. J. Delfyett, H. Shi, S. Gee, I. Nitta, J. C. Connolly, and G. A. Alphonse, "Joint Time–Frequency Measurements of Mode-Locked Semiconductor Diode Lasers and Dynamics Using Frequency-Resolved Optical Gating," *IEEE J. Quant. Elec.*, vol. 35, pp. 487-500, 1999.

[5]   D. H. Auston, A. M. Johnson, P. R. Smith, and J. C. Bean, "Picosecond optoelectronic detection, sampling and correlation measurements in amporphous semiconductors," *Appl. Phys. Lett.*, vol. 37, pp. 371-373, 1980.

[6]   D. T. Reid, M. Padgett, C. McGowan, W. E. Sleat, and W. Sibbett, "Light-emitting diodes as measurement devices for femtosecond laser pulses," *Opt. Lett.*, vol. 22, pp. 233-235, 1997.

[7]   H. P. Weber, "Method for pulsewidth measurement for ultrashort light pulses generated by phase-locked lasers using non-linear optics," *J. Appl. Phys.*, vol. 38, pp. 2231-2234, 1967.

[8]   K. L. Sala, G. A. Kenney-Wallace, and G. E. Hall, "CW Autocorrelation Measurements of Picosecond Laser Pulses," *IEEE J. Quant. Elec.*, vol. QE-16, pp. 990-996, 1980.

[9]   J. P. Curtis and J. E. Carroll, "Autocorrelation systems for the measurement of picosecond pulses from injection lasers," *Int. J. Electron.*, vol. 60, pp. 87-111, 1986.

[10]   J. Bradley and G. H. C. New, "Ultrashort pulse measurements," *Proc. IEEE*, vol. 62, pp. 313-345, 1974.

[11]   J.-C. M. Diels, J. J. Fontaine, I. C. McMichael, and F. Simoni, "Control and measurement of ultrashort pulse shapes (in amplitude and phase) with femtosecond accuracy," *Appl. Opt.*, vol. 24, pp. 1270–1282, 1985.

[12]   J. C. Diels, J. J. Fontaine, and W. Rudolph, "Ultrafast diagnostics," *Revue Phys. Appl.*, vol. 22, pp. 1605-1611, 1987.

[13]   S. D. McDougall, "Monolithic colliding pulse mode-locking of AlGaAs/GaAs and InGaAs/InGaAsP quantum well lasers." Ph.D. Thesis: University of Glasgow, 1997.

[14]   Y. Ning, K. T. V. Grattan, B. T. Meggitt, and A. W. Palmer, "Characteristics of laser diodes for interferiometric use," *Appl. Opt.*, vol. 28, pp. 3657-3661, 1989.

[15]   A. R. Reisinger, J. C.D. David, K. I. Lawley, and A. Yariv, "Coherence of room-temperature CW GaAs/AlGaAs injection laser," *IEEE J. Quant. Elec.*, vol. 15, pp. 1382-1387, 1979.

[16]   "Principles of Autocorrelation," Photonics Research Group, University of Toronto, Web page: http://www.physics.utoronto.ca/~marj/wwwphotonics/FFLAutocorrelation.html.

[17]   J. Yuen, "Detection of Ultrafast Phenomena in Time and Space," presented at Cal-(IT)² Day, California Institute for Telecommunications and Information Technology, Downloaded from: http://www.calit2.net/calit2day/ppts/poster_yuen.ppt, November 2003.

[18]   T. Mindl, P. Hefferle, S. Schneider, and F. Dorr, "Characterisation of a train of subpicosecond optical pulses by fringe-resolved autocorrelation measurements," *Appl. Phys. B*, vol. 31, pp. 201-207, 1983.

[19]   J.-C. Diels and W. Rudolph, "Characteristics of fs light pulses," in *Ultrashort pulse phenomena*. San Diego: Acad. Press, 1996, pp. 1-12.

[20]   K. Naganuma, K. Mogi, and H. Yamada, "General method for ultrashort light pulse chirp measurement," *IEEE J. Quant. Elec.*, vol. QE-25, pp. 1225-1233, 1989.

[21]   Y. Ishida, K. Nagunama, and Y. T, "Self-phase modulation in hybridly mode-locked cw dye lasers," *IEEE J. Quant. Elec.*, vol. QE-21, pp. 69-77, 1985.

[22]   M. M. Karkhanehchi, D. A. Barrow, A. C. Bryce, C. J. Hamilton, and J. H. Marsh, "The influence of single-photon absorption on the performance of the two-photon waveguide autocorrelator," *IEEE J. Quant. Elec.*, vol. 33, pp. 933-936, 1997.

[23]   F. R. Laughton, J. H. Marsh, B. D.A., and E. L. Portnoi, "The two-photon absorption waveguide autocorrelator," *IEEE J. Quant. Elec.*, vol. 30, pp. 838-845, 1994.

[24]   M. M. Karkhanehchi, C. J. Hamilton, and J. H. Marsh, "Autocorrelation Measurements of Mode-Locked Nd:YLF Laser Pulses Using Two Photon Absorption Waveguide Autocorrelator," *IEEE Phot. Tech. Lett.*, vol. 9, pp. 645-647, 1997.

[25]   S. Verghese, N. Zamdmer, Q. Hu, E. R. Brown, and A. Förster, "An optical correlator using a low-temperature-grown GaAs photoconductor," *Appl. Phys. Lett.*, vol. 69(6), pp. 842-844, 1996.

[26]   L. P. Barry, P. G. Bollond, J. M. Dudley, J. D. Harvey, and R. Leonhardt, "Autocorrelation of ultrashort pulses at 1.5 micron based on nonlinear response of silicon photodiodes," *Elec. Lett.*, vol. 32, pp. 1922-1923, 1996.

[27]   J. K. Ranka, A. L. Gaeta, A. Baltuska, M. S. Pshenichnikov, and D. A. Wiersma, "Autocorrelation measurement of 6 fs pulses based on the two-photon-induced photocurrent in aGaAsP photodiode," *Opt. Lett.*, vol. 17, pp. 1344–1346, 1997.

[28]   D. T. Reid, W. Sibbett, J. M. Dudley, L. P. Barry, B. C. Thomsen, and J. D. Harvey, "Commercial semiconductor devices for Two-Photon-Absorption autocorrelation of ultrashort light pulses," *Optics and Photonics News*, vol. 9, pp. 814-820, 1998.

[29]   M. M. Karkhanehchi, J. H. Marsh, and D. C. Hutchings, "The polarisation dependence of two-photon absorption in an AlGaAs waveguide autocorrelator," *Appl. Opt.*, vol. 36, pp. 7799-7804, 1997.

[30]   M. M. Karkhanehchi, "Generation and detection of short optical pulses using semiconductor devices." Ph.D. Thesis: University of Glasgow, 1997.

[31]   Y. Takagi, T. Kobayashi, K. Yoshihara, and S. Imamura, "Multiple- and single-shot autocorrelator based on two-photon conductivity in semiconductors," *Opt. Lett.*, vol. 17, pp. 658–660, 1992.

[32]   H. P. Weber and H. G. Danielmeyer, "Multimode effects in intensity autocorrelation measurements," *Phys. Rev. A.*, vol. 2, pp. 2074-2079, 1970.

[33]   M. W. Street, "TPA Autocorrelation with Orthogonally Polarised Beams (Zero Linear Absorption)." Personal communication, 1998.

[34]   D. C. Hutchings and B. S. Wherret, "Theory of anisotropy of two photon absorption in zinc-blende semiconductors," *Phys. Rev. B.*, vol. 49, pp. 2418-2426, 1994.

[35]   M. D. Dvorak, W. A. Schroeder, D. R. Andersen, A. L. Smirl, and B. S. Wherret, "Measurement of the anisotropy of two-photon absorption coefficients in zinc-blende semiconductors," *IEEE J. Quant. Elec.*, vol. 30, 1994.

CHAPTER 9.

EXPERIMENTAL RESULTS AND DISCUSSION

In this Chapter, the test and measurement results obtained from the different designs and modifications of the fabricated compound-cavity modelocked (CCM) lasers will be presented. Initial device assessment will be described in Section 9.1, while Section 9.2 will focus on the ultrafast characterisation results and the modelocking behaviour of the final generation of CCM devices, followed by a discussion and conclusions.

9.1. Device assessment

In this section, initial assessment results, such as light-current characteristics and spectra, will be given for each device type described in Chapters 5 and 7. The early data presented here were obtained using the broad-area laser pulsed test rig (see "Results", Section 6.2.1) at the departmental Laser Test Lab; subsequent devices were assessed, both in the CW and pulsed current regimes, using the laser characterisation part of the autocorrelator system of Section 8.3.1 of the previous chapter.

9.1.1. Etched-facet lasers

Dry-etched facet devices were the first attempt at making CCM lasers and were briefly described in Sections 5.1.1, 7.1.1 and 7.3.1. Initially, etched-facet broad-area lasers were fabricated. These devices exhibited high thresholds (at least twice as high as cleaved-facet lasers of the same length) and low external quantum efficiencies.

Dry-etched facet CCM lasers were also fabricated and tested. The devices suffered from a high contact resistance (over 30 Ω for a 900 μm long device) and generally exhibited very poor lasing performance, with thresholds of around 90 mA in pulsed regime and a catastrophic failure occurring shortly after threshold. A

typical L-I characteristic is shown in Figure 9.1. The breakdown appeared to be optics-related rather than electric-related, as the failed devices still had a diode I-V characteristic. Furthermore, the breakdown was only observed in the ridge-waveguide devices but not in the broad-area lasers, which can be explained by the fact that the facet power density in the broad area geometry is lower than in the ridge waveguide one.
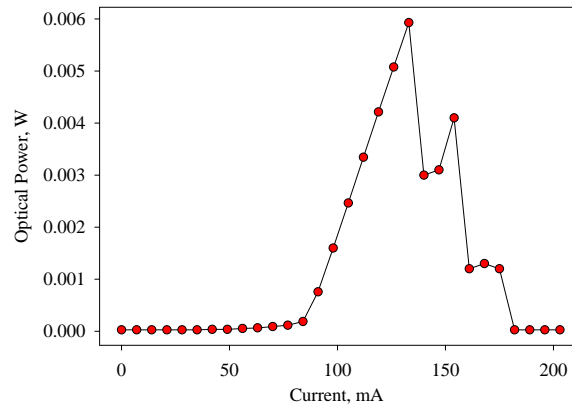
Figure 9.1. Pulsed light-current characteristic of etched-facet CCM lasers showing catastrophic failure shortly above threshold. Current pulsewidth: 0.5 µs, duty cycle: 0.1%.

To improve the performance of etched-facet devices, further development of the dry-etch technology would be required in order to reduce the sidewall roughness of the facets. In addition, the etched facets should be passivated with a protective coating of alumina or silica immediately after etching, as recommended in Ref.[1]. Due to the technological issues and the amount of development work required, no further etched-facet lasers were fabricated.

9.1.2. Cleaved-facet lasers

Cleaved-facet CCM lasers showed much better lasing performance, with the threshold currents and contact resistance reducing as fabrication issues were resolved. The threshold current of CCM lasers with ICR's typically lay in the range 50 to 85 mA for a 960 µm long device, which was 25% to 70% higher than in conventional lasers with identical lengths. The optical power was up to 2.2 mW per facet in the CW regime.

m:n **cavity ratios**

Early studies concentrated on the spectral perturbations caused by the presence of a single, shallow-etched ICR dividing the laser cavity into an *m:n* length ratio. As explained in Chapter 4 (see Section 4.1.2 and also Figure 4.4), the mode spacing $\Delta\Lambda$ of such a cavity is expected to be a "harmonic" of the mode spacing $\Delta\lambda$ of an unperturbed Fabry-Pérot cavity of identical length, with $\Delta\Lambda = (m+n)\,\Delta\lambda$. For ease of reference, the periodic modes separated by a desired $\Delta\Lambda$ will also be referred to as harmonic.
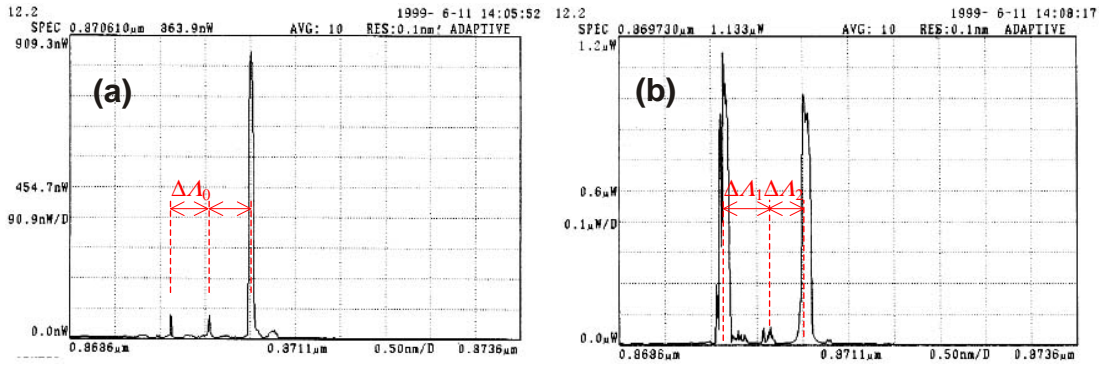
Figure 9.2. Optical spectra of a 5:7 ratio, single-slot CCM laser at two pumping currents: 100 mA **(a)** and 120 mA **(b)**. The spectra can be construed as having either a periodic mode spacing at the 5th harmonic **(a)**, or a non-periodic one at the 5th, 7th and 12th harmonics **(b)**.

Shown in Figure 9.2 are two spectra measured from a 960 μm long CCM laser at two different currents above its threshold of 85 mA under CW pumping. The laser was designed to have a cavity ratio of 5:7 with $\Delta\Lambda = 12\,\Delta\lambda$. One, therefore, should expect to see a spectrum containing a periodic pattern of every 12th mode only. However, the spectra show a more complicated picture: depending on the pumping level, aperiodic mode spacings of 5 $\Delta\lambda$, 7 $\Delta\lambda$ or 12 $\Delta\lambda$ can be observed. Such a mode pattern can be construed in at least two ways, as explained below.

The first interpretation is that, due to cleaving error, the actual cavity ratio was 396 μm:565 μm ≈ 0.701 (instead of the design ratio 400 μm:560 μm = 5:7 ≈ 0.714). The cleaved ratio of 0.701 is close to the ratio 2:3 ≈ 0.667, with $\Delta\Lambda = (2+3)\,\Delta\lambda$. This is consistent with the spectral pattern of Figure 9.2(a), which exhibits a periodic mode spacing $\Delta\Lambda$ that is approximately five times larger than the Fabry-Pérot mode spacing of an identical laser with no ICR. Therefore, for this

pumping level, it appears as though this CCM laser was able to approximate an imperfect 5:7 ratio with a mode pattern that would correspond to a 2:3 ratio.

A different interpretation is more appropriate for the spectrum of Figure 9.2(b) recorded at a higher pumping level. Two modes spaced by approximately 10 – 12 Fabry-Pérot mode intervals dominate the spectrum, with two subdued modes in between. To explain this pattern, the mode discrimination for this particular device was simulated by Dr E.A. Avrutin. The simulation assumed a uniformly pumped cavity just above threshold and is shown in the plot of Figure 9.3. It can be seen that the aperiodic pattern of $\Delta\Lambda_1 = 7 \Delta\lambda$, $\Delta\Lambda_2 = 5 \Delta\lambda$ can be found both in the measured spectrum and in the modal gain simulation, with the strongest modes at $\Delta\Lambda_1 + \Delta\Lambda_2 = 12 \Delta\lambda$.
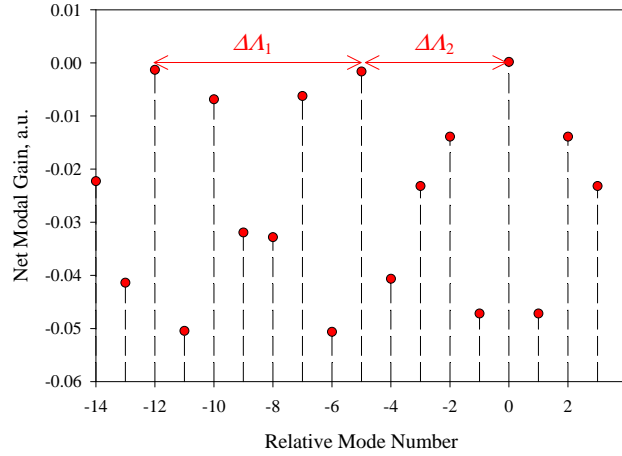
Figure 9.3. Simulated mode discrimination for the uniformly pumped cavity of a 396:565 ratio CCM laser.

In general, the fabricated *m:n* ratio CCM lasers exhibited variable mode patterns, with a mode spacing often affected by the pumping level. Mode competition was also very pronounced in the observed spectra, resulting in aperiodic modal spacing. Such properties of *m:n* cavity lasers are to be expected from the graph of Figure 9.3, where several "non-harmonic" modes enjoy high gain that is similar to that experienced by the desired "harmonic" modes. The poor discrimination between the "harmonic" and "non-harmonic" modes can explain the complicated modal patterns in the spectra of these devices. Due to their poor spectral behaviour, modelocked operation of the *m:n* CCM lasers has not been attempted.

1:*n* cavity ratios

The 1:*n* ratio CCM devices manifested the expected increase in spectral mode separation, with a variable number of modes in the spectrum depending on the compound cavity ratio and pumping conditions. In contrast to *m:n* ratio cavities, 1:*n* devices offer strong suppression of the non-harmonic modes located in the middle of the spectral interval between any two adjacent harmonic modes. At the same time, satellite modes in the vicinity of harmonic modes are not so well discriminated against. This can be seen in the spectra of Figure 9.4(a, b), which were measured from 1:2 and 1:9 ratio CCM lasers. In the first device, $\Delta\Lambda_1 = 3\,\Delta\lambda$, and in the second, $\Delta\Lambda_2 = 10\,\Delta\lambda$, with both lasers using a single-slot ICR to achieve the harmonic multiplication of mode spacing. In both spectra, the harmonic peaks are actually supermodes that contain clusters of closely-spaced Fabry-Pérot modes of the whole cavity. The poor suppression of the satellite modes is due to the low finesse of the shorter sub-cavity, as explained in Section 4.1.2. The finesse can be increased by using more reflective features as ICRs or applying a high-reflection coating to the corresponding facet. After fabricating devices with several ICR configurations (see Section 7.1.2), it was established that multiple deep-etched ICR features were required to achieve satellite-free harmonic modes. CCM lasers containing such ICRs were successfully fabricated, and the results of their spectral and modelocking measurements can be found in Section 9.2.
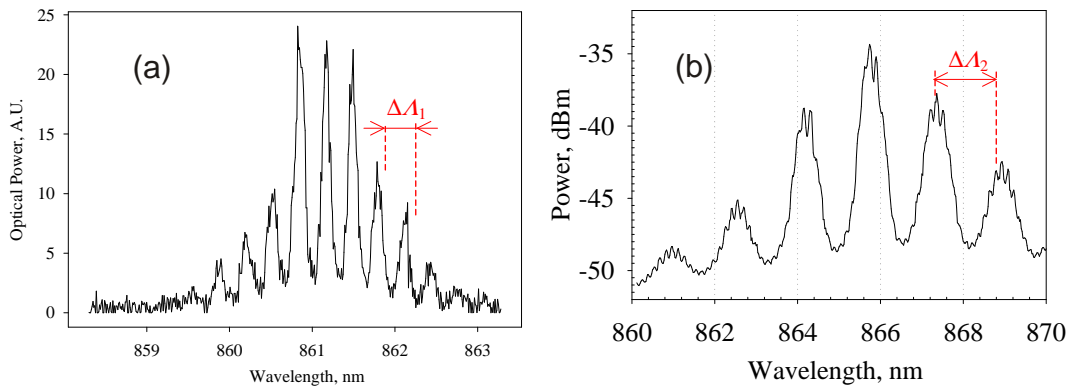
Figure 9.4. Optical spectra of a 1:2 ratio [(**a**), linear scale] and a 1:9 ratio [(**b**), log scale] CCM laser having a single-slot ICR. Both spectra show incomplete resolution of harmonic modes.

9.1.3. Bent-cavity lasers

The design and fabrication of bent-cavity CCM lasers were discussed in Sections 5.3.3 and 7.3.2, respectively. Unfortunately, it has not been possible to obtain any useful data from these devices: while they showed good electrical characteristics and emitted some light, lasing operation was not achieved at any current up to electrical breakdown. Two ridge etch depths were studied, one down to the active layer and the other 0.5 μm past it, but no lasing occurred despite the simulation results, which had predicted that even the shallower etch should provide sufficient lateral confinement of light for the bend radii used. The non-performance of these devices was probably due to technological issues that had not been resolved at the time of fabrication. Owing to the limited resources, it has not been possible to fabricate any further samples of bent-cavity lasers within this Project.

9.2. Autocorrelation and spectral measurement results

It is now time to present the most interesting results achieved in this Project, which will demonstrate ultrafast modelocking operation of the fabricated CCM lasers. These results were obtained from deep-etched ICR devices using the bespoke autocorrelation set-up with a red-laser based TPA detector, see Section 8.4.4. Intensity autocorrelation traces were recorded by the slow stepwise translation of one mirror, with the other, speaker-mounted mirror "dithered" at 85 Hz to reduce the interference effects, as explained in Section 8.3.4. The devices were pumped using 0.8 μs pulses on a duty cycle of 0.3%.

9.2.1. CCM Lasers with single ICR

In these devices, the compound cavity was created by a single deep-etched four-slot PBG ICR, as described in Sections 5.2.4 and 7.1.2 and illustrated in Figure 7.8(b) and Figure 9.8(I-a). The lasers were modelocked by applying a negative bias ($V_{SA} = -1 \div -5.5$ V) to the saturable absorber section and adjusting currents I_1, I_2 through the two gain sections to obtain a spectrum containing evenly-spaced modes only.
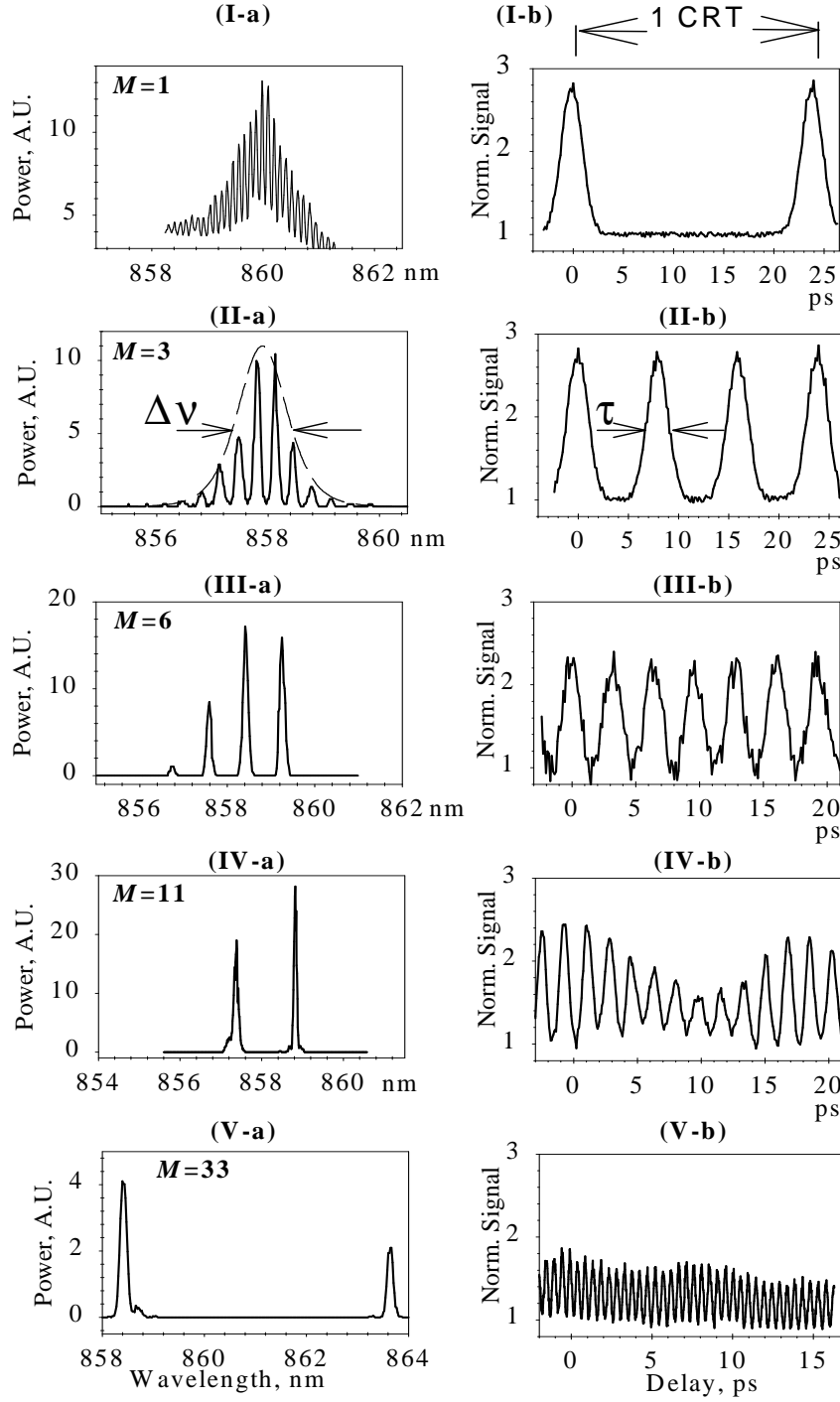
Figure 9.5. Spectra **(a)** and intensity autocorrelation traces **(b)** for CCM devices modelocked at different harmonics M of the cavity round-trip (CRT) frequency. To facilitate direct comparison, the horizontal axes in the spectra and autocorrelations are scaled so as to make up for the change in the device length.

(I):$M = 1$ (fundamental), $f = 43$ GHz, $\Delta\Lambda = \Delta\lambda_{F\text{-}P} = 0.107$ nm, no ICR, $L = 900$ μm;

(II): $M = 3$, $f = 131$ GHz, $\Delta\Lambda = 0.322$ nm, cavity ratio $L_1{:}L_2 = 300$μm:600μm $= 1{:}2$;

(III): $M = 6$, $f = 326$ GHz, $\Delta\Lambda = 0.779$ nm, $L_1{:}L_2 = 120$μm:600μm $= 1{:}5$;

(IV): $M = 11$, $f = 623$ GHz, $\Delta\Lambda = 1.52$ nm, $L_1{:}L_2 = 60$μm:600μm $= 1{:}10$;

(V): $M{=}33$, $f = 2109$ GHz, $\Delta\Lambda = 5.2$ nm, $L_1{:}L_2 = 19$μm:608μm $= 1{:}32$.

207

Figure 9.5 shows the spectra (a) and corresponding intensity autocorrelation traces (b) for CCM devices modelocked at different harmonics M of the cavity round-trip (CRT) frequency. Since the spectrum and autocorrelation are related by the Fourier transform, the mode separation in the frequency domain can be seen to increase with higher harmonic numbers, while the delay between consecutive pulses in the time domain becomes shorter. The CCM modelocking range obtained extends from 131 GHz ($M = 3$) up to 2.1 THz ($M = 33$). At the low frequency end, the plots of Figure 9.5(I) and (II) were obtained from a pair of identical-length lasers, as in Figure 5.1(c), only one of which had an ICR with a cavity ratio of $L_1:L_2$=1:2 ($M = 3$). One can see that the 1:2 ratio CCM laser shows a threefold multiplication of the mode separation, as well as of the pulse repetition rate (131 GHz against 43 GHz).

In Figure 9.5(III), the harmonic number is further doubled ($M = 6$) by positioning the ICR with a sub-cavity ratio of 1:5. Note that, since this device is shorter than the previous one, the modelocking frequency (326 GHz) has more than doubled. The autocorrelation of the 11th harmonic device of Figure 9.5(IV-b) at $f = 623$ GHz contains a slowly-varying envelope at the fundamental modelocking frequency (~56 GHz) due to the beating of unsuppressed Fabry-Pérot modes inside the two peaks of Figure 9.5(IV-a). This is believed to be due to an inaccurate cleaving of the 1:10 ratio, which then fails to provide a sharp cut-off for the unwanted satellite modes. Finally, one can count 33 peaks per CRT in the autocorrelation of Figure 9.5(V-b), which corresponds to a pulse repetition frequency of 2.1 THz. This result was obtained from a 1:32 ratio device, with a target ratio of 1:30 missed due to cleaving error.

In these ultrafast devices, the peak pulse power is too low to affect the autocorrelation contrast ratio, and the conclusion as to whether the laser is operating modelocked or not, can only be drawn by juxtaposing the locked and unlocked cases. The trace of Figure 9.6(a) was obtained from a device with $M = 7$, when the bias on the saturable absorber was switched off during the scan as the translation stage was passing through the zero delay position. The trace of Figure 9.6(b) relates to the ultrafast device with $M = 33$ and was made up of two scans with identical average power but different biases on the absorber for positive and negative delays. In both cases, the correlation peaks can be observed for much longer positive delays than for negative ones. This would indicate a longer coherence time ($\tau_c \gg 1$ CRT),

suggesting that the phases of the two modes are locked under the bias conditions used for positive delays. By contrast, the peaks plotted for negative delays fall off very quickly, which suggests random phases with low coherence, or self-pulsing behaviour. In effect, this information was obtained by using the autocorrelator as a cross-correlator (see Section 8.2.1) to measure the coherence of the CCM laser output. Even though the peaks of Figure 9.6(b) have the same contrast ratio as coherence spikes measured in a linear correlation (less than 2:1), it is still reasonable to assert that the 33rd-harmonic device is modelocked on the basis of the very similar coherence properties between the traces of Figure 9.6(a) and (b).
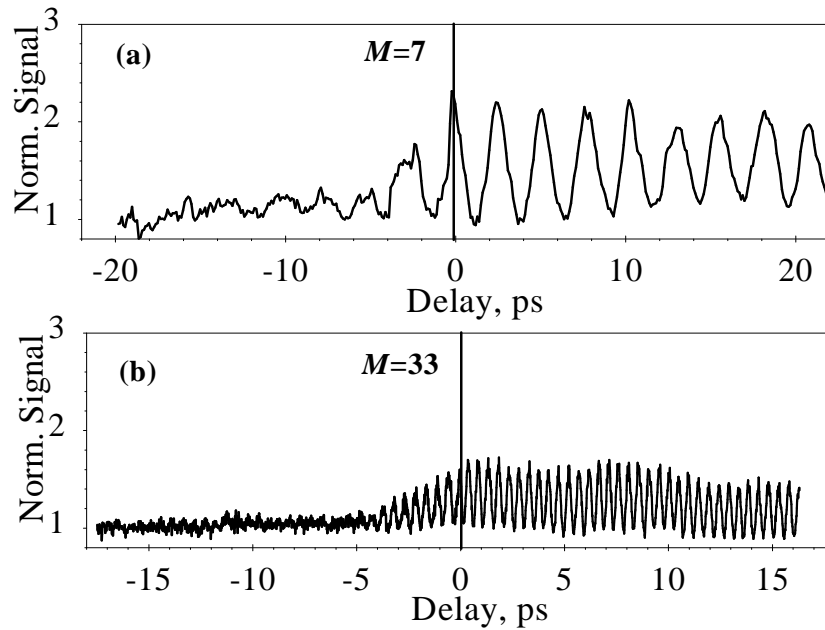
Figure 9.6. Proof of modelocking from intensity cross-correlation: modelocked trace plotted for positive delays ($\tau > 0$), unlocked for negative delays ($\tau < 0$). Note the change in contrast ratio and coherence time. **(a):** 7th harmonic device, $f = 396$ GHz, $I_1 = 20.5$ mA; $I_2 = 60$ mA; $\tau > 0$: $V_{SA} = -2.8$ V; $\tau < 0$: $V_{SA} = 0$ V (float); **(b):** 33rd harmonic device, $f = 2109$ GHz;
          $\tau > 0$: $V_{SA} = -4$ V; $I_1 = 4.4$ mA; $I_2 = 127$ mA;
          $\tau < 0$: $V_{SA} = -1.2$ V; $I_1 = 0$ mA (float); $I_2 = 111$ mA.

9.2.2. Pulse characterisation

A 3rd harmonic CCM laser was used for detailed characterisation of modelocked pulses. It was easier to characterise than high-harmonic devices, thanks to the relatively high peak pulse power, resulting in an intensity autocorrelation trace with a contrast ratio of approximately 2.7:1, as can be seen from the high-resolution

autocorrelation trace of a single pulse shown Figure 9.7(b). The autocorrelation peaks occur on a period of 7.6 ps (131 GHz), as shown in Figure 9.5(II-b).
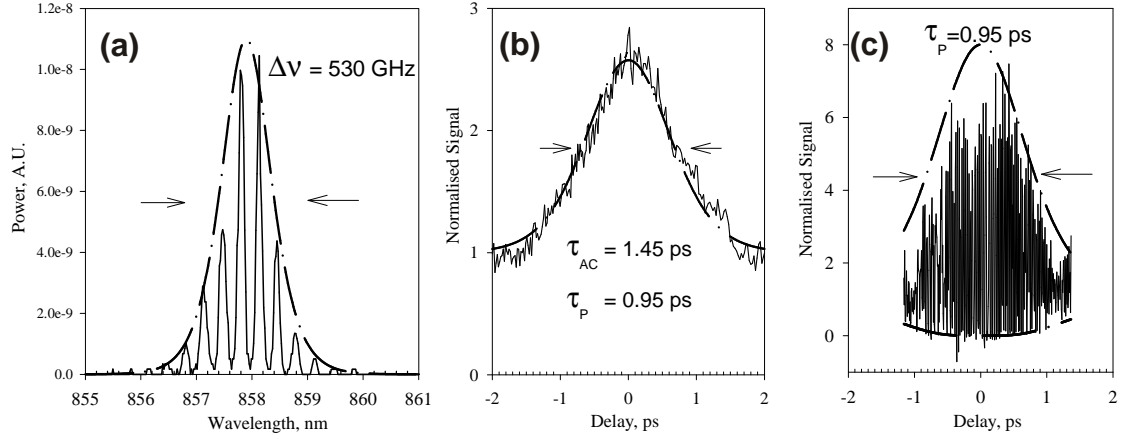
Figure 9.7. (a) Spectrum measured from a modelocked 3rd harmonic CCM device, with cavity sections 600 and 300 μm long (1:2 ratio). The dashed line denotes the spectral envelope for the assumed *sech^2* pulse shape in the transform limit.
(b) Intensity autocorrelation trace of this laser modelocked at 131 GHz. The fitted trace (dashed line) assumes a *sech^2* pulseshape with $\tau_p = 0.95$ ps, which corresponds to the measured autocorrelation peak width $\tau_{ac} = 1.45$ ps.
(c) Corresponding interferometric autocorrelation image. The computed envelope (dashed line) is that of the pulse reconstructed from the intensity autocorrelation **(b)**.

Table 9.1. Temporal, spectral and autocorrelation properties of the *sech^2* pulse shape (after [2]).

Peak type	Profile
Temporal pulse shape [$E^2(t)$]	$\mathrm{sech}^2(t) = \dfrac{1}{\left[\exp t + \exp(-t)\right]^2}$
Spectral envelope	$\mathrm{sech}^2\left(\dfrac{\pi\Omega}{2}\right)$, where Ω is angular optical frequency
Intensity autocorrelation	$\dfrac{3(\tau \cosh \tau - \sinh \tau)}{\sinh^3 \tau}$
Interferometric autocorrelation	$1 + \dfrac{9(\tau \cosh \tau - \sinh \tau)}{\sinh^3 \tau} \pm \dfrac{3(\sinh 2\tau - 2\tau)}{\sinh^3 \tau}$
Ratio between autocorrelation and temporal FWHM peak widths	$\tau_{ac} / \tau_p = 1.543$, where τ_{ac} is autocorrelation peak width and is τ_p the width of the temporal pulse intensity profile.
Transform-limited TBP	$K = 0.315$

Pulse width was estimated assuming a $sech^2$ (hyperbolic secant squared) pulse shape, which produced a better fit to both the intensity autocorrelation and spectral envelopes than other pulse profiles. The properties of $sech^2$ pulses can be found in the literature [2] and are listed in Table 9.1. For the spectrum of Figure 9.7(a) having a spectral envelope of 530 GHz (dashed line), this pulse shape gives a transform-limited pulse width of 0.59 ps. This compares with the 0.95 ps pulse width inferred from the 1.45 ps wide intensity autocorrelation peak of Figure 9.7(b). This discrepancy would suggest that the pulses are chirped, with the pulse width being 1.6 times the transform limit. Another explanation for the apparently large pulse width is the sub-harmonic intensity modulation, such as that visible in the trace of Figure 9.5(IV-b), leading to an aperiodic pulse shape between consecutive pulses, which could result in a smeared-out autocorrelation trace upon averaging across the pulse train, as indicated by Eq.(8.1).

Interferometric autocorrelation measurements of the same laser were carried out using the slow translation of one of the autocorrelator mirrors with a stationary speaker-mounted mirror, as described in Section 8.3.5. The precision of the autocorrelator was insufficient to resolve all the interferometric fringes, which explains the reduced contrast ratio (smaller than the theoretical 8:1) in the recorded trace of Figure 9.7(c). An interferometric envelope (dashed line) corresponding to the actual pulse width of 0.95 ps is plotted to indicate a probable trace shape if the fast fringe oscillations had been fully resolved. Because of the low contrast, it is difficult to draw any conclusions from the interferometric trace of Figure 9.7(c). However, one can say that the recorded image is slightly narrower than the fitted envelope, with a reduced fringe contrast in the wings of the trace, which can be construed as indicating the presence of phase modulation (see Figure 8.2 for an explanation).

In general, the information obtained on the 3rd harmonic CCM laser pulses is in good agreement with the simulations of Figure 4.10. Insufficient contrast ratio and number of modes in the spectra precluded meaningful pulsewidth analysis for higher harmonics, where a reasonable estimate of the pulse duration (FWHM) is $\tau_p \leq 1/2f$, where f is the modelocking frequency. In THz-frequency devices, with a harmonic modelocking spectrum consisting mainly of two modes [as in Figure 9.5(V-a)], a pulsewidth of $\tau_p \leq 0.24$ ps is estimated for a nearly sinusoidal pulse shape.

9.2.3. Effect of ICR type

The behaviour of high-harmonic devices ($M > 11$) was highly sensitive to the depth and number of etched ICR slots and bias conditions, see Table 9.2. The lasers having the most reflective ICRs operated in a single mode when all sections were forward-biased. A second mode would generally appear when one section was reverse biased and currents through the other two were adjusted. In Sections 5.2 and 7.1.2, the four ICR types fabricated in the CCM devices were described; these are shown in the SEM photographs of Figure 9.8(a). The fourth type, a shallow 13-period grating, had virtually no effect on the device performance and is therefore not shown. The estimated values for the reflectivity R_{ICR} and the observed ICR effects are given in Table 9.2.
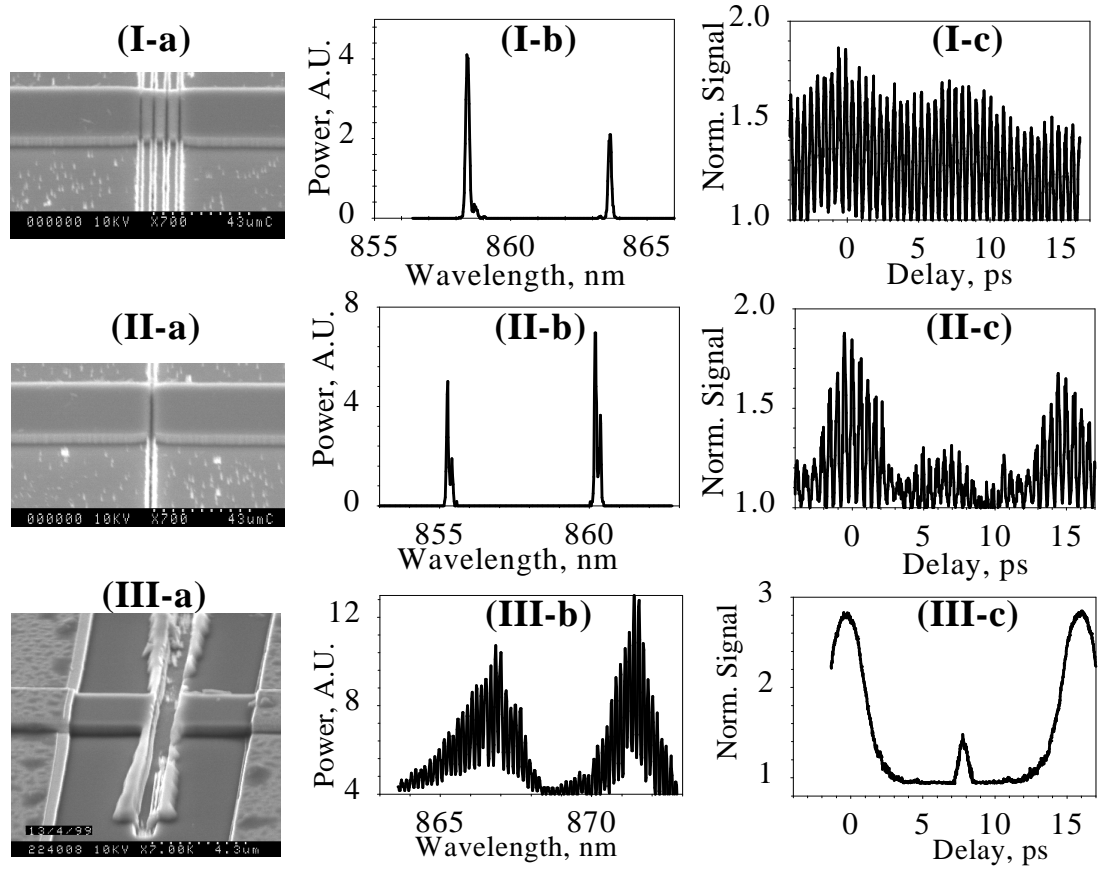
Figure 9.8. SEM photographs of three ICR types with different reflectivities R_{ICR} **(a)**, corresponding spectra **(b)** and intensity autocorrelation traces **(c)** for high-harmonic CCM devices. (I): 4th order PBG mirror of four deep slots (0.1 μm wide x 2 μm deep), $R_{ICR} \sim 0.7$, $M = 33$; (II): Single deep slot (0.2 μm x 2 μm), $R_{ICR} \sim 0.08$, $M = 30$; (III): Single shallow "bow-tie" slot (0.4 μm x 0.6 μm), $R_{ICR} \sim 0.001$; $M = 31$.

For devices incorporating the most reflective ICR, formed by a deep 4-slot PBG mirror [Figure 9.8(I-a)] with an estimated $R_{ICR} \sim 0.7$ (i.e., near the maximum of spectral selectivity in Figure 4.6), all the side modes were effectively suppressed, see Figure 9.8(I-b). As a result, the autocorrelation trace of the 33rd harmonic device of Figure 9.8(I-c) contains almost no low-frequency modulation. By contrast, where a single deep slot was used with an estimated $R_{ICR} \sim 0.08$ [Figure 9.8(II-a)], the satellite Fabry-Pérot modes were not fully suppressed [Figure 9.8(II-b)], and the pulses of [Figure 9.8(II-c)] were strongly modulated at the fundamental CRT frequency. Finally, a single shallow-etched slot with $R_{ICR} \sim 0.001$ in a 1:30 ratio device [Figure 9.8(III-a)] only caused low-depth spectral modulation, as shown in Figure 9.8(III-b). The autocorrelation trace of Figure 9.8(III-c) indicates only fundamental frequency modelocking and contains no visible high-frequency components. It can therefore be concluded that highly reflective ICRs are required for subharmonic-free modelocking of these ultrahigh-frequency devices.

Table 9.2. Behaviour of high-harmonic devices as a function of reflector type and bias conditions.

ICR Type	Estimated Reflectivity	Spectrum (all sections forward biased)	Spectrum (with reverse bias on SA)	Intensity Autocorrelation
4 deep slots	0.7	Single mode	2 harmonic-spaced modes	Near-uniform pulses at harmonic rep. freq.
1 deep slot	0.08	Single mode	2 harmonic-spaced groups of several Fabry-Pérot modes	Pulses at harmonic rep. rate modulated at fundamental freq.
1 shallow slot	0.001	Near single mode	Multiple Fabry-Pérot modes modulated at harmonic spacing	Pulses at fundamental repetition frequency
None	0	Multimode	Broad multimode	Pulses at fundamental repetition frequency

9.2.4. CCM Lasers with twin ICR

This Section reports the performance of the twin-ICR CCM lasers described in Section 4.2.2 and schematically shown in Figure 4.7. Such devices are not to be confused with multiple-slot PBG ICR lasers discussed in the previous section. In Ref.[3], the use of multiple ICRs was proposed with a view to improving side-mode suppression for single-mode operation. In this Project, this idea was developed further to create a device with two ICRs at specific locations to obtain a side mode-

free harmonic spectrum (and unmodulated pulses) with relatively small ICR reflectivities.
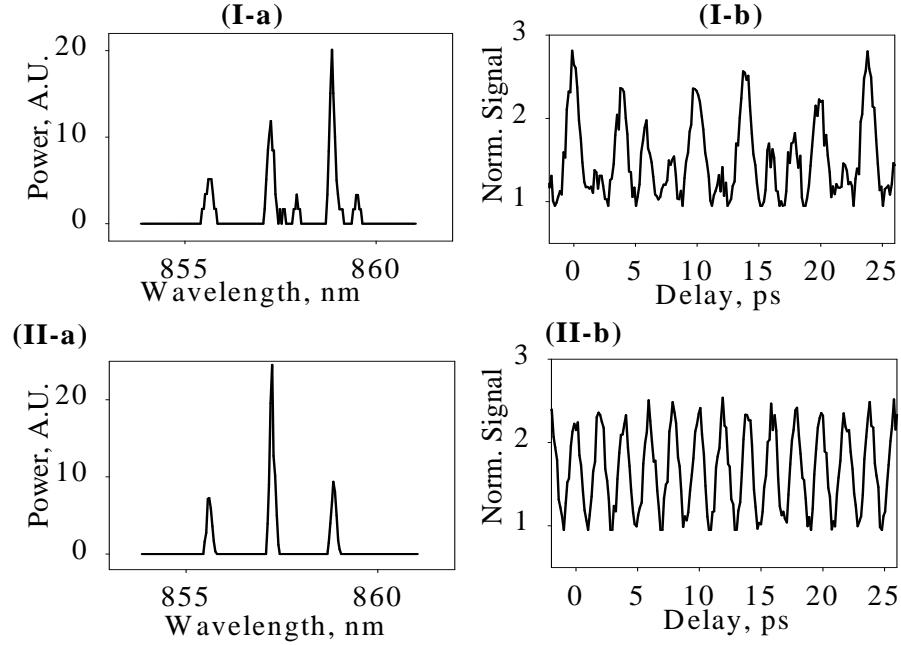
Figure 9.9. Experimental spectra **(a)** and intensity autocorrelation traces **(b)** of 12th harmonic CCM devices ($M = 12$, $f = 504$ GHz, $\Delta\Lambda = 1.29$ nm):
(I): Single deep slot at 5:12 of the cavity length (L_1:L_2 = 375µm:525µm = 5:7), $R_{ICR} \sim 0.08$; **(II):** Twin slots with $R_{ICR} \sim 0.08$ each, positioned at 5/12 and 1/3 of the cavity length.

A pair of same-length CCM lasers was fabricated, with one having a 5:7-ratio ICR only, and the other having both a 5:7 and a 1:2-ratio ICR. The total cavity length was 900 µm. The type of reflector used for both ICRs was that of Figure 9.8(II-a) (single deep slot), which has already been shown to be inadequate for modulation-free modelocking in the single-ICR configuration. The spectrum of the 5:7 ICR-only laser [Figure 9.9(I-a)] does indeed contain residual Fabry-Pérot modes between the harmonic ones, resulting in a highly ambiguous autocorrelation, see Figure 9.9(I-b). The other device, having both slots, exhibits a spectrum free of side-modes [Figure 9.9(II-a)] and a modulation-free autocorrelation at $f = 504$ GHz [Figure 9.9(II-b)]. These results are in good agreement with the theoretical simulations of a similar structure, plotted in Figure 4.10(IV),(V). Because the dual-ICR laser contains fewer slots than the four-slot PBG laser, it also has a threshold current 12% lower than that of a PBG ICR device. It is believed that the twin-ICR approach allows more accurate selection of the desired harmonic number than the single slot approach, as the relative position of the two ICRs is defined lithographically. On the other hand, it

lacks the flexibility of the single-ICR layout, which allows the harmonic number to be chosen at the cleaving stage.

9.3.   CPM laser in an external cavity

It is also appropriate to present an interesting result obtained by the author's colleague Dr M.W. Street from colliding-pulse modelocked (CPM) laser diodes at $\lambda = 850$ nm in an external cavity [4]. The 650 μm-long, 3-section ridge-waveguide lasers, shown schematically in Figure 3.8(b), were fabricated from GaAs/AlGaAs double quantum-well material on a semi-insulating GaAs substrate, with both p and n contacts on the top side of the device. The devices had a 30 μm-long saturable absorber section located in the middle of the cavity.

When these devices were pumped just above threshold with no reverse bias on the saturable absorber, the Fabry-Pérot mode separation observed in the optical spectrum was 0.14 nm. When a reverse bias of -1.58 V was applied to the SA section for a forward current of 42.4 mA in the gain sections, alternate modes in the lasing spectrum were suppressed, so that the modal separation was effectively doubled. A spectrum showing the doubled mode spacing of 0.28 nm is given in Figure 9.10(a). Numerical simulations using the distributed time domain model suggest that this is sufficient evidence to indicate CPM operation at 100 GHz ($M = 2$).
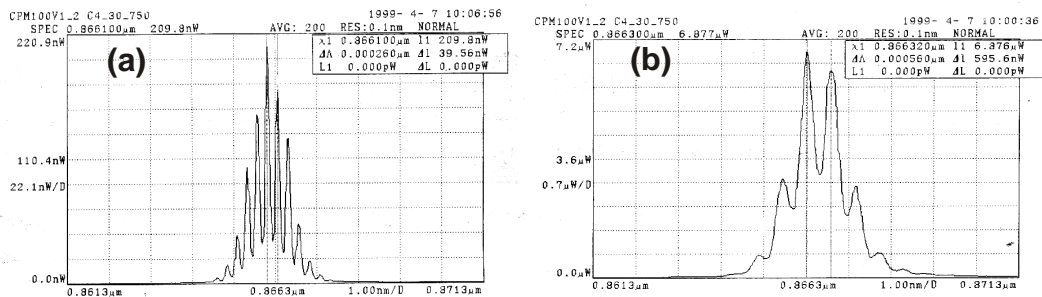
Figure 9.10. Colliding pulse modelocked spectrum at 100 GHz (M=2) **(a)** and spectrum showing enhancement of alternate CPM modes in a hybrid cavity **(b).**

Finally, an external gold reflector was positioned at a distance from the CPM laser facet equal to a quarter of the *optical* length of the laser diode thus forming a "hybrid" semiconductor-air compound cavity with a 1:4 ratio, as illustrated in Figure 9.11. In such a cavity, the fundamental mode spacing is defined by the

semiconductor laser resonator, with further mode selection provided by the relatively weak feedback from the external reflector. It can be shown that, in this case, the "harmonic" mode spacing $\Delta\Lambda$ is given by

$$\Delta\Lambda = M \, \Delta\lambda_{sc}, \text{ with } \frac{n_{sc} L_{sc}}{L_{air}} = \frac{M}{N} \tag{9.1}$$

where is $\Delta\lambda_{sc}$ the mode spacing of the semiconductor laser cavity, M and N are mutually irreducible integers; other symbols as defined in the caption of Figure 9.11. For the case shown, a quadruple ($M = 4$) mode separation compared to a standalone laser cavity is to be expected.
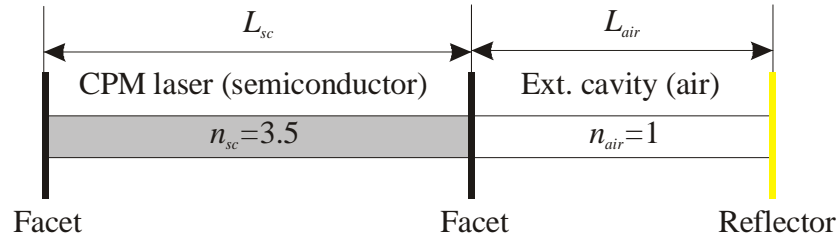
Figure 9.11. Hybrid semiconductor-air cavity formed by placing an external reflector close to the CPM laser. Here, $L_{air} = ¼ \, n_{sc} L_{sc}$, where L_{sc} and L_{air} are the geometrical lengths of the semiconductor and air cavities, respectively, and n_{sc} is the refractive index of the semiconductor.

By placing the CPM laser in such a cavity, the spectrum of Figure 9.10(a) was transformed into that of Figure 9.10(b). In the latter spectrum, alternate CPM modes were largely suppressed and every 4th mode was selected by the "hybrid" semiconductor-air cavity ($\Delta\Lambda = 0.56$ nm). This is consistent with 4th harmonic modelocking at 200 GHz. Here, the term "hybrid" can have two connotations, one being the type of cavity used (semiconductor-air), and the other denoting the cascaded CPM + CCM effect, whereby the initial CPM doubling of the mode separation is further increased by the CCM effect. No autocorrelation studies of the external-cavity CPM lasers have been performed, hence their modelocking operation cannot be corroborated beyond dispute.

Potentially, the external-cavity CCM effect may prove instrumental in adjusting the modelocking frequency of a laser diode after the fabrication stage, and a number of intra/external-cavity CCM/CPM constructions can be devised.

9.4.   Conclusions

All types of the fabricated CCM devices have been assessed and tested. Etched-facet CCM lasers exhibited early catastrophic failure and poor lasing performance, hence their modelocking operation was not attempted. Nor was it possible to characterise bent-cavity devices of various curve radii, owing to their non-performance as lasers.

Conversely, cleaved-facet, straight-waveguide CCM lasers have exhibited reliable lasing operation, lending themselves to spectral and autocorrelation studies. The spectra of *m:n*-cavity ratio devices manifested aperiodic mode spacing, with varying mode patterns at different pumping levels. Such spectral behaviour is thought to be due to the poor mode selection criteria offered by the *m:n*-ratio geometry.

At the same time, CCM lasers having 1*:n*-ratio cavities exhibited the expected periodic mode separation, however, early devices suffered from the poor suppression of unwanted satellite modes in the vicinity of harmonic modes. Increasingly more reflective ICRs were used to improve the finesse of the shorter sub-cavity and obtain stronger suppression of satellite modes. Only devices having deep-etched photonic-bandgap ICRs were able to deliver the satellite-free harmonic spectra that were suitable for autocorrelation measurements.

Autocorrelation studies confirmed the modelocking operation of these devices at selected harmonic numbers from 3 to 33, with corresponding repetition frequencies from 131 GHz up to 2.1 THz. In low-harmonic devices, the judgement as to the modelocked nature of the laser output was made by comparing the autocorrelation contrast ratio in the locked and unlocked cases; in high-harmonic devices, owing to their low peak power, the lasers' coherence times were compared in the two cases. In these terahertz devices, as the spectrum consisted mainly of two modes, the output was expected to have a near-sinusoidal envelope. The estimated pulse width for a 3rd-harmonic device was 0.95 ps, which is approximately 1.6 times the Fourier transform limit defined by the lasing spectrum. This would suggest the presence of frequency chirp or sub-harmonic intensity modulation in the generated pulse trains.

The modelocking behaviour was very sensitive to the type of ICR used. Only 4-slot PBG ICR lasers produced subharmonic-free THz-frequency output. Other types of ICR, with smaller reflectivities, resulted in pulse trains either at the fundamental repetition frequency ($M = 1$) or at the target harmonic but strongly modulated at that frequency. Generally, poorly resolved harmonic modes in the optical spectrum lead to low-frequency modulation in the corresponding autocorrelation. It is also expected that more accurate cavity cleaving should provide enhanced suppression of the unwanted satellite modes.

A twin-reflector CCM laser was engineered by an appropriate choice of the two ICR positions. Modelocked at 504 GHz, this laser has a lower threshold current than a 4-slot PBG device of the same length. It is believed that, although less flexible than the single-ICR, the twin-ICR approach is particularly promising in terms of device stability, as it combines the two different, yet complementary mode selection mechanisms provided by the 1:k and m:n-ratio geometries.

Finally, in a separate experiment, a modelocked CPM laser placed in an external cavity demonstrated a doubling of the mode separation through the CCM effect created by the hybrid semiconductor-air cavity. While no autocorrelation measurements were performed to confirm definitively that the external-cavity CPM laser was modelocked, the observed spectral transformation suggests that CPM and CCM effects can be cascaded to achieve even higher multiplication of the modelocking frequency. This approach also opens up a plethora of integration possibilities, where the modelocking frequency can be controlled by adjusting the external resonator. Further suggestions developing this idea are given in Section 11.4.6 of Chapter 11.

9.5.   References

[1]   P. Vettiger, M.K. Benedict, G.L. Bona, P. Buchmann, E.C. Cahoon, K. Datwyler, H.P. Dietrich, A. Moser, H.K. Seitz, O. Voegeli, D.J. Webb, and P. Wolf, "Full-Wafer Technology - A new approach to large-scale laser fabrication and integration," *IEEE J. Quant. Elec.*, vol. 27, pp. 1319-1331, 1991.

[2]   J.-C. Diels and W. Rudolph, "Diagnostic techniques," in *Ultrashort pulse phenomena*. San Diego: Acad. Press, 1996, pp. 365-400.

[3]   D.A. Kozlowski, J.S. Young, J.M.C. England, and R.G.S. Plumb, "Longitudinal mode control in 1.3 mm Fabry-Perot lasers by mode suppression," *IEE Proc.-Optoelectron.*, vol. 143 (1), pp. 71-76, 1996.

[4]   M. W. Street, D. A. Yanson, E. A. Avrutin, S. D. McDougall, I. G. Thayne, J. H. Marsh, and J. S. Roberts, "Sub-THz passive harmonic modelocking effects in external-reflector compound cavity laser diodes," presented at 1999 LEOS Annual Meeting; Conference Proceedings, v.2, pp.703-4, 1999.

CHAPTER 10.

OPTICAL HETERODYNING USING EXTERNAL-CAVITY

DUAL-WAVELENGTH LASER SOURCE

10.1. Overview

Parallel to the core work on CCM laser diodes, activities on the realisation of another approach to generating terahertz-modulated optical signals were carried out, albeit with a smaller level of effort. The approach consists in heterodyning two optical signals (such as two laser wavelengths) and down-converting their difference frequency into free-space THz radiation using a photomixer device. The principles of optical heterodyning with photomixers were explained in Section 2.3.2, with a device schematic and photographs given in Figures 2.12 and 2.13. Photomixers require semiconductor materials that have short carrier lifetimes, such as low-temperature-grown GaAs, which are essential for the ultrafast operation of these photoconductive elements. Photomixers can be pumped by a tuneable optical source containing only two narrow-linewidth frequency components, in the spectral range that is absorbed by the semiconductor material.

The objective of this part of the Project was to build a transportable, breadboard-mounted optical heterodyning set-up incorporating a tuneable dual-wavelength diode laser in an external grating cavity, illuminating an antenna-loaded photomixer. The set-up was then to be transported to the University of St. Andrews, where a bolometer system was to be used to measure the radiated THz power. Although it has not been possible to develop a functional heterodyne THz source within the timescale of this Project, it is nonetheless instructive to present the activities undertaken and the results obtained.

10.2. Photomixer devices

Initially, it was intended to reproduce the original experiment performed by E.R. Brown *et al.* [1, 2] on a low-temperature-grown (LTG) GaAs photomixer pumped by two single-mode lasers, in which continuous, free-space electromagnetic waves at up to 3.8 THz were generated. Prior to the start of the Project, similar photomixer devices had been fabricated at the University of Glasgow. The material used was ion-bombarded InP supplied by the Ioffe Institute, Russia, as preliminary results [3] suggested that this material may have a carrier lifetime shorter than that of LTG-GaAs.

Photomixer devices were also fabricated by the author in amorphous silicon on quartz substrates at the behest of St Andrews University. The devices had a similar design to the one used previously, but contained a variation of finger size and spacing in the photomixing region. The fabrication process consisted of the steps of resist patterning using e-beam lithography, metallisation and lift-off. After that, the devices were shipped to the University of Dundee for amorphous Si deposition. The e-beam lithography comprised two exposure steps, the first for the high-resolution definition of the sub-micron finger electrode structure, and the second to expose the large-area spiral antenna. A similar process was used for the fabrication of the photoconductive-switch autocorrelator detectors described in Section 8.4.2, with identical interdigitated structures. Difficulty was encountered when attempting to write the photomixer patterns on quartz substrates due to the charging up of the dielectric substrate during e-beam writing. A thin (15 nm) titanium layer was evaporated on top of the resist to prevent the charge build-up due to exposure to the electron beam.

Photographs of the fabricated antenna-loaded photomixer devices on quartz substrates are presented in Figure 10.1. The devices could not be tested until after amorphous Si deposition in Dundee. St. Andrews University did subsequent tests only to discover that the photomixers had a short-circuit electrical characteristic, apparently due to the out-diffusion of gold from the contact metal into the silicon. Regrettably, no further photomixers were fabricated.
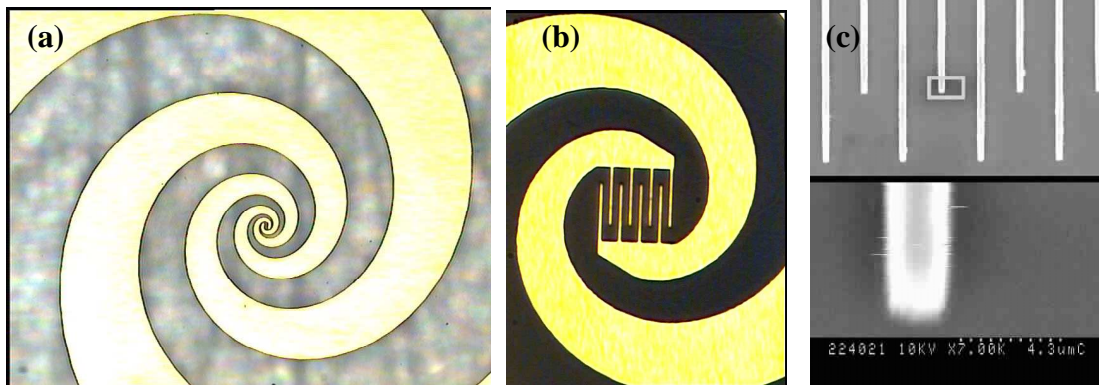
Figure 10.1. Optical photographs **(a,b)** and SEM image **(c)** of the fabricated antenna photomixers on a quartz substrate. The photographs **(b,c)** show the magnified finger structure. The electrode size is 0.2 µm x 10 µm on a 1.7 µm period.

10.3. External-cavity laser source

The generation of heterodyne optical signals using laser diodes has been the subject of extensive research. A Type-II modulated signal (see the definition of Figure 2.1) containing two extremely narrow-linewidth spectral components is essential for optical-to-microwave down-conversion. Indeed, a frequency offset of 1 THz in the 850 nm wavelength range corresponds to a difference of only 2.5 nm in the spectrum domain, therefore each line must be ideally less than a few kilohertz wide, which corresponds to a single longitudinal mode of a typical diode laser cavity [4].

10.3.1. Two-colour, narrow-linewidth optical THz sources

One approach to generating such high-quality signals relies on two single-mode lasers emitting at different wavelengths, the output of which is combined to obtain the desired signal. Two stabilised DBR lasers were used in the original [2] and subsequent [5] THz photomixing experiments. The outputs of two external-grating-tuned laser diodes were combined in Ref.[6] to obtain a beating note at a THz frequency, which was also characterised using autocorrelation measurements. In Ref.[7], two widely tuneable wavelengths (up to 17 nm apart at $\lambda = 800$ nm) were obtained from a laser diode array in a single-grating external cavity, with the wavelengths selected by a moveable V-shaped double-stripe end mirror.

In all above configurations, certain locking and stabilisation schemes had to be employed to reduce the frequency and phase fluctuations between the two laser sources. The problem can be alleviated by integrating the two laser cavities on a single chip and merging them with a Y-coupler, as was done with DFB [8] and DBR [9] lasers.

The ultimate solution, however, would be to generate the two optical signals in the same laser cavity, which will ensure high frequency and phase coherence between them. This can be achieved by means of an external grating-loaded cavity [10], a sampled grating in a DBR laser [11], or filtering out two distant modes from the spectrum of a modelocked laser [12]. In Ref.[13], high-purity dual-wavelength output with a frequency difference of 15 GHz was obtained from an actively-modelocked DFB laser integrated with a passive cavity. In this Project, two THz-frequency offset wavelengths were obtained from a source containing a single laser in a cavity with two gratings, with each grating responsible for tuning the corresponding wavelength.

10.3.2. Laser diode in an external grating cavity

A system comprising a laser diode placed in a long external-mirror resonator can be thought of as a compound cavity configuration, with the inside laser facet performing the function of an ICR. However, the mode selection mechanisms operative in C^3 lasers (Section 4.1.2) are not very effective in this case, as the external (air) cavity typically has an optical length that is tens of times longer than that of the semiconductor cavity. Correspondingly, the mode spacing of the external cavity is tens of times smaller, with much narrower resonance peaks than in the semiconductor cavity. As a result, it may prove difficult to obtain high suppression ratios for unwanted longitudinal modes of the semiconductor cavity and achieve wavelength tuning by varying the length of the external cavity.

When terminated by a plane mirror, the external cavity returns light at all wavelengths that meet the Fabry-Pérot condition. However, if a highly dispersive optical element is used as the second facet of the external cavity, an additional constraint is imposed on frequencies selected for feedback. Through its ability to diffract very small wavelength intervals back into the lasing medium, such a dispersive element can potentially choose a single laser cavity mode for feedback,

dramatically shifting the balance of power in the competition among lasing cavity modes from one mode to another. In this way, external feedback can force a multimode laser diode to operate in a single mode. Furthermore, the dispersive element enables one to "drag" the operation of the lasing medium to other modes away from the gain peak. However, to enable continuous tuning and high side-mode suppression ratios, the semiconductor cavity's own resonances must be suppressed, so that the only modes present are those of the combined semiconductor-air cavity. This is usually achieved by applying an anti-reflection coating to the inside laser facet.
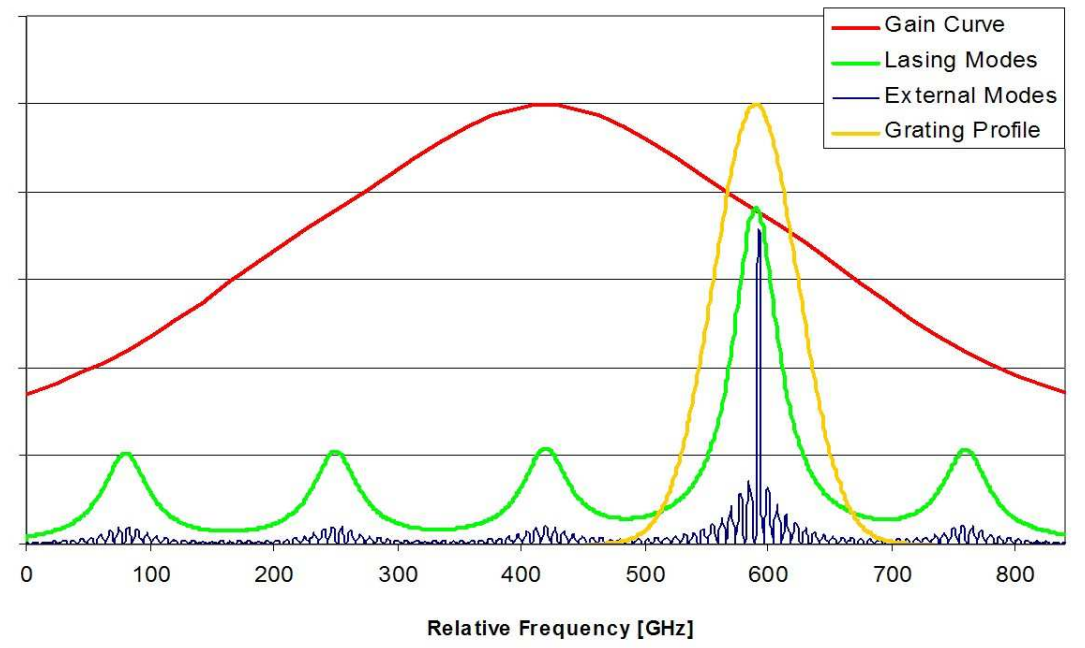
Figure 10.2. Spectral selectivities of the laser diode cavity, external cavity and the diffraction grating superimposed on the gain curve of the laser medium [14].

A holographic diffraction grating is an ideal candidate for such a dispersing element. Indeed, the grating allows the selection of a single lasing cavity mode to be reflected back into the diode laser cavity. The characteristic spectral widths of the modes of the semiconductor cavity and those of the external cavity in relation to the spectral selectivity of the grating are shown in Figure 10.2.

Light diffraction by a grating is illustrated in Figure 10.3 and is governed by the equation:

$$m\lambda = d(\sin\alpha + \sin\beta),$$

(10.1)

where α and β are, respectively, the angle between the incident beam and the normal to the grating surface, and the angle between the diffracted beam and the normal; d is the groove spacing, and m is an integer representing the order of diffraction. The angles α and β must be equal in order for the diffracted ray to travel along the path of the incident ray, thus providing feedback into the laser cavity. Such a grating arrangement is known as the Littrow configuration, where the grating equation (10.1) now takes the form

$$m\lambda = 2d \sin \alpha_L,$$ (10.2)

where α_L is referred to as the Littrow angle. Consequently, the wavelength diffracted into the laser is changed by simply changing α_L as the grating is rotated, so that the dispersion plane remains perpendicular to the surface of the grating.
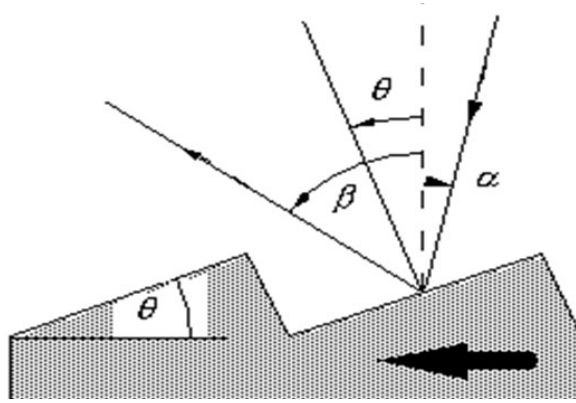
Figure 10.3. Diffraction by a blazed holographic diffraction grating [14].

The diffraction efficiency of a grating can be increased by redistributing and concentrating most of the diffracted energy into a particular frequency and/or diffraction order, which effectively enhances the reflectivity of the grating mirror for that particular wavelength. This is accomplished by "blazing" the grating, which alters its ruling profile, so that the groove shape is in the form of a right triangle with a characteristic angle known as the blazing angle. The blazing angle is denoted θ in the schematic of Figure 10.3. The efficiency of the grating at a particular wavelength is optimised by setting the grating in the Littrow configuration, then altering the blaze angle until the concentration of diffracted energy falls into a particular Littrow angle at the wavelength of interest. As such, gratings come blazed for different wavelengths. Consequently, by incorporating such a grating into the external cavity in the Littrow configuration, with a blazing angle corresponding to the desired

wavelength, the finesse of the external cavity at that particular wavelength can be increased, leading to enhanced feedback into the laser diode.

10.3.3. Description of the laser set-up

The two-colour external-cavity laser set-up, shown in the schematic of Figure 10.4, was assembled on a precision optical breadboard bench. A broad-area AlGaAs/GaAs laser diode, with one facet anti-reflection coated, was bonded onto a gold-plated copper heatsink using indium balls and flux, similarly to CCM devices (see Step 33, Table 7.1). The heatsink-mounted laser was inserted in a water-cooled Peltier stage and operated in the CW regime using a Newport current laser driver. The external cavity was loaded with two gold-plated 1200 lines/mm Spectragon diffraction gratings in the Littrow configuration blazed for 850 nm. The output from the coated facet was divided between the two gratings using a non-polarising beam-splitter. A beam expander was used to widen the beam waist and increase the beam interaction with the grating surface. By rotating each grating, a very narrow wavelength range could be selected from the diffracted beam and retro-reflected along the path of the original ray back into the laser cavity. Linear translation in one of the grating arms was used to adjust the path length difference between the two arms. Output was collected from the outside (uncoated) laser facet and coupled into a lensed multi-mode fibre, which was connected to a spectrum analyser. No computer control or measurement automation was employed.
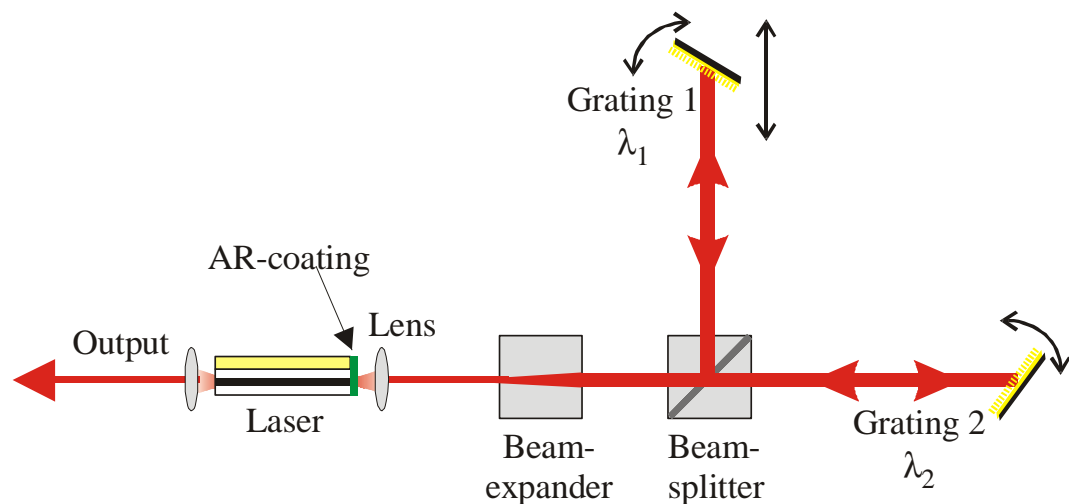
Figure 10.4. Dual-wavelength external-cavity laser set-up.

10.3.4. Anti-reflection facet coatings

In order to suppress the Fabry-Pérot modes of the laser diode and make it suitable for use as a gain block in the external grating-loaded cavity, the inside facet must be anti-reflection (AR) coated with dielectric layer(s) such as silica, alumina or titanium dioxide. In order to fully suppress the effect of semiconductor cavity modes, the coating must have a reflectivity under 1% or even lower (0.1% being the industry standard for many applications). The theory, application and characterisation of dielectric coatings are widely available in the literature (see, e.g., [15]).

The reflectivity of the AR coatings can be assessed by comparing the performance of the laser before and after coating. The mode ripple in the superluminescence spectrum of a facet-coated laser [16] or change in its lasing threshold in an external cavity [17] can be used for accurate characterisation of ultra-low AR coatings. In this Project, a rather crude estimate of a coating's reflectivity was made by measuring the optical powers P_c and P_u emitted by the coated and uncoated facets, respectively, under identical bias. The measured powers are related to the coated R_c and uncoated R_u facet reflectivities as follows:

$$\frac{P_c}{P_u} = \frac{1-R_c}{1-R_u}\sqrt{\frac{R_u}{R_c}}, \tag{10.3}$$

wherefrom the coated facet reflectivity R_c can be found by assuming $R_c \approx 30\%$ for the as-cleaved facet. This method, also known as the front-to-back power ratio technique, is often used to obtain a rough estimate of the coated facet reflectivity from knowledge of the reflectivity of the opposite facet.

Single-layer coatings, although of very simple design, are much more sensitive to thickness variations and have a much narrower bandwidth compared to multi-layer coatings. Commercially available software can be used to design single and multi-layer coatings, e.g., *FilmTek 2000* by Scientific Computing International, Inc. A graph showing the computed reflectivity of a three-layer AR coating optimised for $\lambda = 860$ nm is shown in Figure 10.5. The curves are plotted for a range of effective modal indices of an AlGaAs/GaAs waveguide. While a theoretical reflectivity of virtually zero can be modelled for a target wavelength, in reality the imperfections associated with the non-uniformity of deposited films and mounting

geometry result in substantial deviations from the modelled performance, which makes the deposition of ultra-low AR facet coatings a difficult technical challenge.
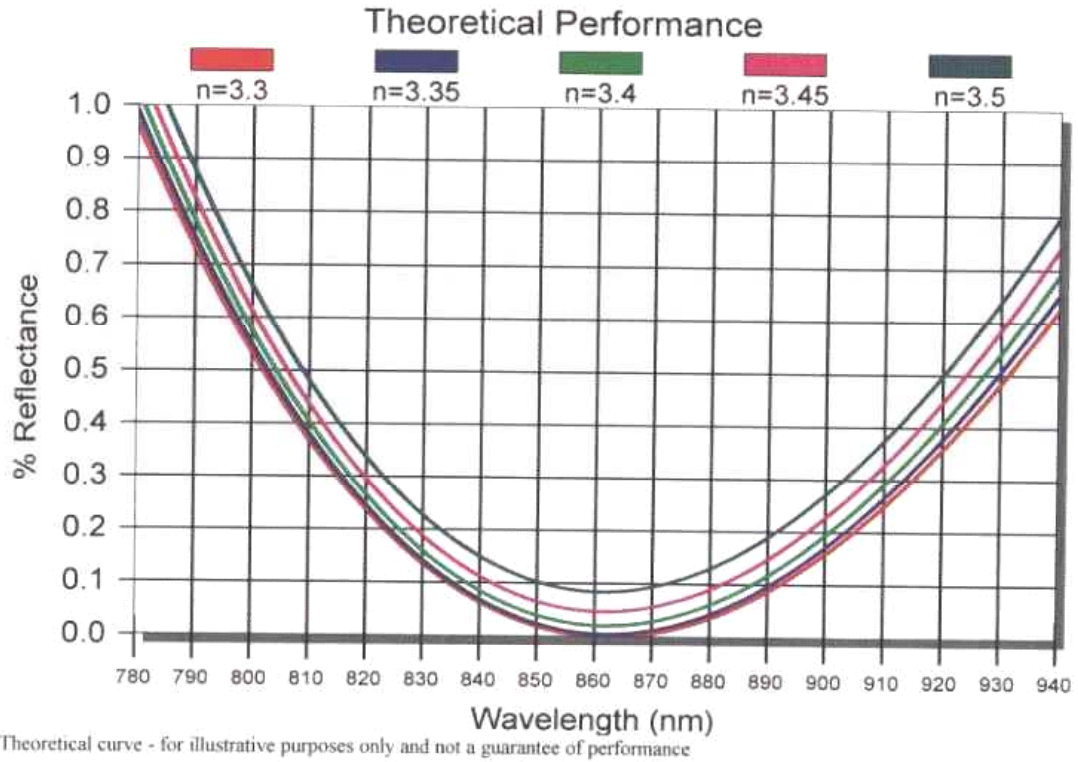
Figure 10.5. Modelled reflectivity of a 3-layer AR coating as a function of wavelength for different refractive indices of the waveguide (courtesy of Melles Griot Ltd.)

Silica and alumina-based antireflection coatings were deposited using an in-house sputterer. The coatings consisted of a single layer, which had an optical thickness of a quarter-wavelength. Using the front-to-back ratio method, the reflectivity of the coated facets was estimated to be as high as 8%. Broad-area lasers were then supplied to Heriot-Watt University, where they were AR-coated using a purpose-modified evaporator. However, the measured reflectivities were still as high as 6%. Finally, the coating of some lasers was outsourced to the Melles Griot Coating Facility (presently CVI Technical Optics Ltd.) on the Isle of Man. The expected performance of the three-layer coating is shown in Figure 10.5. A whole laser sample was hand-delivered to the site, where it was cleaved into bars immediately before coating. This was done to reduce facet oxidation due to prolonged exposure to air. The bars were then facet-coated using a specially designed jig in a Satis ion-assisted evaporator. The measured reflectivity was around 2.3%, which was the best value of all the attempts.

10.4. Results

It has proved impossible to obtain pure single or two-mode operation using the AR-coated broad-area laser in the set-up of Figure 10.4. Owing to the poor AR coatings (with $R_c > 1\%$), the coated devices were still lasing even without external feedback. By placing the device in the external cavity with one grating blocked, it was possible to reduce the spectral width of the laser's output and tune it within a range of 5 nm.
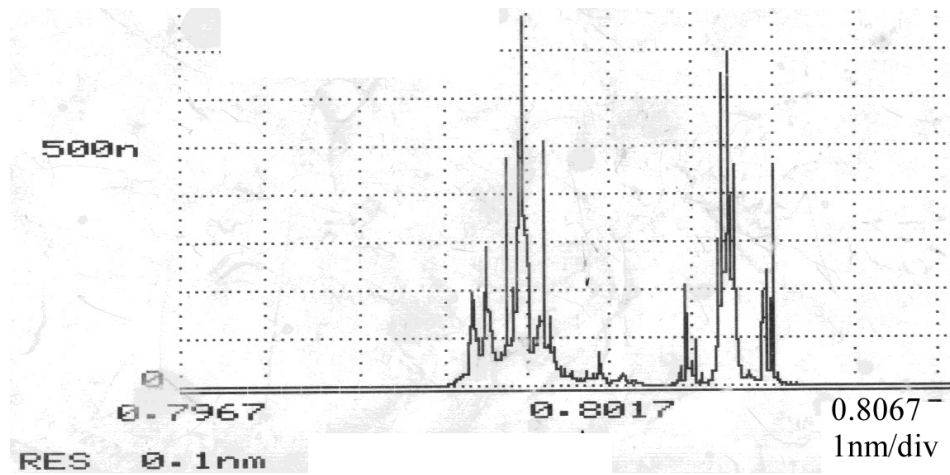
Figure 10.6. Typical lasing spectrum of the dual-wavelength, external-cavity laser source.

However, the measured spectrum contained a cluster of modes rather than a single mode. A similar spectral peak was obtained with the use of the other grating, with both gratings selecting two independently tuneable peaks and a typical spectrum shown in Figure 10.6. The maximum inter-peak separation was 3 nm (~ 1.2 THz), however, the two peaks themselves were extremely broad (1 nm ~ 0.4 THz). Such broad linewidths would preclude the use of this source in any practicable THz down-converter.

10.5. Conclusions

THz photomixers for down-conversion experiments have been fabricated in amorphous silicon. However, the devices suffered from an electrical problem, which is thought to be linked to the diffusion of contact metal into the semiconductor and the difficulty in using non-conducting quartz substrates with e-beam lithography. At

the same time, the photoconductive switch autocorrelators of Section 8.4.2 fabricated on LTG GaAs substrates using the same technology, demonstrated excellent electrical characteristics. Therefore, it is hoped that if similar photomixers were fabricated on a LTG GaAs substrate, no such fabrication problems would occur.

Unfortunately, neither has it been possible to obtain good data from the implemented optical heterodyning set-up. The dual-wavelength, external-cavity laser source has failed to deliver the spectrally-narrow lines required for optical heterodyning and down-conversion experiments, although some tuneability was demonstrated. This was due to the poor AR coating of the inside laser facet, which did not provide sufficient suppression of the intra-cavity modes, resulting in poor sensitivity to external feedback.

In conclusion, it has been impossible to carry out down-conversion and photomixing experiments with the level of effort and resource available to this line of research within the Terahertz Project. In the author's opinion, whilst photomixers definitely merit further studies, as these devices have demonstrated the highest optical-to-microwave conversion efficiencies to date, the dual-wavelength external cavity source has a number of shortcomings compared to the CCM devices. The *pros* and *cons* of the two sources are listed in Table 10.1. It is suggested that the down-conversion of CCM lasers with photomixers would offer the most promising way forward.

Table 10.1. Comparative characteristics of the external cavity source vs. CCM lasers.

Dual-wavelength external-cavity laser	CCM laser
Wavelength/frequency tuneability (+)	Rigid, compact, monolithic (+)
High output power (+)	Phase-locked output expected to give higher conversion efficiency (+)
Simple device structure (single-section broad-area laser) (+)	Complex device (ridge waveguide, ICR, SA) (-)
Poor rigidity and robustness (-)	Poor tuneability (-)
Ultra-low AR coatings required (-)	

10.6. References

[1]   E. R. Brown, K. A. McIntosh, K. B. Nichols, and C. L. Dennis, "Photomixing up to 3.8 THz in low-temperature-grown GaAs," *Appl. Phys. Lett.*, vol. 66, pp. 285-287, 1995.

[2]   K. A. McIntosh, E. R. Brown, K. B. Nichols, O. B. McMahon, W. F. DiNatale, and T. M. Lyszczarz, "Terahertz photomixing with diode lasers in low-temperature-grown GaAs," *Appl. Phys. Lett.*, vol. 67, pp. 3844-6, 1995.

[3]   G. S. Sokolovskii, E. U. Rafailov, A. G. Deryagin, V. I. Kuchinskii, E. L. Portnoi, A. Moujoud, M. Ochiai, and H. Temkin, "Picosecond InP photoconductors produced by deep implantation of heavy ions," *Proc. SPIE: Infrared Detectors for Remote Sensing: Physics, Materials, and Devices*, vol. 2816, pp. 106-109, 1996.

[4]   R. Wyatt, "Spectral Linewidth of External Cavity Semiconductor Lasers with Strong, Frequency Selective Feedback," *Electron. Lett.*, vol. 21, pp. 658-659, 1985.

[5]   P. Chen, G. A. Blake, M. C. Gaidis, E. R. Brown, K. A. McIntosh, S. Y. Chou, M. I. Nathan, and F. Williamson, "Spectroscopic applications and frequency locking of THz photomixing with distributed-Bragg-reflector diode lasers in low-temperature-grown GaAs," *Appl. Phys. Lett.*, vol. 71, pp. 1601-3, 1997.

[6]   N. Onodera, "THz optical beat frequency generation by modelocked semiconductor lasers," *Electron. Lett.*, vol. 32, pp. 1013-1014, 1996.

[7]   C. L. Wang and C. L. Pan, "Tunable multiterahertz beat signal generation from a two-wavelength laser-diode array," *Opt. Lett.*, vol. 20, pp. 12921294, 1995.

[8]   C. Laperle, M. Poirier, M. Svilans, and M. Tetu, "Microwave generation with monolithic dual-wavelength DFB lasers," presented at IEEE/LEOS Summer Topical Meeting, Montreal, Quebec, Canada, 11-15 August 1997.

[9]   M. Maeda, T. Hirata, M. Suehiro, M. Hihara, A. Yamaguchi, and H. Hosomatsu, "Photonic integrated circuit combining two GaAs distributed Bragg reflector laser diodes for generation of the beat signal," *Jpn. J. Appl. Phys.*, vol. 31, pp. L183-L185, 1991.

[10]   M. Tani, P. Gu, M. Hyodo, K. Sakai, and T. Hidaka, "Generation of Coherent Terahertz Radiation by Photomixing of Dual-Mode Lasers.," *Opt. & Q. Elec.*, vol. 32, pp. 503-520, 2000.

[11]   Y. Matsui, M. D. Pelusi, S. Arahira, and Y. Ogawa, "Beat frequency generation up to 3.4 THz from simultaneous two-mode lasing operation of sampled-grating DBR laser," *Electron. Lett.*, vol. 35, pp. 472-474, 1999.

[12]   M. D. Pelusi, H. F. Liu, and D. Novak, "THz optical beat frequency generation from a single mode locked semiconductor laser," *Appl. Phys. Lett.*, vol. 71, pp. 449-451, 1997.

[13]   A. C. Bordonalli, B. Cai, A. J. Seeds, and P. J. Williams, "Generation of microwave signals by active mode locking in a gain bandwidth restricted laser structure," *IEEE Phot.Techn. Lett.*, vol. 8, pp. 151-153, 1996.

[14]   B. Azmoun and S. Metz, "Recipe for locking an extended cavity diode laser from the ground up." Webpage: http://laser.physics.sunysb.edu/~bazmoun/RbSpectroscopy/: Stony Brook University.

[15]   T. R. Chen, Y. Zhuang, X. J. Xu, P. Derry, N. Bar-Chaim, A. Yariv, B. Yu, Q. Z. Wang, and Y. Q. Zhou, "Applications of a dielectric coating to semiconductor lasers," *Optics & Laser Techn.*, vol. 22, pp. 245-254, 1990.

[16]   I. P. Kaminow, G. Eisenstein, and L. W. Stulz, "Measurement of the modal reflectivity of an antireflection coating on a superluminescent diode," *IEEE J. Quant. Electronics*, vol. QE-19, pp. 493-495, 1983.

[17]   L. Stokes, "Accurate measurement of reflectivity over wavelength of a laser diode antireflection coating using an external cavity laser," *J. Lightw. Techn.*, vol. 11, pp. 1162-1167, 1993.

CHAPTER 11.

SUMMARY AND CONCLUSIONS

This is the final chapter of the Thesis, where the results obtained in this Project will be summarised and key achievements recapped. Novel inventive steps stemming from this work will be listed. A number of suggestions for future work will also be given.

11.1. Summary of conducted research

The research effort within this Project concentrated on the generation of optical signals carrying terahertz-frequency modulation. Two methods were pursued: the first one was to obtain a THz beat note from the dual-wavelength output of a laser diode in an external grating-loaded cavity, while the other one was to generate optical pulses at THz repetition frequencies using harmonic-modelocked compound-cavity laser diodes. The second approach is believed to provide higher-quality THz modulation than the first one due to the phase-locking of optical modes and enhanced inter-mode coherence.

The realisation of the first method has demonstrated the tuneability of the two-wavelength source and its potential for optical heterodyning applications (see Chapter 10). However, owing the technological difficulties (poor anti-reflection facet coatings) and the comparatively low level of effort, the linewidth requirements for an optical THz source have not been fulfilled. The two optical wavelengths obtained contained multiple modes with a combined linewidth of the order of the THz beat frequency being generated. Such poor linewidths precluded the use of the realised laser source in optical-to-THz down-conversion experiments.

By contrast, the second method of generating a THz envelope on an optical carrier using ultrafast modelocked lasers has formed the main focus of the Project and yielded some very remarkable results. The fabricated AlGaAs/GaAs devices utilised a novel type of harmonic modelocking, which allowed the pulse repetition

frequency to be multiplied by a factor defined by the device geometry. The frequency multiplication was achieved by creating a novel monolithic compound cavity with the use of highly reflective photonic-bandgap microstructures. Technological processes for the fabrication of these microstructures and precision cleaving of the resulting devices were developed.

Autocorrelation studies were used to confirm the modelocking operation of these devices at selected harmonic numbers from 3 to 33, with corresponding repetition frequencies from 131 GHz up to a record high of 2.1 THz. To the author's knowledge at the time of writing, this is the highest modelocking frequency achieved from a semiconductor laser, or, indeed, any type of laser. This demonstrates the suitability of the compound-cavity harmonic-modelocking technique for the generation of microwave-modulated optical power in the terahertz range. With the optical power concentrated mainly in two dominant modes, these lasers should be particularly suitable for local oscillator applications where a sinusoidal output is desired.

It is believed that the THz-modulated optical signals obtained with either of the two methods realised in this Project can be most efficiently down-converted into free-space radiation using photomixers incorporating an integrated terahertz antenna. To ensure adequate responsivity at THz modulation speeds, the photomixer devices were fabricated in ion-bombarded InP and amorphous Si, with both semiconductors having a short carrier lifetime. While the fabricated photomixers suffered from technological problems, a process for the fabrication of these devices has been developed. Due to time constraints, no photomixing experiments have been attempted.

11.2. Key achievements

Shown below is a bullet-point list of the most significant and novel results (in the author's view) achieved in the course of the Project. A reference to the description of each point in the Thesis is given in parentheses.

- Novel compound-cavity laser diodes incorporating 1D photonic-bandgap micostructures (Section 5.2.4).

- Definition of narrow (~ 100 nm) deep-etched slots to form PBG features (Section 7.1.2).

- Precision cleaving to ±4 μm using a wet-etch initiation process (Section 7.1.3).

- Fabrication of photoconductive switch autocorrelators and photomixers with sub-micron inter-digitated features (Sections 8.4.2 and 10.2).

- Characterisation of detector non-linearity and autocorrelation calibration procedure (Sections 8.4.3 and 8.4.4).

- Compound-cavity devices showing desired spectral transformations (Section 9.1.2).

- Autocorrelation results confirming the modelocking operation of these devices with pulse repetition frequencies from 131 GHz up to a record high of 2.1 THz (Section 9.2.1).

- Investigation of the effect of the type of intermediate reflector on modelocking behaviour (Section 9.2.3).

- Realisation and modelocking of a twin-reflector laser (Section 9.2.4).

- Observation of the external-cavity CCM effect (Section 9.3).

- Tuneable dual-wavelength source in an external cavity loaded with two gratings (Section 10.3.3).

- 16 journal and conference publications presenting the research results (see the Publications section at the beginning of the Thesis).

- Interest of the optoelectronic community in this research [1] (see Appendix for the full text of Ref.[1]).

11.3. Inventive steps

The successful execution of the Project and achievement of the above results have commanded a considerable degree of ingenuity in developing engineering solutions to the many challenges encountered during this work. Here, it is

appropriate to list the novel approaches and methods resulting from this work, which are believed to be the author's original ideas. As all of these developments have already been published by the author in the public domain, there appears to be no scope for intellectual property protection of the results reported in this Thesis.

11.3.1. The PBG ICR cavity

Compound-cavity (CC) laser diodes of most common types, whether the separation between the sub-cavities is formed by an optical cleave (C^3 lasers) or an etched groove (monolithic lasers), suffer from common stability and reproducibility problems. These are associated with the strongly oscillating dependence of the inter-subcavity coupling strength on the air gap width [see Figure 4.2(d)]. Indeed, a variation on the sub-wavelength scale (tens of nanometres) in the size of the gap may result in a vastly different device behaviour. The poor stability and reproducibility of CC lasers have been the most limiting factor in their applications.

However, by employing a periodic PBG structure instead of a single air gap, it should be possible to greatly improve both the stability and control of a CC device. The periodic nature of the PBG feature renders it more robust by averaging out the fabrication errors across several slots and thus reduces the variability associated with a one-off etched feature or a cleaved air gap. It is with such PBG reflectors that the required spectral transformations and harmonic modelocking operation were obtained in the CCM lasers reported in this Thesis.

Intra-cavity PBG reflectors can be used to obtain not only an increase in the mode separation or modelocking frequency of the cavity, but also single-mode operation of a CC laser. Following completion of the Project, further ideas of forming compound cavities with PBG features were developed and co-patented by the author in Ref.[2]. At the time of writing, another patent [3] is being filed, where several embodiments of the diffractive and focusing properties of similar PBG structures are protected.

11.3.2. The twin-ICR cavity

Both the stability and cleaving tolerance of a CC laser can be improved by using several ICR features. This idea is not novel and was employed in Ref.[4] to

obtain single-mode lasing by placing n ICRs at binary fractions $L / 2^n$ of the total cavity length L. All of the resulting cavity ratios are therefore of the 1:k type (here, $k = 2^n$), with an improved side mode suppression due to the "brute force" of repeated use of the same mode selection rules.

In the sub-section "Twin-reflector CCM configuration" of Section 4.2.2, an alternative ICR layout is described and illustrated in Figure 4.7. The approach consists in combining the two different, yet complementary mode selection mechanisms provided by the 1:k and m:n cavity-ratio geometries. The requirements for the integers m, n and k are given in Section 4.2.2. In principle, several complementary 1:k and m:n ratio sub-cavities can be defined within the host laser cavity to obtain optimum performance. It is expected that adequate and more uniform suppression of all non-harmonic modes should be achievable with fewer ICRs in this layout than in that of Ref.[4].

As can be seen from the results of Section 9.2.4, the twin-ICR laser has demonstrated both a satellite-mode-free spectrum and a subharmonic-free autocorrelation. Such devices can also be designed to provide single-mode operation.

11.3.3. The parallel compound cavity

The layout of Figure 5.11 is an improved version of the original parallel cavity design of joint paper [5]. The improved design allows 1:n ratios to be realised in a parallel cavity geometry while preserving high tolerance to cleaving error. See Section 5.3.1 for details.

11.3.4. Wet-etch facilitated precision cleaving

Cleaving error unavoidably limits the precision of compound cavity definition in CCM devices. The process of Section 7.1.3 was developed to improve the cleaving precision by replacing the inaccurate mechanical scribing with lithographically-defined wet-etch pits. Accurate cavity lengths were obtained by cleaving the resulting samples with the application of slight mechanical pressure without the need for a scribe and cleave machine. A cleaving error of only ±4 μm was thus obtained.

11.3.5. Bow-tie slot definition

In Section 7.1.2, the lithographic definition of a shallow slot in a ridge waveguide was described, where the slot and the waveguide could be etched concurrently in one etch step. A bow-tie slot design was developed to overcome the over-exposure and erosion of ridge corners due to exposure proximity effects.

11.3.6. Reciprocal autocorrelation for ease of alignment

The use of light-emitting devices (LEDs and lasers) as non-linear TPA detectors for autocorrelation measurements of modelocked and Q-switched laser diodes is commonly known. Presumably, it should also be straightforward that by forward-biasing such a detector device, one can use its output beam to align the autocorrelator. What may be non-trivial, though, is the suggestion that the laser diode under test may actually be used as a linear detector to the alignment beam from the non-linear detector laser. In such a reciprocal arrangement, the coupling efficiency between the two devices and the overall alignment and calibration of the set-up can be greatly improved. This method was used for the alignment of the autocorrelator of Chapter 8 and is mentioned in Section 8.4.4.

11.4.   Suggestions for future research

The main goal of this Project has been achieved by demonstrating modelocked laser operation at terahertz frequencies. At the same time, this result can be viewed as only a step towards developing more advanced THz sources. The research merits further studies, with some recommendations and ideas proposed below.

11.4.1. Frequency stabilisation

To be truly practicable, a THz frequency source must generate a stable output with a narrow microwave linewidth. For example, atmospheric radiometry in the 1 – 2.5 THz band requires a source that is stable to within 100 kHz and has a linewidth of no more than 100 kHz. However, modelocked laser diodes are known to suffer from timing jitter (fluctuation of the inter-pulse period), which can be reduced by

locking the laser to a sub-harmonic microwave (electrical) signal or a second optical signal. In the case of THz CCM lasers, no electrical stabilisation is viable, as this would prove very inefficient at too low a sub-harmonic of the THz modelocking rate. A brief overview of frequency stabilisation techniques was given in Section 2.2.5.

The autocorrelation data measured from a low-harmonic CCM device suggest that the pulse width is much broader than expected from the lasing spectrum. Whilst this may be explained by the presence of frequency chirp in the pulses, it is improbable that chirp alone could account for such a large deviation in the pulse width (1.6 times). It is suggested that the apparently large pulse width recorded is partly due to the timing jitter in the generated pulse train. While one can only expect to see the effect of timing jitter on the correlation peak width in a cross-correlation (i.e., performed between different pulses), it is possible that some peak broadening can be observed in an autocorrelation, too. This is corroborated by the observation of a decreased autocorrelation peak width in lasers stabilised by sub-harmonic optical pulses, compared to free-running lasers, in Refs.[6, 7]. The stabilised lasers also exhibited a collapse of the microwave linewidth corresponding to their modelocking frequency. Therefore, a similar stabilisation method can be applied to the CCM lasers developed under this Project.
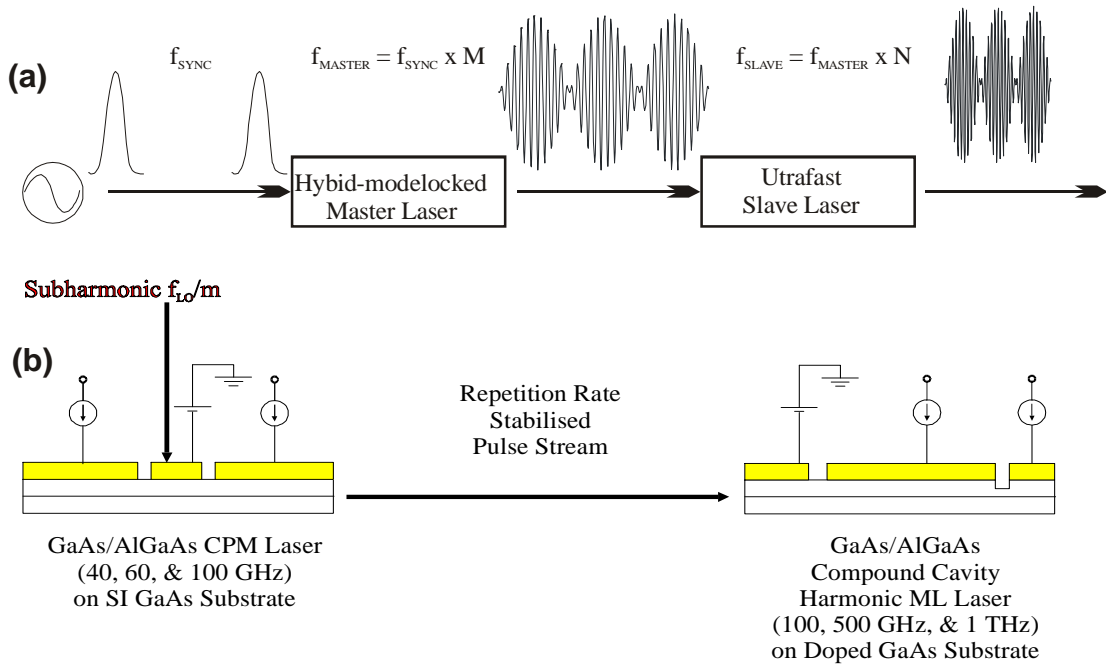
Figure 11.1. Representations of a generic **(a)** and proposed **(b)** cascaded electrical-optical clock synchronisation schemes.

A cascaded electrical-optical synchronisation scheme, such as the one shown in Figure 11.1(a), can be used with the ultrafast CCM lasers. It incorporates a tandem of modelocked lasers, both of which are MW-linewidth-narrowed with the appropriate technique. The master laser is hybrid-modelocked by the application of a "slow" electrical signal to the saturable absorber at frequency f_{SYNC}, which can be an Mth sub-harmonic of the master's modelocking frequency f_{MASTER}. By virtue of electrical synchronisation, the master emits a very stable pulse train, which is used as an optical clock to stabilise the ultrafast slave laser modelocked at the Nth harmonic of the master laser, i.e., $f_{SLAVE} = N f_{MASTER} = N M f_{SYNC}$. Using such a cascaded synchronisation scheme, an $N \times M$ harmonic multiplication of the electrical frequency f_{SYNC} can be achieved.

In the original Project proposal, it was planned to realise such a synchronisation scheme with two types of laser diode, as illustrated in Figure 11.1(b). Initially, a 100 GHz pulse stream was to be generated using a GaAs/AlGaAs colliding-pulse modelocked (CPM) laser, which is frequency-stabilised by locking to a sub-harmonic microwave signal applied to the saturable absorber. The CPM lasers were successfully fabricated by the author's colleagues Dr. M. Street and Dr. H.K. Lee, who have demonstrated a reduction of the timing jitter of the modelocked devices under electrical locking [8]. It was then anticipated that the output of the frequency-stabilised CPM laser at around 100 GHz would be optically injected into a CCM device modelocked at around 1 THz with a view to reducing the timing jitter of the latter.

However, due to time constraints, the above experiment has not been attempted; yet it will still be advantageous to stabilise the fabricated CCM lasers using this configuration. Therefore, it is suggested that future work in this direction should include a frequency stabilisation experiment in order to demonstrate the suitability of the narrow-linewidth CPM/CCM-laser-based source for many demanding terahertz applications.

11.4.2. Down-conversion of a CCM laser using a photomixer

The down-conversion of the modelocked output of a (frequency-stabilised) CCM laser into free-space or guided THz radiation will truly unlock the potential of modelocked laser diodes as ultrahigh frequency sources. Photomixing is believed to

be the preferred down-conversion technique for this type of optical source. Indeed, compared to the existing photomixing pumping schemes reviewed in Section 10.3.1, the proposed source offers significant advantages such as:

- The two or more spectral lines for heterodyning are generated as lasing modes within one laser cavity, which makes redundant the complicated control and phase loop electronics required to lock two individual laser sources.

- Furthermore, the spectral lines are phase-locked to each other by virtue of modelocking, which results in a near-ideal sinusoidal output for the case of two locked modes (Type-II spectrum) or pronounced optical pulses for three or more modes (Type-III spectrum).

- The above characteristics are expected to provide higher optical-to-microwave conversion efficiencies due to the increased modulation depth of the THz envelope on the optical carrier, as can be seen by juxtaposing the signals of Figure 2.1 II(b) and III(b) with the signal II(d) that is produced by a conventional two-colour source.

It is therefore proposed to realise such a source using a CCM laser with the type of photomixer devices fabricated in this Project (Section 10.2) and carry out measurements of the generated THz power.
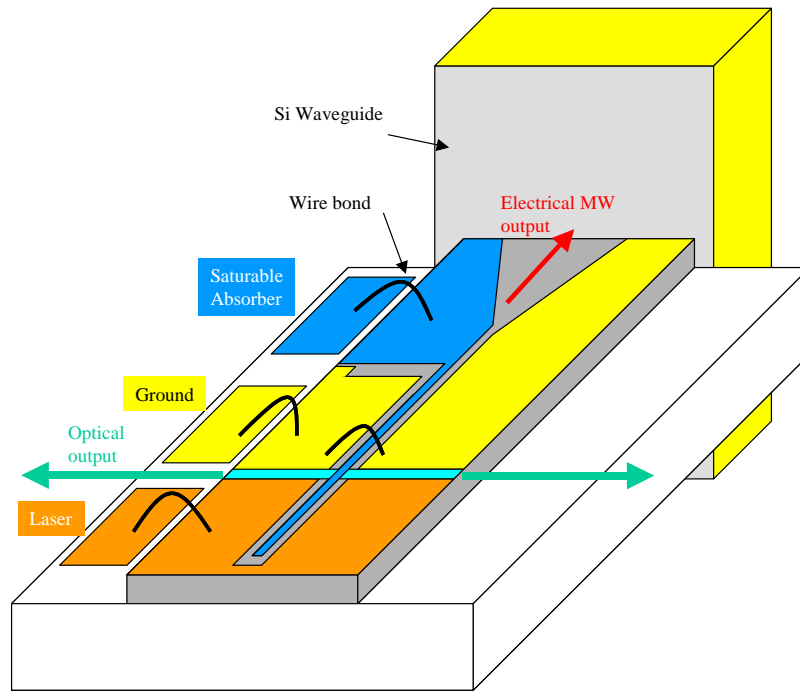
11.4.3. Extraction of a microwave signal from the saturable absorber

Another approach to generating microwave (MW) power can be realised by extracting a high-frequency electrical signal from the passively modelocked laser diode itself. Indeed, the fast optical oscillation at the modelocking frequency will give rise to an electrical modulation on the saturable absorber (SA) at this frequency due to the intensity-varying electro-absorption of photons in the SA section. This modulation, although a very weak one, can be directly extracted from the SA and measured using an RF spectrum analyser.

This approach was verified experimentally by the author's colleague Dr M. Street, who carried out MW-signal extraction experiments using GaAs/AlGaAs CPM lasers on a semi-insulating substrate (i.e., with both p and n contacts on the top side of the device) [9]. The devices had a ground-signal-ground (GSG) split contact

configuration to allow high-frequency signals to be directly injected into/extracted from the SA section. When the devices were modelocked, a MW peak at modelocking frequencies of 40 – 120 GHz was registered in the electrical signal measured from the SA section.

This idea was developed further by proposing to incorporate the CPM laser in a coplanar waveguide on the same semi-insulating substrate, with the SA section being formed by the inner waveguide stripe. The electrical modulation from the SA will then propagate along the waveguide and be emitted by the horn antenna into the bulk silicon waveguide abutting onto the substrate, as illustrated in Figure 11.2 The Si waveguide or lens can be engineered to beam/focus the generated MW radiation in free space as required.

Figure 11.2. Proposed microwave signal extraction scheme using a CPM laser (courtesy of Dr M. Street).

Potentially, one can also use the set-up of Figure 11.2 to extract a MW signal from the SA section of CCM lasers, for which they will also have to be fabricated on a semi-insulating substrate. However, the generated MW powers are expected to be extremely small. The weak signals extracted from the CPM lasers of Ref.[9] at 120 GHz will become even smaller with increasing frequency, which will make this approach impracticable for CCM lasers operating in the terahertz region. Indeed, it is doubtful whether the electrical bandwidth of such devices can be extended beyond

several hundreds of gigahertz even by careful minimisation of the length of the SA section and reduction of *RC*-parasitics. At the same time, the saturable absorbers of harmonic-modelocked laser diodes (both CPM and CCM) can be used as robust and inexpensive microwave sources in multi-GHz applications requiring low input powers, or where amplification can be provided.

11.4.4. Bent-cavity lasers

It will be very interesting to obtain CCM operation from non-linear-cavity lasers. Such devices were designed (see Section 5.3) and fabricated (Section 7.3.2) in this Project, however, no results were obtained due to technological issues. It is hoped that if the fabrication of such lasers is fully developed, they will offer a number of advantages over linear-cavity CCM devices, such as reduced chip dimensions, absence of sub-micron features and improved tolerance to cleaving error.

11.4.5. Quantum-dot CCM laser

The spectra of the ultrahigh-frequency CCM lasers obtained in this Project contain only two modes [see Figure 9.5(IV-a) and (V-a)], with a third mode suppressed by about 20 dB. The number of lasing modes is restricted by the limited gain bandwidth of the quantum-well medium. Quantum-dot material, by contrast, possesses a much wider gain curve due to the natural variation of quantum dot sizes in the active region. It is hoped that an ultrafast quantum-dot CCM laser will modelock with three or more modes in the spectrum, giving out short, well-defined pulses rather than a mere sinusoidal envelope.

11.4.6. External-cavity CCM laser

As a follow-up to the observed external-cavity CCM effect (see Section 9.3), one can engineer a number of interesting external-reflector configurations, where a desired modelocking harmonic can be selected by changing the external mirror position from the laser facet.

A particularly attractive embodiment of this idea would be a twin-ICR laser, similar in principle to the design of Section 11.3.2, with a 1:*k* ratio created by an

ICR, but an *m:n* ratio defined by the external cavity (see Figure 9.11), i.e., the function of the second ICR performed by the inside laser facet. The *m:n* ratio can be easily varied by translating the external mirror, with specific ratio combinations enhanced by the internal (semiconductor) 1:*k* cavity.

To illustrate the feasibility of this idea, a simple estimate of the device geometry can be made. For the internal cavity, assume an ICR defining a ratio of 1:2 with a harmonic $M = 3$, as in the example of Figure 4.7. For the external cavity, Eq.(9.1) will be used to obtain harmonics *M* that are multiples of 3. Such harmonics can be created with a multitude of *m:n* ratios, hence only the ratios achievable with the shortest external cavity (to minimise the loss of unguided light in free space) will be used. Assuming an 800 μm-long laser diode with a semiconductor refractive index $n_{sc} \sim 3.5$, one can calculate the length of the external cavity (i.e., the position of the external mirror measured from the facet) using Eq.(9.1). The calculated data are plotted in Figure 11.3(a).
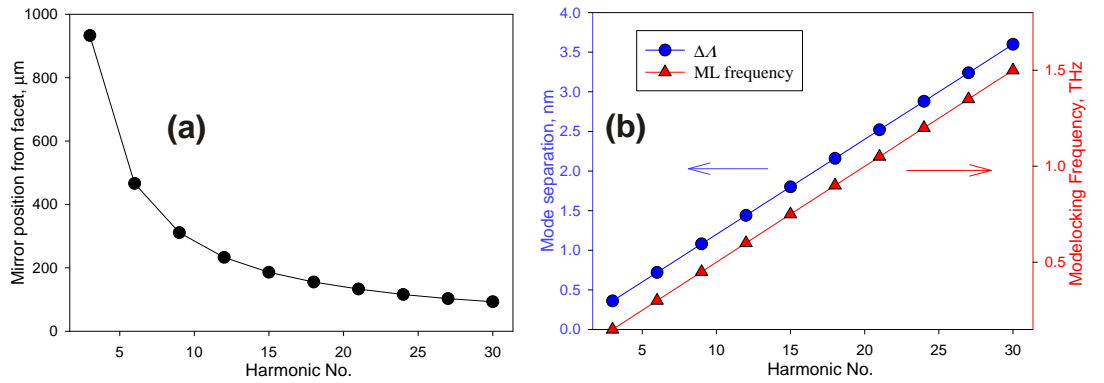
Figure 11.3. Calculated external cavity length for different harmonic numbers in a 800 μm-long laser **(a)** and corresponding tuning curve showing harmonic multiplication of mode separation Δ*Λ* and modelocking frequency **(b).**

It can be seen that for higher harmonics to be selected, the mirror needs to be brought increasingly close to the laser facet. This will lead to an increasing amount of external feedback entering the laser cavity owing to an increased *Q*-factor of the external cavity, which will aid in the preferential selection of increasingly further separated harmonic modes. Recalling the analysis of the CCM laser results of Section 9.4, one notes that side-mode-free spectra at high harmonics were only obtained with highly reflective ICRs, or, in other words, high-finesse sub-cavities, which acted as Fabry-Pérot etalons. The mode selectivity in the proposed external-cavity device is expected to be self-adjusting, as the *Q*-factor/finesse of the free-

space etalon is automatically increased by reducing the latter's length to tune the device to higher harmonics. A non-planar (e.g., concave, parabolic) mirror can be used to optimise the amount of feedback between the external and internal cavities. The feedback can also be controlled by applying anti/high-reflection coating to the inside laser facet.

Another possible embodiment of the same principle is to replace the external metal mirror with a semiconductor saturable-absorber mirror (known as a "SESAM") and remove the saturable absorber section from the laser. A SESAM mirror has been shown to induce modelocking in solid-state lasers by providing the saturable absorption and reflection functions simultaneously [10].

If modelocked, the external cavity CCM laser would offer frequency tuneability in the range from tens of GHz to over 1 THz. If used as a multi-colour source (whether modelocked or not), its mode separation can be quasi-continuously tuned from ~0.5 nm to several nm, as illustrated in Figure 11.3(b). Such a compact laser source with a sub-millimetre external cavity could provide an attractive alternative to the bulky grating-loaded set-up described in Section 10.3.

11.4.7. Multi-slot single-mode laser

The idea of a monolithic twin-ICR laser (Section 11.3.2) can be developed further to create a multi-slot device, in which the ICRs are designed to cancel the different mode patterns in order to obtain lasing in a single mode only. Here, the reflectivities of the individual ICRs are assumed to be small compared to the facet reflectivity, so that their contributions can be treated additively. In essence, this is the approach of Ref.[4], where single-mode operation was obtained by etching n ICRs at binary fractions $L / 2^n$ of the total cavity length L. In this layout, the contribution of the n-th slot is to suppress all but every 2^n-th mode, with $\Delta \Lambda_n = 2^n \Delta \lambda_0$. However, some modes enhanced by low-order slots are also enhanced by higher-order ones, which may result in the incomplete suppression of such modes. For example, every other mode selected by a 1:1-ratio cavity (1st slot at $L / 2$) is also enhanced by a 1:3 cavity (2nd slot at $L / 4$); alternate modes of the 1:3 cavity and every 4th mode of the 1:1 cavity are supported by a 1:7 cavity, etc.

This problem can be overcome by placing ICRs at such fractions of the cavity that no mode intervals are shared by any two 1:n sub-cavities. This can be achieved if a series of prime numbers, rather than a power series, is used to define such fractions, i.e., ICRs are positioned at L / P_n, where P_n is the n-th prime number (1, 2, 3, 5…) corresponding to the n-th ICR. The slot positions and corresponding cavity ratios are schematically shown in the cavity of Figure 11.4(a) for $P_2 = 2$ through $P_{12} = 31$. For higher numbers, the separation between consecutive ICRs approaches several wavelengths and would lead to diffraction effects. In this layout, no common "harmonic" is enhanced by any two ICRs. In other words, no "harmonic" selected by any one ICR has a "sub-harmonic".
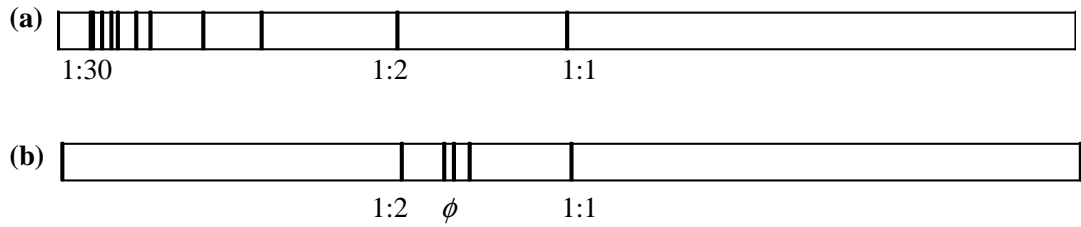
Figure 11.4. Multi-slot single-mode laser cavities for ICR layouts based on prime **(a)** and Fibonacci **(b)** numbers.

The same effect can also be achieved with slots dividing the cavity into m:n ratios. There is more than one way of doing so, as several m and n combinations can give an identical harmonic number. It is proposed that a converging series should be used to define m and n, since the "high-harmonic" ICRs would be much closer spaced than the "low-harmonic" ones, yielding higher reflection for higher harmonics due to diffraction effects. A suitable candidate for such a series are Fibonacci numbers (each number being the sum of the previous two), with the ratio between two consecutive numbers converging rapidly to the "golden section" $\phi \approx 0.618$. As ϕ is an irrational number, it cannot be accurately represented by any m:n ratio, hence no "harmonic" modes are expected in the spectrum. With F_k being the k-th Fibonacci number and $F_1 = F_2 = 1$, the sub-cavity ratio defined by the k-th slot is F_k:F_{k+1} and the corresponding "harmonic" number $M_k = F_{k+2}$. Befittingly, all F_k:F_{k+1} ratios are irreducible, i.e., F_k and F_{k+1} have no common factors for any k, which qualifies them for use as integers m and n. A cavity with the ratios 1:1, 1:2, 2:3, 3:5 and 5:8 defined by the first six Fibonacci numbers is illustrated in Figure

11.4(b), with the *m:n* ratios rapidly approaching ϕ for increasing *m* and *n* values (or increasing *k*).

Both the 1*:n* and *m:n* cavity-ratio designs described here are expected to provide superior side-mode suppression than the methods reported in the literature. They are not, however, intended to provide wavelength tuneability; conversely, their design is aimed at delivering stable single-mode operation for a broad range of bias conditions. Comprehensive numerical simulations of the proposed device structures are required to corroborate their anticipated spectral properties.

11.4.8. PBG mirror CCM laser

A major challenge with the fabricated CCM devices was precision cavity ratio control. Inevitably, facet cleaving causes a cavity length error of several microns, with a deviation from the target cavity ratio as a result. On the other hand, etched-facet devices failed to deliver satisfactory lasing performance to be used for autocorrelation and spectral measurements. Furthermore, in order to improve the harmonic mode selection by enhancing the finesse of the shorter sub-cavity, it is desirable to increase the reflectivity not only of the ICR but also of the opposite laser facet. This is usually achieved by depositing a high-reflectance facet coating, which adds a complicated processing step with poor controllability.
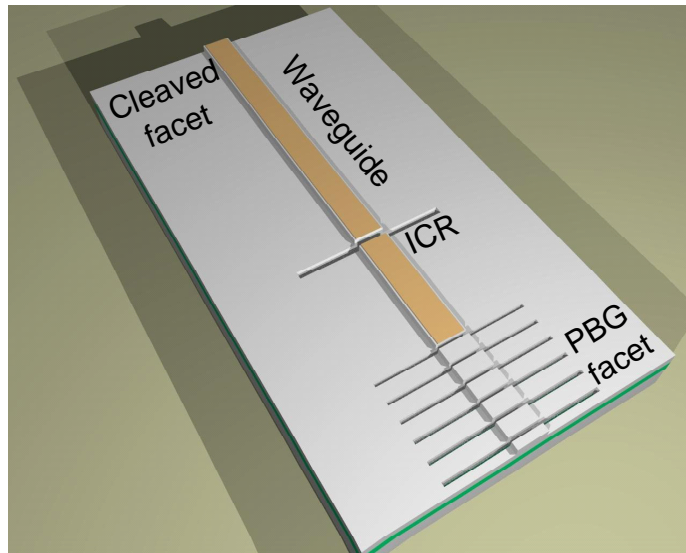
Figure 11.5. Schematic of a compound-cavity laser with a PBG mirror (courtesy of D. Brown, [11]).

Both an improved cavity ratio precision and high cavity finesse can be attained by replacing a cleaved facet with a PBG microstructure. Such a structure would be very similar to the multi-slot PBG ICR features employed in the fabricated CCM devices, possibly differing only in the number of PBG periods required to obtain desired reflectivity. Indeed, such a PBG-mirror device is already being fabricated by D. Brown, who is completing his Ph.D. research at St. Andrews University. The laser, shown schematically in Figure 11.5, incorporates one cleaved and one PBG mirror facet, and a single-slot ICR. On the author's advice, it is planned to replace the single-slot ICR with another PBG structure to avoid the stability and repeatability problems associated with a one-off etched feature. The PBG mirror laser is intended for wavelength-tuneable single-mode operation, with the tuning achieved by varying the pumping level of the shorter (etalon) cavity to adjust its optical length. No modelocking operation has been planned, hence the device does not includes a saturable absorber. Early results of the laser's performance are reported in Ref.[11].

11.5. Conclusions

It is now time to complete the Thesis with key conclusions from the work carried out under the Terahertz Project.

The harmonic CCM model of Chapter 4, predicting the ultrafast modelocking operation of compound-cavity semiconductor lasers, has been successfully utilised. As predicted, the fabricated devices were modelocked at the design harmonics of the fundamental pulse repetition frequency. Compound cavities defined with highly reflective PBG microstructures and a precision cleaving technique proved indispensable to the high-frequency modelocking operation of the CCM devices.

The realised modelocking frequencies of up to 2.1 THz have demonstrated the suitability of the CCM technique for the generation of microwave-modulated optical power in the terahertz range. However, more work is required to make a CCM-laser-based source truly practicable.

Some form of frequency stabilisation and locking is desirable to improve the quality of the generated THz signal. The cascaded electrical-optical clock synchronisation scheme of Section 11.4.1 is deemed to be the most appropriate

frequency locking method. It is recommended that the optical output of the frequency-stabilised CCM-laser source should be down-converted into THz radiation using a photomixer device loaded, e.g., with an antenna or coplanar transmission line. A coherent, narrow-microwave-linewidth, compact and robust terahertz source based on CCM laser diodes would be an ideal candidate for many of the important applications reviewed in Chapter 1. At lower frequencies, the extraction of a MW signal directly from the saturable absorber section may prove an attractive option

It should also be noted that the technology and device designs developed here for CCM operation can be utilised to build non-modelocked devices with remarkable spectral characteristics. For example, a comb of narrow-linewidth, equidistant modes can be generated with a CC-type laser. Wavelength tuneability can also be achieved by placing the device in an external cavity, as suggested in Section 11.4.6. Using broad-gain media, such as quantum dots, may prove particularly beneficial for these applications (Section 11.4.5).

By intentionally deviating from integer sub-cavity ratios and using PBG structures as reflectors/mirrors, one can realise reliable compound-cavity lasers emitting in a single longitudinal mode, thus rivalling the expensive DFB and DBR devices. Alternatively, multi-ICR designs can be employed to achieve single-mode operation, as proposed in Section 11.4.7.

Finally, it is hoped that the research presented in this Thesis has advanced the frontier of terahertz-wave generation and will make the largely disused THz frequency region more accessible. It is also the author's sincere hope that this research will be continued and many of the ideas and concepts proposed here will be explored and bear fruit.

Finis coronat opus

11.6. References

[1]   K. Zetie, "Compound-Cavity Diodes Promise T-Rays," *Technology World, Photonics Spectra*, pp. 55, Sept. 2001.

[2]   C. J. M. Smith, D. A. Yanson, and J. H. Marsh, "Multi-section laser with photonic crystal mirrors." UK Patent No. 0218548.6, 2002.

[3]   D. A. Yanson, "Diffractive In-plane Frequency-selective Focusing Optical Coupler (DIFFOC)-based photonic devices." UK Patent, 2003 (being filed at the time of writing).

[4]   D. A. Kozlowski, J. S. Young, J. M. C. England, and R. G. S. Plumb, "Longitudinal mode control in 1.3 mm Fabry-Perot lasers by mode suppression," *IEE Proc.-Optoelectron.*, vol. 143 (1), pp. 71-76, 1996.

[5]   E. A. Avrutin, F. Camacho, A. C. Bryce, C. J. Hamilton, D. Yanson, J. M. Arnold, and J. H. Marsh, "Analysis of monolithic parallel-compound-cavity semiconductor lasers for high brightness, single-frequency, and short-pulse operation," presented at The Conference on Lasers and Electro-Optics (CLEO"99), Baltimore, 24-29 May 1999, paper CTuK55.

[6]   S. Arahira, Y. Katoh, D. Kunimatsu, and Y. Ogawa, "Stabilization and timing jitter reduction of 160 GHz colliding-pulse modelocked laser diode by subhamronic-frequency pulse injection," *IEEE Trans. Electron.*, vol. E83-C, pp. 966-973, 2000.

[7]   S. Arahira, S. Kutsuzawa, and Y. Ogawa, "Extreme Timing Jitter Reduction of a Passively Mode-Locked Laser Diode by Optical Pulse Injection," *IEEE J. Quant. Electronics*, vol. 35, No. 12, pp. 1805-1811, 1999.

[8]   H. K. Lee, M. W. Street, I. G. Thayne, A. C. Bryce, and J. H. Marsh, "Efficient direct modulation of colliding pulse mode-locked lasers on semi-insulating substrate at 1.5 um,," presented at 8th IEEE International Symposium on High Performance Electron Devices for Microwave and Optoelectronic Applications, Glasgow, UK, 13-14 Nov., 2000.

[9]   M. W. Street, S. D. McDougall, D. A. Yanson, A. C. Bryce, I. G. Thayne, J. H. Marsh, E. A. Avrutin, and J. S. Roberts, "Low-Jitter Optical Pulse Generation at Sub-THz Repetition Rates Using Hybrid Colliding Pulse Mode-locked Semiconductor Lasers," Unpublished manuscript.

[10]   S. Schon, M. Haiml, L. Gallmann, and U. Keller, "Fluoride semiconductor saturable-absorber mirror for ultrashort pulse generation," *Opt. Lett.*, vol. 27, pp. 1845-1847, 2002.

[11]   D. H. Brown, M. B. Flynn, L. O. Faolain, W. Sibbett, and T. F. Krauss, "Coupled Cavity Lasers Incorporating Bragg Mirrors," presented at LEOS'03 Annual Meeting, Tucson, Arizona, Paper WL6, 29 Oct. 2003.

APPENDICES

Process sheet for the fabrication of cleaved-facet CCM lasers

Name:	
Sample ID:	
Wafer No. :	
Draw a sketch of sample shape	
Sample size (width x height, mm)	
Date Started:	
Device Version:	CC-14

1. Cleaving & Cleaning 1. Cleave the sample to size. Width: 8.6...9.1 mm; Height: 13..16mm 2. Ultrasonic in acetone for 5mins. Use big flat beaker or flat bottom dish. 3. Ultrasonic in methanol for 5mins 4. Rinse in running RO water for 5 min 5. Blow dry 6. Inspect. Repeat if there are spots/stains on the surface	**Date:** **Comments**
2. SiO$_2$/Si$_3$N$_4$ Deposition 1. Deposit 300nm of PECVD SiO$_2$ or Si$_3$N$_4$	**Date:**
3. EBL 0: Writing of Slots & Reg. Markers (**"Simple" Job**) 1. Spin 12% Ald. for 60s at 5000rpm 2. Swab the back of the sample with a cotton bud dipped in acetone 3. Bake at 180ºC for 1hr 4. Spin 4% ELV. for 60s at 5000rpm 5. Swab the back of the sample with a cotton bud dipped in acetone 6. Bake at 180ºC for 2hrs 7. Submit job and transfer job files. Refer to Data Sheet for details. 8. After writing, develop for 45s in 1:2 MIBK at 23°C and inspect	**Date:** **Job name:**
4. Dry Etching of Slots & Reg. Markers 1. Dry etch the SiO$_2$ / Si$_3$N$_4$ mask with CHF$_3$ in S100 or BP80. Assume an etch rate of 15 nm/min for SiO$_2$ and 10nm/min for Si$_3$N$_4$ (eg to etch 200nm of SiO$_2$ specify ~ 15min). Over-etch slightly. <u>Tip:</u> specify you want 600nm of SiO$_2$/Si$_3$N$_4$ etched instead of real 300. 2. Dry etch GaAs/AlGaAs with SiCl$_4$ gas in RIE80 / S100 for 18 min. 3. Inspect surface carefully. 4. Inspect quality of slots in SEM	**Date:**
5. Removal of Resist and SiO$_2$ / Si$_3$N$_4$ 1. Strip resist in warm acetone/steam bath for ~2h. Leave overnight. 2. Ultrasonic for 5min 3. Rinse in Methanol and then in water for 3 min. Blow dry. 4. Strip SiO$_2$ / Si$_3$N$_4$ in 1:4 HF silica etchant for 30s. 5. Inspect & repeat steps 1-3 until there are no traces of resist on surface. 6. Rinse in water for 3 min. 7. Inspect	**Date:**
6. SiO$_2$/Si$_3$N$_4$ Deposition 1. Deposit 200nm of PECVD SiO$_2$ or Si$_3$N$_4$ 2. Inspect. Redo if there are spots or stains on the surface.	**Date:**
7. EBL 1: Writing of Ridges & Text (Reg. Job)	**Date:**

1. Spin 4% Elv. for 60s at 5000rpm 2. Swab the back of the sample with a cotton bud dipped in acetone 3. Bake at 180ºC for 3hr 4. Submit job and transfer job files. Refer to Data Sheet for details. 5. After writing, develop for 30s in 1:3 MIBK at 23°C and inspect	**Job name:** **Marker used:**
8. Dry Etching of Ridges & Text 1. Dry etch the SiO_2 / Si_3N_4 mask with CHF_3 in S100 or BP80. Assume an etch rate of 15 nm/min for SiO_2 and 10nm/min for Si_3N_4 (eg to etch 200nm of SiO_2 specify ~ 15min). Over-etch slightly. Tip: specify you want 400nm of SiO_2/Si_3N_4 etched instead of real 200 2. Dry etch ridges in GaAs/AlGaAs with $SiCl_4$ gas in RIE80 / S100 to required depth using interferometer (focus spot in the bottom left corner on either of the 2 exposed TLM sites) 3. Inspect surface carefully under optical microscope and in SEM	**Date:** **Ridge height:**
9. Removal of Resist & Silica/Nitride Follow **Step 5.**	**Date:**
10. SiO_2/Si_3N_4 Deposition & Anneal 1. Deposit 300nm of PECVD SiO_2 2. Anneal the sample @ 360ºC for 3 min. to degas SiO_2 3. Inspect. Redo if there are spots or stains on the surface.	**Date:**
11. EBL 2: Writing of Windows & Cleaving Nicks **(Reg. Job)** 1. Spin 15% Ald. for 60s at 5000rpm 2. Swab the back of the sample with a cotton bud dipped in acetone 3. Bake at 180ºC for 3hr 4. Spin 4% Elv. for 60s at 5000rpm 5. Swab the back of the sample with a cotton bud dipped in acetone 6. Bake at 180ºC for 3hr 7. Submit job and transfer job files. Refer to Data Sheet for details. Ask operator to allow 5 mm of free space on either side of your sample. 8. After writing, develop for 35s in 1:2 MIBK at 23°C and inspect	**Date:** **Job name:** **Marker used:**
12. Wet Etching of Contact Windows & Nicks; Removal of PMMA 1. Wet-etch the sample in 1:4 HF silica etchant for 25s. (Dry-etching is also possible but it may be harder to strip resist). 2. Inspect. Make sure windows in SiO_2 / Si_3N_4 are not over-etched. 3. Use hot acetone to remove PMMA mask. Leave in acetone overnight. 4. Rinse in methanol and IPA, blow dry.	**Date:**
13. EBL 3: Writing of Contact Lift-off & TLM Pattern (Reg. Job) 1. Spin 15% Ald. for 60s at 5000rpm 2. Swab the back of the sample with a cotton bud dipped in acetone 3. Bake at 180ºC for 1hr 4. Spin 4% ELV. for 60s at 5000rpm 5. Swab the back of the sample with a cotton bud dipped in acetone 6. Bake at 180ºC for 2hrs 7. Submit job and transfer job files. Refer to Data Sheet for details. Ask operator to allow 5 mm of free space on either side of your sample. 8. After writing, develop for 45s in 1:1 MIBK at 23°C and inspect	**Date:** **Job name:** **Marker used:**
14. Ashing 1. Mount the sample epitaxial side up on a glass cover slip with S1818 resist and bake for 10 mins @ 120°C 2. Ash sample in oxygen for 1 min in the B3 cleanroom asher.	**Date:**
15. p-Contact Evaporation & Lift-off 1. Submit sample for p-contact evaporation (Ti/Pd/Au 30/30/150nm).	**Date:**

2. Evaporate Ti/Au 20/100nm in the 2nd floor evaporator. Rock the sample about the axis parallel to the ridges during evaporation. 3. Lift-off in acetone and separate cover slip from sample. Agitate gently. 4. Leave in acetone overnight. 5. Change acetone and place the covered beaker in the steam bath for 1h. 6. Rinse in methanol and water, and blow-dry	
16. Photolithography 1: Masking Main Pattern 1. Spin S1828 for 30s at 4000rpm 2. Bake at 90ºC for 30mins 3. Expose vertical edges with cleaving nicks for 60s using any suitable blanket (Cr) mask 4. Develop for 30s in 1:4 MF351 developer : water	**Date:** **Job name:**
17. Wet-etching of Cleaving Nicks (*) 1. Wet-etch the sample in $H_2SO_4:H_2O_2:H_2O$ 1:8:40 for 2hr. 2. Inspect to see if deep triangular pits have been formed (depth ~ 80μm).	**Date:**
18. Thinning 1. Spin S1818 for 30s at 4000rpm to protect surface 2. Mount the sample epitaxial side down on a glass cover slip with S1818 3. Bake at 120ºC for 30mins 4. Mount cover slip and sample on metal post with wax and lap until ~200μm thick 5. Immerse sample in hot acetone to separate the cover slip and strip resist. Change acetone 2 or 3 times. 6. Rinse in methanol and water, and blow-dry 7. Inspect	**Date:**
19. n-Contact Evaporation & Anneal 1. Mount the sample epitaxial side down on a glass cover slip with S1818 2. Bake at 120ºC for 10mins 3. Immerse sample in concentrated H_2SO_4 for 1 min. 4. Place the sample in a beaker with RO water and rinse in running water under the RO tap for 1 min. Blow dry 5. Submit the sample for n-contact evaporation 6. Separate cover slip from sample in acetone. 7. Rinse in water & blow dry 8. Anneal the sample at 360ºC for 60s (Recipe 9). Make sure that a ramp-up step is included in the recipe. 9. Inspect 10. Perform TLM measurements with the HP Parametric Analyser.	**Date:**
20. Isolation Etch 1. Wet etch in $NH_3:H_2O_2$ 1:20 for 5s to remove the p++ layer between device sections 2. Rinse in RO water 3. Blow dry	**Date:**
21. Cleaving 1. Mount the sample epitaxial side up on adhesive film 2. Scribe and separate the sample into two halves (left & right). 3. Cleave each half using the etched nicks. 4. Scribe along and separate devices if required.	**Date:**
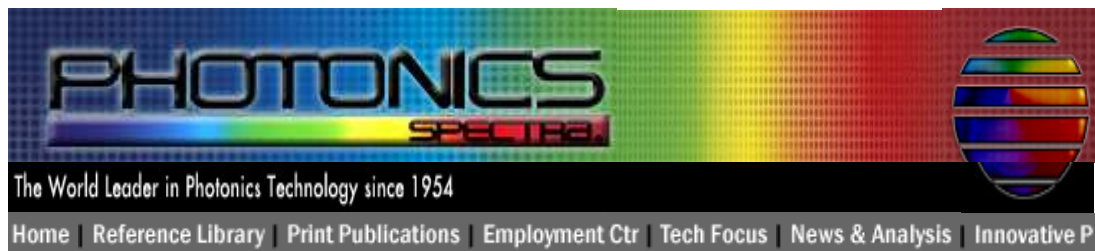
Article published in *Photonics Spectra,* **September 2001**

Photonics TechnologyWorld
September 2001 Edition

Send News to photonics@laurin.com or submit online here

Compound-Cavity Diodes Promise T-Rays

GLASGOW, UK -- The last few decades have been marked by the rapid opening of the high-frequency electromagnetic spectrum for communications, detection and imaging. Remarkably quiet, however, has been the terahertz region, those frequencies between microwaves and the infrared, but that, too, is changing. A new laser diode source with terahertz repetition frequencies may offer an optical path to the generation of terahertz radiation.

These terahertz rays have a wavelength sufficiently short to provide resolution better than 1 mm but long enough to minimize Rayleigh scattering. They are safe and noninvasive, but they can penetrate skin and packaging materials. In addition, a variety of measurement techniques can be employed to distinguish different organic materials, to image tracks on semiconductors or to measure water content in fuel. Applications in medical diagnostics are clear, and terahertz imaging has already been used to observe tooth decay at a very early stage.

The problem has been finding reliable sources of T-rays. Dan A. Yanson of Glasgow University and his colleagues there and at York University may have found a way to access the terahertz region using GaAs/AlGaAs compound-cavity laser diodes. The devices were designed, fabricated and tested at Glasgow, and the Semiconductor Growth Facility at Sheffield University supplied the GaAs material.

The 860-nm lasers are mode-locked to a harmonic of their fundamental round-trip frequency. The compound-cavity devices consist of two gain sections, a saturable absorber and an intracavity slot reflector. It is possible to choose the harmonic by controlling the relative lengths on either side of the reflector, and the researchers were able to produce 2.2 mW of optical power sinusoidally modulated at 2.1 THz by using a wet-etch technique to control the length of the cavities to within a few microns.

Challenge and promise

The laser, which the researchers described in the June 4 issue of *Applied Physics Letters*, may find application as a local oscillator source in detection circuits for atmospheric sensing and astronomy. In telecommunications, it could be employed as an optical clock in time division multiplexing or as a wavelength comb generator in wavelength division multiplexing schemes.

To produce pure T-rays, the optical signal must be down-converted with a terahertz photomixer. Yanson believes that, although the efficiency of such conversion is less than 1 percent, the mode-locked lasers have the potential to generate useful power levels for many applications, including terahertz imaging.

"Whilst direct generation of terahertz radiation presents a challenge," he said, "the down-conversion of optical power into the microwave region is a promising way forward."

by Ken Zetie